Detailed Test–Particle Simulations of Energetic Particles Interacting with Magnetized Plasmas

by

Victor Arendt

A Thesis submitted to the Faculty of Graduate Studies of
The University of Manitoba
in partial fulfillment of the requirements of the degree of

DOCTOR OF PHILOSOPHY

Department of Physics and Astronomy
University of Manitoba
Winnipeg

Abstract

An important research area in space physics and astrophysics is the transport of energetic, charged particles, such as electrons, protons, and muons, in magnetic turbulence, with active research in this field going back to Jokipii (1966). For example, the magnetic turbulence in the solar wind, arising from the combination of the motion of the solar wind plasma and the Sun's magnetic field, deflects energetic charged particles away from their initial trajectories. These particles may have originated in the Sun (solar energetic particles), or from sources outside the solar system such as supernova remnants (galactic cosmic rays) or active galactic nuclei (extra–galactic cosmic rays). Regardless of their origin, these high energy particles will be deflected in the heliospheric magnetic field, with transport being described by diffusion coefficients parallel and perpendicular to the local mean field. Research over the years has shown that the perpendicular transport needs to be described by theoretical models that are highly non–linear. Test–particle simulations performed using various analytical turbulence models have allowed these theoretical descriptions of particle transport to be improved by providing numerical results to compare with theoretical predictions. In this work, a test–particle code has been developed using a new trajectory solver that allows for better energy conservation and position accuracy. This is then used in simulations performed to test the predictions of theory in the limit of small Kubo number turbulence.

Acknowledgements

I would like to thank ...

My parents, Lawrence and Katharina Arendt for their support throughout my education.

My supervisor, Dr. Andreas Shalchi, for taking me on as a graduate student.

Dr. Jason Fiege, for the discussions on the numerical implementation of various equations.

Kelvin Au, for giving feedback on the colour coding of various figures.

The secretaries in the Physics department offices, for answering all my questions regarding grad studies requirements.

Contents

List of Figures

List of Tables

List of Acronyms

General Acronyms

ACEPTS	Astrophysical Charged Energetic Particle Transport Simulator
cgs units	centimeters–grams–seconds units
HMF	Heliospheric Magnetic Field
HPC	High Performance Computing
IPM	Interplanetary Medium
ISEE	International Sun–Earth Explorer
ISM	Interstellar Medium
MHD	Magnetohydrodynamics
NOAA	National Oceanic and Atmospheric Administration
SEP	Solar Energetic Particle
SHO	Simple Harmonic Oscillator
VLISM	Very Local Interstellar Medium

Turbulence Model Acronyms

SNS model	Standard Noisy Slab model
NRMHD model	Noisy Reduced MHD model

MNS model	Modified Noisy Slab model
GNS model	Gaussian Noisy Slab model
F3D model	Full 3D model

Theory Acronyms

FLPD theory	Field Line – Particle Decorrelation theory
FLRW	Field Line Random Walk
NLGC theory	Non–Linear Guiding Center theory
QLT	Quasi–Linear Theory
TGK formulation	Taylor–Green–Kubo formulation
UNLT theory	Unified Non–Linear Transport theory

Numerical Method Acronyms

FFT	Fast Fourier Transform
IRM method	Instantaneous Rotation Matrix method
PQ	Momentum–Position
QP	Position–Momentum
RK	Runge–Kutta

List of Symbols

Units

AU	Astronomical Unit. Average distance between the Earth and the Sun. 1 AU $= 1.496 \cdot 10^{13}$ cm.
µG	microGauss. Magnetic field unit.
eV	Electron Volts. Energy unit used for particle energies. 1 eV $= 1.602 \cdot 10^{-12}$ ergs.
V	Volt. Unit for particle rigidity (energy) used by Palmer (1982).
MV	Megavolt.
GV	Gigavolt.

Mathematical Constants

e	Euler's number. $e = 2.71828\ldots$
i	Imaginary number. $i = \sqrt{-1}$
π	Pi. Ratio between circumference and diameter of a circle. $\pi = 3.14159\ldots$

Physical Constants

c	Speed of light
m	Particle mass
q	Particle charge

Generic Scalar, Vector, and Matrix Symbols

a	Scalar quantity, magnitude of a vector ($a = \|\vec{a}\|$)
$\vec{a}$	Vector quantity, components denoted a_i
$\hat{a}$	Unit vector quantity, magnitude of one
$\|a\|$	Absolute value (magnitude) of a, applies to scalars and vectors
$\bar{\bar{a}}$	Matrix quantity, components denoted a_{ij}
$\vec{F}(\vec{x}, t)$	Vector field quantity
$\delta\vec{F}(\vec{x}, t)$	Vector field quantity, turbulence component

Fourier Transforms

$\tilde{F}(\vec{k}, t)$	Spatial Fourier transform of a scalar field
$\tilde{\vec{F}}(\vec{k}, t)$	Spatial Fourier transform of a vector field
$\vec{k}$	Fourier wave mode vector

Mathematical Operations

$\langle \cdots \rangle$	Averaging operation
$\vec{v} \cdot \vec{u}$	Vector dot product
$\vec{v} \times \vec{u}$	Vector cross product
$\vec{v} \otimes \vec{u}$	Vector outer product
$\Re \cdots$	Real component of the following quantity
$a^\dagger$	Complex conjugate of a
Δ	Difference operator, context dependent

General Symbols

t	Time
$\vec{x}$	Position. Individual components are x, y, and z
$\vec{v}$	Velocity
v	Speed
ℓ_0	Generic length scale

Functions and Special Quantities

${}_nF_m(\cdots)$	Hypergeometric function
$\mathrm{erf}(x)$	Error function
$J_i(x)$	Bessel function of the first kind
$K_i(x)$	Modified Bessel function of the second kind
$\Gamma(x)$	Gamma function
$\delta(x)$	Dirac delta function, scalar
$\delta(\vec{x})$	Dirac delta function, vector
δ_{ij}	Kronecker delta
ϵ_{ijk}	Levi–Civita symbol
$\Theta(x)$	Step function

MHD Symbols

$\vec{B}$	Magnetic field
$\vec{E}$	Electric field
$\vec{J}$	Current density
$\vec{v}$	Velocity field[1]

---

[1] Only applies to the MHD equations at the start of Chapter 2.

v_A Alfvén speed

ρ Density, generic

ρ_p Proton density, used to calculate v_A

ρ_e Charge density

Particle Symbols: Theory

$\vec{p}$ Particle momentum

R_B Magnetic rigidity

R_L Larmor radius

$\vec{V}$ Guiding center velocity

$\vec{X}_{GC}$ Guiding center position

$\vec{\beta}$ Particle velocity divided by the speed of light

γ Lorentz factor

μ Pitch angle cosine; cosine of the angle between the particle velocity and the mean magnetic field

ϕ Time integral of the magnetic field along the particle trajectory; has scalar, vector, and matrix forms

Model Symbols in Physical Space: Theory

B_0 Mean magnetic field strength

K Kubo number

L_{r_i} Integral scale for position r_i; $r_i = \|, \perp$

L_U Ultra scale

$R_{i,c}$ Magnetic correlation function along axis i

R_{nm} Two–point, two–time magnetic correlation tensor component

δB	Root mean square magnetic turbulence field strength, usually given in relation to B_0
ℓ_i	Length scale along axis i; $i = x, y, z$ or $i = \parallel, \perp$

Model Symbols in Fourier Space: Theory

$C(s)$	Slab model spectrum normalization function
$D(s, q)$	2D model spectrum normalization function
$g^{model}(\vec{k})$	Spectral function for field model *model*, sometimes written as $g(\vec{k}, s, q)$
$G(\vec{k}, s, q)$	Indefinite integral of the spectral function
$k_\parallel$	Fourier wave mode component parallel to the z axis
$k_\perp$	Magnitude of the Fourier wave mode component in the xy plane
k_ϕ	Angle of the Fourier wave mode from the x axis in the xy plane
P_{nm}^{model}	Spectral tensor component for field model *model*
q	Energy spectral index
s	Inertial spectral index
$\Gamma(\vec{k}, t)$	Dynamical correlation tensor
σ_{ij}	Angular component of the spectral tensor

Diffusion Symbols: Theory

$D_{\mu\mu}$	Pitch angle diffusion coefficient
d_{ii}	Generic running diffusion coefficient
$d_{FL}(z)$	Running diffusion coefficient, field lines
$d_\parallel(t)$	Running parallel diffusion coefficient, particles
$d_\perp(t)$	Running perpendicular diffusion coefficient, particles

Δx	Displacement, field lines and particles
$\left\langle (\Delta x)^2 \right\rangle$	Mean square displacement
$\bar{\bar{\kappa}}$	Tensor of diffusion and drift coefficients, particles
κ_{ii}	Generic diffusion coefficient
κ_{FL}	Diffusion coefficient, field lines
$\kappa_{\parallel}$	Parallel diffusion coefficient, particles
$\kappa_{\perp}$	Perpendicular diffusion coefficient, particles
λ_i	Mean free path along axis i[2]
$\tau_{\parallel}$	Parallel scattering time
$\rho(\Delta x)$	Displacement distribution function

Scale Factors

B_0	Magnetic field scale factor, equal to the mean magnetic field strength
Ω	Particle gyrofrequency in the absence of turbulence, time scale factor
ℓ_p	Model primary length scale, usually $\ell_{\parallel}$
ℓ_s	Model secondary length scale, usually $\ell_{\perp}$

Particle Symbols: Scaled

$\vec{R}$	Unit–less particle velocity; related to R_B and R_L
T	Scaled time
$\vec{X}$	Unit–less particle position

---

[2] At the start of Chapter 3, λ is used without a subscript as a generic variable.

Model Symbols in Physical Space: Scaled

$\vec{b}$	Scaled total magnetic field
$\bar{\bar{b}}$	Cross product matrix for the magnetic field; $b_{ij} = \epsilon_{ijk} b_k$
δb	Root mean square of the ratio between the energy in the turbulence and the energy in the mean field.
$\vec{\delta b}$	Scaled magnetic turbulence field

Model Symbols in Fourier Space: Scaled

k_z	Scaled parallel Fourier wave mode component ($k_\parallel$)
k_r	Scaled perpendicular Fourier wave mode component ($k_\perp$)

Model Symbols in Numerical Methods

$\tilde{A}(\vec{k}, t)$	Complex Fourier wave amplitude; shortened to $\tilde{A}(\vec{k})$ for static models.
$A(\vec{k})$	Fourier wave amplitude magnitude; shortened to A_n and A_{nm}
k_{max}	Maximum wave mode
k_{min}	Minimum wave mode
k_p	Scaled primary Fourier wave mode component; usually $k_\parallel$
k_s	Scaled secondary Fourier wave mode component; usually $k_\perp$
$\mathbb{V}$	System volume; volume element denoted $\mathrm{d}\mathbb{V}$
$\phi(\vec{k})$	Phase offset for each Fourier wave mode; shortened to ϕ_n and ϕ_{nm}

Diffusion Symbols: Scaled

$D_{FL}(z)$	Scaled running diffusion coefficient, field lines
$D_\parallel(t)$	Scaled running parallel diffusion coefficient, particles
$D_\perp(t)$	Scaled running perpendicular diffusion coefficient, particles

K_{FL}	Scaled diffusion coefficient, field lines
$K_{\parallel}$	Scaled parallel diffusion coefficient, particles
$K_{\perp}$	Scaled perpendicular diffusion coefficient, particles
ΔX	Scaled displacement, field lines and particles
Λ_i	Scaled mean free path along axis i
σ_i^2	Scaled mean square displacement along axis i
$\tau_{\parallel}'$	Scaled parallel scattering time

Numerical Method Symbols

Symbols here are unique to Chapter 4 and Appendices A and B

Simple Harmonic Oscillator Symbols

E	Total energy
p	Generalized particle momentum
q	Generalized particle position
t	Generalized time
τ	Initial SHO phase offset

Particle in a Magnetic Field Symbols

$\vec{A}$	Magnetic potential field
$\vec{B}$	Magnetic field
E	Total energy
$\vec{F}$	Force acting on a particle
H	Hamiltonian
m	Particle mass
p	Particle momentum

q	Particle charge
r, x	Particle position
t	Time
v	Particle velocity
γ	Lorentz factor
ϵ_{ijk}	Levi–Civita symbol
ω	Gyrofrequency, replaces magnetic field
ϕ	Rotation angle of particle from the x axis

Runge–Kutta Method Symbols

a, b, c	Method coefficients
f	Derivative of function being solved
h	Change in independent variable
k	Method intermediate step result
y	Function to solve
α	Energy drift coefficients
β	Solution expansion coefficients
λ	Independent variable

Symplectic Method Symbols

A, B, C, D	SHO solution expansion coefficients
P	Method momentum coefficients
Q	Method position coefficients
α	Particle in a magnetic field energy drift coefficients
β	Particle in a magnetic field velocity expansion coefficients
γ, λ, σ	SHO solution energy expansion coefficients

IRM Method Symbols

$\bar{\bar{I}}$	Identity matrix
$\bar{\bar{M}}$	Velocity/momentum update matrix
$\bar{\bar{M}}'$	Position update matrix
P	Method momentum coefficients
Q	Method position coefficients
$\bar{\bar{R}}_{ij}$	Method projection matrices
$\delta(T; f)$	Error analysis function
ξ	Cumulative sum of method momentum coefficients

Chapter 1

Introduction

When considering the objects that make up the universe, some of the first things that come to mind are galaxies, stars, and planets. Other objects such as black holes and nebula may also be thought of. While these objects are separated by large distances, the space between them is not empty, but is instead filled with a combination of dust, gas, and plasma that is collectively known as the interstellar medium (ISM) outside the solar system and the interplanetary medium (IPM) within it. Embedded within these media are electromagnetic fields that influence the motion of charged particles, such as electrons, protons, and alpha particles that move through them. Some of these charged particles are part of this medium in the form of a plasma and coupled to the electromagnetic fields present as described by the laws of magnetohydrodynamics (MHD). Other particles have been injected into this medium after being accelerated to high energy by various processes such as diffusive shock acceleration in supernovae and supernova remnants (Malkov and Drury, 2001) or from active galactic nuclei (Kronberg and Lovelace, 2015, Pierre Auger Collaboration et al., 2007). Known as *cosmic rays* or *energetic particles*, the paths of high energy ions is influenced by the medium they are moving through and the fields embedded in it.

1.1 The Astrophysical Environment and Energetic Particles

1.1.1 The Solar Wind

Filling our solar system is the solar wind: an outflow of plasma from the Sun. Using observations of the motion of comet tails Biermann (1951, 1952, 1957) suggested that there must be a gas flowing away from the Sun with a velocity between $5 \cdot 10^7$ to $1.5 \cdot 10^8$ cm s^{-1} and a density near Earth of around 500 hydrogen atoms per cubic centimetre. Today, we know from measurements performed by the *Ulysses* spacecraft in the 1990s that the solar wind has a velocity of approximately $4 \cdot 10^7$ cm s^{-1} near the Sun's equator and approximately $7.5 \cdot 10^7$ cm s^{-1} outside the equatorial region (McComas et al., 2003). Near the L1 Lagrange point, the solar wind speed has an average of around $4 \cdot 10^7$ cm s^{-1} and an average density of around 3 protons per cubic centimetre (NOAA, 2024). Data from *Voyagers 1* and *2* show that the electron density between 80 to 90 AU[1] is between 0.0012 and 0.0044 electrons per cubic centimetre, which then increases at the heliopause (around 120 AU) to between 0.039 and 0.055 electrons per cubic centimetre (Gurnett and Kurth, 2019).

1.1.2 Heliospheric Magnetic Field

Utilizing the observations of Biermann, Parker (1958) predicted that the outflow of plasma from the Sun will drag the Sun's magnetic field out into the interplanetary space, forming the heliospheric magnetic field (HMF). The field lines in this model take the shape of what is now referred to as the Parker spiral. Measurements from the L1 Lagrange point give a field strength of between 10 to 100 microGauss (µG) at the L1 point (NOAA, 2024).

As noted by Parker (1958), the resulting spiral pattern for the magnetic field is the result of an idealized model of the solar wind. In reality, fluctuations in the solar wind alter the shape of the magnetic field, leading to non–linear effects such as magnetic turbulence. The magnetic field can be modelled as[2]

$$\vec{B}(\vec{x},t) = \vec{B}_0(\vec{x},t) + \delta\vec{B}(\vec{x},t) \tag{1.1}$$

---

[1] An Astronomical Unit (AU) is the mean distance between the Sun and Earth.

[2] This can be applied to any magnetic system, not just the solar wind.

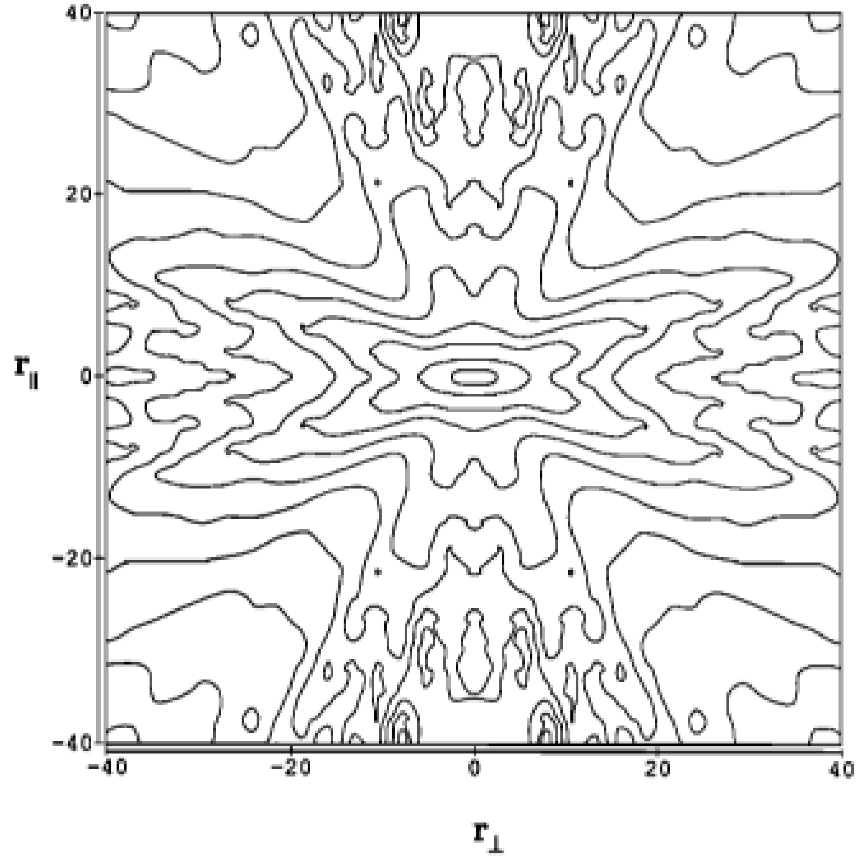

Figure 1.1: Contour plot of the magnetic correlation function for the solar wind by Matthaeus et al. (1990). Data is plotted as a function of distance parallel and perpendicular to the mean magnetic field, with units of 10^{10} cm. *Reprinted with permission from The American Geophysical Union–Matthaeus et al. (1990).*

where $\vec{B}_0(\vec{x},t)$ is the background field and $\delta\vec{B}(\vec{x},t)$ describes the distortions in the field. As discussed in Matthaeus et al. (1990), the two perspectives on dynamics of the HMF can be summarized as either the view that the fluctuations are due to "significant non–linear interactions" or that they are the result of the "superposition of noninteracting MHD modes," which at that point were modelled as *Slab* or *Isotropic* fluctuations.[3] Regardless of the cause, Matthaeus et al. (1990) used data from the ISEE 3 spacecraft to calculate the two–dimensional correlation function[4] for magnetic field in the solar wind (see Figure 1.1) as a function of the distance parallel or perpendicular to the

---

[3] See Chapter 2 for a definition of the models.

[4] Also defined in Chapter 2.

mean magnetic field. This analysis showed that the HMF could not be described by either purely slab or isotropic fluctuations, but rather that it also contained "quasi–two–dimensional, nearly incompressible fluctuations." Based on this, Bieber et al. (1994) proposed that the HMF be modelled as a combination of slab modes and a new *2D* model in which both the magnetic field and corresponding modes are confined to the xy plane.

In addition to correlation functions, there is also the related correlation length scale: the distance that two points can be separated by and still have the turbulence be correlated. Wicks et al. (2009, 2010) found that the correlation length scale of the solar wind magnetic turbulence at around 1 AU is on the order of 0.01 AU.[5]

1.1.2.1 Very Local Interstellar Medium Data

Even after exiting the solar system, the *Voyager* spacecraft have continued transmitting data back to Earth. Reported in Burlaga et al. (2015), *Voyager 1* observed that the magnetic turbulence in the very local interstellar medium (*VLISM*)[6] was dominated by compressible fluctuations with a Kolmogorov–like spectrum ($k^{-5/3}$). Three years later, Burlaga et al. (2018) reported that the magnetic turbulence observed by *Voyager 1* had transitioned to be nearly incompressible with a similar Kolmogorov–like spectrum. Furthermore, Burlaga et al. (2018) reported that the average magnetic field was 4.4 µG and that the ratio between the fluctuations and the average field was 0.02. Zank et al. (2019) showed that this transition from compressible to incompressible turbulence is a result of three–wave interactions in fast magnetosonic waves which converts the turbulence to Alfvén waves and zero frequency two–dimensional vortices.

1.1.2.2 A Note on Compressible and Incompressible Turbulence

When describing turbulence, there are two broad categories: compressible turbulence and incompressible turbulence. Compressible turbulence is defined as having a component of the turbulence parallel to the background mean field, such that $\vec{B}_0 \cdot \delta\vec{B} \neq 0$. This turbulence is termed compressible. On the other hand, incompressible turbulence has its fluctuations confined to the plane perpendicular to the mean field with no density perturbations.

---

[5] The theory and importance of correlation scales is discussed in Chapters 2 and 3, respectively.

[6] Defined by Zank (2015), Zank et al. (2017) as "that region of the interstellar medium surrounding the Sun that is modified or mediated by heliospheric processes or material."

1.1.3 Energetic Particles

The first part of this section is a summary of the 1936 Nobel prize in physics award ceremony speech, given by Professor H. Pleijel on December 10, 1936. (Nobel Prize Outreach, 1936)

By the year 1911, scientists knew that ionizing radiation could be found anywhere on Earth. At the time, the source of the radiation wasn't known, although it was thought to be the breakdown of radioactive elements in the Earth's crust. In 1911 and 1912, Victor Hess made measurements of the ionization rate in the atmosphere by taking electroscopes up in hot air balloons. While his measurements showed a decrease in the ionization rate up to around one kilometre above ground level, which is consistent with ground based sources, the ionization rate increased above this altitude such that at five kilometres the ionizing radiation was double the intensity at ground level. Further measurements by other researchers showed that the radiation intensity at just over 9 kilometres was about 40 times that at ground level. From this Hess concluded that the radiation must be coming from beyond Earth's atmosphere. By the time Victor Hess was awarded half the Nobel prize in physics in 1936 for his research, it had been found that this radiation (named cosmic rays or cosmic radiation) was reaching Earth from every direction. The second half of the 1936 Nobel prize in physics went to Carl Anderson for the discovery of the positron by observing cosmic rays in a cloud chamber. These observations also showed that cosmic rays consisted of charged particles, not just high energy photons.

Cosmic rays can be classified based on the amount of kinetic energy they possess. The lowest energy particles are *solar energetic particles* (SEPs), sometimes referred to as *solar cosmic rays*, with kinetic energies between 10 and 10^9 eV (Shalchi, 2009). These cosmic rays were first indirectly detected by Forbush (1946) and have been determined to come from the sun. At 10^6 eV are anomalous cosmic rays, named due to their composition of elements that are difficult to ionize. Produced when neutral particles are ionized and accelerated at the boundary between the solar wind and ISM, the particles are thought to originate between 75 and 100 AU from the sun (Shalchi, 2009). Galactic cosmic rays are energetic particles originating outside the solar system but within the Milky Way, with energies between 10^9 and 10^{15} eV (1–10^5 GeV). Particles of these energies can be produced via diffusive shock acceleration (Malkov and Drury, 2001, Ackermann et al., 2013) in supernova remnants, such as the Crab Nebula (Sekido et al., 1951). Ultra–high energy particles, with energies greater than 10^{15} eV, have been shown to come from active galactic nuclei using both observation (Pierre Auger Collaboration et al., 2007, Kronberg and Lovelace, 2015) and theory (Honda and Honda, 2004). These particles are also referred to as extra–galactic cosmic rays, since their origin is outside our Galaxy. Table 1.1 summarizes this classification of energetic particles.

Particle Energy	Particle Type	Source Example
10–10^9 eV	Solar Energetic Particles	The Sun
10^6 eV	Anomalous Cosmic Rays	ISM/IPM Boundary Shock
10^9–10^{15} eV	Galactic Cosmic Rays	Supernova Remnants
$\geq 10^{15}$ eV	Extra Galactic Cosmic Rays	Active Galactic Nuclei

Table 1.1: Summary of the classification of energetic charged particles with source examples.

When these particles move through a magnetized plasma, such as the interplanetary medium, their motion is affected by both the plasma and the magnetic fields embedded in said plasma. Parker (1965) describes what is now known as the Parker transport equation, which describes the motion of energetic charged particles in a magnetized plasma. This equation is given by

$$\frac{\partial f}{\partial t} = \vec{\nabla} \cdot [\bar{\bar{\kappa}} \cdot \vec{\nabla} f] - \vec{u} \cdot \vec{\nabla} f + \frac{1}{3}[\vec{\nabla} \cdot \vec{u}] \frac{\partial f}{\partial \ln p} + S, \tag{1.2}$$

where $f = f(\vec{x}, p, t)$ is the distribution of the particles as a function of position $\vec{x}$, momentum magnitude p, and time t; $\bar{\bar{\kappa}}$ is the tensor of diffusion and drift coefficients, $\vec{u}$ is the bulk plasma velocity, and S describes any sources or sinks present. The terms in the equation describe various transport processes: $\vec{u} \cdot \vec{\nabla} f$ describes the convection of the particles by the background plasma travelling at speed $\vec{u}$, $\frac{1}{3}[\vec{\nabla} \cdot \vec{u}] \frac{\partial f}{\partial \ln p}$ describes the adiabatic change in energy, and $\vec{\nabla} \cdot [\bar{\bar{\kappa}} \cdot \vec{\nabla} f]$ describes the diffusion and drift of the particles due to the magnetic field (Engelbrecht et al., 2022).

Related to the diffusion coefficients is the mean free path (see Chapter 3.3.2 for the relation), the average distance a particle travels before scattering. In 1982, Palmer (1982) published a review of observational data and concluded that at 1 AU, the parallel mean free paths of particles with magnetic rigidity between $5{\cdot}10^5$ and $5{\cdot}10^9$ V (0.5 MV to 5 GV) was between 0.08 and 0.3 AU. The magnetic rigidity (R_B) of a

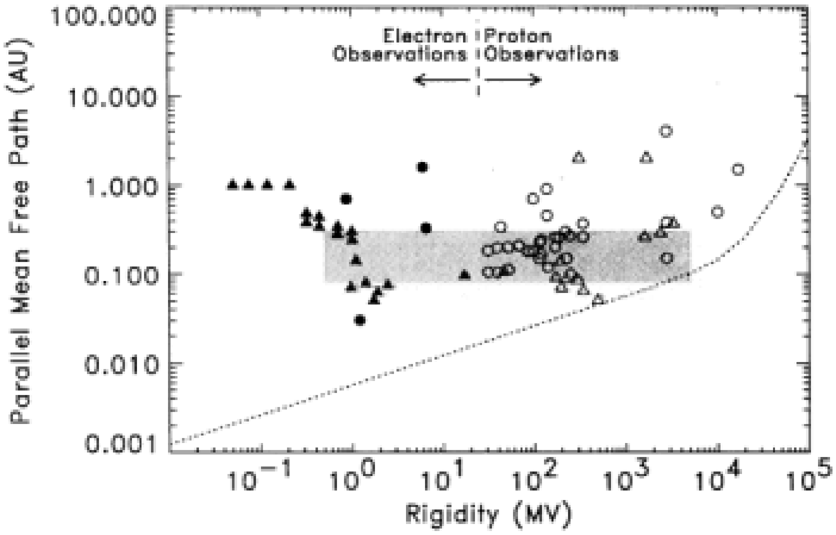

Figure 1.2: Cosmic ray mean free paths as a function of rigidity (MV). Filled symbols are electron results, while open symbols are proton results. Actual values are denoted with circles, while triangles represent data where only the lower limit is known. The shaded band in the middle is the "consensus range" detailed by Palmer (1982). The dotted line is the prediction of standard quasi–linear theory using a magnetostatic, dissipationless slab geometry (Jokipii, 1966). Reprinted with permission from The American Astronomical Society–Bieber et al. (1994)

particle, which can be viewed as the resistance said particle has to being deflected by a magnetic field, is defined (in cgs units) as

$$R_B = \frac{pc}{|q|}, \tag{1.3}$$

where p is the momentum of the particle, q is the particle charge, and c is the speed of light. This result has since become known as the *Palmer consensus range.* Bieber et al. (1994) revisited the results, distinguishing the observation by both particle type (electrons and protons) and whether the mean free path was an actual value or just a lower limit. The resulting analysis (see Figure 1.2) demonstrated that at low rigidity, electron and proton scattering are fundamentally different and have a speed dependency, not just a rigidity dependence at small values of R_B (Bieber et al., 1994).

Beyond their use in the transport of energetic particles in the solar system, diffusion coefficients of energetic particles are required in the exploration of other astrophysical fields, such as the timescale for particle acceleration in perpendicular shocks (Zank et al., 2004) and the acceleration of particles in supernova remnants (Berezhko et al., 2002, Berezhko and Völk, 2007) and active galactic nuclei (Honda and Honda, 2004).

1.2 Theoretical Background

The scenario assumed in this work is as follows: charged energetic particles are moving through a magnetized background plasma. Based on the solar wind density, it is assumed that the particles do not interact with each other or the plasma itself, only the fields embedded in the plasma. Furthermore, it is assumed that the particles are moving fast enough relative to the background plasma that the temporal changes in fields can be ignored. This assumption can be justified using the data presented for the solar wind. To do this, however, several quantities need to be defined. Already, the magnetic rigidity has been defined in (1.3). An alternative definition of the magnetic rigidity is

$$R_B = BR_L \tag{1.4}$$

where B is the magnetic field strength and R_L is the Larmor radius. In this work, we define a unit–less rigidity as

$$R = \frac{R_B}{B_0 \ell_0} = \frac{R_L}{\ell_0} = \frac{pc}{qB_0\ell_0} \tag{1.5}$$

where ℓ_0 is a characteristic length scale for the turbulence the particle is moving through and we have set $B = B_0$.

Next, consider the solar wind data from the L1 Lagrange point (NOAA, 2024): the average speed of the solar wind is around $4 \cdot 10^7$ cm s^{-1} and the average magnetic field[7] is about 52 µG. Using a value of 0.01 AU for ℓ_0, so that it is approximately equal to the turbulence correlation length, the unit–less rigidity for solar wind protons at 1 AU is approximately $5.4 \cdot 10^{-4}$. For electrons with the same velocity, the unit–less rigidity drops to $2.9 \cdot 10^{-7}$. In the VLISM, the unit–less rigidity becomes $6.3 \cdot 10^{-3}$ for protons and $3.5 \cdot 10^{-6}$ for electrons, assuming a similar correlation scale and particle speed.

Finally, consider the Alfvén speed (Alfvén, 1942) of the solar wind,

$$v_A = \frac{B_0}{\sqrt{4\pi\rho_p}}, \tag{1.6}$$

---

[7] Including both mean field and turbulence.

where B_0 is the mean field in Gauss and ρ_p is the thermal proton density. Using the data from NOAA (2024), at 1 AU the Alfvén speed is approximately $6.5 \cdot 10^6$ cm s^{-1}; while in the outer heliosphere it is around $6.3 \cdot 10^6$ cm s^{-1}, assuming that the proton density is the same as the reported electron density (Gurnett and Kurth, 2019) and a magnetic field strength of 1 µG. Both of these velocities are smaller than the solar wind speed (NOAA, 2024).

In this work, unit–less rigidities considered are all greater than the computed values for solar wind protons and electrons. Therefore, the particles considered are moving much faster than any changes in the background medium, and the time dependence of the fluctuations can be ignored.

1.2.1 Particle Motion

As mentioned, the scenario assumed in this work is that the charged particles of interest are collision-less and therefore only interact with the electromagnetic fields. The motion of the particles is therefore described by the Newton-Lorentz equation, which, in cgs units, is

$$\frac{\mathrm{d}\vec{p}}{\mathrm{d}t} = q\left[\vec{E}(\vec{x},t) + \vec{\beta} \times \vec{B}(\vec{x},t)\right]. \tag{1.7}$$

Here, $\vec{x}$ is the particle position at time t, $\vec{\beta}$ is the particle velocity ($\vec{v}$) divided by the speed of light (c), $\vec{p} = \gamma m \vec{v}$ is the relativistic particle momentum, γ is the Lorentz factor, q is the charge on the particle, and $\vec{E}$ and $\vec{B}$ are respectively the electric and magnetic fields. A common assumption is that the electric and magnetic fields can be split into a mean field component, $\vec{F}_0$, and turbulent component, $\delta\vec{F}$, such that

$$\vec{F}(\vec{x},t) = \vec{F}_0 + \delta\vec{F}(\vec{x},t) \tag{1.8}$$

where $\vec{F}$ is the field in question. The mean field component, $\vec{F}_0$, is an externally imposed field, while the turbulent component, $\delta\vec{F}$ is derived from a combination of models based on magnetohydrodynamics and observational data (such as data from the DISCOVR spacecraft (NOAA, 2024)), and has a volume average of zero. As the plasma has a high conductivity, we assume that the mean electric field is zero. This allows the coordinate system to be orientated so that the mean magnetic field is parallel to the z axis. The Newton-Lorentz force is therefore

$$\frac{\mathrm{d}\vec{p}}{\mathrm{d}t} = qB_0\vec{\beta} \times \hat{z} + q\left[\delta\vec{E}(\vec{x},t) + \vec{\beta} \times \delta\vec{B}(\vec{x},t)\right]. \tag{1.9}$$

In the absence of any turbulence, the energetic particles undergo helical motion around the mean magnetic field. Due to the presence of magnetic turbulence, the energetic particles are slowly but surely deflected from their original trajectory. Electric turbulence results in a similar deflection, along with a spread in the velocities of the ensemble. These processes are known as spatial diffusion and momentum diffusion, and are described using diffusion and drift coefficients. Magnetic turbulence leads to spatial diffusion, while electric turbulence leads to both spatial and momentum diffusion. While the drift coefficients may be of interest in some applications, they are not significant in transport theories considered in this work, and are therefore assumed to be zero. Furthermore the turbulence models considered here do not have an electric field component, and therefore only spatial diffusion is present.[8]

1.2.1.1 Particle Motion in Magnetic Turbulence

In the absence of electric fields, the Newton-Lorentz force becomes

$$\frac{\mathrm{d}\vec{p}}{\mathrm{d}t} = \frac{qB_0}{c}\vec{v} \times \frac{\vec{B}}{B_0}. \tag{1.10}$$

Since the magnetic force conserves the kinetic energy of the particle, the force can be further rearranged to read

$$\frac{\mathrm{d}\vec{v}}{\mathrm{d}t} = \frac{qB_0}{\gamma mc}\vec{v} \times \vec{b}, \tag{1.11}$$

where

$$\vec{b} = \vec{B}/B_0. \tag{1.12}$$

Furthermore, the ratio $\frac{qB_0}{\gamma mc}$ can be identified as the unperturbed synchrotron frequency (Ω).

In numerical work, it is common to scale the equations being solved in a way that renders them unit-less. There are several advantages in doing so, with a primary one being that it becomes possible to see general effects more easily. Another advantage is that the scaling can be done such that physical values are no longer required, only the ratios of them are. For a particle in a magnetic field, there are several ways to scale the equations, each one relating to how the synchrotron frequency is handled. In this field, the common method for scaling the equations is to absorb the synchrotron

---

[8] The electric fluctuations in Alfvén waves are proportional to the magnetic fluctuations by the ratio of the Alfvén speed and the speed of light. As will be shown in later in this chapter this ratio is much less than one, and therefore the electric fields can be fully ignored.

frequency into a unit-less time by the relation

$$T = \Omega t. \tag{1.13}$$

Having scaled the time by Ω and the magnetic field by B_0, the only remaining quantity required is a length scale. There are two possible ways to obtain this: the length scale can be set by scaling the position directly or the velocity can be scaled directly and the length scale calculated from the ratio of the velocity scale and the time scale.

In this field, the common method is to scale the position by a characteristic length scale ℓ_0 of the magnetic turbulence the particle is moving through. For example, when solving analytical theory the equations for the mean square displacement along a given axis are often scaled by the length scale of that axis. The scaled equations of motion are therefore

$$\frac{\mathrm{d}\vec{R}}{\mathrm{d}T} = \vec{R} \times \vec{b}(\vec{X}, T), \tag{1.14a}$$

$$\frac{\mathrm{d}\vec{X}}{\mathrm{d}T} = \vec{R}; \tag{1.14b}$$

where $\vec{b} = \vec{B}/B_0 = \hat{z} + \delta\vec{b}$ is the scaled magnetic field, $T = \Omega t$ is the scaled time, $\vec{R}$ is a vector version of the unit–less rigidity (1.5) and is used as the scaled velocity, and

$$\vec{X} = \frac{\vec{x}}{\ell_0} \tag{1.15}$$

is the scaled position. The scaling of quantities is further discussed in Chapter 5.3

The exact solution of (1.14) can be found by first defining the matrix

$$\bar{\bar{b}}_{ij} = \epsilon_{ijk} b_k \tag{1.16}$$

so that the acceleration can be expressed as

$$\dot{\vec{R}} = \bar{\bar{b}}\vec{R}, \tag{1.17}$$

which leads to (for example see Boas (2006))

$$\vec{R}(T + T_0) = \exp\left[\int\limits_{T_0}^{T+T_0} \mathrm{d}T'\ \bar{\bar{b}}(\vec{X}(T'), T')\right] \vec{R}(T_0). \tag{1.18}$$

Next, by defining

$$\phi_i(T) = \int\limits_{T_0}^{T+T_0} \mathrm{d}T' b_i(\vec{X}(T'), T') \tag{1.19}$$

the velocity can be written as

$$\vec{R}(T+T_0) = \left[\big[1 - \cos\phi(T)\big] \frac{\vec{\phi}(T) \otimes \vec{\phi}(T)}{\phi^2(T)} + \cos\phi(T) \bar{\bar{I}} + \sin\phi(T) \frac{\bar{\bar{\phi}}(T)}{\phi(T)} \right] \vec{R}(T_0) \tag{1.20}$$

where $\vec{\phi}(T) \otimes \vec{\phi}(T)$ is the outer product of $\vec{\phi}(T)$ with itself and $\bar{\bar{I}}$ is the identity matrix. Although (1.20) gives the *exact* solution, it is not necessarily an *analytical* one. With the inclusion of turbulence, the trajectory (T, $\vec{X}(T)$, $\vec{R}(T)$) of any given particle depends on both the initial conditions and the field configuration, making the trajectory in phase space unique.

While the trajectory of a particle is unique, the displacement of the particle is not: two particles may have different starting conditions, but have the same displacement along a given axis. A perfect example of this is particle motion in slab turbulence (defined in Chapter 2.2.1): two particles can have the same initial velocity and z-coordinate, but have different starting points in the xy plane. Since this form of turbulence depends only on the z coordinate, the displacement vectors of the two particles are identical for their entire trajectory. From this example it can be seen that if provided with the velocity and position of a particle, it is possible to determine the unique trajectory. However, if the displacement is provided instead of the position it is not possible to determine the trajectory. In terms of correlation functions, it would be said that the particle displacement has become decorrelated from the initial conditions.

When describing the motion of an ensemble of particles in magnetic turbulence, it is often convenient to do so via statistical theories rather than an actual ensemble of particle trajectories. Examples of such theories are the Quasi–Linear Theory (QLT, Jokipii (1966)), the Non–Linear Guiding Center (NLGC, Matthaeus et al. (2003)) Theory, and the Unified Non–Linear Transport (UNLT, Shalchi (2010, 2017), Lasuik and Shalchi (2017)) Theory (see Chapter 3.3 for a description of these theories and others). These theories employ various correlation functions in the calculation of important quantities, such as the spatial diffusion coefficients.

1.2.2 Particle Diffusion

Spatial diffusion is defined by

$$\kappa_{ii} = \lim_{t\to\infty} \frac{1}{2}\frac{\mathrm{d}}{\mathrm{d}t} \left\langle (\Delta x_i(t))^2 \right\rangle , \tag{1.21}$$

where $\langle(\Delta x_i(t))^2\rangle$ is the mean square displacement of the system along axis i. When comparing analytical calculations to results from test particle simulations, a quantity called the running diffusion coefficient is used since it is not possible to run simulations for an infinite amount of time. The running diffusion coefficient is defined as

$$d_{ii}(t) = \frac{1}{2}\frac{\mathrm{d}}{\mathrm{d}t} \left\langle (\Delta x_i(t))^2 \right\rangle \tag{1.22}$$

so that the diffusion coefficient is then

$$\kappa_{ii} = \lim_{t\to\infty} d_{ii}(t). \tag{1.23}$$

As previously mentioned, in the absence of turbulence, particles undergo helical motion. In this case, the particle trajectories can be parameterized as

$$\begin{bmatrix} x(t) \\ y(t) \\ z(t) \end{bmatrix} = \begin{bmatrix} \frac{v\sqrt{1-\mu^2}}{\omega}\cos(\omega t + \varphi) + x_0 \\ -\frac{v\sqrt{1-\mu^2}}{\omega}\sin(\omega t + \varphi) + y_0 \\ v\mu t + z_0 \end{bmatrix} \tag{1.24}$$

where ω is the gyro-frequency, φ is the initial phase of the velocity, and μ is the cosine of the angle between the velocity and the mean magnetic field. Referred to as the *pitch angle cosine*,

$$\mu = v_z/v \tag{1.25}$$

is an important quantity in the transport of particles.

1.2.2.1 Diffusion Regimes

When considering the motion of an ensemble of particles, it is often assumed that the mean square displacement is proportional to time by

$$\left\langle (\Delta x_i(t))^2 \right\rangle \propto t^{\sigma}, \tag{1.26}$$

and therefore the diffusion coefficient has the proportionality relation

$$d_{ii}(t) \propto \frac{\sigma}{2} t^{\sigma-1}. \tag{1.27}$$

The motion parallel to the mean field is ballistic in the absence of turbulence. Magnetic turbulence deflects the particle motion parallel to the mean field, scattering them. The possible behaviour resulting from this scattering is summarized in Table 1.2.

σ	Diffusion Regime	Diffusion Coefficient
$\sigma = 2$	ballistic motion	linear
$1 < \sigma < 2$	super-diffusion	monotonically increasing
$\sigma = 1$	normal diffusion	constant
$\sigma < 1$	sub-diffusion	monotonically decreasing

Table 1.2: Classification of diffusion regimes (Shalchi, 2009). *Reproduced with permission from Springer Nature.*

Often, a system will start in one regime and then at some point transitions to another. As seen in Figure 1.3, the ensemble motion in slab turbulence[9] in both the parallel (1.3a) and perpendicular (1.3b) directions starts off as ballistic motion, and then respectively transitions to normal diffusive or sub-diffusive motion.

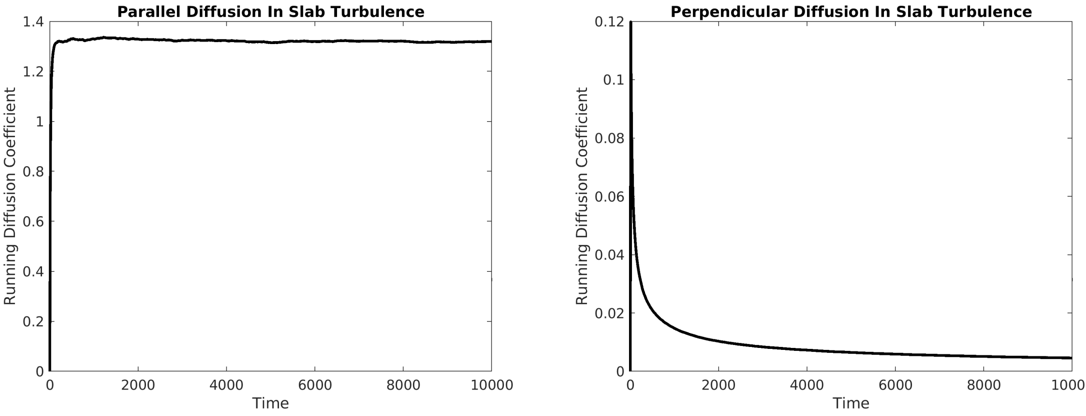

(a) Running parallel diffusion (b) Running perpendicular diffusion

Figure 1.3: Example of diffusion in slab turbulence. The turbulence energy fraction is $(\delta B/B_0)^2 = 1.0$ and the particle rigidity is $R = 1.0$.

While using (1.21) and (1.22) as the respective mathematical definitions of the diffusion and running diffusion coefficients is useful in analytical theories, it is numerically problematic. The reason for this is that numerical data is often noisy, and taking

---

[9] Details on the slab model can be found in 2.2.1.

a derivative numerically will only amplify the noise. As a result, it is convenient to define the running diffusion coefficient as

$$d_{ii}^{N}(t) = \frac{1}{2t}\left\langle (\Delta x_i(t))^2 \right\rangle \tag{1.28}$$

when analyzing simulation data. If the system becomes diffusive, both definitions will converge in the limit of $t \to \infty$.

1.2.3 Accuracy In Numerical Methods

Anytime numerical work is compared to analytical work, a primary concern is the accuracy of the numerical calculations. Ideally, the only error present would by systematic errors due to floating point truncation, which can be minimized by using floating point data types that have a higher number of bits. Practically, there is also an error in the final results due to the type of numerical method utilized, although this too can be minimized by a proper choice of numerical method. For example, when using Runge–Kutta (RK) methods (such as the methods of Fehlberg (1969), or Dormand and Prince (1980)) the accuracy can be improved by decreasing the size of the step in the independent variable or increasing the order of the method used, or a combination of both. Unfortunately, the price of increasing the accuracy in this way is that the number of times the differential equation must be evaluated also increases, resulting in a longer run time required to find the solution. Adaptive Runge–Kutta methods attempt to solve this by estimating the local truncation error and then taking as large a step as possible while keeping the local error below a given threshold.

In physics, there are often various conservation laws that can be taken advantage of when checking the accuracy of a numerical solution. For particle trajectories, some examples of this would be conservation of angular momentum in central potential problems or conservation of momentum in elastic collisions. For a particle in a magnetic field, the applicable law is the conservation of kinetic energy. Unfortunately, solutions from explicit RK methods often do not obey the applicable conservation laws. A prime example of this is the RK solution for a simple harmonic oscillator (SHO), which suffers from unidirectional energy drift (see Appendix A for a derivation). Furthermore, as the error in the RK solution is proportional to current energy and the step size used, adaptive RK methods only amplify the energy drift by taking as large a step size as possible.

As the velocity differential equation of a particle in a magnetic field is similar to the SHO differential equations, it too suffers the same unidirectional energy drift. Worse still, this energy drift will alter the change in position of each step, which will feed back into the acceleration if the magnetic field is a function of position. Depending on the form of the magnetic field, this has the potential to lead to the solution becoming wildly inaccurate in a relatively short time. Furthermore, since it is expected that the scattering of the particles by the magnetic field is governed by resonance interactions between the particle velocity and the wave modes of the magnetic field (see Chapter 3), changes in the magnitude of the velocity will change what interactions are possible.

1.3 Thesis Goals

The goals of this work are to use the noisy slab and full 3D turbulence models (Chapter 2) to study the behaviour of the diffusion coefficients in turbulence with low Kubo numbers (defined in Chapter 3.2.4.3) and compare the results with time–dependent analytical theory (defined in Chapter 3). To that end, a numerical method for calculating particle trajectories in magnetic fields is developed and presented (Chapter 4) which has superior phase and position accuracy compared to existing methods. The method for generating the magnetic fields, which is based off of the method used by other researchers in this field, is discussed (Chapter 5) along with the methods used to solve the equations provided by analytical theory for particle transport. Results are then presented and compared with the analytical theory (Chapter 6).

1.3.1 Related Publications

In addition to being presented here, some of the results and methods have also been published in the following articles:[10]

Chapter 3 A. Shalchi and V. Arendt, *On the Relevance of Magnetic Correlation Functions in Energetic Particle Transport Theory*, Brazilian Journal of Physics, Volume 54, Issue 4, article id.126, August 2024.

Chapter 4 V. Arendt, *Numerical methods, energy conservation, and a new method for particle motion in magnetic fields*, Mathematics and Computers in Simulation, Volume 205, p. 142-185, March 2023.

---

[10] Articles are listed in the order of the chapter they are first used in.

Chapter 6 V. Arendt and A. Shalchi, *Detailed Test-Particle Simulations of Energetic Particles Interacting with Magnetized Plasmas II. Three-Dimensional Turbulence with Small Kubo Numbers*, Advances in Space Research, 2025, In Press.

Simulations for Shalchi and Arendt (2024b) and Arendt and Shalchi (2025) were performed by V. Arendt, at the direction of A. Shalchi. Analysis by both V. Arendt and A. Shalchi. Manuscripts prepared by A. Shalchi with contributions from V. Arendt.

1.3.2 Other Publications

Publications with results not presented in this work:

- A. Shalchi and V. Arendt, *Distribution Functions of Energetic Particles Experiencing Compound Subdiffusion*, The Astrophysical Journal, Volume 890, Issue 2, id.147, 13 pp, February 2020.
- V. Arendt and A. Shalchi, *Detailed test-particle simulations of energetic particles interacting with magnetized plasmas I. Two-component turbulence*, Advances in Space Research, Volume 66, Issue 8, p. 2001-2023, October 2020.
- A. Shalchi and V. Arendt, *Simulations of field line random walk in noisy slab turbulence*, Advances in Space Research, Volume 74, Issue 9, pp. 4238-4249, November 2024.

Chapter 2

Describing Magnetic Turbulence

There are multiple different approaches for describing magnetic turbulence. The primary one is using the equations of *magnetohydrodynamics (MHD)*: a system of non-linear equations describing the coupling of various fields such as density, pressure, velocity, and electromagnetic fields. In cgs units, these equations are:

$$\frac{\partial \rho}{\partial t} = -\vec{\nabla}\left[\rho \vec{v}\right]; \tag{2.1a}$$

$$\rho\left[\frac{\partial \vec{v}}{\partial t} + \left[\vec{v}\cdot\vec{\nabla}\right]\vec{v}\right] = -\vec{\nabla}P + \rho_e \vec{E} + \frac{\vec{J}\times\vec{B}}{c}; \tag{2.1b}$$

$$\eta \vec{J} = \vec{E} + \frac{\vec{v}}{c}\times\vec{B}; \tag{2.1c}$$

$$\vec{\nabla}\cdot\vec{E} = 4\pi\rho_e; \tag{2.1d}$$

$$\vec{\nabla}\cdot\vec{B} = 0; \tag{2.1e}$$

$$\vec{\nabla}\times\vec{E} = -\frac{1}{c}\frac{\partial \vec{B}}{\partial t}; \tag{2.1f}$$

$$\vec{\nabla}\times\vec{B} = \frac{4\pi}{c}\vec{J} + \frac{1}{c}\frac{\partial \vec{E}}{\partial t}. \tag{2.1g}$$

Here (2.1a) is the mass continuity equation, where ρ is the density of a given fluid and $\vec{v}$ is the velocity field for said fluid; each fluid present requires its own continuity equation. The second equation, (2.1b), is Euler's equation, relating the change in the velocity field of a given fluid to the gradient of the pressure P and the force density. In MHD this force is the Lorentz force, where ρ_e is the charge density, $\vec{E}$ is the electric field, $\vec{J}$ is the current density, $\vec{B}$ is the magnetic field, and c is the speed of light. Here it has also been assumed that the viscosity is negligible. The third equation, (2.1c), is

Ohm's law, relating the current density to the electric, magnetic, and velocity fields via the resistivity η. The last four equations are Maxwell's equations, relating the electric and magnetic fields to the charge density and current density, respectively, as well as to each other. In addition to the above equations, the equation of state relating the pressure to the density is also required.

Alternatively, one can use statistics to define various turbulence models. While this approach doesn't directly give the turbulence field for all positions and times, it does allow for the grouping of fields based on common properties and configurations which is ideal when examining statistical processes such as diffusion. The mathematical quantity commonly used in this approach is the two-point, two-time magnetic correlation tensor:

$$R_{nm}(\vec{x}, \vec{x}_0, t, t_0) = \langle \delta B_n(\vec{x}, t) \delta B_m(\vec{x}_0, t_0) \rangle \,, \tag{2.2}$$

which describes the relation between the magnetic turbulence field component δB_m at position $\vec{x}_0$ and time t_0 and the magnetic turbulence field component δB_n at position $\vec{x}$ and time t. The angle brackets, $\langle \cdots \rangle$, represents the averaging operator; in this case the quantities being averaged are any variable that is allowed to take a random value.

2.1 Statistical Description

2.1.1 Magnetic Correlation and Spectral Tensors

Often it is assumed that the turbulence in question is both spatially and temporally homogeneous (Shalchi, 2020), meaning that the components of the correlation tensor (2.2) can be written as

$$R_{nm}(\vec{x}, \vec{x}_0, t, t_0) = R_{nm}(\vec{x} - \vec{x}_0, t - t_0). \tag{2.3}$$

For example, Matthaeus et al. (1990) computed the static two–dimensional correlation tensor $R(r_\parallel, r_\perp)$ for the solar wind, as discussed in Chapter 1. If the magnetic field is represented using a Fourier transform,

$$\delta\vec{B}(\vec{x}, t) = \int \mathrm{d}^3k \, \delta\tilde{\vec{B}}(\vec{k}, t) e^{i\vec{k}\cdot\vec{x}}, \tag{2.4}$$

then the correlation tensor components become

$$\begin{aligned} R_{nm}(\vec{x}, \vec{x}_0, t, t_0) &= \langle B_n(\vec{x}, t) B_m(\vec{x}_0, t_0) \rangle \\ &= \left\langle \int \mathrm{d}^3k \int \mathrm{d}^3k' \, \tilde{\delta B}_n(\vec{k}, t) \tilde{\delta B}^{\dagger}_m(\vec{k}', t_0) e^{i\left(\vec{k}\cdot\vec{x} - \vec{k}'\cdot\vec{x}_0\right)} \right\rangle . \end{aligned} \tag{2.5}$$

The temporal behaviour is left as part of the Fourier amplitude $\tilde{\delta\vec{B}}$, which allows for various temporal effects to be included other than just undamped Alfvén waves. Additionally, since any ‘random’ variables present are contained in the Fourier amplitude, the components of the correlation tensor can be written as

$$R_{nm}(\vec{x}, \vec{x}_0, t, t_0) = \int \mathrm{d}^3k \int \mathrm{d}^3k' \, \left\langle \tilde{\delta B}_n(\vec{k}, t) \tilde{\delta B}^{\dagger}_m(\vec{k}', t_0) \right\rangle e^{i\left(\vec{k}\vec{x} - \vec{k}'\vec{x}_0\right)} . \tag{2.6}$$

If the turbulence satisfies (2.3), then the Fourier amplitude correlation is given by

$$\left\langle \tilde{\delta B}_n(\vec{k}, t) \tilde{\delta B}^{\dagger}_m(\vec{k}', t_0) \right\rangle = P_{nm}(\vec{k}, \Delta t) \delta(\vec{k} - \vec{k}'), \tag{2.7}$$

where Δt is the time interval between t_0 and t, and P_{nm} is what is referred to as the *spectral tensor* which is required extensively in the theory of both field line and particle diffusion. Using (2.7) in (2.6) and (2.3), the magnetic correlation tensor is given by

$$R_{nm}(\Delta\vec{x}, \Delta t) = \int \mathrm{d}^3k \, P_{nm}(\vec{k}, \Delta t) e^{i\vec{k}\Delta\vec{x}} \tag{2.8}$$

from which it can be seen that P_{nm} is the Fourier transform of R_{nm}. Alternatively, the spectral tensor can be calculated by

$$P_{nm}(\vec{k}, \Delta t) = \frac{1}{(2\pi)^3} \int \mathrm{d}^3x \, R_{nm}(\vec{x}, \Delta t) e^{-i\vec{k}\vec{x}} \tag{2.9}$$

if the correlation tensor is known.[1]

2.1.1.1 Temporal Behaviour

In general, each component of the spectral tensor can have different temporal behaviour. That said, it is commonly assumed that all components have the same temporal behaviour (Bieber et al., 1994). In this case, the spectral tensor is written

---

[1] Here, the variable transformation $\Delta x \to x$ has been used.

as

$$P_{nm}(\vec{k},\Delta t) = P_{nm}(\vec{k})\Gamma(\vec{k},\Delta t), \tag{2.10}$$

where $P_{nm}(\vec{k})$ is the static spectral tensor and $\Gamma(\vec{k},\Delta t)$ is what is called the *dynamical correlation tensor*. In magnetostatic turbulence $\Gamma(\vec{k},\Delta t) = 1$, while for undamped shear Alfvén waves $\Gamma(\vec{k},\Delta t) = e^{\pm i v_A k_\parallel t}$. A discussion of dynamical turbulence can be found in Shalchi et al. (2006).

2.1.2 Spectral Tensor

If the magnetic turbulence has the same spatial behaviour along all axes, the spectral tensor can be split using

$$P_{nm}(\vec{k}) = g(\vec{k})\varphi_{nm}(\vec{k}), \tag{2.11}$$

where $g(\vec{k})$ is what is called the *spectral function* and $\varphi_{nm}(\vec{k})$ is a tensor describing the relation between the orientation of the Fourier wave mode, $\hat{k}$ and orientation of the magnetic field, $\delta\tilde{\vec{B}}(\vec{k},t)$. For incompressible axi-symmetric turbulence, the spectral function can be written as

$$g(\vec{k}) = g(k_\parallel, k_\perp), \tag{2.12}$$

while φ_{nm} takes the form

$$\varphi_{nm}(\vec{k}) = \begin{cases} \delta_{nm} & k_\perp = 0; n, m \neq z \\ \delta_{nm} - \dfrac{k_n k_m}{k_\perp^2} & k_\perp \neq 0; n, m \neq z \end{cases} \tag{2.13}$$

such that the spectral tensor can be written as

$$\bar{\bar{P}}(\vec{k}) = g(k_\parallel) \begin{bmatrix} 1 & 0 & 0 \\ 0 & 1 & 0 \\ 0 & 0 & 0 \end{bmatrix} \tag{2.14a}$$

if $k_\perp = 0$ or

$$\bar{\bar{P}}(\vec{k}) = g(k_\parallel, k_\perp) \begin{bmatrix} 1-\cos^2 k_\phi & -\cos k_\phi \sin k_\phi & 0 \\ -\cos k_\phi \sin k_\phi & 1-\sin^2 k_\phi & 0 \\ 0 & 0 & 0 \end{bmatrix} \tag{2.14b}$$

otherwise.

2.1.2.1 Power Law Spectra

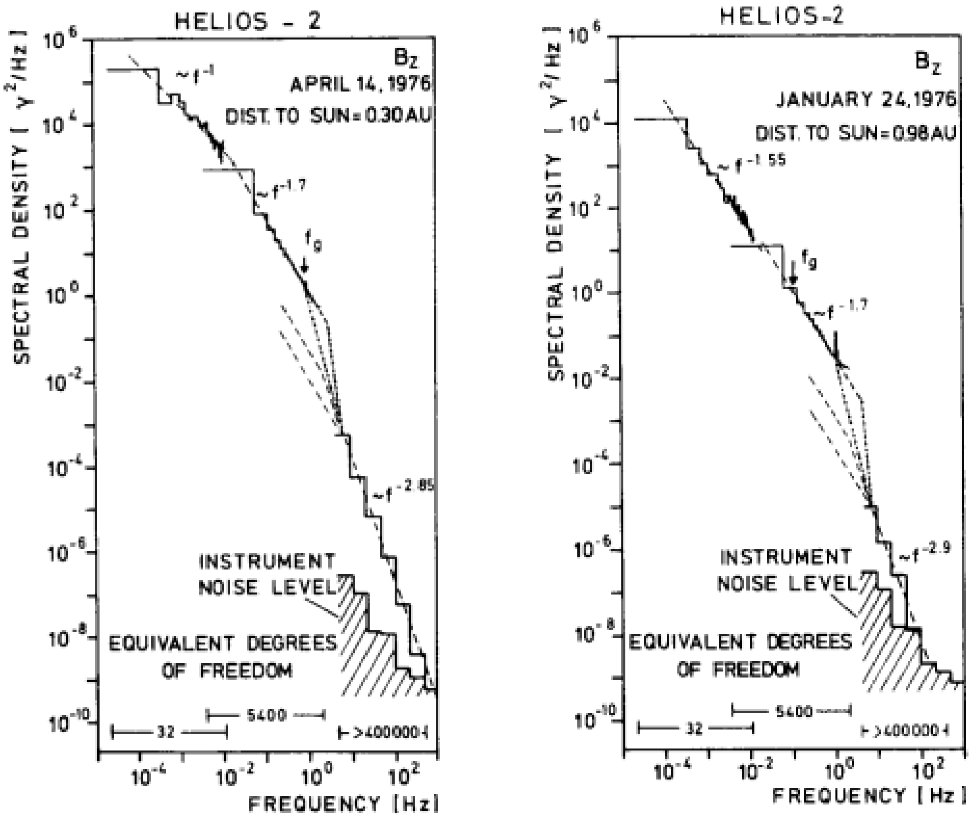

Figure 2.1: Power law spectrum for the B_z component of the solar wind at heliocentric distance of 0.30 AU (left) and 0.98 AU (right). The relation between frequency and wave number is discussed in Bieber et al. (1996), and are proportional to each other. The prediction of Kolmogorov (1941) that the inertial range spectral index is $s = 5/3$ is close to the measured value of $s = 1.7$ seen in the spectrum (mid–frequency range in figure). *This figure was originally published in NASA Conference Publication – Denskat and Neubauer (1983). Reused under public licence.*

A commonly used spectral function is that of a power law (for example, see the models defined later in this chapter), given by (Shalchi and Weinhorst, 2009)

$$g(k) = N(s,q)\delta B^2 \ell \frac{\left[k\ell\right]^q}{\left[1+\left[k\ell\right]^2\right]^{\frac{s+q}{2}}} \tag{2.15}$$

where s and q are what are referred to as *spectral indices*, ℓ is the length scale of the model, δB^2 is the mean square magnetic amplitude, and $N(s,q)$ is the normalization function for the model. The behaviour of this function falls into one of several categories depending on the value of $k\ell$ (Zhou and Matthaeus, 2005). Small wave numbers ($k\ell \ll 1$), corresponding to large scale structure, form what is known as the energy range, so named because it is the scale at which energy is injected into the turbulence. In this region, the spectra scales as

$$g(k) \propto k^q \tag{2.16}$$

which is why q is referred to as the energy spectral index. Normalization considerations,

$$\int_0^\infty \mathrm{d}k\, N(s,q)\delta B^2 \ell \frac{\left[k\ell\right]^q}{\left[1+\left[k\ell\right]^2\right]^{\frac{s+q}{2}}} = 1, \tag{2.17}$$

require that the spectral index q be greater than negative one in general (Zwillinger, 2012), although some models may restrict this value further.

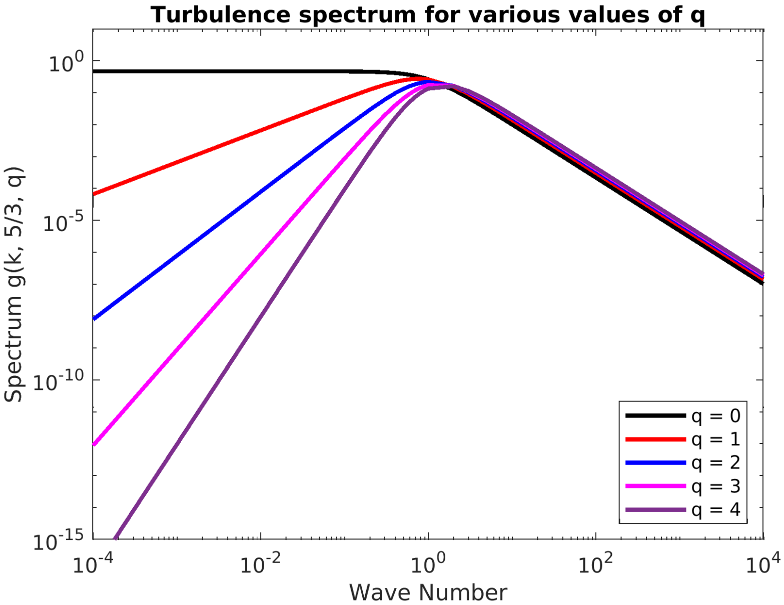

Figure 2.2: Power law spectrum for various values of q, with $s = 5/3$.

Large wave numbers ($k\ell \gg 1$), corresponding to small scale structure, form the inertial range. In this range, energy is transferred to progressively small scales (larger wave numbers), and is unaffected by the dynamics of either ultra small scales or large scales. The spectrum in this regime goes as

$$g(k) \propto k^{-s}, \tag{2.18}$$

with normalization considerations requiring that s is greater than one. In most models, the value of s is set to 5/3 based on the work Kolmogorov (1941) and results from various spacecrafts, such as the *Helios 2* spacecraft (Denskat and Neubauer, 1983) shown in Figure 2.1. Figure 2.2 shows the spectra for $s = 5/3$ and integer values of q from zero to four. While not present in (2.15), there is also the *dissipation* range which occurs at small scales. This range is so named because it is the scale at which energy is dissipated from the system, and is important for solar energetic particles (Bieber et al., 1994). The dissipation scale is not considered in this work.

2.1.2.2 Power Law Spectrum Integral

The general integral of the power law spectrum is given by (for example see Gradshteyn and Ryzhik (2000))

$$G(x,s,q) = \int_0^x \mathrm{d}x' \frac{x'^q}{\left[1+x'^2\right]^{\frac{s+q}{2}}} = \frac{x^{q+1}{}_2F_1\left(\frac{q+1}{2}, \frac{q+s}{2}; \frac{q+3}{2}; -x^2\right)}{q+1} \tag{2.19}$$

where ${}_2F_1(a,b;c;x)$ is the Gaussian hypergeometric function. This function appears in several diffusion theories (see equation 4.32 of Shalchi (2020) for example). If the spectral index q is odd, then there is an analytical solution given by

$$G(x,s,q) = \left[\left[1+x^2\right]^{-\frac{s+q-2}{2}} \sum_{n=0}^{(q-1)/2} a_n x^{2n}\right] - a_0 \tag{2.20}$$

where the coefficients a_n are calculated via the relations

$$\begin{aligned} a_0 &= -\frac{\Gamma\left(\frac{q+1}{2}\right)\Gamma\left(\frac{s-1}{2}\right)}{2\Gamma\left(\frac{s+q}{2}\right)} \\ a_{n-1} &= \frac{2n}{s+q-2n} a_n, \\ a_{(q-1)/2} &= \frac{1}{1-s}, \end{aligned} \tag{2.21}$$

where $\Gamma(\cdots)$ is the gamma function. If the spectrum is normalized, the equations becomes

$$G_N(x,s,q) = \left[\left[1+x^2\right]^{-\frac{s+q-2}{2}} \sum_{n=0}^{(q-1)/2} a'_n x^{2n}\right] - a'_0 \tag{2.22a}$$

with coefficients

$$a'_n = \frac{a_n}{|a_0|}. \tag{2.22b}$$

These equations will be used in 5.1.4 when calculating the wave amplitudes in the test–particle simulations.

2.2 Synthetic Turbulence Models

Presented here are various theoretical models of magnetic turbulence. Not all the models discussed are used in the simulations done for this work; some are simply presented for comparison. The spectral tensor and function for each of the models are initially given as they appear in literature. Section 2.2.9 discusses an alternate form of the spectral tensor that is useful in both analytical theory and simulations. The figures shown in this section are maps of the variations in the magnitude of the turbulence for an example instance of each model. The description of how an instance of a model is created can be found in Section 5.1. The parameters in these figures are derived from those used in the simulations detailed in Chapter 6 and Shalchi and Arendt (2024b).

2.2.1 Slab Turbulence

One of the simplest models of incompressible magnetic turbulence is the *slab model*, which has been used in particle diffusion research since Jokipii (1966). The corresponding spectral tensor is given by

$$P^{Slab}_{nm}(\vec{k}) = g^{Slab}(k_\parallel)\frac{\delta(k_\perp)}{k_\perp}\delta_{nm} \tag{2.23}$$

where $n, m \neq z$. The spectral function proposed by Bieber et al. (1994) and used in this work for this model is

$$g^{Slab}(k_\parallel) = \frac{C(s)}{2\pi}\delta B^2_{Slab}\ell_\parallel \left[1 + \left[k_\parallel \ell_\parallel\right]^2\right]^{-\frac{s}{2}}, \tag{2.24}$$

with normalization constant

$$C(s) = \frac{\Gamma\left(\frac{s}{2}\right)}{2\sqrt{\pi}\,\Gamma\left(\frac{s-1}{2}\right)}. \tag{2.25}$$

Figure 2.3 shows the variation in magnitude of a possible slab turbulence field configuration.

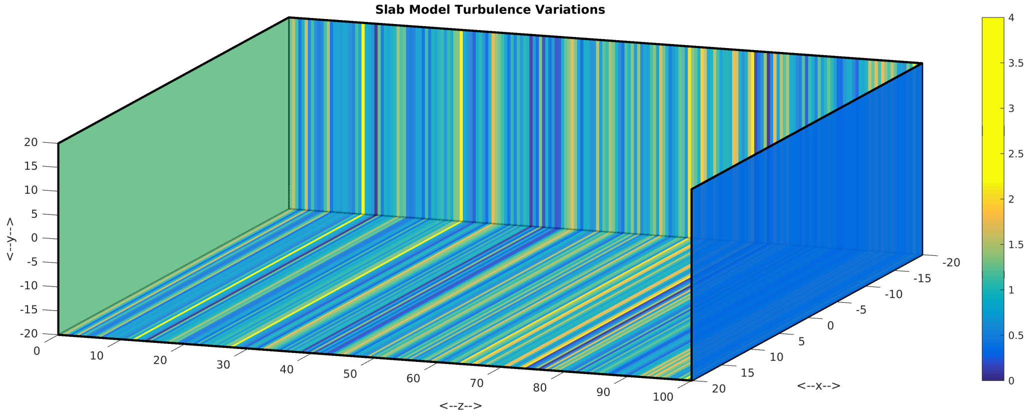

Figure 2.3: Variations in magnitude of a sample slab turbulence field. All axes are scaled by the parallel length scale.

2.2.2 2D Turbulence

The *2D turbulence* model is similar to the slab model in that it is a reduced dimensional model of incompressible turbulence. In this model the wave vector is confined to the xy plane, giving this model the transverse complexity that the slab model lacks. The spectral tensor describing this model is

$$P^{2D}_{nm}(\vec{k}) = g^{2D}(k_\perp)\frac{\delta(k_\parallel)}{k_\perp}\left[\delta_{nm} - \frac{k_n k_m}{k_\perp^2}\right] \tag{2.26}$$

where $n, m \neq z$. Shalchi and Weinhorst (2009) proposed

$$g^{2D}(k_\perp) = \frac{2}{\pi}D(s,q)\delta B^2_{2D}\ell_\perp \frac{\left[k_\perp \ell_\perp\right]^q}{\left[1 + \left[k_\perp \ell_\perp\right]^2\right]^{\frac{s+q}{2}}} \tag{2.27}$$

as the spectral function, where $D(s,q)$ is the normalization function given by

$$D(s,q) = \frac{\Gamma\left(\frac{s+q}{2}\right)}{2\Gamma\left(\frac{q+1}{2}\right)\Gamma\left(\frac{s-1}{2}\right)}. \tag{2.28}$$

Comparing (2.25) and (2.28), it can be easily seen that $C(s) = D(s, q = 0)$. It should be noted that the spectrum can only be normalized for $q > -1$ and $s > 1$. Figure 2.4 shows the variation in magnitude of a possible 2D turbulence field configuration.

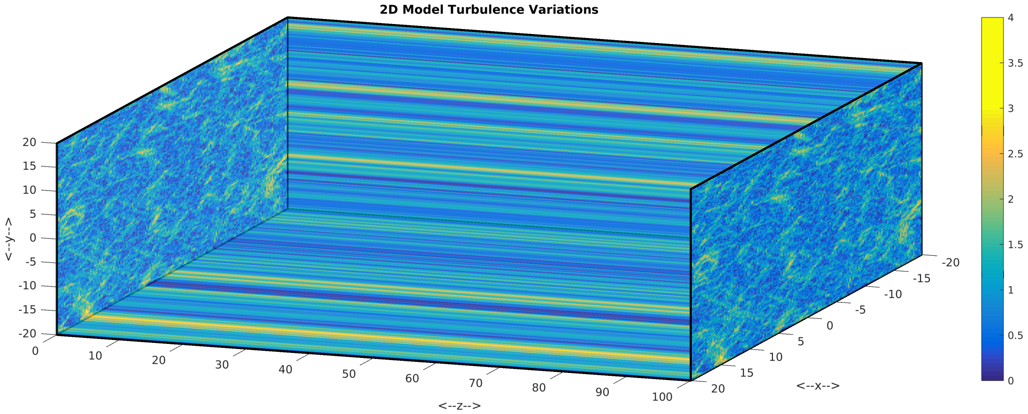

Figure 2.4: Variations in magnitude of a sample 2D turbulence field. All axes are scaled by the perpendicular length scale.

2.2.3 Two–Component Turbulence

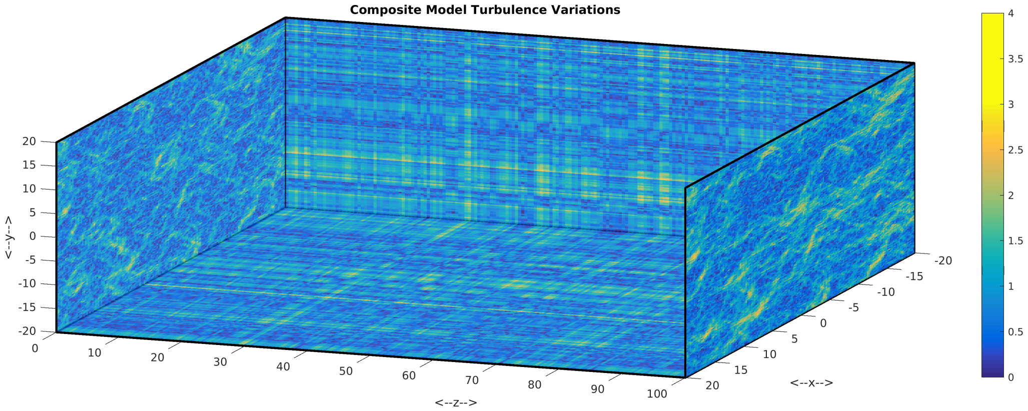

Figure 2.5: Variations in magnitude of a sample two–component turbulence field. The z axis is scaled by the parallel length scale, while the x and y axes are scaled by the perpendicular length scale.

As the wave vectors in the 2D model are orthogonal to those in the slab model, it is possible in linearized MHD to construct a turbulence field that is the linear combination of the two.[2] The result is known as the *two-component model* or *composite model*, and is often used as a model for the solar wind (Matthaeus et al., 1990, 1996, Zank and Matthaeus, 1993, Oughton et al., 1994, Bieber et al., 1996). Furthermore,

---

[2] See Chapter 1 for a brief description of how this model came about.

the use of the model for the solar wind is supported by data from the *ISEE-3* (or *ICE*) spacecraft (Matthaeus et al., 1990). The spectral tensor in this model is given by

$$P_{nm}^{Comp}(\vec{k}) = P_{nm}^{Slab}(\vec{k}) + P_{nm}^{2D}(\vec{k}). \tag{2.29}$$

The magnitudes of the slab and 2D models are often given in terms of the total magnetic field energy density, with solar wind observations giving an energy distribution of $\delta B_{2D}^2 = 0.8\delta B_{Total}^2$ and $\delta B_{Slab}^2 = 0.2\delta B_{Total}^2$ (Bieber et al., 1994). Furthermore, as this is a linear combination, the length scales and spectral indices need not be the same in each model. Figure 2.5 shows the variation in magnitude of a possible two–component turbulence field configuration.

2.2.4 Standard Noisy Slab Turbulence

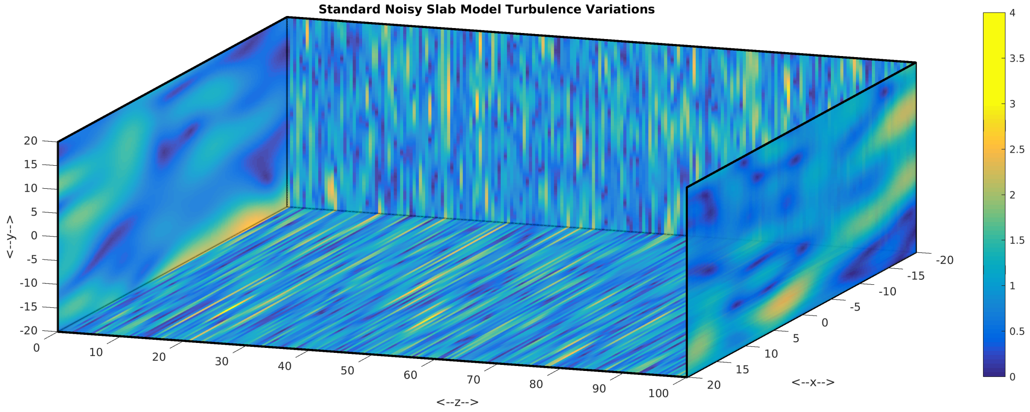

Figure 2.6: Variations in magnitude of a sample standard noisy slab turbulence field. All axes are scaled by the parallel length scale.

Proposed by Shalchi (2015), the *Noisy Slab Model* is as its name implies: a noisy version of the slab model. The noise is added by allowing a small range of wave modes perpendicular to the mean field. The form of the model used in this work is

$$P_{nm}^{SNS}(\vec{k}) = g^{Slab}(k_{\parallel})\frac{2\ell_{\perp}}{k_{\perp}}\Theta(1 - k_{\perp}\ell_{\perp})\left[\delta_{nm} - \frac{k_n k_m}{k_{\perp}^2}\right], \tag{2.30}$$

where $n, m \neq z$ as in the slab model, as proposed in Shalchi (2015). Here, $\Theta(x)$ is the step function, given by

$$\Theta(x) = \begin{cases} 0 & x < 0 \\ 1 & x \geq 0, \end{cases} \tag{2.31}$$

g^{Slab} is the regular slab spectrum as given by (2.24), and $\ell_\perp$ is the perpendicular length scale. In the limit $\ell_\perp = \infty$, the regular slab model is recovered. In this work, the noisy slab model is used to explore particle transport in turbulence with low Kubo numbers.[3] With the introduction of variations for the noisy slab model, this particular version will be referred to as the *Standard Noisy Slab* model or *SNS* model. Figure 2.6 shows the variation in magnitude of a possible standard noisy slab turbulence field configuration.

2.2.5 Noisy Reduced MHD Turbulence

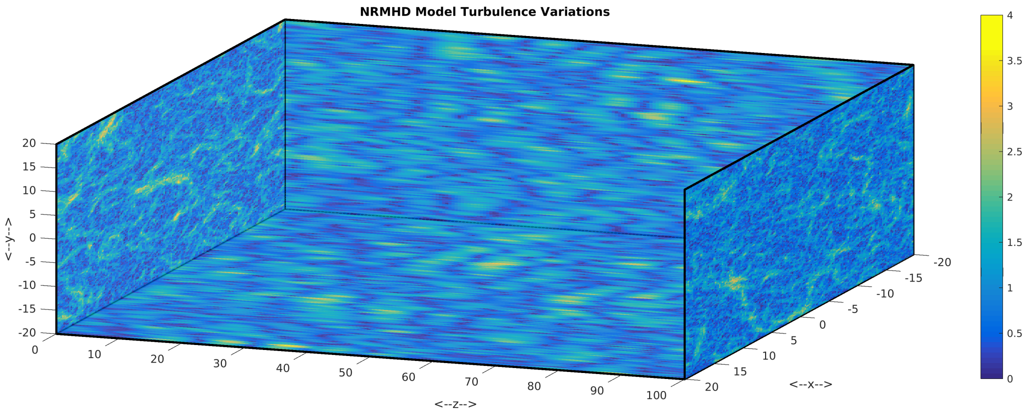

Figure 2.7: Variations in magnitude of a sample NRMHD turbulence field. All axes are scaled by the perpendicular length scale.

The *Noisy Reduced MHD Model* (*NRMHD* model), proposed by Ruffolo and Matthaeus (2013), is the noisy version of the 2D model, leading to some calling it the *Noisy 2D Model*. As with the noisy slab model, the noise in this model is introduced by including modes that are not present in the regular 2D model. The resulting spectral tensor is

$$P_{nm}^{NRMHD}(\vec{k}) = g^{2D}(k_\perp)\frac{\ell_\parallel}{2k_\perp}\Theta(1 - |k_\parallel \ell_\parallel|)\left[\delta_{nm} - \frac{k_n k_m}{k_\perp^2}\right], \tag{2.32}$$

---

[3] See 3.2.4.3 for a discussion and definition of the Kubo number.

where $g^{2D}(k_\perp)$ is the spectral function for the regular 2D model, which is recovered in the case $\ell_\parallel = \infty$. In this model, the wave numbers are reversed compared to the noisy slab model, making it an ideal model to explore particle transport in turbulence with large Kubo numbers. Figure 2.7 shows the variation in magnitude of a possible NRMHD turbulence field configuration.

2.2.6 Modified Noisy Slab Model

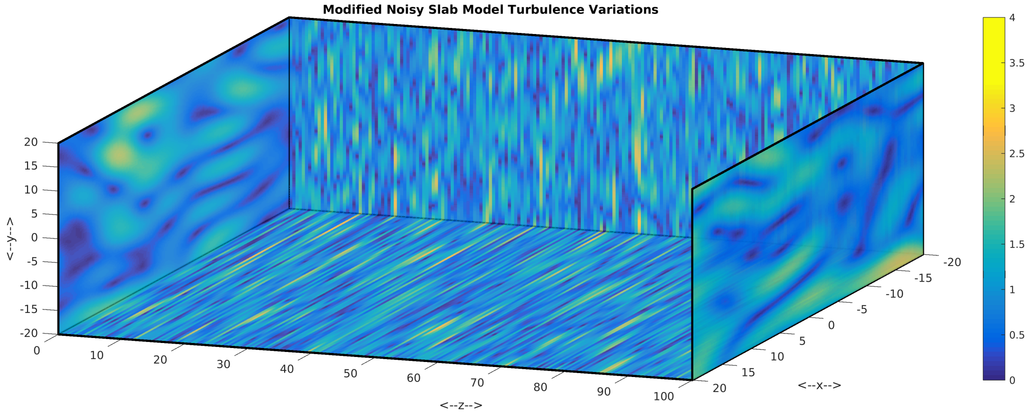

Figure 2.8: Variations in magnitude of a sample modified noisy slab turbulence field. All axes are scaled by the parallel length scale.

The *Modified Noisy Slab Model* (*MNS* model) is a more general version of the standard noisy slab model first introduced in Shalchi and Arendt (2024b) for the purpose of studying the effects of the perpendicular correlation function on particle transport (see Section 2.3). The modification in this model affects the perpendicular component, and is done by using the replacement

$$2\ell_\perp^2\,[k_\perp \ell_\perp]^{-1} \rightarrow 2\,[2+p]\,\ell_\perp^2\,[k_\perp \ell_\perp]^p\,. \tag{2.33}$$

Normalization of the spectra gives the constraint of $p \geq -2$. The spectral tensor for this model is therefore given by

$$P_{nm}^{MNS}(\vec{k}) = g^{Slab}(k_\parallel)\Big[2\,[2+p]\,\ell_\perp^{2+p}\,[k_\perp \ell_\perp]^p\,\Theta(1-k_\perp \ell_\perp)\Big]\left[\delta_{nm} - \frac{k_n k_m}{k_\perp^2}\right]. \tag{2.34}$$

The standard noisy slab model can be recovered by setting $p = -1$. Figure 2.8 shows the variation in magnitude of a possible standard noisy slab turbulence field configuration.

2.2.7 Gaussian Noisy Slab Model

A second variant of the noisy slab model introduced in Shalchi and Arendt (2024b) for studying the effect of the perpendicular correlation function, the *Gaussian Noisy Slab Model* (*GNS* model) does away with step function by replacing it with a Gaussian function:

$$2\ell_\perp^2\left[k_\perp\ell_\perp\right]^{-1}\Theta(1-k_\perp\ell_\perp)\rightarrow\ell_\perp^2\left[k_\perp\ell_\perp\right]^2 e^{-\frac{1}{2}\left[k_\perp\ell_\perp\right]^2}. \tag{2.35}$$

The resulting spectral tensor is given by

$$P_{nm}^{GNS}(\vec{k})=g^{Slab}(k_\parallel)\left[\ell_\perp^2\left[k_\perp\ell_\perp\right]^2 e^{-\frac{1}{2}\left[k_\perp\ell_\perp\right]^2}\right]\left[\delta_{nm}-\frac{k_nk_m}{k_\perp^2}\right]. \tag{2.36}$$

While the small scale perpendicular complexity is no longer limited by the step function, the spectra still rapidly decays as $k_\perp$ increases. While this limits the amount of variation in the magnetic field on small scales, it eliminates long range correlations that will be explored in the next section of this chapter. Figure 2.9 shows the variation in magnitude of a possible standard noisy slab turbulence field configuration.

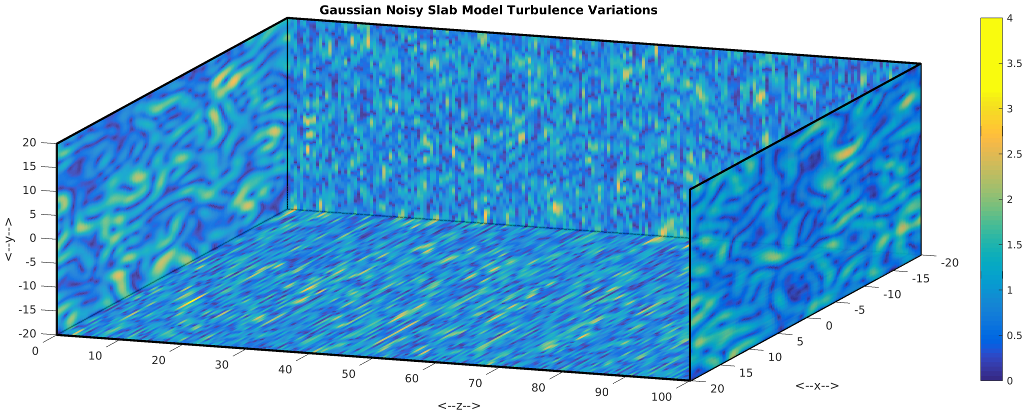

Figure 2.9: Variations in magnitude of a sample Gaussian noisy slab turbulence field. All axes are scaled by the parallel length scale.

2.2.8 Full 3D Turbulence Model

Introduced in Shalchi and Arendt (2024b) with the modified and Gaussian noisy slab models, the *Full 3D Turbulence Model* (*F3D* model) is so named because the spectral tensor uses the full range of all possible wave modes. The spectral tensor for

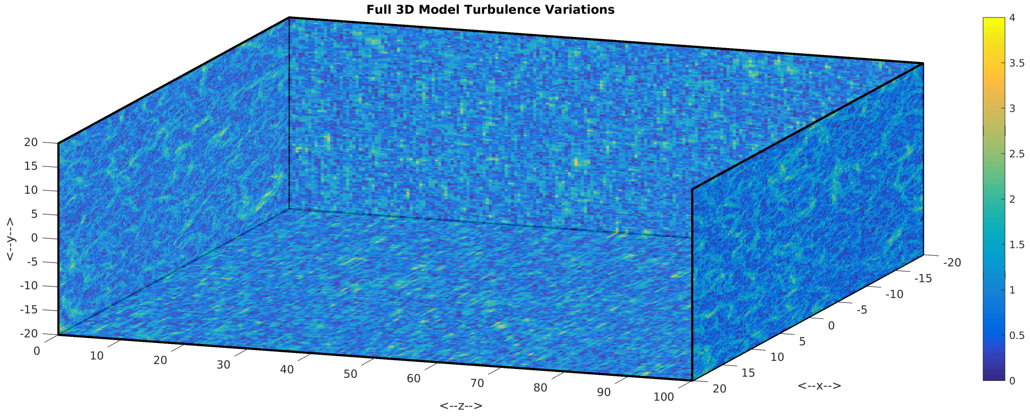

Figure 2.10: Variations in magnitude of a sample full 3D turbulence field. All axes are scaled by the parallel length scale.

this model is given by:

$$P_{nm}^{F3D}(\vec{k}) = g^{Slab}(k_\parallel)\left[2\frac{\ell_\perp}{k_\perp}h^{2D}(k_\perp)\right]\left[\delta_{nm} - \frac{k_n k_m}{k_\perp^2}\right] \tag{2.37}$$

where

$$h^{2D}(k_\perp) = 4D(s,q)\frac{\left[k_\perp \ell_\perp\right]^q}{\left[1+\left[k_\perp \ell_\perp\right]^2\right]^{\frac{s+q}{2}}}. \tag{2.38}$$

In this work it is assumed that the spectral index s is the same in both $g^{Slab}(k_\parallel)$ and $h^{2D}(k_\perp)$, with a value of $5/3$ motivated by the work of Kolmogorov (1941) and solar wind observations. Figure 2.10 shows the variation in magnitude of a possible standard noisy slab turbulence field configuration.

2.2.9 Different Forms of the Spectral Tensor

While the forms of the spectral tensor and spectral function listed for each model are usable as is in theoretical calculations and numerical simulations, it can be convenient to rearrange them into the generic form

$$P_{xx}(\vec{k}) = \frac{1}{2}\delta B^2 \ell_\parallel \ell_\perp^2\, g_\parallel(k_\parallel)\, g_\perp(k_\perp)\, g_\phi(k_\phi) \tag{2.39a}$$

or

$$P_{xx}(\vec{k}) = \delta B_x^2 \ell_\parallel \ell_\perp^2\, g_\parallel(k_\parallel)\, g_\perp(k_\perp)\, g_\phi(k_\phi), \tag{2.39b}$$

Model	$g_\parallel(k_\parallel)$	$g_\perp(k_\perp)$	$g_\phi(k_\phi)$
Slab	$2C(s)\left[1+[k_\parallel\ell_\parallel]^2\right]^{-\frac{s}{2}}$	$\left[k_\perp\ell_\perp\right]^{-1}\delta(k_\perp\ell_\perp)$	$\frac{1}{2\pi}$
2D	$\delta(k_\parallel)$	$4D(s,q)\frac{[k_\perp\ell_\perp]^{q-1}}{[1+[k_\perp\ell_\perp]^2]^{\frac{s+q}{2}}}$	$\frac{1}{\pi}\sin^2(k_\phi)$
NRMHD	$\frac{1}{2}\Theta(1-\lvert k_\parallel\rvert\ell_\parallel)$	$4D(s,q)\frac{[k_\perp\ell_\perp]^{q-1}}{[1+[k_\perp\ell_\perp]^2]^{\frac{s+q}{2}}}$	$\frac{1}{\pi}\sin^2(k_\phi)$
Standard Noisy Slab	$2C(s)\left[1+[k_\parallel\ell_\parallel]^2\right]^{-\frac{s}{2}}$	$\left[k_\perp\ell_\perp\right]^{-1}\Theta(1-k_\perp\ell_\perp)$	$\frac{1}{\pi}\sin^2(k_\phi)$
Modified Noisy Slab	$2C(s)\left[1+[k_\parallel\ell_\parallel]^2\right]^{-\frac{s}{2}}$	$[2+p]\left[k_\perp\ell_\perp\right]^{p}\Theta(1-k_\perp\ell_\perp)$	$\frac{1}{\pi}\sin^2(k_\phi)$
Gaussian Noisy Slab	$2C(s)\left[1+[k_\parallel\ell_\parallel]^2\right]^{-\frac{s}{2}}$	$\frac{1}{2}\left[k_\perp\ell_\perp\right]^{2}e^{-\frac{1}{2}[k_\perp\ell_\perp]^2}$	$\frac{1}{\pi}\sin^2(k_\phi)$
Full 3D	$2C(s)\left[1+[k_\parallel\ell_\parallel]^2\right]^{-\frac{s}{2}}$	$4D(s,q)\frac{[k_\perp\ell_\perp]^{q-1}}{[1+[k_\perp\ell_\perp]^2]^{\frac{s+q}{2}}}$	$\frac{1}{\pi}\sin^2(k_\phi)$

Table 2.1: Alternate forms of the spectral tensor component $P_{xx}(\vec{k})$. Equation (2.39) has been used to rearrange $P_{xx}(\vec{k})$ such that each component is normalized to one in cylindrical coordinates.

using the fact that $\delta B^2 = 2\delta B_x^2$. In this form, $g_\parallel(k_\parallel)$, $g_\perp(k_\perp)$, and $g_\phi(k_\phi)$ are defined by

$$\int_{-\infty}^{\infty} \mathrm{d}k_\parallel\, \ell_\parallel\, g_\parallel(k_\parallel) = 1, \tag{2.40a}$$

$$\int_{0}^{\infty} \mathrm{d}k_\perp\, k_\perp \ell_\perp^2\, g_\perp(k_\perp) = 1, \tag{2.40b}$$

and

$$\int_{0}^{2\pi} \mathrm{d}k_\phi\, g_\phi(k_\phi) = 1, \tag{2.40c}$$

respectively. The form of $g_\parallel(k_\parallel)$ and $g_\perp(k_\perp)$ are especially useful when generating wave amplitudes in numerical simulations. Table 2.1 lists the alternate form for each model discussed.

2.3 Characterizing Turbulence Models

Besides the parallel and perpendicular length scales ($\ell_\parallel$ and $\ell_\perp$), there are several additional length scales that can be used to characterize magnetic turbulence models. The ones discussed here are the *integral scales* and the *ultra scale*. The latter scale is important in theory of field line random walk (see Matthaeus et al. (2007), Shalchi (2020)) while the former, when combined with the perpendicular magnetic correlation function is important in the transport of particles in the turbulence. These characteristics are summarized in Tables 2.2 and 2.3.

2.3.1 Magnetic Correlation Functions

The magnetic correlation functions $R_{c,r_i}(r_i)$ are related to the magnetic correlation tensor (2.2) in that they quantify the correlation of the magnetic field between two points. For axi–symmetic, homogeneous, and static turbulence, this relation is given by[4]

$$R_{i,c}(r_i) = R_{xx}(r_i) = \int \mathrm{d}^3k \, P_{xx}(\vec{k}) e^{ik_i r_i}, \quad r_j = 0, \ j \neq i; \tag{2.41}$$

where r_i is the distance along the axis the correlation function is being calculated on. If $r_i = z$ the function is referred to as the parallel magnetic correlation function, while if $r_i = x$ or $r_i = y$ the function is referred to as the perpendicular magnetic correlation function. These correlation functions often involve special functions such as Bessel or hypergeometric functions (Shalchi, 2020).

2.3.1.1 Parallel Magnetic Correlation Function

By using (2.39) to write the spectral tensor, the parallel magnetic correlation function becomes

$$R_{\parallel,c}(z) = \frac{1}{2}\delta B^2 \int_{-\infty}^{\infty} \mathrm{d}k_\parallel \, \ell_\parallel \, g_\parallel(k_\parallel) e^{ik_\parallel z} \tag{2.42}$$

while the perpendicular correlation function becomes

$$R_{\perp,c}(x) = \frac{1}{2}\delta B^2 \int_{0}^{\infty} \mathrm{d}k_\perp \, k_\perp \ell_\perp^2 \, g_\perp(k_\perp) \int_{0}^{2\pi} \mathrm{d}k_\phi \, g_\phi(k_\phi) e^{ixk_\perp \cos(k_\phi)}. \tag{2.43}$$

---

[4] This is a generalization of the forms used in Shalchi and Arendt (2024b).

Model	$R_{\parallel,c}(z)$	$R_{\perp,c}(x)$
Slab	$\frac{\delta B^2}{\Gamma\left(\frac{s-1}{2}\right)}\left[\frac{\lvert z\rvert}{2\ell_\parallel}\right]^{\frac{s-1}{2}} K_{\frac{s-1}{2}}\left(\frac{\lvert z\rvert}{\ell_\parallel}\right)$	$\frac{1}{2}\delta B^2$
2D	$\frac{1}{2}\delta B^2$	$\frac{\delta B^2}{\Gamma\left(\frac{s-1}{2}\right)}\left[\frac{x}{2\ell_\perp}\right]^{\frac{s-1}{2}} K_{\frac{s-1}{2}}\left(\frac{x}{\ell_\perp}\right)$
NRMHD	$\frac{1}{2}\delta B^2\,\frac{\sin\left(z/\ell_\parallel\right)}{z/\ell_\parallel}$	$\frac{\delta B^2}{\Gamma\left(\frac{s-1}{2}\right)}\left[\frac{x}{2\ell_\perp}\right]^{\frac{s-1}{2}} K_{\frac{s-1}{2}}\left(\frac{x}{\ell_\perp}\right)$
Standard Noisy Slab	$\frac{\delta B^2}{\Gamma\left(\frac{s-1}{2}\right)}\left[\frac{\lvert z\rvert}{2\ell_\parallel}\right]^{\frac{s-1}{2}} K_{\frac{s-1}{2}}\left(\frac{\lvert z\rvert}{\ell_\parallel}\right)$	$\frac{1}{2}\delta B^2\,{}_1F_2\left(\frac{1}{2}; 2, \frac{3}{2}; -\left[\frac{x}{2\ell_\perp}\right]^2\right)$
Modified Noisy Slab	$\frac{\delta B^2}{\Gamma\left(\frac{s-1}{2}\right)}\left[\frac{\lvert z\rvert}{2\ell_\parallel}\right]^{\frac{s-1}{2}} K_{\frac{s-1}{2}}\left(\frac{\lvert z\rvert}{\ell_\parallel}\right)$	$\frac{1}{2}\delta B^2\,{}_1F_2\left(\frac{p+2}{2}; 2, \frac{p+4}{2}; -\left[\frac{x}{2\ell_\perp}\right]^2\right)$
Gaussian Noisy Slab	$\frac{\delta B^2}{\Gamma\left(\frac{s-1}{2}\right)}\left[\frac{\lvert z\rvert}{2\ell_\parallel}\right]^{\frac{s-1}{2}} K_{\frac{s-1}{2}}\left(\frac{\lvert z\rvert}{\ell_\parallel}\right)$	$\frac{1}{2}\delta B^2\, e^{-\frac{x^2}{2\ell_\perp^2}}$
Full 3D	$\frac{\delta B^2}{\Gamma\left(\frac{s-1}{2}\right)}\left[\frac{\lvert z\rvert}{2\ell_\parallel}\right]^{\frac{s-1}{2}} K_{\frac{s-1}{2}}\left(\frac{\lvert z\rvert}{\ell_\parallel}\right)$	$\frac{\delta B^2}{\Gamma\left(\frac{s-1}{2}\right)}\left[\frac{x}{2\ell_\perp}\right]^{\frac{s-1}{2}} K_{\frac{s-1}{2}}\left(\frac{x}{\ell_\perp}\right)$

Table 2.2: Parallel and perpendicular magnetic correlation functions for various models. Results summarized from Shalchi (2008) and Shalchi and Arendt (2024b).

If the model has a power law spectra for $g_\parallel$ with $q = 0$, the parallel magnetic correlation is

$$R_{\parallel,c}(z) = 2C(s)\delta B^2 \int_0^\infty \mathrm{d}k_\parallel\, \ell_\parallel\, \frac{\cos(k_\parallel z)}{\left[1 + \left[k_\parallel \ell_\parallel\right]^2\right]^{s/2}} \tag{2.44}$$

which has solution (see Shalchi (2008))

$$R_{\parallel,c}(z) = \frac{2\sqrt{\pi}}{\Gamma(s/2)} C(s)\delta B^2 \left[\frac{|z|}{2\ell_\parallel}\right]^{\frac{s-1}{2}} K_{\frac{s-1}{2}}\left(\frac{|z|}{\ell_\parallel}\right) \tag{2.45}$$

where $K_\nu(x)$ is the modified Bessel function of the second kind. Expanding $C(s)$ allows the result to be rewritten as

$$R_{\parallel,c}(z) = \frac{\delta B^2}{\Gamma\left(\frac{s-1}{2}\right)} \left[\frac{|z|}{2\ell_\parallel}\right]^{\frac{s-1}{2}} K_{\frac{s-1}{2}}\left(\frac{|z|}{\ell_\parallel}\right). \tag{2.46}$$

2.3.1.2 Perpendicular Magnetic Correlation Function

For models with a power law spectra for $g_\perp$, the perpendicular magnetic correlation is

$$
\begin{aligned}
R_{\perp,c}(x) &= \frac{1}{2}\delta B^2 \int\limits_0^\infty \mathrm{d}k_\perp\, \ell_\perp\, 4D(s,q) \frac{\left[k_\perp \ell_\perp\right]^q}{\left[1+\left[k_\perp \ell_\perp\right]^2\right]^{\frac{s+q}{2}}} \int\limits_0^{2\pi} \mathrm{d}k_\phi\, \frac{1}{\pi} \sin^2(k_\phi) e^{ixk_\perp \cos(k_\phi)} \\
&= 4\left[\frac{x}{\ell_\perp}\right]^{-1} D(s,q)\, \delta B^2 \int\limits_0^\infty \mathrm{d}k_\perp\, \ell_\perp\, \frac{\left[k_\perp \ell_\perp\right]^{q-1}}{\left[1+\left[k_\perp \ell_\perp\right]^2\right]^{\frac{s+q}{2}}}\, J_1(k_\perp x)\,.
\end{aligned}
\tag{2.47}
$$

If we restrict q to 3, the result is (see Shalchi (2008))

$$
R_{\perp,c}(x) = \frac{2\delta B^2}{\Gamma\left(\frac{s+3}{2}\right)} D(s,3) \left[\frac{x}{2\ell_\perp}\right]^{\frac{s-1}{2}} K_{\frac{s-1}{2}}\left(\frac{x}{\ell_\perp}\right) \tag{2.48}
$$

which can be further reduced to

$$
R_{\perp,c}(x) = \frac{\delta B^2}{\Gamma\left(\frac{s-1}{2}\right)} \left[\frac{x}{2\ell_\perp}\right]^{\frac{s-1}{2}} K_{\frac{s-1}{2}}\left(\frac{x}{\ell_\perp}\right) \tag{2.49}
$$

which is identical in form to the parallel magnetic correlation function for a power law with $q = 0$. Table 2.2 summarizes the magnetic correlation functions for the models discussed in Section 2.2.

2.3.2 Integral Scale

The general form of the integral scales for axi-symmetric, magnetostatic turbulence is given by[5]

$$
\delta B_x^2 L_{r_i} = \int\limits_0^\infty \mathrm{d}r_i\, R_{xx}(\vec{r}), \quad r_j = 0,\ j \neq i; \tag{2.50}
$$

where L_{r_i} is the integral scale, R_{xx} is the xx component of the magnetic correlation tensor (2.8), and r_i is the axis for which the scale is being calculated. Effectively, the parallel and perpendicular integral scales are the integral of the respective magnetic correlation function. Given that the correlation functions involve modified Bessel or generalized hypergeometric functions, the integral scale is more easily calculated as

$$
\delta B_x^2 L_{r_i} = \int \mathrm{d}^3k\, P_{xx}(\vec{k}) \int\limits_0^\infty \mathrm{d}r_i\, e^{ik_i r_i}. \tag{2.51}
$$

---

[5] This is a generalization of the equations given in Shalchi (2020).

Using (see Zwillinger (2012))

$$\int_{0}^{\infty} \mathrm{d}r_i \, e^{ik_i r_i} = \pi \delta(k_i) \tag{2.52}$$

the integral scales become

$$L_\parallel = \pi \int_{-\infty}^{\infty} \mathrm{d}k_\parallel \, \ell_\parallel \, g_\parallel(k_\parallel) \delta(k_\parallel) = \pi g_\parallel(0) \ell_\parallel \tag{2.53a}$$

and

$$L_\perp = \pi \int_{-\infty}^{\infty} \mathrm{d}k_x \int_{-\infty}^{\infty} \mathrm{d}k_y \, \ell_\perp^2 \, g_\perp(k_\perp) g_\phi(k_\phi) \delta(k_x). \tag{2.53b}$$

For the perpendicular integral scale $g_\perp(k_\perp)$ and $g_\phi(k_\phi)$ need to be converted from cylindrical to Cartesian coordinates. For the slab model this becomes

$$L_\perp = \frac{1}{2} \int_{-\infty}^{\infty} \mathrm{d}k_y \, \ell_\perp \, g_\perp(|k_y|) = \infty, \tag{2.54a}$$

while for the other models the equation is

$$L_\perp = \ell_\perp \int_{-\infty}^{\infty} \mathrm{d}k_y \, \ell_\perp \, g_\perp(|k_y|) = 2\ell_\perp \int_{0}^{\infty} \mathrm{d}k_y \, \ell_\perp \, g_\perp(k_y) \tag{2.54b}$$

where we have taken advantage of the symmetry of the spectrum. The computed parallel and perpendicular integral scales for the models considered in this work are listed in Table 2.3

2.3.3 Ultra Scale

The ultra scale L_U is defined (Matthaeus et al., 2007) by

$$\delta B_x^2 L_U^2 = \int \mathrm{d}^3 k \, P_{xx}(\vec{k}) k_\perp^{-2}. \tag{2.55}$$

Using (2.39) to replace the spectral tensor allows the ultra scale to be written as

$$L_U^2 = \ell_\perp^2 \int_{0}^{\infty} \mathrm{d}k_\perp \, \ell_\perp \, [k_\perp \ell_\perp]^{-1} \, g_\perp(k_\perp). \tag{2.56}$$

Model	$L_\parallel$	$L_\perp$	L_U	Restrictions
Slab	$2\pi C(s)\ell_\parallel$	∞	∞	NA
2D	∞	$\frac{2\Gamma(q/2)\Gamma(s/2)}{\Gamma([q+1]/2)\Gamma([s-1]/2)}\ell_\perp$	$\sqrt{\frac{s-1}{q-1}}\ell_\perp$	$q > 1$
NRMHD	$\pi\ell_\parallel$	$\frac{2\Gamma(q/2)\Gamma(s/2)}{\Gamma([q+1]/2)\Gamma([s-1]/2)}\ell_\perp$	$\sqrt{\frac{s-1}{q-1}}\ell_\perp$	$q > 1$
Standard Noisy Slab	$2\pi C(s)\ell_\parallel$	∞	∞	NA
Modified Noisy Slab	$2\pi C(s)\ell_\parallel$	$2\frac{p+2}{p+1}\ell_\perp$	$\sqrt{1+\frac{2}{p}}\ell_\perp$	$p > 0$
Gaussian Noisy Slab	$2\pi C(s)\ell_\parallel$	$\sqrt{\frac{\pi}{2}}\ell_\perp$	$\frac{1}{\sqrt{2}}\ell_\perp$	NA
Full 3D	$2\pi C(s)\ell_\parallel$	$\frac{2\Gamma(q/2)\Gamma(s/2)}{\Gamma([q+1]/2)\Gamma([s-1]/2)}\ell_\perp$	$\sqrt{\frac{s-1}{q-1}}\ell_\perp$	$q > 1$

Table 2.3: Integral scales and the ultra scale for turbulence models discussed in this work. *Originally published in Shalchi (2020) in Space Science Reviews (Springer Nature). Reproduced under CC BY 4.0 licence. Updated with data from Shalchi and Arendt (2024b).*

For an example of the ultra scale, consider a power law spectrum for $g_\perp$, such as that used in 2D turbulence (2.27). In this case, the equation for the ultra scale is given by

$$L_U^2 = 4D(s,q)\ell_\perp^2 \int_0^\infty \mathrm{d}k_\perp\, \ell_\perp \frac{\left[k_\perp \ell_\perp\right]^{q-2}}{\left[1+\left[k_\perp\ell_\perp\right]^2\right]^{\frac{s+q}{2}}} \tag{2.57}$$

for which the result is

$$L_U = \sqrt{\frac{s-1}{q-1}}\ell_\perp. \tag{2.58}$$

Table 2.3 lists the ultra scale for the models discussed in Section 2.2.

Chapter 3

Diffusion Theory

Throughout the years, various theories have been proposed to explain the motion of charged, energetic particles in astrophysical magnetic turbulence. The earliest of these was Quasi-Linear Theory (*QLT*), proposed by Jokipii (1966). While effectively a perturbation theory, QLT showed the need to distinguish between motion parallel and perpendicular to the mean field. The QLT description of parallel scattering is that the particles scatter off of specific parallel wave modes, which are given by the resonance equation

$$k_{\|} v \mu \pm n\Omega = 0 \tag{3.1}$$

where v is the particle velocity, μ is the cosine of the angle between the velocity and the mean field (called the pitch–angle cosine), $\Omega = qB_0/\gamma mc$ is the gyro frequency associated with the mean field, and $k_{\|}$ is the wave mode the particle is scattering off of. Equation (3.1) can be rearranged to read

$$k_{\|} R_L \mu = \mp n \tag{3.2}$$

where R_L is the Larmor radius of the particle. Perpendicular diffusion in QLT is tied to the random walk of the magnetic field lines, leading to the prediction of an energy independent perpendicular mean free path.[1] Overtime, several short comings of QLT became apparent, such as the inability to describe scattering when the particle velocity is perpendicular to the mean field (for example, see Shalchi (2005b)), and that the predictions for perpendicular transport did not match the results of test

---

[1] The relation between mean free paths and diffusion coefficients is discussed in 3.3.2.

particle simulations. This led to the proposal of other theories, such as:[2]

- Non–Linear Guiding Center (NLGC) Theory of Matthaeus et al. (2003)
- Unified Non–Linear Transport (UNLT) Theory
  - Diffusive UNLT Theory (Shalchi, 2010)
  - Time–dependent UNLT Theory (Shalchi, 2017, Lasuik and Shalchi, 2017)
- Field Line – Particle Decorrelation (FLPD) Theory. (Shalchi, 2021)

3.1 General Calculations of Diffusion Coefficients

As discussed in Chapter 1.2.2, the diffusion coefficients are calculated using equations (1.21) and (1.22). While these are specifically for particles, the equations can be generalized to any quantity as

$$d(\lambda) = \frac{1}{2}\frac{\mathrm{d}}{\mathrm{d}\lambda}\left\langle (\Delta x(\lambda))^2 \right\rangle \tag{3.3a}$$

and

$$\kappa = \lim_{\lambda\to\infty} d(\lambda) \tag{3.3b}$$

where λ is the dependent variable. In the context of particle transport, $\lambda = t$ and the diffusion coefficients have units of length squared per second; while for field line diffusion $\lambda = z$ and the diffusion coefficient has units of length. The problem in both cases is to either determine the mean square displacement as a function of λ from theory and then take the derivative, or to take the derivative and then determine the resulting function from theory. In the case where the distribution function is known, the diffusion coefficient(s) can be directly calculated as

$$d(\lambda) = \frac{1}{2}\frac{\mathrm{d}}{\mathrm{d}\lambda}\int \mathrm{d}\Delta x\,(\Delta x)^2 \rho(\Delta x, \lambda) \tag{3.4}$$

where $\rho(\Delta x, \lambda)$ is the distribution function at Δx and λ. A variant of this method (see (1.28)) is used when analyzing numerical data. In analytical theory, the primary tool for dealing with this is the Taylor–Green–Kubo (TGK) formulation (Taylor, 1922, Green, 1951, Kubo, 1957).

---

[2] There are other theories that were proposed besides those listed here. However, they are not relevant to this work.

3.1.1 TGK Formulation

The essence of the TGK forumation is that the displacement, $\Delta x(\lambda)$, can be written as

$$\Delta x(\lambda) = \int_0^\lambda \mathrm{d}\lambda' \, \frac{\mathrm{d}x}{\mathrm{d}\lambda}(\lambda'), \tag{3.5}$$

meaning that the equation for the running diffusion coefficient can be written as

$$d(\lambda) = \frac{1}{2}\frac{\mathrm{d}}{\mathrm{d}\lambda} \int_0^\lambda \mathrm{d}\lambda' \int_0^\lambda \mathrm{d}\lambda'' \left\langle \frac{\mathrm{d}x}{\mathrm{d}\lambda}(\lambda')\frac{\mathrm{d}x}{\mathrm{d}\lambda}(\lambda'') \right\rangle. \tag{3.6}$$

Then, if the correlation function

$$\left\langle \frac{\mathrm{d}x}{\mathrm{d}\lambda}(\lambda')\frac{\mathrm{d}x}{\mathrm{d}\lambda}(\lambda'') \right\rangle \tag{3.7}$$

is homogeneous in λ, only the difference in λ matters. In this case, the running diffusion coefficient can be written as

$$d(\lambda) = \int_0^\lambda \mathrm{d}\lambda' \left\langle \frac{\mathrm{d}x}{\mathrm{d}\lambda}(\lambda')\frac{\mathrm{d}x}{\mathrm{d}\lambda}(0) \right\rangle \tag{3.8a}$$

and the diffusion coefficient as

$$\kappa = \int_0^\infty \mathrm{d}\lambda' \left\langle \frac{\mathrm{d}x}{\mathrm{d}\lambda}(\lambda')\frac{\mathrm{d}x}{\mathrm{d}\lambda}(0) \right\rangle. \tag{3.8b}$$

A particle specific derivation of (3.8) can be found in Shalchi (2009).

As a final note, (3.8a) combined with (3.3a) can be used to relate the second derivative of the mean square displacement to the correlation function by

$$\frac{\mathrm{d}^2}{\mathrm{d}\lambda^2} \left\langle (\Delta x(\lambda))^2 \right\rangle = 2 \left\langle \frac{\mathrm{d}x}{\mathrm{d}\lambda}(\lambda)\frac{\mathrm{d}x}{\mathrm{d}\lambda}(0) \right\rangle, \tag{3.9}$$

which is used in analytical theory to calculate the running diffusion coefficient when the correlation function as a function of λ can be defined, such as in time–dependent UNLT theory (see Section 3.3.6.2) and FLPD theory (see Section 3.3.8).

3.2 Field Line Diffusion

Field line diffusion, more commonly referred to as *Field Line Random Walk (FLRW)*, describes the probability of finding a field line at a given point in space after travelling a certain distance along the z-axis. As such, the independent variable here is the position along the z-axis, rather than time as in the case of particle diffusion, and therefore the field line diffusion coefficient has units of length.

3.2.1 Diffusion Coefficient Derivation

To derive the running field line diffusion coefficient, first consider the field line equation:

$$\frac{\mathrm{d}x}{B_x} = \frac{\mathrm{d}y}{B_y} = \frac{\mathrm{d}z}{B_z}, \tag{3.10}$$

which can be rearranged to read

$$\frac{\mathrm{d}x}{\mathrm{d}z} = \frac{B_x}{B_z} \tag{3.11a}$$

and

$$\frac{\mathrm{d}y}{\mathrm{d}z} = \frac{B_y}{B_z}. \tag{3.11b}$$

Using (3.11) in (3.6) yields

$$d_{xx}(\Delta z) = \frac{1}{2}\frac{\mathrm{d}}{\mathrm{d}z}\int\limits_{z_0}^{z}\mathrm{d}z'\int\limits_{z_0}^{z}\mathrm{d}z'' \left\langle \frac{B_x}{B_z}\left(\vec{x}(z')\right)\frac{B_x}{B_z}\left(\vec{x}(z'')\right)\right\rangle \tag{3.12a}$$

for the x component and

$$d_{yy}(\Delta z) = \frac{1}{2}\frac{\mathrm{d}}{\mathrm{d}z}\int\limits_{z_0}^{z}\mathrm{d}z'\int\limits_{z_0}^{z}\mathrm{d}z'' \left\langle \frac{B_y}{B_z}\left(\vec{x}(z')\right)\frac{B_y}{B_z}\left(\vec{x}(z'')\right)\right\rangle \tag{3.12b}$$

for the y component. If the turbulence is axi–symmetric about the z axis, then there is only one field line diffusion coefficient:

$$d_{xx}(\Delta z) = d_{yy}(\Delta z) = d_{FL}(\Delta z). \tag{3.13}$$

Furthermore, in incompressible turbulence the z component of the magnetic field consists of only the mean field and can be removed from the integral, which leads to the equation:[3]

$$d_{FL}(\Delta z) = \frac{1}{2B_0^2}\frac{\mathrm{d}}{\mathrm{d}z}\int\limits_{z_0}^{z}\mathrm{d}z'\int\limits_{z_0}^{z}\mathrm{d}z'' \left\langle \delta B_x(\vec{x}(z'))\,\delta B_x(\vec{x}(z''))\right\rangle, \tag{3.14}$$

---

[3] In theory z_0 is generally set to zero due to the assumption of homogeneous turbulence.

with an associated mean square displacement calculated by (Shalchi and Kourakis, 2007)

$$\left\langle (\Delta x(z))^2 \right\rangle = \frac{1}{B_0^2} \int\limits_{z_0}^{z} \mathrm{d}z' \int\limits_{z_0}^{z} \mathrm{d}z'' \, \langle \delta B_x(\vec{x}(z'))\, \delta B_x(\vec{x}(z'')) \rangle \,. \tag{3.15}$$

Finally, if the field is represented as a Fourier transform, as per (2.4), the equation for the field line diffusion coefficient is written as

$$d_{FL}(\Delta z) = \frac{1}{2B_0^2} \frac{\mathrm{d}}{\mathrm{d}z} \int\limits_{z_0}^{z} \mathrm{d}z' \int\limits_{z_0}^{z} \mathrm{d}z'' \int \mathrm{d}^3k \int \mathrm{d}^3k' \left\langle \tilde{\delta B}_x(\vec{k}) \tilde{\delta B}_x^{\dagger}(\vec{k}') e^{i\left(\vec{k}\vec{x}(z') - \vec{k}'\vec{x}(z'')\right)} \right\rangle . \tag{3.16}$$

For any field with transverse complexity, this equation is non-linear, while for those fields that lack transverse complexity it can be solved exactly.

While (3.16) calculates the field line diffusion coefficient directly, it is often more convenient to take the second derivative with respect to z and express the result as a second order, non-linear equation for the mean square displacement. In this form the equation is

$$\frac{\mathrm{d}^2}{\mathrm{d}z^2} \left\langle (\Delta x)^2 \right\rangle = \frac{1}{B_0^2} \frac{\mathrm{d}^2}{\mathrm{d}z^2} \int\limits_{z_0}^{z} \mathrm{d}z' \int\limits_{z_0}^{z} \mathrm{d}z'' \int \mathrm{d}^3k \int \mathrm{d}^3k' \left\langle \tilde{\delta B}_x(\vec{k}) \tilde{\delta B}_x^{\dagger}(\vec{k}') e^{i\left[\vec{k}\vec{x}(z') - \vec{k}'\vec{x}(z'')\right]} \right\rangle . \tag{3.17}$$

The field line diffusion coefficient can be found from the result by either using (3.3) after solving for the mean square displacement, or by integrating (3.17) with respect to z.

3.2.2 Field Line Diffusion in Slab Turbulence

An ideal example of a turbulent field that lacks transverse complexity and has an exact field line diffusion equation is the slab turbulence model discussed in Chapter 2.2.1. For this model (3.16) can be reduced to

$$\frac{\mathrm{d}^2}{\mathrm{d}z^2} \left\langle (\Delta x)^2 \right\rangle = \frac{1}{B_0^2} \frac{\mathrm{d}^2}{\mathrm{d}z^2} \int\limits_{z_0}^{z} \mathrm{d}z' \int\limits_{z_0}^{z} \mathrm{d}z'' \int \mathrm{d}^3k \int \mathrm{d}^3k' \left\langle \tilde{\delta B}_x(\vec{k}) \tilde{\delta B}_x^{\dagger}(\vec{k}') \right\rangle e^{i\left[k_\parallel z' - k'_\parallel z''\right]} . \tag{3.18}$$

As the slab model is being considered, the magnetic correlation can be replaced by the xx component of the spectral tensor using (2.23), resulting in

$$\frac{\mathrm{d}^2}{\mathrm{d}z^2}\left\langle(\Delta x)^2\right\rangle = \frac{2\pi}{B_0^2}\frac{\mathrm{d}^2}{\mathrm{d}z^2}\int\limits_{-\infty}^{\infty}\mathrm{d}k_\parallel\, g^{Slab}(k_\parallel)\int\limits_{z_0}^{z}\mathrm{d}z'\int\limits_{z_0}^{z}\mathrm{d}z''\, e^{ik_\parallel(z'-z'')}. \tag{3.19}$$

Integrating over z' and z'' yields

$$\frac{\mathrm{d}^2}{\mathrm{d}z^2}\left\langle(\Delta x)^2\right\rangle = \frac{2\pi}{B_0^2}\frac{\mathrm{d}^2}{\mathrm{d}z^2}\int\limits_{-\infty}^{\infty}\mathrm{d}k_\parallel\, g^{Slab}(k_\parallel)\frac{e^{ik_\parallel z}-e^{ik_\parallel z_0}}{ik_\parallel}\frac{e^{-ik_\parallel z}-e^{-ik_\parallel z_0}}{-ik_\parallel} \tag{3.20}$$

which can be rearranged to read

$$\frac{\mathrm{d}^2}{\mathrm{d}z^2}\left\langle(\Delta x)^2\right\rangle = \frac{4\pi}{B_0^2}\int\limits_{-\infty}^{\infty}\mathrm{d}k_\parallel\, g^{Slab}(k_\parallel)\cos(k_\parallel\Delta z). \tag{3.21}$$

Finally, the field line diffusion coefficient is found by integrating with respect to z and taking the limit of $z\to\infty$:

$$\kappa_{FL}^{Slab} = C(s)\frac{\delta B^2}{B_0^2}\ell_\parallel\int\limits_{-\infty}^{\infty}\mathrm{d}k_\parallel\,\left[1+[k_\parallel\ell_\parallel]^2\right]^{-\frac{s}{2}}\int\limits_{z_0}^{\infty}\mathrm{d}z\,\cos\left(k_\parallel\Delta z\right). \tag{3.22}$$

Note that here (2.24) is taken as the spectrum of the turbulence. In order to deal with the z integral, the relation

$$\int\limits_{-\infty}^{\infty}\mathrm{d}z\, e^{i(k-k')z} = 2\pi\delta(k-k') \tag{3.23}$$

is used (Zwillinger, 2012), for which a change of variables from z to $z'=\Delta z$ is required. This leads to the diffusion coefficient being given by

$$\kappa_{FL}^{Slab} = \pi C(s)\ell_\parallel\frac{\delta B^2}{B_0^2}\int\limits_{-\infty}^{\infty}\mathrm{d}k_\parallel\,\left[1+[k_\parallel\ell_\parallel]^2\right]^{-\frac{s}{2}}\delta(k_\parallel) \tag{3.24}$$

As pointed out in Shalchi (2005a), taking this equation at face value is problematic: there is no energy in the turbulence at $k=0$. However, the Dirac delta came about from using the limit $z\to\infty$, which is not physically permitted. As such, the interpretation is that the function is evaluated in the limit $k_\parallel\to 0$, which results in

$$\kappa_{FL}^{Slab} = \pi C(s)\ell_\parallel \frac{\delta B^2}{B_0^2} \tag{3.25}$$

for a spectrum given by (2.24).

3.2.3 Field Line Diffusion in 2D Turbulence

If the slab model is an ideal example of turbulence without transverse complexity, the 2D model (see Chapter 2.2.2) is the opposite: the spatial dependency of this model is entirely in the xy plane. As with the slab model, the starting equation used here is (3.17), except here there is no explicit dependence on z on either side of the equation. Furthermore, the orientation of the field amplitudes $\tilde{\delta B}$ are coupled to the orientation of the wave vector $\vec{k}$. This can be overcome, however, through the use of *Corrsin's Independence Hypothesis* (Corrsin, 1959) (also referred to as Corrsin's approximation), which is known in other research fields as the *random phase approximation.* The derivation contained here follows that of Shalchi (2020); an alternate derivation can be found in Shalchi and Kourakis (2007).

Using Corrsin's approximation allows for the complex exponential to be split from the Fourier amplitude correlation, resulting in

$$\left\langle \tilde{\delta B}_x(\vec{k})\tilde{\delta B}_x^\dagger(\vec{k}')e^{i\left[\vec{k}\vec{x}(z')-\vec{k}'\vec{x}(z'')\right]}\right\rangle = \left\langle \tilde{\delta B}_x(\vec{k})\tilde{\delta B}_x^\dagger(\vec{k}')\right\rangle\left\langle e^{i\left[\vec{k}\vec{x}(z')-\vec{k}'\vec{x}(z'')\right]}\right\rangle \tag{3.26}$$

which allows us to write (3.17) as

$$\frac{\mathrm{d}^2}{\mathrm{d}z^2}\left\langle(\Delta x)^2\right\rangle = \frac{1}{B_0^2}\int \mathrm{d}^3k\, P_{xx}(\vec{k})\frac{\mathrm{d}^2}{\mathrm{d}z^2}\int_{z_0}^{z}\mathrm{d}z'\int_{z_0}^{z}\mathrm{d}z''\left\langle e^{i\vec{k}\left[\vec{x}(z')-\vec{x}(z'')\right]}\right\rangle \tag{3.27}$$

using (2.7) to replace the Fourier amplitude correlation with the spectral tensor. To proceed, the *Leibniz integral rule* is employed:

$$\frac{\mathrm{d}}{\mathrm{d}z}\int_{a(z)}^{b(z)}\mathrm{d}t\, f(z,t) = f\big(z,b(z)\big)\frac{\mathrm{d}}{\mathrm{d}z}b(z) - f\big(z,a(z)\big)\frac{\mathrm{d}}{\mathrm{d}z}a(z) + \int_{b(z)}^{a(z)}\mathrm{d}t\,\frac{\partial}{\partial z}f(z,t). \tag{3.28}$$

Using $a(z) = z_0$ and $b(z) = z$, the first derivative is found to be[4]

$$\begin{aligned}&\frac{\mathrm{d}^2}{\mathrm{d}z^2}\int\limits_{z_0}^{z}\mathrm{d}z'\int\limits_{z_0}^{z}\mathrm{d}z''\left\langle e^{i\vec{k}\left[\vec{x}(z')-\vec{x}(z'')\right]}\right\rangle\\ =&\frac{\mathrm{d}}{\mathrm{d}z}\int\limits_{z_0}^{z}\mathrm{d}z'\ \left[\left\langle e^{i\vec{k}\left[\vec{x}(z')-\vec{x}(z)\right]}\right\rangle+\left\langle e^{i\vec{k}\left[\vec{x}(z)-\vec{x}(z')\right]}\right\rangle\right]\end{aligned} \tag{3.29}$$

which can also be written as

$$\frac{\mathrm{d}^2}{\mathrm{d}z^2}\int\limits_{z_0}^{z}\mathrm{d}z'\int\limits_{z_0}^{z}\mathrm{d}z''\left\langle e^{i\vec{k}\left[\vec{x}(z')-\vec{x}(z'')\right]}\right\rangle = 2\Re\frac{\mathrm{d}}{\mathrm{d}z}\int\limits_{z_0}^{z}\mathrm{d}z'\left\langle e^{i\vec{k}\left[\vec{x}(z')-\vec{x}(z)\right]}\right\rangle. \tag{3.30}$$

Next, it is assumed that the function being averaged on the right hand side depends only on the difference in z, allowing us to use

$$\int\limits_{z_0}^{z}\mathrm{d}z'\left\langle e^{i\vec{k}\left[\vec{x}(z')-\vec{x}(z)\right]}\right\rangle = \int\limits_{0}^{z}\mathrm{d}z'\left\langle e^{i\vec{k}\left[\vec{x}(z')-\vec{x}(0)\right]}\right\rangle. \tag{3.31}$$

Finally, (3.28) can be applied a second time to find

$$\frac{\mathrm{d}^2}{\mathrm{d}z^2}\int\limits_{z_0}^{z}\mathrm{d}z'\int\limits_{z_0}^{z}\mathrm{d}z''\left\langle e^{i\vec{k}\left[\vec{x}(z')-\vec{x}(z'')\right]}\right\rangle = 2\Re\left\langle e^{i\vec{k}\Delta\vec{x}}\right\rangle. \tag{3.32}$$

3.2.3.1 Characteristic Function

Before continuing, the quantity being averaged and integrated needs to be defined. Called the *characteristic function*,

$$\left\langle e^{i\vec{k}\Delta\vec{x}}\right\rangle = \int\mathrm{d}k\,\rho(\Delta\vec{x})e^{i\vec{k}\Delta\vec{x}} \tag{3.33}$$

is the Fourier transform of the distribution function for the quantity in question. For a Gaussian distribution function given by[5]

$$\rho_{FL}(x,y) = \frac{1}{\sqrt{2\pi\left\langle(\Delta x)^2\right\rangle}}e^{-\frac{x^2+y^2}{2\left\langle(\Delta x)^2\right\rangle}} \tag{3.34}$$

---

[4] A variable redefinition of $z'' \to z'$ has been used in the second term on the right.

[5] A Gaussian distribution is often used for both particles (for example, see Matthaeus et al. (2003), Shalchi (2017), Lasuik and Shalchi (2017)) and field lines (see Shalchi and Kourakis (2007) for example). Lasuik and Shalchi (2018) considered the effect of non–Gaussian distributions in particle transport theory, showing that there was only a minor effect on the resulting diffusion coefficient.

the characteristic function is

$$\tilde{\rho} = e^{-\frac{1}{2}\left\langle(\Delta x)^2\right\rangle k_\perp^2}. \tag{3.35}$$

3.2.3.2 Solving the Equation for 2D Turbulence

Combining (3.27) with (3.32) and (3.35) and using (2.26) for the 2D spectral tensor yields

$$\frac{\mathrm{d}^2}{\mathrm{d}z^2}\left\langle(\Delta x)^2\right\rangle = \frac{2\pi}{B_0^2}\int\limits_0^\infty \mathrm{d}k_\perp\, g^{2D}(k_\perp) e^{-\frac{1}{2}\left\langle(\Delta x)^2\right\rangle k_\perp^2}. \tag{3.36}$$

As per Shalchi (2011), this equation can be solved first by defining $\sigma = \langle(\Delta x)^2\rangle$ and multiplying both sides by σ' to get

$$\sigma'\sigma'' = \frac{2\pi}{B_0^2}\int\limits_0^\infty \mathrm{d}k_\perp\, g^{2D}(k_\perp)\sigma' e^{-\frac{1}{2}\sigma k_\perp^2} \tag{3.37}$$

from which we find

$$\frac{\mathrm{d}}{\mathrm{d}z}\left(\sigma'\right)^2 = -\frac{8\pi}{B_0^2}\int\limits_0^\infty \mathrm{d}k_\perp\, \frac{g^{2D}(k_\perp)}{k_\perp^2}\frac{\mathrm{d}}{\mathrm{d}z}e^{-\frac{1}{2}\sigma k_\perp^2}. \tag{3.38}$$

Integrating both sides with respect to z and assuming that $\sigma \gg 1$ in the limit of $z \to \infty$ results in[6]

$$\lim_{z\to\infty}\left(\sigma'\right)^2 = \frac{8\pi}{B_0^2}\int\limits_0^\infty \mathrm{d}k_\perp\, \frac{g^{2D}(k_\perp)}{k_\perp^2} \tag{3.39}$$

from which we find that field line diffusion coefficient for 2D turbulence is

$$\kappa_{FL} = \left[\frac{2\pi}{B_0^2}\int\limits_0^\infty \mathrm{d}k_\perp\, \frac{g^{2D}(k_\perp)}{k_\perp^2}\right]^{1/2} \tag{3.40}$$

by using the relation from (3.3b). Comparing this to the ultra scale (Chapter 2.3.3), it can be seen that the field line diffusion coefficient for 2D turbulence (2.27) is equal to

$$\kappa_{FL}^{2D} = \sqrt{2\frac{\delta B^2}{B_0^2}L_U} = \sqrt{2\frac{s-1}{q-1}\ell_\perp\frac{\delta B}{B_0}}. \tag{3.41}$$

---

[6] This simply corresponds to the assumption that the field lines are diffusive in the limit $z \to \infty$.

3.2.4 General Field Line Diffusion

In general, the turbulence wave vectors are neither completely parallel to the mean field nor fully confined to the xy plane. For these models, we go back to (3.32) and consider the right hand side of it. For the cases of incompressible turbulence, such as those considered in Chapter 2, we can break the characteristic function into parallel and perpendicular components, such that

$$\left\langle e^{i\vec{k}\Delta\vec{x}}\right\rangle = e^{ik_\parallel \Delta z}\left\langle e^{i\vec{k}_\perp \Delta\vec{x}_\perp}\right\rangle. \tag{3.42}$$

Note that since Δz is the independent variable in this case, there is nothing to average over.

Using this with (3.27) and (3.32) and assuming a Gaussian field line distribution function yields

$$\frac{\mathrm{d}^2}{\mathrm{d}z^2}\left\langle(\Delta x)^2\right\rangle = \frac{2}{B_0^2}\int \mathrm{d}^3k\, P_{xx}(\vec{k})\cos(k_\parallel \Delta z)e^{-\frac{1}{2}\left\langle(\Delta x)^2\right\rangle k_\perp^2} \tag{3.43}$$

for the field line diffusion equation, as per Shalchi and Kourakis (2007). If the spectral tensor can be expressed by (2.39), then (3.43) can be written as

$$\begin{aligned}\frac{\mathrm{d}^2}{\mathrm{d}z^2}\left\langle(\Delta x)^2\right\rangle = \frac{\delta B^2}{B_0^2}&\int_{-\infty}^{\infty}\mathrm{d}k_\parallel\, \ell_\parallel\, g_\parallel(k_\parallel)\cos(k_\parallel \Delta z)\\ &\times\int_0^\infty \mathrm{d}k_\perp\, k_\perp\, \ell_\perp^2\, g_\perp(k_\perp)e^{-\frac{1}{2}\left\langle(\Delta x)^2\right\rangle k_\perp^2}.\end{aligned} \tag{3.44}$$

We will now apply this equation to the noisy slab model and the full 3D model defined in Chapter 2.

3.2.4.1 Field Line Diffusion in Noisy Turbulence

Using the noisy slab model, (2.30), in (3.44) (see Shalchi (2019a)) results in[7]

$$\begin{aligned}\frac{\mathrm{d}^2}{\mathrm{d}z^2}\left\langle(\Delta x)^2\right\rangle = \frac{\delta B^2}{B_0^2}&\int_{-\infty}^{\infty}\mathrm{d}k_\parallel\, \ell_\parallel\, 2C(s)\frac{\cos(k_\parallel z)}{\left[1+\left[k_\parallel \ell_\parallel\right]^2\right]^{\frac{s}{2}}}\\ &\times\int_0^\infty \mathrm{d}k_\perp\, \ell_\perp\, \Theta(1-k_\perp \ell_\perp)e^{-\frac{1}{2}\left\langle(\Delta x)^2\right\rangle k_\perp^2}.\end{aligned} \tag{3.45}$$

---

[7] It has been assumed here that $z_0 = 0$.

As a starting point for solving the equation, we define

$$\begin{aligned} k_z &= k_\parallel \ell_\parallel, & k_r &= k_\perp \ell_\perp, \\ z' &= z/\ell_\parallel, & \sigma_x^2 &= \left\langle (\Delta x)^2 \right\rangle / \ell_\perp^2 \end{aligned} \tag{3.46}$$

which allows (3.45) to be written as

$$\frac{\mathrm{d}^2 \sigma_x^2}{\mathrm{d}z'^2} = 2 \frac{\ell_\parallel^2}{\ell_\perp^2} \frac{\delta B^2}{B_0^2} \int_0^\infty \mathrm{d}k_z \, 2C(s) \frac{\cos(k_z z')}{[1 + k_z^2]^{\frac{s}{2}}} \int_0^1 \mathrm{d}k_r \, e^{-\frac{1}{2}\sigma_x^2 k_r^2}, \tag{3.47}$$

Integration over k_r yields

$$\frac{\mathrm{d}^2 \sigma_x^2}{\mathrm{d}z'^2} = 2 \frac{\ell_\parallel^2}{\ell_\perp^2} \frac{\delta B^2}{B_0^2} \left[\sqrt{\frac{\pi}{2\sigma_x^2}} \operatorname{erf}\left(\sqrt{\frac{\sigma_x^2}{2}} \right) \right] \int_0^\infty \mathrm{d}k_z \, 2C(s) \frac{\cos(k_z z')}{[1 + k_z^2]^{\frac{s}{2}}}. \tag{3.48}$$

It is important to note that the quantity in brackets ($[\cdots]$) goes to one should the length scale corresponding to the noise go to infinity, which recovers the equation for the regular slab model. The remaining integral for the noisy slab model has been solved in Chapter 2.3, resulting in

$$\frac{\mathrm{d}^2 \sigma_x^2}{\mathrm{d}z'^2} = \frac{4}{\Gamma\left(\frac{s-1}{2}\right)} \frac{\ell_\parallel^2}{\ell_\perp^2} \frac{\delta B_x^2}{B_0^2} \left[\frac{|z'|}{2} \right]^{\frac{s-1}{2}} K_{\frac{s-1}{2}}(|z'|) \left[\sqrt{\frac{\pi}{2\sigma_x^2}} \operatorname{erf}\left(\sqrt{\frac{\sigma_x^2}{2}} \right) \right]. \tag{3.49}$$

The relation $\delta B^2 = 2\delta B_x^2$ has also been used. Neither of these equations can be solved analytically.

3.2.4.2 Field Line Diffusion in the Full 3D Model

The field line diffusion equation for the full 3D model (2.37) is

$$\begin{aligned} \frac{\mathrm{d}^2}{\mathrm{d}z^2} \left\langle (\Delta x)^2 \right\rangle = 2 \frac{\delta B^2}{B_0^2} & \int_0^\infty \mathrm{d}k_\parallel \, \ell_\parallel \, 2C(s) \frac{\cos(k_\parallel z)}{\left[1 + \left[k_\parallel \ell_\parallel \right]^2 \right]^{\frac{s}{2}}} \\ & \times \int_0^\infty \mathrm{d}k_\perp \, \ell_\perp \, 4D(s,q) \frac{\left[k_\perp \ell_\perp \right]^q}{\left[1 + \left[k_\perp \ell_\perp \right]^2 \right]^{\frac{s+q}{2}}} e^{-\frac{1}{2}\left\langle (\Delta x)^2 \right\rangle k_\perp^2}. \end{aligned} \tag{3.50}$$

Integrating over $k_\parallel$ leads to

$$\frac{\mathrm{d}^2 \sigma_x^2}{\mathrm{d}z'^2} = \frac{16 D(s,q)}{\Gamma\left(\frac{s-1}{2}\right)} \frac{\ell_\parallel^2}{\ell_\perp^2} \frac{\delta B_x^2}{B_0^2} \left[\frac{|z'|}{2} \right]^{\frac{s-1}{2}} K_{\frac{s-1}{2}}(|z'|) \int_0^\infty \mathrm{d}k'_\perp \frac{{k'_\perp}^q}{\left[1 + {k'_\perp}^2 \right]^{\frac{s+q}{2}}} e^{-\frac{1}{2}\sigma_x^2 {k'_\perp}^2}, \tag{3.51}$$

where (3.46) has been used. As with the noisy slab model, this equation cannot be solved analytically.

3.2.4.3 Introducing the Kubo Number

A common feature in (3.49) and (3.51) is the presence of the product of the square of the length scale ratio and field energy density ratio. This ratio is the square of what is referred to as the Kubo number (Kubo, 1963), which is defined as

$$K = \frac{\ell_\parallel}{\ell_\perp}\frac{\delta B_x}{B_0} \tag{3.52}$$

and is important in diffusion theory for both field lines and particles. In general, the Kubo number is one of the few variables that cannot be scaled away by combining it with other quantities, and therefore it controls the behaviour of the diffusion coefficients. Given the equation for the Kubo number, any quantity that is a function of the magnetic turbulence strength can be rewritten as a function of the Kubo number. For example, the field line diffusion coefficients for Slab and 2D turbulence (3.41) can be written as

$$\frac{\ell_\parallel \kappa_{FL}^{Slab}}{\ell_\perp^2} = \pi C(s)\frac{\ell_\parallel^2}{\ell_\perp^2}\frac{\delta B^2}{B_0^2} = \pi C(s) K^2 \tag{3.53a}$$

and

$$\frac{\ell_\parallel \kappa_{FL}^{2D}}{\ell_\perp^2} = \sqrt{2\frac{s-1}{q-1}}\frac{\ell_\parallel}{\ell_\perp}\frac{\delta B}{B_0} = \sqrt{2\frac{s-1}{q-1}}K. \tag{3.53b}$$

respectively. From these equations, it can be seen that the field line diffusion in slab turbulence is proportional to the square of the Kubo number, while for 2D turbulence the proportionality is linear. In Chapter 5, the Kubo number will be used to replace the magnetic field strength in the equations used to analyze simulation data.

3.2.5 Diffusive Approximation

One possible simplification of (3.43) and (3.44) is to assume that the field lines are immediately diffusive. In this case the field line mean square displacement is

$$\left\langle (\Delta x(z))^2 \right\rangle = 2\kappa_{FL}|z| \tag{3.54}$$

where κ_{FL} is the field line diffusion. With this approximation, (3.43) becomes[8]

$$\kappa_{FL} = \frac{1}{2} \lim_{z\to\infty} \frac{\mathrm{d}}{\mathrm{d}z} \left\langle (\Delta x)^2 \right\rangle = \frac{1}{B_0^2} \int\limits_{-\infty}^{\infty} \mathrm{d}z \int \mathrm{d}^3k \, P_{xx}(\vec{k}) \cos(k_\parallel z) e^{-\kappa_{FL}|z|k_\perp^2} \tag{3.55}$$

Solving the integral over z results in (Kadomtsev and Pogutse, 1979, Matthaeus et al., 1995)

$$\kappa_{FL} = \frac{1}{B_0^2} \int \mathrm{d}^3k \, P_{xx}(\vec{k}) \frac{\kappa_{FL} k_\perp^2}{k_\parallel^2 + \kappa_{FL}^2 k_\perp^4}. \tag{3.56}$$

If the spectral tensor can be expressed using (2.39), then the field line diffusion can be calculated by

$$\kappa_{FL} = \frac{\delta B_x^2}{B_0^2} \int\limits_{-\infty}^{\infty} \mathrm{d}k_\parallel \, \ell_\parallel \, g_\parallel(k_\parallel) \int\limits_{0}^{\infty} \mathrm{d}k_\perp \, k_\perp \ell_\perp^2 \, g_\perp(k_\perp) \frac{\kappa_{FL} k_\perp^2}{k_\parallel^2 + \kappa_{FL}^2 k_\perp^4}. \tag{3.57}$$

3.3 Particle Diffusion

When considering the diffusion of particles the TGK formulation, (3.8), becomes

$$d_{ii}(t) = \int\limits_0^t \mathrm{d}t' \, \left\langle v_i(t') v_i(0) \right\rangle \tag{3.58}$$

where we have used $\lambda = t$. Likewise, the equation for the mean square displacement, (3.9), becomes

$$\frac{\mathrm{d}^2}{\mathrm{d}t^2} \left\langle (\Delta x_i(t))^2 \right\rangle = 2 \left\langle v_i(t) v_i(0) \right\rangle . \tag{3.59}$$

In both cases, the averaging operator $\langle \cdots \rangle$ is an average over a two–point, two–time phase space distribution function

$$\rho(\vec{x}, \vec{x}_0, \vec{v}, \vec{v}_0, t, t_0). \tag{3.60}$$

The equations can therefore be written as

$$d_{ii}(t) = \int\limits_0^t \mathrm{d}t' \int \mathrm{d}^3x \int \mathrm{d}^3x_0 \int \mathrm{d}^3v \int \mathrm{d}^3v_0 \;\, v_i v_{0i} \, \rho(\vec{x}, \vec{x}_0, \vec{v}, \vec{v}_0, t', 0) \tag{3.61a}$$

---

[8] A secondary assumption here is that $z_0 = 0$. This can also be done with a change of coordinates.

and

$$\frac{\mathrm{d}^2}{\mathrm{d}t^2}\left\langle(\Delta x_i(t))^2\right\rangle = 2\int \mathrm{d}^3x \int \mathrm{d}^3x_0 \int \mathrm{d}^3v \int \mathrm{d}^3v_0 \; v_i v_{0i}\, \rho(\vec{x}, \vec{x}_0, \vec{v}, \vec{v}_0, t, 0), \tag{3.61b}$$

respectively, where we have used the assumption $t_0 = 0$. As mentioned in Chapter 1, while the trajectories in phase space are completely unique, the displacements are not, and it can therefore be assumed that the initial spatial distribution of particles is unimportant for calculations involving the displacement. The equations can therefore be written as

$$d_{ii}(t) = \int_0^t \mathrm{d}t' \int \mathrm{d}^3x \int \mathrm{d}^3v \int \mathrm{d}^3v_0 \; v_i v_{0i}\, \rho(\Delta\vec{x}, \vec{v}, \vec{v}_0, t') \tag{3.62a}$$

for the TGK formulation and

$$\frac{\mathrm{d}^2}{\mathrm{d}t^2}\left\langle(\Delta x_i(t))^2\right\rangle = 2\int \mathrm{d}^3x \int \mathrm{d}^3v \int \mathrm{d}^3v_0 \; v_i v_{0i}\, \rho(\Delta\vec{x}, \vec{v}, \vec{v}_0, t'), \tag{3.62b}$$

for the mean square displacement.

3.3.1 Quasi–Linear Theory

The first theory to describe the motion of charged particles in astrophysical turbulence was the *Quasi–Linear Theory* (or *QLT*) of Jokipii (1966). In QLT, the equations for the diffusion coefficients are evaluated using the trajectories of the particles calculated as if there was no turbulence, making QLT a first–order perturbation theory. Unfortunately, parallel diffusion coefficients calculated from QLT theory do not agree with the results from test particle simulations for most turbulence models, while the perpendicular diffusion coefficients are incorrect for all turbulence models (see Tautz et al. (2008), Shalchi (2009) for examples). Despite this, the equations for parallel diffusion will be discussed in the next subsection.

While the theory fails in the calculation of the diffusion coefficients, one important result that comes from this theory is that there is a sharp resonance condition that affects the scattering of charged particles (Teufel and Schlickeiser, 2002). The resonance is given by

$$k_\parallel v\mu + n\Omega = 0. \tag{3.63}$$

where n is any positive or negative integer. In terms of the unit–less quantities given in Chapter 1.2.1.1, this condition can be expressed as

$$k_\parallel \ell_0 = -\frac{n}{R\mu}. \tag{3.64}$$

Given the inaccuracies of QLT, it is expected that the real resonance condition is broadened (Shalchi, 2009).

3.3.2 Fokker–Planck Equation

As mentioned at the start of this chapter, there are multiple different paths that can be followed when calculating particle transport parameters. The *Fokker–Planck* equation is an equation for calculating the particle distribution as a function of position, velocity, and time. While the full Fokker–Planck equation contain terms for describing additional effects such as stochastic acceleration and perpendicular transport (see Schlickeiser (2002) for a discussion), it is the two–dimensional Fokker–Planck equation that is often used to calculate correlations used in other theories. The two–dimensional Fokker–Planck equation is given by

$$\frac{\partial f}{\partial t} + v\mu \frac{\partial f}{\partial z} = \frac{\partial}{\partial \mu}\left[D_{\mu\mu}(\mu)\frac{\partial f}{\partial \mu}\right] \tag{3.65}$$

where $f = f(z, \mu, t)$ is the particle distribution as a function of position z, pitch–angle cosine μ and time t. The quantity $D_{\mu\mu}(\mu)$ is the diffusion coefficient for μ, referred to as the *pitch–angle Fokker–Planck coefficient*, and can be calculated by

$$D_{\mu\mu} = \int_0^\infty \mathrm{d}t \, \langle \dot{\mu}(t)\dot{\mu}(0)\rangle \tag{3.66}$$

using the TGK formulation. The pitch–angle coefficient can be related to the parallel diffusion and mean free path (Jokipii, 1966) by the equation

$$\lambda_\parallel = \frac{3}{v}\kappa_\parallel = \frac{3v}{8}\int_{-1}^{1} \mathrm{d}\mu \, \frac{[1-\mu^2]^2}{D_{\mu\mu}(\mu)}. \tag{3.67}$$

The relation between the parallel mean free path and the diffusion coefficient will be discussed in the next section.

3.3.2.1 Running Diffusion Coefficient

One of the applications of the Fokker–Planck equation is in the calculation of the running diffusion coefficients. By assuming an isotropic pitch–angle Fokker–Planck coefficient (Shalchi et al., 2009),

$$D_{\mu\mu} = D\left[1-\mu^2\right] \tag{3.68}$$

where D is a function of the turbulence and particle physical properties but not μ, Shalchi et al. (2011) derived an equation for the running diffusion coefficient. The derivation was done by first transforming the Fokker–Planck equation into Fourier space, such that

$$f(z,\mu,t) = \int\limits_{-\infty}^{\infty} \mathrm{d}k_\parallel \, F(k_\parallel,\mu,t)e^{ik_\parallel z} \tag{3.69}$$

and

$$\frac{\partial F}{\partial t} + iv\mu k_\parallel F = D\frac{\partial}{\partial \mu}\left[[1-\mu^2]\frac{\partial F}{\partial \mu}\right]. \tag{3.70}$$

The function F was then expanded using Legendre polynomials P_n, so that

$$F(\mu,t) = \sum_{n=0}^{\infty} C_n(t)P_n(\mu). \tag{3.71}$$

On using (3.71) in (3.70), Shalchi et al. (2011) derived the recursion relation for the coefficients

$$\dot{C}_n = -Dn[n+1]C_n - ivk_\parallel\frac{n}{2n-1}C_{n-1} - ivk_\parallel\frac{n+1}{2n+3}C_{n+1} \tag{3.72}$$

with

$$\dot{C}_0 = -\frac{1}{3}ivk_\parallel C_1. \tag{3.73}$$

By using a two–dimensional subspace approximation ($C_m = 0$ for $m \geq 2$)[9], the function F can be expressed as

$$F(k_\parallel,\mu,t) = C_0 + \mu C_1 \tag{3.74}$$

while (3.72) and (3.73) combined to read

$$\ddot{C}_0 = -2D\dot{C}_0 - \frac{1}{3}v^2k_\parallel^2C_0. \tag{3.75}$$

---

[9] Lasuik and Shalchi (2019) also examined the one– and three–dimensional approximations and found that the one–dimensional solution was not useful while the three-dimensional was too complex to be of use.

With the ansatz

$$C_0 = be^{\omega t} \tag{3.76}$$

and initial conditions $z(0) = 0$ and $\mu(0) = \mu_0$, Shalchi et al. (2011) found that

$$\omega_{\pm}(k_{\parallel}) = -D \pm \sqrt{D^2 - \frac{1}{3}v^2 k_{\parallel}^2} \tag{3.77a}$$

and

$$b_{\pm}(k_{\parallel}) = \mp \frac{ivk_{\parallel} + \omega_{\pm}}{2\pi \left[\omega_{+} - \omega_{-}\right]}, \tag{3.77b}$$

which means the function F can be expressed as

$$\begin{aligned} F(k_{\parallel}, \mu, t) = {} & b_{+}(k_{\parallel}) e^{\omega_{+}(k_{\parallel})t} + b_{-}(k_{\parallel}) e^{\omega_{-}(k_{\parallel})t} \\ & - \frac{3\mu}{ivk_{\parallel}} \left[\omega_{+}(k_{\parallel}) b_{+}(k_{\parallel}) e^{\omega_{+}(k_{\parallel})t} + \omega_{-}(k_{\parallel}) b_{-}(k_{\parallel}) e^{\omega_{-}(k_{\parallel})t}\right]. \end{aligned} \tag{3.77c}$$

Having obtained these results, Shalchi et al. (2011) were able to obtain equations for the particle distribution's characteristic function (3.33)

$$\left\langle e^{\pm ik_{\parallel}z} \right\rangle_{Particles} = \frac{\omega_{+}(k_{\parallel}) e^{\omega_{-}(k_{\parallel})t} - \omega_{-}(k_{\parallel}) e^{\omega_{+}(k_{\parallel})t}}{\omega_{+}(k_{\parallel}) - \omega_{-}(k_{\parallel})} \tag{3.78a}$$

and the pitch–angle correlation

$$\left\langle \mu\mu_0 e^{-ik_{\parallel}z} \right\rangle = \frac{1}{3} \frac{\omega_{+}(k_{\parallel}) e^{\omega_{+}(k_{\parallel})t} - \omega_{-}(k_{\parallel}) e^{\omega_{-}(k_{\parallel})t}}{\omega_{+}(k_{\parallel}) - \omega_{-}(k_{\parallel})} \tag{3.78b}$$

which is required in perpendicular transport theories (see 3.3.6). Furthermore, (3.78b) can be used to derive an equation for the parallel velocity correlation (Shalchi et al., 2011)

$$\langle v_z(t) v_z(0) \rangle = v^2 \langle \mu(t)\mu(0) \rangle = v^2 \left\langle \mu\mu_0 e^{-ik_{\parallel}z} \right\rangle \Big|_{k_{\parallel}=0} = \frac{v^2}{3} e^{-2Dt}. \tag{3.79}$$

Given that the integral of the velocity correlation is equal to the diffusion coefficient as per the TGK formulation, the parameter D is found to be

$$D = \frac{v^2}{6\kappa_{\parallel}} = \frac{v}{2\lambda_{\parallel}}, \tag{3.80}$$

where the relation

$$\lambda_{\parallel} = \frac{3\kappa_{\parallel}}{v} \tag{3.81}$$

has been used to relate the parallel mean free path and diffusion coefficient. With this definition of D, $\omega_\pm$ can be expressed as

$$\omega_\pm = -\frac{v}{2\lambda_\parallel} \pm \sqrt{\left[\frac{v}{2\lambda_\parallel}\right]^2 - \frac{1}{3}v^2 k_\parallel^2}. \tag{3.82}$$

Integrating (3.79) the running parallel diffusion coefficient is found to be

$$d_\parallel(t) = \frac{v^2}{6D}\left[1 - e^{-2Dt}\right]. \tag{3.83}$$

Using (3.80), the running parallel diffusion coefficient can also be written as either

$$d_\parallel(t) = \frac{v\lambda_\parallel}{3}\left[1 - \exp\!\left(-\frac{v}{\lambda_\parallel}t\right)\right] \tag{3.84a}$$

or

$$d_\parallel(t) = \kappa_\parallel\left[1 - \exp\!\left(-\frac{v^2}{3\kappa_\parallel}t\right)\right]. \tag{3.84b}$$

By integrating (3.3a), the parallel mean square displacement is found to be

$$\left\langle(\Delta z(t))^2\right\rangle = \frac{2}{3}v\lambda_\parallel t - \frac{2}{3}\lambda_\parallel^2\left[1 - \exp\!\left(-\frac{v}{\lambda_\parallel}t\right)\right] \tag{3.85a}$$

or equivalently

$$\left\langle(\Delta z(t))^2\right\rangle = 2\kappa_\parallel t - \frac{6\kappa_\parallel^2}{v^2}\left[1 - \exp\!\left(-\frac{v^2}{3\kappa_\parallel}t\right)\right]. \tag{3.85b}$$

The application of these equations in analysis of test particles simulations will be described in 5.4.1.

3.3.2.2 Theoretical Parallel Diffusion Coefficient Calculation

As will be discussed in detail in Chapters 5 and 6, the parallel mean free path for the simulations perform for this work is computed via fitting (3.85) to numerical data. However, it is possible to use QLT to make a prediction for the parallel mean free path by combining (3.67) with an equation for $D_{\mu\mu}$. The equation used for $D_{\mu\mu}$ (see Teufel and Schlickeiser (2002)) is

$$\begin{aligned} D_{\mu\mu} = \frac{\pi\Omega^2\left[1-\mu^2\right]}{2B_0^2} \sum_{n=-\infty}^{\infty} \int \mathrm{d}^3k\, \delta(v\mu k_\parallel + n\Omega) \\ \times \left[\begin{aligned} & J_{n+1}^2\!\left(\frac{k_\perp v_\perp}{\Omega}\right) P_{RR}(\vec{k}) + J_{n-1}^2\!\left(\frac{k_\perp v_\perp}{\Omega}\right) P_{LL}(\vec{k}) \\ & - J_{n+1}\!\left(\frac{k_\perp v_\perp}{\Omega}\right) J_{n-1}\!\left(\frac{k_\perp v_\perp}{\Omega}\right)\left[P_{RL}(\vec{k})e^{2ik_\phi} + P_{LR}(\vec{k})e^{-2ik_\phi}\right] \end{aligned}\right] \end{aligned} \tag{3.86}$$

where k_ϕ is the cylindrical coordinate angle for mode $\vec{k}$ and the spectral tensor has been computed using the left– and right–handed components of the magnetic field. These are related to the Cartesian components by

$$\delta B_L = \frac{1}{\sqrt{2}}\left[\delta B_x + i\delta B_y\right] \tag{3.87a}$$

and

$$\delta B_R = \frac{1}{\sqrt{2}}\left[\delta B_x - i\delta B_y\right] \tag{3.87b}$$

By using (2.7), the components of the spectral tensor for the left– and right–handed field decomposition are

$$\begin{aligned} P_{RR}(\vec{k}) &= \frac{1}{2}\left[P_{xx}(\vec{k}) + P_{yy}(\vec{k})\right], \\ P_{LL}(\vec{k}) &= \frac{1}{2}\left[P_{xx}(\vec{k}) + P_{yy}(\vec{k})\right], \\ P_{LR}(\vec{k}) &= \frac{1}{2}\left[P_{xx}(\vec{k}) - P_{yy}(\vec{k})\right] + \frac{1}{2}i\left[P_{xy}(\vec{k}) + P_{yx}(\vec{k})\right], \\ P_{RL}(\vec{k}) &= \frac{1}{2}\left[P_{xx}(\vec{k}) - P_{yy}(\vec{k})\right] - \frac{1}{2}i\left[P_{xy}(\vec{k}) + P_{yx}(\vec{k})\right]. \end{aligned} \tag{3.88}$$

Slab Turbulence Example

For the slab model, this reduces to

$$\begin{aligned} P_{RR}(\vec{k}) = P_{LL}(\vec{k}) &= \frac{1}{4\pi}\delta B^2 \ell_\parallel \ell_\perp^2 g_\parallel(k_\parallel) g_\perp(k_\perp) \\ P_{RL}(\vec{k}) = P_{LR}(\vec{k}) &= 0 \end{aligned} \tag{3.89}$$

where the alternate form of the spectral tensor has been used (see Chapter 2.2.9 and Table 2.1). Therefore, in the slab model, the pitch–angle diffusion coefficient is

$$\begin{aligned} D_{\mu\mu} = {} & \frac{\pi C(s)\ell_\parallel \Omega^2}{4}\left[1-\mu^2\right]\frac{\delta B^2}{B_0^2}\sum_{n=-\infty}^{\infty}\int_{-\infty}^{\infty} \mathrm{d}k_\parallel\, \delta(v\mu k_\parallel + n\Omega)\left[1 + [k_\parallel \ell_\parallel]^2\right]^{-\frac{s}{2}} \\ & \times \int_0^\infty \mathrm{d}k_\perp \left[J_{n+1}^2\left(\frac{k_\perp v_\perp}{\Omega}\right) + J_{n-1}^2\left(\frac{k_\perp v_\perp}{\Omega}\right)\right]\delta(k_\perp), \end{aligned} \tag{3.90}$$

where the integral over k_ϕ has been performed. Integrating over $k_\perp$ gives

$$\int_0^\infty \mathrm{d}k_\perp \left[J_{n+1}^2\left(\frac{k_\perp v_\perp}{\Omega}\right) + J_{n-1}^2\left(\frac{k_\perp v_\perp}{\Omega}\right)\right]\delta(k_\perp) = \begin{cases} 1 & n = \pm 1 \\ 0 & \text{otherwise} \end{cases} \tag{3.91}$$

such that the equation for $D_{\mu\mu}$ becomes

$$D_{\mu\mu} = \frac{\pi C(s)\ell_\parallel\Omega^2}{2}\left[1-\mu^2\right]\frac{\delta B^2}{B_0^2}\int\limits_{-\infty}^{\infty}\mathrm{d}k_\parallel\,\frac{\left[\delta(v\mu k_\parallel+\Omega)+\delta(v\mu k_\parallel-\Omega)\right]}{\left[1+\left[k_\parallel\ell_\parallel\right]^2\right]^{\frac{s}{2}}} \tag{3.92}$$

Using (see Zwillinger (2012) for example)

$$\delta(ax) = \frac{1}{|a|}\delta(x) \tag{3.93}$$

and the symmetry in the spectrum, the pitch–angle diffusion coefficient for the slab model is finally found to be

$$D_{\mu\mu} = \frac{\pi C(s)\ell_\parallel\Omega^2}{v|\mu|}\left[1-\mu^2\right]\frac{\delta B^2}{B_0^2}\left[1+\left[\frac{\ell_\parallel\Omega}{v|\mu|}\right]^2\right]^{-\frac{s}{2}}. \tag{3.94}$$

This equation can be rearranged to find (Shalchi, 2009)

$$D_{\mu\mu} = \frac{\pi C(s)v}{\ell_\parallel}\frac{\delta B^2}{B_0^2}\left[1-\mu^2\right]|\mu|^{s-1}\frac{R^{s-2}}{\left[1+\mu^2R^2\right]^{\frac{s}{2}}} \tag{3.95}$$

where we have used the unit–less rigidity, (1.5), to remove $v/\ell_\parallel\Omega$.

Turbulence with Transverse Complexity

For the non–slab models discussed in the previous chapter, (3.88) becomes

$$\begin{aligned} P_{RR}(\vec{k}) = P_{LL}(\vec{k}) &= \frac{\delta B^2}{4\pi}\ell_\parallel\ell_\perp^2 g_\parallel(k_\parallel)g_\perp(k_\perp) \\ P_{LR}(\vec{k}) = P_{RL}^\dagger(\vec{k}) &= -\frac{\delta B^2}{4\pi}\ell_\parallel\ell_\perp^2 g_\parallel(k_\parallel)g_\perp(k_\perp)e^{2ik_\phi}, \end{aligned} \tag{3.96}$$

and (3.86) becomes

$$\begin{aligned} D_{\mu\mu} = \frac{\pi\ell_\parallel\Omega^2}{4}\left[1-\mu^2\right]\frac{\delta B^2}{B_0^2}\sum_{n=-\infty}^{\infty}\int\limits_{-\infty}^{\infty}\mathrm{d}k_\parallel\,\delta(v\mu k_\parallel+n\Omega)g_\parallel(k_\parallel) \\ \times\int\limits_0^{\infty}\mathrm{d}k_\perp\,k_\perp\ell_\perp^2\left[J_{n+1}\left(\frac{k_\perp v_\perp}{\Omega}\right)+J_{n-1}\left(\frac{k_\perp v_\perp}{\Omega}\right)\right]^2 g_\perp(k_\perp) \end{aligned} \tag{3.97}$$

where the integral over k_ϕ has been performed. Using (see Boas (2006) for example)

$$J_{n+1}(x)+J_{n-1}(x) = \frac{2n}{x}J_n(x) \tag{3.98}$$

and integrating over $k_\parallel$ yields

$$\begin{aligned} D_{\mu\mu} = {} & \frac{\pi \ell_\parallel \Omega^2}{v|\mu|} \left[1-\mu^2\right] \left[\frac{\ell_\perp \Omega}{v_\perp}\right]^2 \frac{\delta B^2}{B_0^2} \sum_{n=-\infty}^{\infty} n^2 g_\parallel\!\left(\frac{n\Omega}{v|\mu|}\right) \\ & \times \int_0^\infty \mathrm{d}k_\perp\, k_\perp^{-1} J_n^2\!\left(\frac{k_\perp v_\perp}{\Omega}\right) g_\perp(k_\perp). \end{aligned} \tag{3.99}$$

This can be further simplified by using $v_\perp^2 = v^2[1-\mu^2]$ and $x = k_\perp \ell_\perp$ to find

$$D_{\mu\mu} = \frac{\pi \ell_\parallel \ell_\perp^2 \Omega^4}{v^3|\mu|} \frac{\delta B^2}{B_0^2} \sum_{n=-\infty}^{\infty} n^2 g_\parallel\!\left(\frac{n\Omega}{v|\mu|}\right) \int_0^\infty \mathrm{d}k_\perp\, k_\perp^{-1} J_n^2\!\left(\frac{k_\perp v_\perp}{\Omega}\right) g_\perp(k_\perp). \tag{3.100}$$

If the parallel spectrum is symmetric, then the sum over n can be reduced to

$$D_{\mu\mu} = \frac{2\pi \ell_\parallel \ell_\perp^2 \Omega^4}{v^3|\mu|} \frac{\delta B^2}{B_0^2} \sum_{n=1}^{\infty} n^2 g_\parallel\!\left(\frac{n\Omega}{v|\mu|}\right) \int_0^\infty \mathrm{d}k_\perp\, k_\perp^{-1} J_n^2\!\left(\frac{k_\perp v_\perp}{\Omega}\right) g_\perp(k_\perp). \tag{3.101}$$

At this point, a model needs to be specified in order to solve the equation.

Full 3D Turbulence

For the full 3D turbulence model, the pitch–angle diffusion coefficient can be written as

$$\begin{aligned} D_{\mu\mu} = {} & 16\pi C(s) D(s,q) \frac{v}{\ell_\parallel} \frac{\ell_\perp^2}{\ell_\parallel^2} \frac{\delta B^2}{B_0^2} |\mu|^{s-1} R^{s-4} \sum_{n=1}^{\infty} \left[\frac{n^2}{[n^2+\mu^2 R^2]^{\frac{s}{2}}} \right. \\ & \left. \times \int_0^\infty \mathrm{d}r\, J_n^2\!\left(r \frac{\ell_\parallel}{\ell_\perp} R \sqrt{1-\mu^2}\right) \frac{r^{q-2}}{[1+r^2]^{\frac{s+q}{2}}} \right], \end{aligned} \tag{3.102}$$

where the unit–less rigidity, (1.5), has again been used to remove $v/\ell_\parallel\Omega$, and the variable substitution $r = k_\perp \ell_\perp$ has been used. Solving the equations for $D_{\mu\mu}$ and $\lambda_\parallel$, (3.67), were done numerically by A. Shalchi at this point.

3.3.3 Compound Sub–Diffusion

When discussing diffusive particle transport, what is generally being referred to is *normal* diffusion, as defined in Chapter 1. Another important type of transport is what is called *compound sub–diffusion* (see Shalchi (2020) for a review). In this state of transport, the perpendicular scattering of particles is suppressed by the parallel scattering. The physical picture of this type of transport is that the particles are bound to the magnetic fields lines, and are unable to 'jump' to another field line. As a result, when the particles scatter, they reverse direction along the field line and retrace their path. While parallel scattering in this proceeds as normal diffusion, perpendicular transport is now sub–diffusive, described by (see Webb et al. (2006), Shalchi and Kourakis (2007))

$$\left\langle (\Delta x)^2 \right\rangle = 4\kappa_{FL}\sqrt{\frac{\kappa_{\parallel} t}{\pi}} \tag{3.103}$$

such that the running diffusion coefficient is

$$d_{xx}(t) = \kappa_{FL}\sqrt{\frac{\kappa_{\parallel}}{\pi t}}. \tag{3.104}$$

Using (1.28) to define the diffusion coefficient for simulation data yields

$$d_{xx}(t) = 2\kappa_{FL}\sqrt{\frac{\kappa_{\parallel}}{\pi t}}. \tag{3.105}$$

This type of perpendicular transport is primarily seen in turbulence that lacks transverse complexity, such as slab turbulence (Jokipii et al., 1993, Jones et al., 1998).

3.3.4 Guiding Center Coordinates

One of the common features in particle transport theories is the use of what are referred to as the guiding center coordinates, as opposed to the actual particle position. The reasoning behind this is that the particle motion can be broken into two components: the motion of the center of rotation, called the guiding center, and the orbital motion around it. In both NLGC theory (Chapter 3.3.5) and UNLT theory (Chapter 3.3.6), the guiding center position is defined in cgs units by (see Schlickeiser (2002))

$$\vec{X}_{GC} = \vec{x} + \frac{\gamma m c}{q}\frac{\vec{v}\times\vec{B}_0}{B_0^2} \tag{3.106}$$

where $\vec{B}_0 = B_0\hat{z}$. The velocity of the guiding center is the total derivative of the position,

$$\vec{V} = \vec{v} + \frac{\left[\vec{v}\times[\vec{B}_0 + \delta\vec{B}]\right]\times\vec{B}_0}{B_0^2}, \tag{3.107a}$$

which can be expanded using the triple vector product to read

$$\vec{V} = v_z\hat{z} + v_z\frac{\delta\vec{B}}{B_0} - \frac{\vec{B}_0\cdot\delta\vec{B}}{B_0^2}\vec{v}. \tag{3.107b}$$

If the turbulence is incompressible, then the third term on the right vanishes, resulting in

$$\vec{V} = \left[v_z \frac{\delta B_x}{B_0},\ v_z \frac{\delta B_y}{B_0},\ v_z\right] \tag{3.108a}$$

or equivalently

$$\vec{V} = \frac{\vec{v} \cdot \vec{B}_0}{B_0^2} \vec{B} \tag{3.108b}$$

where $\vec{B} = \vec{B}_0 + \delta\vec{B}$. Using the guiding center coordinates filters out the orbital motion of the particle, while giving the motion across the mean field as a function of the parallel velocity and the turbulence field. Figure 3.1 shows an example of a particle trajectory in slab turbulence, accompanied by the guiding center position.

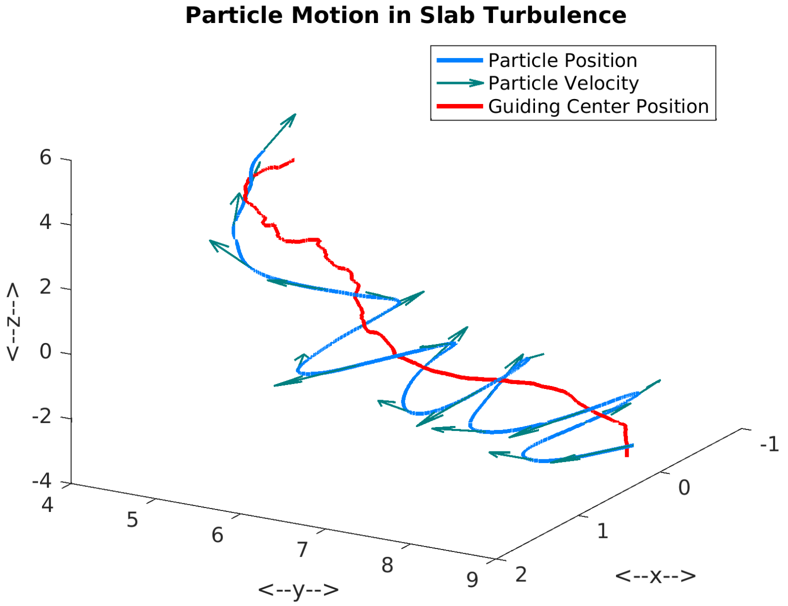

Figure 3.1: Example of guiding center coordinates in slab turbulence. The blue line shows the particle position, while the blue–green arrows show the particle velocity. The thick red line is the guiding center position, as defined by (3.106).

3.3.4.1 Validity of the Guiding Center Coordinates

A question that can be asked is "how valid is the use of guiding center coordinates instead of the particle position?" This was explored by Qin and Shalchi (2016) using the two–component model (2.2.3) as the test model and computing the following quantities from test–particle simulation data:

$$\kappa_{xx}^{P} = \int_0^\infty \mathrm{d}t \left\langle v_x(t) v_x(0) \right\rangle, \tag{3.109a}$$

$$\kappa_{xx}^{GC} = \int_0^\infty \mathrm{d}t \left\langle V_x(t) V_x(0) \right\rangle, \tag{3.109b}$$

$$D_{xx}^{P}(t) = \frac{1}{2}\frac{\mathrm{d}}{\mathrm{d}t}\left\langle \left(\Delta x(t)\right)^2 \right\rangle, \tag{3.109c}$$

$$D_{xx}^{GC}(t) = \frac{1}{2}\frac{\mathrm{d}}{\mathrm{d}t}\left\langle \left(\Delta X_{GC}(t)\right)^2 \right\rangle \tag{3.109d}$$

Equation 3.109(a) is the diffusion coefficient as defined by the TGK formulation for the particle velocity, while 3.109(b) is the same but with the guiding center velocity. Equations 3.109(c)-(d) are the running diffusion coefficients using the derivative of the mean square displacement for the particle and guiding center positions, respectively. From these results Qin and Shalchi (2016) calculated the ratio of the particle and guiding center results:

$$a^2 = \kappa_{xx}^{P}/\kappa_{xx}^{GC}, \tag{3.110a}$$

$$b^2 = D_{xx}^{P}(t)/D_{xx}^{GC}(t). \tag{3.110b}$$

The simulations Qin and Shalchi (2016) performed involved varying both the amount of energy in the slab turbulence component relative to the total energy and the particle energy. What Qin and Shalchi (2016) found was that both a^2 and b^2 were both approximately one across all considered particle energies and turbulence energy distributions. These results are important in the context of both the non–linear guiding center theory and the unified non–linear transport theory, which are discussed next, since they show the validity of using the guiding center coordinates.

3.3.5 Non–Linear Guiding Center Theory

The first systematic theory for perpendicular diffusion was the *Non–Linear Guiding Center* or *NLGC* theory of Matthaeus et al. (2003). The premise of NLGC theory is that the particle velocity used in (3.8) can be replaced with the velocity of the guiding center which is assumed to follow the magnetic field lines. In Matthaeus et al. (2003) the guiding center velocity $\tilde{\vec{v}}$ is expressed as

$$V_x = a v_z \frac{\delta B_x}{B_0}, \qquad V_y = a v_z \frac{\delta B_y}{B_0}, \qquad V_z = v_z, \tag{3.111}$$

where the parameter a is an unknown value determined by comparing the results of the theory to numerical simulations. Given the results of Qin and Shalchi (2016), non–unity values of the parameter must be the result of the approximations used in computing the resulting correlation functions required by the TGK formulation (Shalchi, 2020).

Using (3.111) in the TGK formulation yields

$$\kappa_\perp = \frac{a^2}{B_0^2}\int_0^\infty \mathrm{d}t \left\langle v_z(t)v_z(0)\delta B_x(\vec{x}(t),t)\delta B_x(\vec{x}(0),0)\right\rangle, \tag{3.112}$$

to which NLGC applies a series of approximations and assumptions to make the theory tractable. The first of these is that the fourth order correlation is equal to the product of two second order correlations, so that

$$\kappa_\perp = \frac{a^2}{B_0^2}\int_0^\infty \mathrm{d}t \left\langle v_z(t)v_z(0)\right\rangle\left\langle\delta B_x(\vec{x}(t),t)\delta B_x(\vec{x}(0),0)\right\rangle. \tag{3.113}$$

Next, NLGC assumes that the velocity correlation can be modelled using a decaying exponential

$$\left\langle v_z(t)v_z(0)\right\rangle = \frac{v^2}{3}e^{-\frac{vt}{\lambda_\parallel}}, \tag{3.114}$$

which, at the time, was based off the earlier work of Bieber and Matthaeus (1997). The magnetic correlation function can be identified with the xx component of the magnetic correlation tensor (see 2.2). By using a Fourier representation of the magnetic field, the equation becomes

$$\kappa_\perp = \frac{a^2v^2}{3B_0^2}\int_0^\infty \mathrm{d}t \int \mathrm{d}^3k \int \mathrm{d}^3k'\ e^{-\frac{vt}{\lambda_\parallel}}\left\langle \delta\tilde{B}_x(\vec{k})\delta\tilde{B}_x^\dagger(\vec{k}')e^{i\left[\vec{k}\vec{x}(t)-\vec{k}'\vec{x}(0)\right]}\right\rangle. \tag{3.115}$$

As with field line diffusion, the positions here are not arbitrary coordinates; rather they are the position of the particles. This means that Corrsin's approximation (see (3.26)) must be used, and the equation becomes

$$\kappa_\perp = \frac{a^2v^2}{3B_0^2}\int_0^\infty \mathrm{d}t \int \mathrm{d}^3k \int \mathrm{d}^3k'\ e^{-\frac{vt}{\lambda_\parallel}}\left\langle \delta\tilde{B}_x(\vec{k})\delta\tilde{B}_x^\dagger(\vec{k}')\right\rangle\left\langle e^{i\left[\vec{k}\vec{x}(t)-\vec{k}'\vec{x}(0)\right]}\right\rangle. \tag{3.116}$$

Next, the magnetic amplitude correlation is replaced with the spectral tensor as per (2.7) and the equation is integrated over k' so that the diffusion coefficient can be calculated by

$$\kappa_\perp = \frac{a^2 v^2}{3B_0^2} \int_0^\infty \mathrm{d}t \int \mathrm{d}^3k \; e^{-\frac{vt}{\lambda_\parallel}} P_{xx}(\vec{k}, t) \left\langle e^{i\vec{k}\Delta\vec{x}(t)} \right\rangle. \tag{3.117}$$

The final quantity in (3.117) can be identified as the characteristic function associated with the particle distribution. To proceed, Matthaeus et al. (2003) assumed that the system was instantaneously diffusive, which allowed for the particle distribution to be modelled as a Gaussian with $\sigma_i^2 = 2\kappa_{ii}t$. Furthermore, Matthaeus et al. (2003) assumed that the dynamical correlation tensor (see Section 2.1.1.1) could be modelled as

$$\Gamma\left(\vec{k}, t\right) = e^{-\gamma(\vec{k})t}. \tag{3.118}$$

Integrating over time therefore results in the non-linear equation

$$\kappa_\perp = \frac{a^2 v^2}{3B_0^2} \int \mathrm{d}^3k \, \frac{P_{xx}(\vec{k})}{\frac{v}{\lambda_\parallel} + \kappa_\perp k_\perp^2 + \kappa_\parallel k_\parallel^2 + \gamma(\vec{k})}. \tag{3.119}$$

If $P_{xx}(\vec{k})$ can be expressed using (2.39), then the NLGC equation can be written as

$$\kappa_\perp = \frac{a^2 v^2}{3} \frac{\delta B_x^2}{B_0^2} \int_{-\infty}^\infty \mathrm{d}k_\parallel \int_0^\infty \mathrm{d}k_\perp \, \frac{k_\perp \ell_\parallel \ell_\perp^2 g_\parallel(k_\parallel) g_\perp(k_\perp)}{\frac{v}{\lambda_\parallel} + \kappa_\perp k_\perp^2 + \kappa_\parallel k_\parallel^2 + \gamma(\vec{k})}. \tag{3.120}$$

For static turbulence, γ is equal to zero.

3.3.5.1 NLGC Application: Slab Turbulence

One of the known short comings of NLGC theory is its prediction of diffusive perpendicular transport in slab turbulence (Giacalone, 2013), compared to the sub–diffusive behaviour observed in numerical simulations (Giacalone and Jokipii, 1994, 1999, Qin et al., 2002, Arendt and Shalchi, 2018). For this model of turbulence, the NLGC equation becomes[10]

$$\kappa_\perp = a^2 \frac{v^2}{3} \frac{\delta B_x^2}{B_0^2} \int_{-\infty}^\infty \mathrm{d}k_\parallel \, \ell_\parallel \, 2C(s) \left[1 + k_\parallel^2 \ell_\parallel^2\right]^{-\frac{s}{2}} \left[\frac{v}{\lambda_\parallel} + \kappa_\parallel k_\parallel^2\right]^{-1}. \tag{3.121}$$

As the integrand is positive for all values of k, its integral will be non-zero. Therefore, the resulting non-zero perpendicular diffusion coefficient must be interpreted as normal diffusion. Since there is no transverse complexity ($k_\perp = 0$) in the slab model,

---

[10] This calculation assumes the spectral function is given by (2.24).

the perpendicular distribution of the particles is not required in the calculations and the equation is linear. This means that the incorrect result must stem from one of the assumptions made to simplify the correlation function, not the particle distribution.

3.3.6 Unified Non–Linear Transport Theory

The *Unified Non–Linear Transport*, or UNLT, theory can be split into two categories: the diffusive version of the theory (Shalchi, 2010) and the time–dependent version (Shalchi, 2017, Lasuik and Shalchi, 2017). The theory begins with the same assumption of NLGC: particle coordinates can be replaced with the guiding center coordinates. Where NLGC and UNLT begin to diverge is in the simplification of the perpendicular velocity correlation:

$$\begin{aligned}&\Big\langle v_z(t)v_z(0)\delta B_x(\vec{x},t)\delta B_x(\vec{x}_0,0)\Big\rangle\\ &=\int \mathrm{d}^3k\int \mathrm{d}^3k'\Big\langle \delta\tilde{B}_x(\vec{k})\delta\tilde{B}_x^{\dagger}(\vec{k}')\Big\rangle\begin{cases}\Big\langle v_z(t)v_z(0)\Big\rangle\Big\langle e^{i\left[\vec{k}\vec{x}(t)-\vec{k}'\vec{x}(0)\right]}\Big\rangle & \text{NLGC}\\ \Big\langle v_z(t)v_z(0)e^{i\left[\vec{k}\vec{x}(t)-\vec{k}'\vec{x}(0)\right]}\Big\rangle & \text{UNLT}\end{cases},\end{aligned} \tag{3.122}$$

which leads to different equations for the perpendicular diffusion coefficient. Furthermore, while UNLT theory uses the Fokker–Planck equation to derive an equation for the velocity–phase correlation, the results depend on whether the diffusive or time–dependent version of the theory is being used. It is important to note that, like NLGC theory, both versions of UNLT theory require the introduction of the factor a^2 for some turbulence models.

3.3.6.1 Diffusive UNLT Theory

Diffusive UNLT theory is so named as it is based on of the assumption that the system is immediately diffusive in all directions. The derivation used here is based on the derivation in Shalchi (2010). To begin, the Fokker–Planck equation is modified to include the effects of perpendicular diffusion:

$$\frac{\partial f}{\partial t}+v\mu\frac{\partial f}{\partial z}=\frac{\partial}{\partial \mu}\left[D_{\mu\mu}\frac{\partial f}{\partial \mu}\right]+D_{\perp}\left[\frac{\partial^2 f}{\partial x^2}+\frac{\partial^2 f}{\partial y^2}\right]. \tag{3.123}$$

What is needed is an equation for the time integral of the velocity–phase correlation function:

$$T(\vec{k})=\frac{1}{v^2}\Big\langle v_z(t)v_z(0)e^{i\left[\vec{k}\vec{x}(t)-\vec{k}'\vec{x}(0)\right]}\Big\rangle=\Big\langle \mu\mu_0 e^{i\left[\vec{k}\vec{x}(t)-\vec{k}'\vec{x}(0)\right]}\Big\rangle, \tag{3.124}$$

such that the perpendicular diffusion coefficient for homogeneous, static turbulence, (3.122), is

$$\kappa_\perp = \frac{a^2 v^2}{B_0^2} \int \mathrm{d}^3 k \, P_{xx}(\vec{k}) \Re \left[T(\vec{k}) \right] \tag{3.125}$$

where the Fourier amplitude correlation has been replaced with the xx component of the spectral tensor. In order to solve (3.125), UNLT theory uses the Fourier transform of (3.123) to derive an equation for $T(\vec{k})$:

$$T(\vec{k}) = \frac{1}{3} \frac{1}{\frac{v}{\lambda_\parallel} + \frac{4}{3}\kappa_\perp k_\perp^2 + \frac{[v k_\parallel]^2}{3\kappa_\perp k_\perp^2}}. \tag{3.126}$$

Therefore, the UNLT equation for the perpendicular diffusion coefficient is

$$\kappa_\perp = \frac{a^2 v^2}{3 B_0^2} \int \mathrm{d}^3 k \, \frac{P_{xx}(\vec{k})}{\frac{v}{\lambda_\parallel} + \frac{4}{3}\kappa_\perp k_\perp^2 + \frac{[v k_\parallel]^2}{3\kappa_\perp k_\perp^2}}. \tag{3.127}$$

If the spectral tensor is expressed using (2.39), then the diffusive UNLT equation becomes

$$\kappa_\perp = a^2 \frac{v^2}{3} \frac{\delta B_x^2}{B_0^2} \int_{-\infty}^{\infty} \mathrm{d}k_\parallel \int_{0}^{\infty} \mathrm{d}k_\perp \, \frac{\ell_\parallel g_\parallel(k_\parallel) \, k_\perp \ell_\perp^2 g_\perp(k_\perp)}{\frac{v}{\lambda_\parallel} + \frac{4}{3}\kappa_\perp k_\perp^2 + \frac{[v k_\parallel]^2}{3\kappa_\perp k_\perp^2}}. \tag{3.128}$$

3.3.6.2 Time–dependent UNLT Theory

The derivation of time–dependent version of UNLT theory starts off in a similar manner compared to the diffusive version with the guiding center velocity correlation being calculated via (3.122). Unlike the diffusive version of the theory, however, the time–dependent theory utilizes an additional approximation for the velocity–phase correlation function:

$$\left\langle v_z(t) v_z(0) e^{i\left[\vec{k}\vec{x}(t) - \vec{k}'\vec{x}(0)\right]} \right\rangle = \left\langle v_z(t) v_z(0) e^{i\left[k_\parallel z(t) - k'_\parallel z(0)\right]} \right\rangle \left\langle e^{i\left[\vec{k}_\perp \vec{x}_\perp(t) - \vec{k}'_\perp \vec{x}_\perp(0)\right]} \right\rangle. \tag{3.129}$$

As a result, the mean square displacement along the x axis for homogeneous turbulence can be expressed as

$$\frac{\mathrm{d}^2}{\mathrm{d}t^2} \left\langle (\Delta x)^2 \right\rangle = \frac{2a^2}{B_0^2} \int \mathrm{d}^3 k \, P_{xx}(\vec{k}) \left\langle v_z(t) v_z(0) e^{i k_\parallel \Delta z(t)} \right\rangle \left\langle e^{i \vec{k}_\perp \Delta \vec{x}_\perp(t)} \right\rangle. \tag{3.130}$$

The equation for the first correlation in (3.130) is found using the Fokker–Planck equation as shown in Section 3.3.2, with solution

$$\begin{aligned}\xi(k_\parallel, t) &= \left\langle v_z(t) v_z(0) e^{ik_\parallel \Delta z(t)} \right\rangle = v^2 \left\langle \mu(t)\mu(0) e^{ik_\parallel \Delta z(t)} \right\rangle \\ &= \frac{v^2}{3} \frac{\omega_+ e^{\omega_+ t} - \omega_- e^{\omega_- t}}{\omega_+ - \omega_-} \end{aligned} \tag{3.131}$$

where $\omega_\pm$ is defined by

$$\omega_\pm = -\frac{v}{2\lambda_\parallel} \pm \sqrt{\left[\frac{v}{2\lambda_\parallel}\right]^2 - \frac{1}{3}\left[v k_\parallel\right]^2}. \tag{3.132}$$

The second correlation can be recognized as the perpendicular characteristic function, the Fourier transform of the particle distribution in the xy plane, as per (3.33). If the particles have a Gaussian distribution in the xy plane, then $\left\langle (\Delta x)^2 \right\rangle$ can be calculated by the second–order non–linear equation

$$\frac{\mathrm{d}^2}{\mathrm{d}t^2} \left\langle (\Delta x)^2 \right\rangle = \frac{2a^2}{B_0^2} \int \mathrm{d}^3 k \, P_{xx}(\vec{k}) \xi(k_\parallel, t) e^{-\frac{1}{2}\left\langle (\Delta x)^2 \right\rangle k_\perp^2}. \tag{3.133}$$

Using (2.39) for the spectral tensor allows the equation to be written as

$$\begin{aligned}\frac{\mathrm{d}^2}{\mathrm{d}t^2} \left\langle (\Delta x)^2 \right\rangle = 2a^2 \frac{\delta B_x^2}{B_0^2} &\int_{-\infty}^{\infty} \mathrm{d}k_\parallel \, \ell_\parallel \, g_\parallel(k_\parallel) \xi(k_\parallel, t) \\ \times &\int_0^{\infty} \mathrm{d}k_\perp \, k_\perp \ell_\perp^2 \, g_\perp(k_\perp) e^{-\frac{1}{2}\left\langle (\Delta x)^2 \right\rangle k_\perp^2}. \end{aligned} \tag{3.134}$$

In order to compare to the diffusive version of UNLT theory, consider a scenario in which the perpendicular motion is immediately diffusive. In this case (3.133) can be rearranged to read

$$\kappa_\perp = a^2 \frac{v^2}{3} \frac{1}{B_0^2} \int \mathrm{d}^3 k \, P_{xx}(\vec{k}) \int_0^{\infty} \mathrm{d}t \, \frac{\omega_+ e^{\omega_+ t} - \omega_- e^{\omega_- t}}{\omega_+ - \omega_-} e^{-\kappa_\perp k_\perp^2 t}. \tag{3.135}$$

Solving the time integral yields

$$\kappa_\perp = a^2 \frac{v^2}{3} \frac{1}{B_0^2} \int \mathrm{d}^3 k \, \frac{P_{xx}(\vec{k})}{\frac{v}{\lambda_\parallel} + \kappa_\perp k_\perp^2 + \frac{[v k_\parallel]^2}{3\kappa_\perp k_\perp^2}} \tag{3.136a}$$

or equivalently

$$\kappa_\perp = a^2 \frac{v^2}{3} \frac{\delta B_x^2}{B_0^2} \int\limits_{-\infty}^{\infty} \mathrm{d}k_\parallel \int\limits_{0}^{\infty} \mathrm{d}k_\perp \frac{\ell_\parallel g_\parallel(k_\parallel)\, k_\perp \ell_\perp^2 g_\perp(k_\perp)}{\frac{v}{\lambda_\parallel} + \kappa_\perp k_\perp^2 + \frac{[vk_\parallel]^2}{3\kappa_\perp k_\perp^2}}. \tag{3.136b}$$

which is slightly different from the diffusive UNLT equation (3.128). The reason for this difference is that diffusive UNLT takes into account the pitch–angle by averaging over it, while time–dependent UNLT ignores it (Shalchi, 2020).

3.3.6.3 UNLT Application: Slab Turbulence

Consider the application of UNLT theory to perpendicular transport in slab turbulence. Using the spectral tensor as defined by (2.23) and assuming that $a^2 = 1$, diffusive UNLT yields

$$\kappa_\perp = 4\pi \frac{v^2}{3} \frac{1}{B_0^2} \int\limits_{0}^{\infty} \mathrm{d}k_\perp \int\limits_{0}^{\infty} \mathrm{d}k_\parallel \frac{g_{Slab}(k_\parallel)\delta(k_\perp)}{\frac{v}{\lambda_\parallel} + \frac{4}{3}\kappa_\perp k_\perp^2 + \frac{[vk_\parallel]^2}{3\kappa_\perp k_\perp^2}}. \tag{3.137}$$

Integration over $k_\perp$ results in a $1/0$ in the denominator, which means that the right hand side is zero. Diffusive UNLT therefore predicts a perpendicular diffusion coefficient of zero, in line with numerical simulation showing sub–diffusive behaviour. Time–dependent UNLT yields

$$\frac{\mathrm{d}^2}{\mathrm{d}t^2} \left\langle (\Delta x)^2 \right\rangle = 2 \frac{v^2}{3} \frac{\delta B^2}{B_0^2} \int\limits_{0}^{\infty} \mathrm{d}k_\parallel\, \ell_\parallel \frac{2C(s)}{\left[1 + [k_\parallel \ell_\parallel]^2\right]^{\frac{s}{2}}} \frac{\omega_+ e^{\omega_+ t} - \omega_- e^{\omega_- t}}{\omega_+ - \omega_-} \tag{3.138}$$

which can be rearranged to read

$$d_\perp(t) = \frac{v^2}{3} \frac{\delta B^2}{B_0^2} \int\limits_{0}^{\infty} \mathrm{d}k_\parallel\, \ell_\parallel \frac{2C(s)}{\left[1 + [k_\parallel \ell_\parallel]^2\right]^{\frac{s}{2}}} \int\limits_{0}^{t} \mathrm{d}t' \frac{\omega_+ e^{\omega_+ t'} - \omega_- e^{\omega_- t'}}{\omega_+ - \omega_-}, \tag{3.139}$$

again assuming $a^2 = 1$. Solving the time integral results in

$$d_\perp(t) = \frac{v^2}{3} \frac{\delta B^2}{B_0^2} \int\limits_{0}^{\infty} \mathrm{d}k_\parallel\, \ell_\parallel \frac{2C(s)}{\left[1 + [k_\parallel \ell_\parallel]^2\right]^{\frac{s}{2}}} \frac{e^{\omega_+ t} - e^{\omega_- t}}{\omega_+ - \omega_-}; \tag{3.140}$$

and with $\Re(\omega_\pm) \leq 0$, the running perpendicular diffusion coefficient is therefore monotonically decreasing, as expected for sub–diffusion.

3.3.6.4 UNLT Application: Noisy Slab Turbulence

Having considered the application of UNLT theory to perpendicular transport in slab turbulence, now consider its application to transport in noisy slab turbulence.

In this scenario, the UNLT equations are

$$\kappa_\perp = \frac{v^2}{3}\frac{\delta B^2}{B_0^2}\int\limits_0^\infty \mathrm{d}k_\parallel\,\ell_\parallel \int\limits_0^{1/\ell_\perp} \mathrm{d}k_\perp\,\ell_\perp \frac{2C(s)\left[1+[k_\parallel \ell_\parallel]^2\right]^{-\frac{s}{2}}}{\frac{v}{\lambda_\parallel}+\frac{4}{3}\kappa_\perp k_\perp^2+\frac{[vk_\parallel]^2}{3\kappa_\perp k_\perp^2}} \tag{3.141a}$$

for diffusive UNLT and

$$\frac{\mathrm{d}^2}{\mathrm{d}t^2}\left\langle(\Delta x)^2\right\rangle = 2\frac{\delta B^2}{B_0^2}\int\limits_0^\infty \mathrm{d}k_\parallel\,\ell_\parallel \frac{2C(s)\xi(k_\parallel,t)}{\left[1+[k_\parallel\ell_\parallel]^2\right]^{\frac{s}{2}}}\int\limits_0^{1/\ell_\perp}\mathrm{d}k_\perp\,e^{-\frac{1}{2}\left\langle(\Delta x)^2\right\rangle k_\perp^2} \tag{3.141b}$$

for time–dependent UNLT. Unfortunately, neither of these can be solved in the general case. That said, it is possible to simplify the time–dependent UNLT equation by solving the integral for $k_\perp$. This results in

$$\begin{aligned}\frac{\mathrm{d}^2}{\mathrm{d}t^2}\left\langle(\Delta x)^2\right\rangle = \frac{2}{3}v^2\frac{\delta B^2}{B_0^2}&\sqrt{\frac{\pi\ell_\perp^2}{2\left\langle(\Delta x)^2\right\rangle}}\,\mathrm{erf}\left(\sqrt{\frac{\left\langle(\Delta x)^2\right\rangle}{2\ell_\perp^2}}\right)\\ &\times\int\limits_0^\infty \mathrm{d}k_\parallel\,\ell_\parallel\frac{2C(s)}{\left[1+[k_\parallel\ell_\parallel]^2\right]^{\frac{s}{2}}}\frac{\omega_+e^{\omega_+t}-\omega_-e^{\omega_-t}}{\omega_+-\omega_-}.\end{aligned} \tag{3.142}$$

As with the regular slab model, it has been assumed here that $a=1$.

3.3.6.5 UNLT Application: Full 3D Turbulence

Finally, consider the application of UNLT theory to the full 3D turbulence model. Here, the UNLT equations are

$$\begin{aligned}\kappa_\perp = \frac{v^2}{3}\frac{\delta B^2}{B_0^2}&\int\limits_0^\infty \mathrm{d}k_\parallel\,\ell_\parallel\frac{2C(s)}{\left[1+\left[k_\parallel\ell_\parallel\right]^2\right]^{\frac{s}{2}}}\\ &\times\int\limits_0^\infty \mathrm{d}k_\perp\,\ell_\perp 4D(s,q)\frac{[k_\perp\ell_\perp]^q}{[1+[k_\perp\ell_\perp]^2]^{\frac{s}{2}}}\frac{1}{\frac{v}{\lambda_\parallel}+\frac{4}{3}\kappa_\perp k_\perp^2+\frac{[vk_\parallel]^2}{3\kappa_\perp k_\perp^2}}\end{aligned} \tag{3.143a}$$

and

$$\begin{aligned}\frac{\mathrm{d}^2}{\mathrm{d}t^2}\left\langle(\Delta x)^2\right\rangle = \frac{2}{3}v^2\frac{\delta B^2}{B_0^2}&\int\limits_0^\infty \mathrm{d}k_\perp\,\ell_\perp\,4D(s,q)\frac{[k_\perp\ell_\perp]^q}{[1+[k_\perp\ell_\perp]^2]^{\frac{s}{2}}}e^{-\frac{1}{2}\left\langle(\Delta x)^2\right\rangle k_\perp^2}\\ &\times\int\limits_0^\infty \mathrm{d}k_\parallel\,\ell_\parallel\,\frac{2C(s)}{\left[1+\left[k_\parallel\ell_\parallel\right]^2\right]^{\frac{s}{2}}}\frac{\omega_+e^{\omega_+t}-\omega_-e^{\omega_-t}}{\omega_+-\omega_-}\end{aligned} \tag{3.143b}$$

for diffusive and time–dependent UNLT theory, respectively, where it has again been assumed that $a^2 = 1$. Neither integral can be solved analytically.

3.3.7 General Features of NLGC and UNLT Theory

At this point consider NLGC thoery and both forms of UNLT theory from a general perspective. In essence, both theories can be summarized as follows:

1. It is assumed that the guiding center coordinates, as defined by (3.106), can be used instead of the particle coordinates when calculating the diffusion coefficients.[11]

   $$v(t) \rightarrow V(t) = a\left[\frac{\vec{v}\cdot\vec{B}_0}{B_0^2}\right]\vec{B} = av_z\frac{\vec{B}}{B_0}$$

2. Using the TGK formulation (see (3.8)), the diffusion coefficient is calculated via the velocity correlation.

   $$d_\perp(t) = \frac{a^2}{B_0^2}\int\limits_0^t \mathrm{d}t' \left\langle v_z(t)v_z(0)\delta B_x(\vec{x}(t),t)\delta B_x(\vec{x}_0,0)\right\rangle$$
   $$\kappa_\perp = \lim_{t\rightarrow\infty} d_\perp(t)$$

3. The magnetic field is described via a Fourier transform. Corrsin's approximation (see (3.26)) is used to separate the magnetic Fourier amplitude from the rest of the correlation, breaking the fourth order correlation into two second order correlations.

   $$\begin{aligned}&\left\langle v_z(t)v_z(0)\delta B_x(\vec{x}(t),t)\delta B_x(\vec{x}_0,0)\right\rangle\\ &\quad= \int \mathrm{d}^3k\int \mathrm{d}^3k' \left\langle v_z(t)v_z(0)\delta B_x(\vec{k},t)\delta B_x^\dagger(\vec{k}',0)e^{i\left[\vec{k}\vec{x}-\vec{k}'\vec{x}_0\right]}\right\rangle && \text{Fourier}\\ &\quad= \int \mathrm{d}^3k\int \mathrm{d}^3k' \left\langle \delta B_x(\vec{k},t)\delta B_x^\dagger(\vec{k}',0)\right\rangle\left\langle v_z(t)v_z(0)e^{i\left[\vec{k}\vec{x}-\vec{k}'\vec{x}_0\right]}\right\rangle && \text{Corrsin}\end{aligned}$$

4. The magnetic amplitude correlation is replaced with the spectral tensor as per

---

[11] As discussed in Section 3.3.5, the parameter a should have a value of 1, with non–unity values due to approximations used in the next steps.

(2.7). The Dirac delta function is dealt with by integrating over k'.

$$\int \mathrm{d}^3k \int \mathrm{d}^3k' \left\langle \delta B_x(\vec{k},t)\delta B_x^\dagger(\vec{k}',0)\right\rangle \left\langle v_z(t)v_z(0)e^{i\left[\vec{k}\vec{x}-\vec{k}'\vec{x}_0\right]}\right\rangle$$

$$= \int \mathrm{d}^3k \int \mathrm{d}^3k'\, P_{xx}(\vec{k},t)\delta^3(\vec{k}-\vec{k}')\left\langle v_z(t)v_z(0)e^{i\left[\vec{k}\vec{x}-\vec{k}'\vec{x}_0\right]}\right\rangle \qquad \text{Spectral Tensor}$$

$$= \int \mathrm{d}^3k\, P_{xx}(\vec{k},t)\left\langle v_z(t)v_z(0)e^{i\vec{k}\Delta\vec{x}}\right\rangle \qquad \text{Integral}$$

5. The fundamental difference between these two theories is in how the velocity–phase correlation is handled.

$$\left\langle v_z(t)v_z(0)e^{i\vec{k}\Delta\vec{x}}\right\rangle = F(\vec{k},t) \qquad \text{Theory dependent}$$

6. With the velocity–phase correlation function computed, the diffusion coefficient can be found.

$$d_\perp(t) = \frac{a^2}{B_0^2}\int_0^t \mathrm{d}t' \int \mathrm{d}^3k\, P_{xx}(\vec{k},t')F(\vec{k},t') \qquad \text{General}$$

$$\kappa_\perp = \frac{a^2v^2}{3B_0^2}\int \mathrm{d}^3k\, \frac{P_{xx}(\vec{k})}{\frac{v}{\lambda_\parallel} + \kappa_\perp k_\perp^2 + \kappa_\parallel k_\parallel^2 + \gamma(\vec{k})} \qquad \text{NLGC}$$

$$\kappa_\perp = \frac{a^2v^2}{3B_0^2}\int \mathrm{d}^3k\, \frac{P_{xx}(\vec{k})}{\frac{v}{\lambda_\parallel} + \frac{4}{3}\kappa_\perp k_\perp^2 + \frac{[vk_\parallel]^2}{3\kappa_\perp k_\perp^2}} \qquad \text{UNLT}$$

$$\frac{\mathrm{d}^2}{\mathrm{d}t^2}\left\langle(\Delta x)^2\right\rangle = \frac{2a^2}{B_0^2}\int \mathrm{d}^3k\, P_{xx}(\vec{k})\xi(k_\parallel,t)e^{-\frac{1}{2}\left\langle(\Delta x)^2\right\rangle k_\perp^2} \qquad \text{UNLT}$$

An alternative way of writing the general form of the diffusion coefficient is

$$d_\perp(t) = \frac{a^2}{B_0^2}\int_0^t \mathrm{d}t' \int \mathrm{d}^3k \int \mathrm{d}^3k'\, P_{xx}(\vec{k},t')\delta^3(\vec{k}-\vec{k}')F(\vec{k}',t').$$

The Dirac delta in the equation describes the coupling between the velocity–phase correlation and the magnetic field: the velocity–phase correlation couples to the magnetic field at equal scales. The final perpendicular transport theory considered in this work, the *Field Line – Particle Decorrelation* (or *FLPD*) theory of Shalchi (2021), results in a coupling between P_{xx} and F which is not described via a Dirac delta function. Instead a resonance function is introduced by considering the decorrelation between the magnetic field lines and the particle trajectories.

3.3.8 Field Line – Particle Decorrelation Theory

The Field Line – Particle Decorrelation theory of Shalchi (2021) can be derived by first considering the phenomenon of compound sub–diffusion. This occurs when perpendicular diffusion of the particles is suppressed by their parallel diffusive motion, resulting in sub-diffusive transport in the perpendicular direction. From a physical perspective, this occurs when particles are bound to a given field line. Webb et al. (2006) presented a description of this type of motion based on the *Chapman–Kolmogorov* equation (for example, see Gardiner (1985)):

$$f_\perp(x,y;t) = \int\limits_{-\infty}^{\infty} \mathrm{d}z\, f_{FL}(x,y;z) f_\parallel(z;t) \tag{3.145}$$

where $f_\perp(x,y;t)$ is the particle distribution in the xy plane as a function of time t, $f_{FL}(x,y;z)$ is the field line distribution in the xy plane based on the position along the z axis, and $f_\parallel(z;t)$ is the particle distribution along the z axis as a function time. The right hand side of the equation is a convolution of the field line distribution and the particle's parallel distribution. As noted in Shalchi (2021), modelling the parallel distribution is not trivial due to the fact that the particles are not instantaneously diffusive in the parallel direction (see (3.85) for example). The particle mean square displacement along the x axis can be calculated from (3.145) by

$$\begin{aligned}
\left\langle (\Delta x(t))^2 \right\rangle &= \int\limits_{-\infty}^{\infty} \mathrm{d}x \int\limits_{-\infty}^{\infty} \mathrm{d}y\, x^2 f_\perp(x,y;t) \\
&= \int\limits_{-\infty}^{\infty} \mathrm{d}x \int\limits_{-\infty}^{\infty} \mathrm{d}y\, x^2 \int\limits_{-\infty}^{\infty} \mathrm{d}z\, f_{FL}(x,y;z) f_\parallel(z;t) \\
&= \int\limits_{-\infty}^{\infty} \mathrm{d}z\, \left\langle (\Delta x(z))^2 \right\rangle_{FL} f_\parallel(z;t)
\end{aligned} \tag{3.146}$$

where $\left\langle (\Delta x(z))^2 \right\rangle_{FL}$ is the mean square displacement of the field lines along the x axis as a function of z. An underlying assumption in (3.146) is that the initial particle distribution is a delta function.

As with the previously discussed theories, the preference is to work in Fourier space, which can be accomplished by defining

$$f_\parallel(z;t) = \int\limits_{-\infty}^{\infty} \mathrm{d}k'_\parallel \, F(k'_\parallel;t) e^{ik'_\parallel z}. \tag{3.147}$$

The particle's perpendicular mean square displacement can therefore be calculated as

$$\left\langle (\Delta x(t))^2 \right\rangle = \int\limits_{-\infty}^{\infty} \mathrm{d}z \, \left\langle (\Delta x(z))^2 \right\rangle_{FL} \int\limits_{-\infty}^{\infty} \mathrm{d}k'_\parallel \, F(k'_\parallel;t) e^{ik'_\parallel z} \tag{3.148a}$$

or equivalently

$$\left\langle (\Delta x)^2 \right\rangle (t) = \int\limits_{-\infty}^{\infty} \mathrm{d}z \int\limits_{-\infty}^{\infty} \mathrm{d}k'_\parallel \, F(k'_\parallel;t) \left\langle (\Delta x(z))^2 \right\rangle_{FL} e^{ik'_\parallel z}. \tag{3.148b}$$

Next, the complex exponential is expressed as

$$e^{ik'_\parallel z} = -\frac{1}{{k'_\parallel}^2} \frac{\mathrm{d}^2}{\mathrm{d}z^2} e^{ik'_\parallel z} \tag{3.149}$$

so that (3.148) can be written as

$$\left\langle (\Delta x(t))^2 \right\rangle = -\int\limits_{-\infty}^{\infty} \mathrm{d}z \int\limits_{-\infty}^{\infty} \mathrm{d}k'_\parallel \, F(k'_\parallel;t) {k'_\parallel}^{-2} \left\langle (\Delta x(z))^2 \right\rangle_{FL} \frac{\mathrm{d}^2}{\mathrm{d}z^2} e^{ik'_\parallel z}. \tag{3.150}$$

Using integration by parts twice, the derivative can be transferred from the complex exponential to the field line mean square displacement, so that

$$\left\langle (\Delta x(t))^2 \right\rangle = -\int\limits_{-\infty}^{\infty} \mathrm{d}z \int\limits_{-\infty}^{\infty} \mathrm{d}k'_\parallel \, F(k'_\parallel;t) {k'_\parallel}^{-2} \, e^{ik'_\parallel z} \, \frac{\mathrm{d}^2}{\mathrm{d}z^2} \left\langle (\Delta x(z))^2 \right\rangle_{FL}. \tag{3.151}$$

To proceed, FLPD theory uses the results of Shalchi and Kourakis (2007) (see (3.43)), in which an equation for the second derivative of the field line mean square displacement was derived:

$$\frac{\mathrm{d}^2}{\mathrm{d}z^2} \left\langle (\Delta x(z))^2 \right\rangle_{FL} = \frac{2}{B_0^2} \int \mathrm{d}^3k \, P_{xx}(\vec{k}) \cos(k_\parallel z) e^{-\frac{1}{2}\left\langle (\Delta x(z))^2 \right\rangle_{FL} k_\perp^2}. \tag{3.152}$$

Therefore the particle mean square displacement is

$$\begin{aligned}\left\langle (\Delta x(t))^2 \right\rangle = -\frac{2}{B_0^2} \int \mathrm{d}^3 k \int\limits_{-\infty}^{\infty} \mathrm{d}k'_\parallel \, P_{xx}(\vec{k}) \, F(k'_\parallel; t) {k'_\parallel}^{-2} \\ \times \int\limits_{-\infty}^{\infty} \mathrm{d}z \, \cos(k_\parallel z) e^{-\frac{1}{2}\left\langle (\Delta x(z))^2 \right\rangle_{FL} k_\perp^2 + i k'_\parallel z}.\end{aligned} \tag{3.153}$$

By using the diffusion approximation for field lines,

$$\left\langle (\Delta x(z))^2 \right\rangle \approx 2\kappa_{FL} |z| \tag{3.154}$$

the z integral can be solved to find

$$\begin{aligned}&\frac{2\pi}{2\pi} \int\limits_{-\infty}^{\infty} \mathrm{d}z \, \cos(k_\parallel z) e^{-\kappa_{FL}|z| k_\perp^2 + i k'_\parallel z} \\ &= 2\pi \left[\frac{1}{2\pi} \frac{\kappa_{FL} k_\perp^2}{(k_\parallel + k'_\parallel)^2 + \kappa_{FL}^2 k_\perp^4} + \frac{1}{2\pi} \frac{\kappa_{FL} k_\perp^2}{(k_\parallel - k'_\parallel)^2 + \kappa_{FL}^2 k_\perp^4} \right] \\ &= 2\pi \left[R_+(\vec{k}, k'_\parallel) + R_-(\vec{k}, k'_\parallel) \right] = 2\pi R(\vec{k}, k'_\parallel)\end{aligned} \tag{3.155}$$

where the resonance functions

$$R_\pm(\vec{k}, k'_\parallel) = \frac{1}{2\pi} \frac{\kappa_{FL} k_\perp^2}{(k_\parallel \pm k'_\parallel)^2 + \kappa_{FL}^2 k_\perp^4} \tag{3.156a}$$

and

$$R(\vec{k}, k'_\parallel) = R_+(\vec{k}, k'_\parallel) + R_-(\vec{k}, k'_\parallel) \tag{3.156b}$$

"describe the coupling between particles and magnetic field lines" (Shalchi, 2021).[12] Note that here the resonance functions have an additional factor of $1/2\pi$ in them, as compared to how they are defined in Shalchi (2021). The particle's perpendicular mean square displacement can therefore be calculated via

$$\left\langle (\Delta x(t))^2 \right\rangle = -\frac{4\pi}{B_0^2} \int \mathrm{d}^3 k \int\limits_{-\infty}^{\infty} \mathrm{d}k'_\parallel \, P_{xx}(\vec{k}) \, R(\vec{k}, k'_\parallel) \, F(k'_\parallel; t) {k'_\parallel}^{-2}. \tag{3.157}$$

In order to find an expression for $F(k'_\parallel; t)$, recall that it is defined as the Fourier transform of the particle distribution along the z axis by (3.147). As discussed in Section 3.2.3.1, the result of the Fourier transform of a distribution function is its

---

[12] The resonance functions can also be written as $R(k_\parallel, k_\perp, k'_\parallel)$.

associated characteristic function. Using

$$F(k_\parallel, t) = \frac{1}{2\pi}\frac{\omega_+ e^{\omega_- t} - \omega_- e^{\omega_+ t}}{\omega_+ - \omega_-} \tag{3.158}$$

for the characteristic function, (3.157) becomes

$$\left\langle (\Delta x(t))^2 \right\rangle = -\frac{2}{B_0^2}\int \mathrm{d}^3k \int\limits_{-\infty}^{\infty} \mathrm{d}k'_\parallel \, P_{xx}(\vec{k}), R(\vec{k}, k'_\parallel)\, \frac{\omega_+ e^{\omega_- t} - \omega_- e^{\omega_+ t}}{\omega_+ - \omega_-} {k'_\parallel}^{-2}. \tag{3.159}$$

Recalling that the mean square displacement can be related to the velocity correlation via (3.9), the second derivative of the function is taken to find

$$\frac{\mathrm{d}^2}{\mathrm{d}t^2}\left\langle (\Delta x(t))^2 \right\rangle = \frac{2}{B_0^2}\int \mathrm{d}^3k \int\limits_{-\infty}^{\infty} \mathrm{d}k'_\parallel \, P_{xx}(\vec{k})\, R(\vec{k}, k'_\parallel)\, \frac{\omega_+\omega_-}{{k'_\parallel}^2}\frac{\omega_+ e^{\omega_+ t} - \omega_- e^{\omega_- t}}{\omega_+ - \omega_-}. \tag{3.160}$$

Using (3.82), $\omega_+\omega_-$ is found to be

$$\omega_+\omega_- = \frac{1}{3}v^2 k_\parallel^2 \tag{3.161}$$

and (3.160) becomes

$$\begin{aligned} \frac{\mathrm{d}^2}{\mathrm{d}t^2}\left\langle (\Delta x(t))^2 \right\rangle &= \frac{2}{B_0^2}\int \mathrm{d}^3k \int\limits_{-\infty}^{\infty} \mathrm{d}k'_\parallel \, P_{xx}(\vec{k})\, R(\vec{k}, k'_\parallel)\, \frac{v^2}{3}\frac{\omega_+ e^{\omega_+ t} - \omega_- e^{\omega_- t}}{\omega_+ - \omega_-} \\ &= \frac{2}{B_0^2}\int \mathrm{d}^3k \int\limits_{-\infty}^{\infty} \mathrm{d}k'_\parallel \, P_{xx}(\vec{k})\, R(\vec{k}, k'_\parallel)\, \xi(k'_\parallel, t). \end{aligned} \tag{3.162}$$

The final step in the derivation of FLPD theory involves taking into account the effect of the transverse complexity of the turbulence on particle transport. Shalchi (2021) accomplishes this by including the factor $e^{-\frac{1}{2}\left\langle (\Delta x)^2 \right\rangle k_\perp^2}$, so that the equation of FLPD theory is

$$\frac{\mathrm{d}^2}{\mathrm{d}t^2}\left\langle (\Delta x(t))^2 \right\rangle = \frac{2}{B_0^2}\int \mathrm{d}^3k \int\limits_{-\infty}^{\infty} \mathrm{d}k'_\parallel \, P_{xx}(\vec{k})\, R(\vec{k}, k'_\parallel)\, \xi(k'_\parallel, t)\, e^{-\frac{1}{2}\left\langle (\Delta x)^2 \right\rangle k_\perp^2} \tag{3.163a}$$

or equivalently

$$\begin{aligned}\frac{\mathrm{d}^2}{\mathrm{d}t^2}\left\langle (\Delta x(t))^2 \right\rangle = 2\frac{\delta B_x^2}{B_0^2} &\int\limits_{-\infty}^{\infty} \mathrm{d}k'_\parallel \, \xi(k'_\parallel, t) \int\limits_{0}^{\infty} \mathrm{d}k_\perp \, k_\perp \ell_\perp^2 \, g_\perp(k_\perp) e^{-\frac{1}{2}\left\langle (\Delta x)^2 \right\rangle k_\perp^2} \\ &\times \int\limits_{-\infty}^{\infty} \mathrm{d}k_\parallel \, \ell_\parallel \, g_\parallel(k_\parallel) \, R(k_\parallel, k_\perp, k'_\parallel).\end{aligned} \tag{3.163b}$$

It should be noted that while the resonance function $R_\pm(\vec{k}, k'_\parallel)$ depends on $k_\perp$, the actual resonance is between $k_\parallel$ and $k'_\parallel$. As such, there is no $k'_\perp$ in FLPD theory.

3.3.8.1 Diffusive FLPD Theory

Shalchi (2021) also considered the application of the diffusive approximation, $\left\langle (\Delta x(t))^2 \right\rangle = 2\kappa_\perp t$, to FLPD theory. Integrating (3.163) over time and using a diffusive approximation yields

$$\begin{aligned}\kappa_\perp &= \frac{v^2}{3B_0^2} \int \mathrm{d}^3k \int\limits_{-\infty}^{\infty} \mathrm{d}k'_\parallel \, P_{xx}(\vec{k}) \, R(\vec{k}, k'_\parallel) \, \frac{\kappa_\perp k_\perp^2}{\omega_+\omega_- + [\omega_+ + \omega_-]\kappa_\perp k_\perp^2 + \kappa_\perp^2 k_\perp^4} \\ &= \frac{v^2}{3B_0^2} \int \mathrm{d}^3k \int\limits_{-\infty}^{\infty} \mathrm{d}k'_\parallel \, P_{xx}(\vec{k}) \, R(\vec{k}, k'_\parallel) \, \frac{\kappa_\perp k_\perp^2}{\frac{v}{\lambda_\parallel}\kappa_\perp k_\perp^2 + \kappa_\perp^2 k_\perp^4 + \frac{1}{3}[v k'_\parallel]^2} && \text{(3.164a)} \\ &= \frac{v^2}{3B_0^2} \int \mathrm{d}^3k \int\limits_{-\infty}^{\infty} \mathrm{d}k'_\parallel \, \frac{P_{xx}(\vec{k}) \, R(\vec{k}, k'_\parallel)}{\frac{v}{\lambda_\parallel} + \kappa_\perp k_\perp^2 + \frac{[v k'_\parallel]^2}{3\kappa_\perp k_\perp^2}}. && \text{(3.164b)}\end{aligned}$$

Alternatively, (3.164) can be written as

$$\kappa_\perp = \frac{v^2}{3}\frac{\delta B_x^2}{B_0^2} \int\limits_{-\infty}^{\infty} \mathrm{d}k_\parallel \int\limits_{-\infty}^{\infty} \mathrm{d}k_\parallel{}' \int\limits_{0}^{\infty} \mathrm{d}k_\perp \, k_\perp \ell_\perp^2 \ell_\parallel \, \frac{g_\parallel(k_\parallel) \, g_\perp(k_\perp) \, R(k_\parallel, k_\perp, k'_\parallel)}{\frac{v}{\lambda_\parallel} + \kappa_\perp k_\perp^2 + \frac{[v k'_\parallel]^2}{3\kappa_\perp k_\perp^2}} \tag{3.164c}$$

if the spectral tensor is written using (2.39). This can be compared with the equation for diffusive UNLT, (3.127): if there is no transverse complexity, (3.164) reduces to (3.136) rather than (3.127), as the pitch–angle averaging is not taken into account.

3.3.8.2 FLPD Application: Examples

Consider the application of FLPD theory to slab turbulence. Using (2.23) and (2.24) for the spectral tensor and spectral function respectively, the equation of FLPD becomes

$$\frac{\mathrm{d}^2}{\mathrm{d}t^2}\left\langle(\Delta x(t))^2\right\rangle = \frac{\delta B^2}{B_0^2}\int\limits_0^\infty \mathrm{d}k_\perp\,\delta(k_\perp)e^{-\frac{1}{2}\left\langle(\Delta x)^2\right\rangle k_\perp^2}\int\limits_{-\infty}^\infty \mathrm{d}k_\parallel\,\ell_\parallel\frac{2C(s)}{\left[1+[k_\parallel\ell_\parallel]^2\right]^{\frac{s}{2}}} \\ \times\int\limits_{-\infty}^\infty \mathrm{d}k_\parallel'\,R(\vec{k},k_\parallel')\,\xi(k_\parallel',t). \tag{3.165}$$

Using the relation

$$\lim_{\gamma\to 0}\frac{1}{\pi}\frac{\gamma}{x^2+\gamma^2} = \delta(x) \tag{3.166}$$

the resonance functions become

$$R_\pm(k_\parallel,0,k_\parallel') = \frac{1}{2}\delta(k_\parallel\pm k_\parallel'). \tag{3.167}$$

Since the integrals are symmetric in both $k_\parallel$ and $k_\parallel'$, after integrating over $k_\perp$ the resonance functions can be written as

$$R(k_\parallel,0,k_\parallel') = \delta(k_\parallel - k_\parallel'). \tag{3.168}$$

As a result, upon integrating over $k_\parallel'$ the FLPD equation becomes

$$\frac{\mathrm{d}^2}{\mathrm{d}t^2}\left\langle(\Delta x)^2\right\rangle = \frac{2}{3}v^2\frac{\delta B^2}{B_0^2}\int\limits_0^\infty \mathrm{d}k_\parallel\,\ell_\parallel\frac{2C(s)}{\left[1+[k_\parallel\ell_\parallel]^2\right]^{\frac{s}{2}}}\frac{\omega_+e^{\omega_+t}-\omega_-e^{\omega_-t}}{\omega_+-\omega_-}, \tag{3.169}$$

which is exactly the same as (3.138), the time–dependent UNLT equation for slab turbulence.

Now consider the application of FLPD theory to the noisy slab turbulence and full 3D turbulence models. In this case, the FLPD equation becomes

$$\frac{\mathrm{d}^2}{\mathrm{d}t^2}\left\langle(\Delta x)^2\right\rangle = 2\frac{\delta B_x^2}{B_0^2}\int\limits_0^{1/\ell_\perp} \mathrm{d}k_\perp\,\ell_\perp e^{-\frac{1}{2}\left\langle(\Delta x)^2\right\rangle k_\perp^2}\int\limits_{-\infty}^\infty \mathrm{d}k_\parallel'\,\xi(k_\parallel',t) \\ \times\int\limits_{-\infty}^\infty \mathrm{d}k_\parallel\,\ell_\parallel\,\frac{2C(s)}{\left[1+[k_\parallel\ell_\parallel]^2\right]^{\frac{s}{2}}}R(k_\parallel,k_\perp,k_\parallel') \tag{3.170}$$

for the noisy slab model and

$$\begin{aligned}\frac{\mathrm{d}^2}{\mathrm{d}t^2}\left\langle(\Delta x)^2\right\rangle = 2\frac{\delta B_x^2}{B_0^2}\int\limits_0^\infty \mathrm{d}k_\perp\,\ell_\perp 4D(s,q)\frac{[k_\perp\ell_\perp]^q}{\left[1+[k_\perp\ell_\perp]^2\right]^{\frac{s+q}{2}}}e^{-\frac{1}{2}\left\langle(\Delta x)^2\right\rangle k_\perp^2} \\ \times\int\limits_{-\infty}^{\infty}\mathrm{d}k_\parallel'\,\xi(k_\parallel',t)\int\limits_{-\infty}^{\infty}\mathrm{d}k_\parallel\,\ell_\parallel\,\frac{C(s)}{\left[1+[k_\parallel\ell_\parallel]^2\right]^{\frac{s}{2}}}R(k_\parallel,k_\perp,k_\parallel')\end{aligned} \tag{3.171}$$

for the full 3D model, neither of which can be analytically reduced. As can be seen from these examples, FLPD theory provides the same result as UNLT theory when the turbulence in question doesn't contain any transverse complexity and gives different results when the turbulence has transverse complexity.

Chapter 4

Instantaneous Rotation Matrix Methods

Copyright Permissions

The contents of this chapter were originally published in **Numerical Methods, Energy Conservation, And A New Method For Particle Motion in Magnetic Fields** in the journal *Mathematics and Computers in Simulation* (Arendt, 2023). The journal publishing agreement allows the author to reuse the contents of the article in this thesis. As the sole author of the article, no other permissions are required. The body of the article has therefore been reproduced here, while the appendices of the article have been reproduced in Appendix A and Appendix B. Due to differences in page formatting, figures and tables may not appear in the same locations in the text or be formatted the same compared to the original article. Cross–referencing between figures, tables, chapters, sections, and appendices was also updated to be consistent with the rest of this thesis. Additionally, several typographical errors have been corrected, with a full list at the end of the chapter.

On Mathematical Notation and Scaling

The mathematical notation and scaling of quantities used in this chapter are the same as used in Arendt (2023), which is not the same as that used in the rest of this work. The article was written with generic use in mind, and therefore scaling anything outside of the magnetic field was avoided if possible. Conversions between

Quantity	Arendt (2023)	This Work	Relation
Time	t	T	$T = \Omega t$
Position	$\vec{x}$	$\vec{X}$	$\vec{X} = \vec{x}/\ell$
Velocity	$\vec{v}$	$\vec{R}$	$\vec{R} = \vec{v}/\Omega\ell$
Magnetic Field	$\vec{\omega}$	$\vec{b}$	$\vec{b} = \vec{\omega}/\Omega$

Table 4.1: Conversion of quantities found in Arendt (2023) and this section and those in the rest of this work. The quantity Ω is the relativistic gyro-frequency as defined in 1.2.1.1

the quantities found in Arendt (2023) and the rest of this work are shown in Table 4.1.

Abstract

This article mathematically examines the energy conservation of explicit Runge–Kutta methods and basic symplectic integration methods for a simple harmonic oscillator and a particle in a magnetic field. With the demonstration of the failure of these methods to conserve the energy of a particle in a magnetic field, a new integration method is presented for this type of system where energy conservation is dictated by the type of floating point variable used, not the size of the time step or the method order. Higher order versions of the method improve the accuracy in the calculation of the particle position and allow for more accurate calculations of the velocity in a spatially varying field. Furthermore, the new method is demonstrated to have improved phase accuracy when compared to several common implicit methods.

4.1 Introduction

When solving the equations of motion for a particle or system of particles numerically, a common issue is ensuring that the total energy of the system is conserved by the solution. One of the simplest systems to consider is that of the one-dimensional simple harmonic oscillator. Unfortunately, common explicit Runge–Kutta methods do not conserve the total energy of this simple system, although the energy conservation can be improved by decreasing the time step. Of course, this leads to a competition between how accurate the results need to be and how long it takes to obtain the results. Using adaptive Runge–Kutta methods doesn't improve the result, as taking larger time steps increases the energy drift. Alternatively, symplectic integration methods (Ruth, 1983, Yoshida, 1990) can be used to achieve greater accuracy without requiring as small a time step, with the energy oscillating around the initial value.

In astrophysics one problem is the motion of charged, energetic particles in a variable magnetic field. Theories that calculate the properties of an ensemble in these fields (see Shalchi (2009, 2020) for a review) are often compared with test particle simulations, and therefore accuracy in the calculated trajectories is required. For example, one of the primary quantities of interest in these theories are the spatial diffusion coefficients, for which these theories assume a pure magnetic system (no electric fields). Since the electric field is absent and particle-particle interactions are neglected, the particle energies in any test particle simulation must be conserved for comparisons with theory to be valid. As with the simple harmonic oscillator, using explicit Runge–Kutta methods to solve the equations of motion for this system will result in energy drift. Unfortunately, applying the same symplectic methods as used for the simple harmonic oscillator to the system also results in energy drift, albeit of a much greater magnitude, as these methods were designed for systems where the Hamiltonian is separable. To address this, implicit methods that conserve energy have been developed over time (see Ripperda et al. (2018) for a recent review). Unfortunately, while these methods conserve energy, the error is shifted onto the phase of rotation.

In the following, the simple harmonic oscillator and a particle in a magnetic field are considered as test cases (Section 4.2) for energy conservation in explicit Runge–Kutta methods (see Section 4.3 and A) and basic symplectic methods (see Section 4.4 and B). Then, having shown mathematically why and how these methods fail for a particle in a magnetic field, a new class of integration methods is presented (Section 4.5).[1] It will be shown that this new method provides superior energy conservation compared to common explicit Runge–Kutta and symplectic methods for a particle in a magnetic field, and superior phase accuracy compared to several implicit methods that have analytical forms.

---

[1] This method was briefly described in Arendt and Shalchi (2018), where it used inverse trigonometric functions to calculate rotation matrices. In this article, the use of inverse trigonometric functions has been replaced in favour of projection matrices calculated directly from the components of the magnetic field vector in Cartesian coordinates.

4.2 Test Cases: Analytical Solutions

In the analysis of the energy conservation of Runge–Kutta and symplectic integration methods two test cases will be considered: the simple harmonic oscillator (SHO) and a particle in a magnetic field.

4.2.1 Test Case: Simple Harmonic Oscillator

The first case being considered is that of the one-dimensional simple harmonic oscillator with the form

$$E = \frac{1}{2}\left[p^2 + q^2\right], \tag{4.1}$$

where E is the total energy, with equations of motion

$$\dot{q} = p, \tag{4.2a}$$

$$\dot{p} = -q; \tag{4.2b}$$

where p and q are respectively unit–less momentum and position. The well known solution for these equations is

$$q(t) = q_0 \cos(t) + p_0 \sin(t) \tag{4.3a}$$

$$p(t) = p_0 \cos(t) - q_0 \sin(t), \tag{4.3b}$$

or equivalently

$$q(t) = \sqrt{2E}\cos(t \pm \tau) \tag{4.4a}$$

$$p(t) = -\sqrt{2E}\sin(t \pm \tau) \tag{4.4b}$$

where τ is the initial phase of the oscillator.

4.2.2 Test Case: Particle in a Magnetic Field

There are two formulations of a particle in a magnetic field: the Newtonian formulation and the Hamiltonian formulation.

4.2.2.1 Newtonian Formulation

The classical Newtonian formulation in cgs units of a charged particle interacting with a magnetic field is given by the Lorentz force:

$$\vec{F} = \frac{\mathrm{d}\vec{p}}{\mathrm{d}t} = q\frac{\vec{v}}{c} \times \vec{B}(\vec{x}, t), \tag{4.5}$$

where $\vec{p}$ is the relativistic momentum, $\vec{v}$ is the particle velocity, $\vec{x}$ is the particle position, q is the charge on the particle, c is the speed of light, and $\vec{B}$ is magnetic field. Although the equation here is in cgs units for relativistic particles, the results are generally applicable. Equation 4.5 can be rearranged to read

$$\frac{\mathrm{d}\vec{v}}{\mathrm{d}t} = \vec{v} \times \vec{\omega}(\vec{x}, t), \tag{4.6}$$

where $\vec{\omega}$ is defined in cgs units as

$$\vec{\omega}(\vec{x}, t) = \frac{q\vec{B}(\vec{x}, t)}{\gamma m c}. \tag{4.7}$$

It should be noted that since there is no electric field in this system, (4.5) can also be written as

$$\frac{\mathrm{d}\vec{p}}{\mathrm{d}t} = \vec{p} \times \vec{\omega}(\vec{x}, t) \tag{4.8}$$

since the velocity and momentum are related to each other by $\vec{p} = \gamma m \vec{v}$.

If the magnetic field is uniform and static, then $|\vec{\omega}|$ is the gyro–frequency for non–relativistic particles or synchrotron frequency for relativistic particles. In component form, 4.6 can be written as

$$\frac{\mathrm{d}v_i}{\mathrm{d}t} = \epsilon_{ijk} v_j \omega_k(\vec{x}, t), \tag{4.9}$$

from which the quantity $\bar{\bar{\omega}}$ can be defined as

$$\bar{\bar{\omega}}_{ij}(\vec{x}, t) = \epsilon_{ijk} \omega_k(\vec{x}, t) \tag{4.10}$$

such that the change in velocity is

$$\frac{\mathrm{d}\vec{v}}{\mathrm{d}t} = \bar{\bar{\omega}}(\vec{x}, t)\vec{v}, \tag{4.11}$$

yielding the solution

$$\vec{v}(t + t_0) = e^{\bar{\bar{\omega}} t} \vec{v}(t_0). \tag{4.12}$$

Several properties of the matrix $\bar{\bar{\omega}}$ will be used throughout this article: first, that the matrix is anti–symmetric; and second, that since $\vec{v} \times \vec{\omega} = \bar{\bar{\omega}}\vec{v}$, then $(\vec{v} \times \vec{\omega}_1) \times \vec{\omega}_2 = \bar{\bar{\omega}}_2 \bar{\bar{\omega}}_1 \vec{v}$.

4.2.2.2 Hamiltonian Formulation

The Hamiltonian for a non–relativistic particle in a magnetic field in cgs units can be written as

$$H = \frac{\left[\vec{p} - \frac{q}{c}\vec{A}(\vec{r},t)\right]^2}{2m}, \tag{4.13}$$

where $\vec{p}$ is the canonical momentum given by

$$\vec{p} = m\vec{v} + \frac{q}{c}\vec{A}(\vec{r},t). \tag{4.14}$$

The equations of motion are

$$\dot{\vec{r}} = \vec{\nabla}_p H = \frac{\vec{p}}{m} - \frac{q}{mc}\vec{A}(\vec{r},t), \tag{4.15a}$$

$$\dot{\vec{p}} = -\vec{\nabla}_r H = \frac{-1}{2m}\vec{\nabla}_r\left[\vec{p} - \frac{q}{c}\vec{A}(\vec{r},t)\right]^2. \tag{4.15b}$$

In the analysis of numerical methods, the canonical momentum and Hamiltonian will be redefined as a quantity per unit mass. The first step is to define

$$\vec{A}'(\vec{r},t) = \frac{q}{mc}\vec{A}(\vec{r},t) \tag{4.16}$$

so that

$$\vec{\nabla} \times \vec{A}'(\vec{r},t) = \vec{\omega}(\vec{r},t). \tag{4.17}$$

Next, the canonical momentum is redefined as

$$\vec{p} = \vec{v} + \frac{q}{mc}\vec{A}(\vec{r},t) = \vec{v} + \vec{A}'(\vec{r},t) \tag{4.18}$$

and the Hamiltonian, 4.13, becomes

$$H' = \frac{H}{m} = \frac{1}{2}\left[\vec{p} - \vec{A}'(\vec{r},t)\right]^2. \tag{4.19}$$

With this transformation, the equations of motion become

$$\dot{\vec{r}} = \vec{p} - \vec{A}'(\vec{r},t) \tag{4.20a}$$

and

$$\dot{\vec{p}} = -\frac{1}{2}\vec{\nabla}_r\left[\vec{p} - \vec{A}'(\vec{r},t)\right]^2. \tag{4.20b}$$

Using the identity

$$\frac{1}{2}\vec{\nabla}\left[\vec{u}\cdot\vec{u}\right] = \vec{u} \times \left[\vec{\nabla} \times \vec{u}\right] + \left[\vec{u}\cdot\vec{\nabla}\right]\vec{u} \tag{4.21}$$

the change in the canonical momentum can be written as

$$\dot{\vec{p}} = \left[\vec{p} - \vec{A}'(\vec{r},t)\right] \times \vec{\omega}(\vec{r},t) + \left[\left[\vec{p} - \vec{A}'(\vec{r},t)\right] \cdot \vec{\nabla}\right] \vec{A}'(\vec{r},t). \tag{4.22}$$

If the magnetic field is constant, then the magnetic potential can be expressed as[2]

$$\vec{A}'(\vec{r}) = \frac{1}{2}\vec{\omega} \times \vec{r}, \tag{4.23}$$

and the Hamiltonian as

$$H' = \frac{1}{2}\left[\vec{p} + \frac{1}{2}\vec{r} \times \vec{\omega}\right]^2. \tag{4.24}$$

The change in canonical momentum and position become

$$\dot{\vec{p}} = \frac{1}{2}\left[\vec{p} + \frac{1}{2}\vec{r} \times \vec{\omega}\right] \times \vec{\omega} \tag{4.25a}$$

and

$$\dot{\vec{r}} = \left[\vec{p} + \frac{1}{2}\vec{r} \times \vec{\omega}\right], \tag{4.25b}$$

respectively. Alternatively, (4.10) can be used to write these equations as

$$\dot{\vec{p}} = \frac{1}{2}\bar{\bar{\omega}}\left[\vec{p} + \frac{1}{2}\bar{\bar{\omega}}\vec{r}\right], \tag{4.26a}$$

$$\dot{\vec{r}} = \left[\vec{p} + \frac{1}{2}\bar{\bar{\omega}}\vec{r}\right], \tag{4.26b}$$

which is the form that will be used during analysis in this article.

---

[2] This isn't the only way the vector potential can be expressed, however, this expression readily allows the results to be expressed in a vector format.

4.3 Explicit Runge-Kutta Methods

4.3.1 General Form

The general form of an explicit Runge–Kutta (RK) integration method with $N+1$ intermediate steps can be expressed as:

$$\begin{aligned}
y' &= f(y, \lambda) \\
k_0 &= f(y_0, \lambda_0) \\
&\vdots \\
k_n &= f\left(y_0 + \sum_{i=0}^{n-1} a_{ni} k_i h, \lambda + c_n h\right) \\
&\vdots \\
k_N &= f\left(y_0 + \sum_{i=0}^{N-1} a_{Ni} k_i h, \lambda + c_N h\right) \\
y(\lambda_0 + h) &= y_0 + h \sum_{n=0}^{N} b_n k_n
\end{aligned} \tag{4.27}$$

where λ is the independent variable, h is the current step size, and a_{ni}, b_n, and c_n are the coefficients of integration. Adaptive step size methods include the error estimator step

$$y^* = y_0 + h \sum_{n=0}^{N} b_n^* k_n. \tag{4.28}$$

The coefficients for these methods can be conveniently expressed via a *Butcher-Tableau* (Butcher, 1964):

$$\begin{array}{c|c} \bar{\bar{c}} & \bar{\bar{a}} \\ \hline & \bar{\bar{b}} \\ & \bar{\bar{b}}^* \end{array} = \begin{array}{c|ccccc} 0 & 0 & \cdots & \cdots & 0 \\ c_1 & a_{10} & 0 & \cdots & 0 \\ \vdots & \vdots & \ddots & \ddots & \vdots \\ c_N & a_{N0} & \cdots & a_{N,N-1} & 0 \\ \hline & b_0 & \cdots & \cdots & b_N \\ & b_0^* & \cdots & \cdots & b_N^* \end{array} \tag{4.29}$$

Here, $\bar{\bar{c}}$ is a column vector containing the coefficients for calculating the time at each intermediate point; $\bar{\bar{a}}$ is a square matrix containing the coefficients for calculating the intermediate points from previously computed intermediate function evaluations; and $\bar{\bar{b}}$ is a row vector containing the set of coefficients for calculating the updated point from the computed intermediate function evaluations. Adaptive methods also use $\bar{\bar{b}}^*$ for calculating an alternate solution that is used to estimate the truncation error of the updated solution. The results of expanding the updated point for the considered test cases can be found in Appendix A.

4.3.2 Energy Conservation

As already mentioned in the introduction, explicit RK methods do not conserve the total energy of a simple harmonic oscillator or the kinetic energy of a particle in a magnetic field. The derivation of this violation is found in Appendix A, and the results are summarized here.

4.3.2.1 Simple Harmonic Oscillator

As per (A.14), the energy drift per step of a RK method for a SHO is

$$E(t+h) = E(t)\left[1 + \sum_{m=m_0}^{M} \alpha_{2m} h^{2m}\right] \tag{4.30}$$

where m_0 is the index of the first non-zero α term. The total energy drift after time $T = \sum_i h_i$ is therefore

$$E(t_0+T) = E(t_0)\prod_i \left[1 + \sum_{m=m_0}^{M} \alpha_{2m} h_i^{2m}\right]. \tag{4.31}$$

Of note is that the direction of the energy drift depends only on the RK method used, not the step size; and that using larger step sizes increases the energy drift rate. This is where the trade off between the number of steps required and the desired accuracy comes in: doubling the the step size will halve the time required to complete the calculations but will increase the energy drift by a factor of 4^{m_0}. Conversely, halving the time step will double the time required while reducing the energy drift by a factor of $1/4^{m_0}$. For the fourth order RK methods considered in Appendix A.1.4, the first non-zero α term is α_6, meaning that energy is conserved to sixth order.

4.3.2.2 Particle in a Magnetic Field

As shown in Appendix A.1.3, both the Newtonian and Hamiltonian formulations of a particle in a uniform, static magnetic field have the same energy drift per step of

$$E(t+h) = E_{\|}(t) + E_{\perp}(t)\left[1 + \sum_{m=1}^{M} \alpha_{2m} |\vec{\omega} h|^{2m}\right] \tag{4.32}$$

as per (A.21). This results in a total energy drift of

$$E(t_0+T) = E_{\|}(t_0) + E_{\perp}(t_0)\prod_{i}\left[1 + \sum_{m=m_0}^{M} \alpha_{2m} |\vec{\omega} h_i|^{2m}\right] \tag{4.33}$$

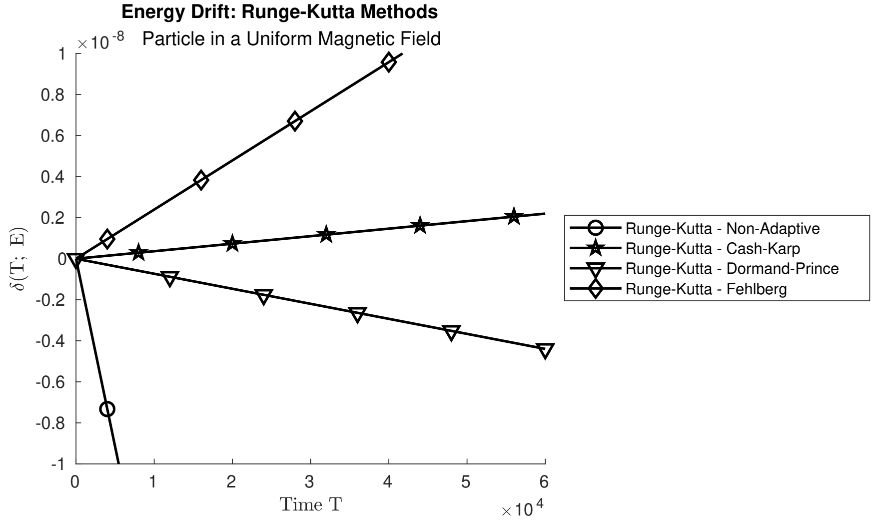

Figure 4.1: Energy drift in Runge-Kutta methods for a particle in a uniform magnetic field.

From (A.21) the energy drift in the Newtonian formulation for a spatially or temporally varying field has the same base energy drift per step as in a uniform static field, plus additional terms for the variation in the field at the intermediate points k_n. With the values of α_{2m} being the same as those for the SHO in the fourth order methods considered in Appendix A.1.4, the kinetic energy is conserved to sixth order. Figure 4.1 shows the resulting energy drift in the RK methods considered in Appendix A.1.4 applied to the scenario defined in Section 4.5.5.1. For comparison purposes, the step size has been held constant.

4.4 Symplectic Methods

Symplectic integration methods are a set of differential equation solvers based on Hamilton's equations of motion (for example, see Ruth (1983), Yoshida (1990)):

$$\frac{\mathrm{d}p_i}{\mathrm{d}t} = -\frac{\partial H}{\partial q_i} \tag{4.34a}$$

$$\frac{\mathrm{d}q_i}{\mathrm{d}t} = \frac{\partial H}{\partial p_i}, \tag{4.34b}$$

where H is the Hamiltonian of the system, and q_i and p_i are respectively the generalized position and momenta of the system. These equations can be expressed with matrices and vectors as either

$$\frac{\mathrm{d}}{\mathrm{d}t}\begin{bmatrix} p_i \\ q_i \end{bmatrix} = \begin{bmatrix} 0 & -1 \\ 1 & 0 \end{bmatrix} \begin{bmatrix} \partial_{p_i} \\ \partial_{q_i} \end{bmatrix} H \tag{4.35a}$$

or

$$\frac{\mathrm{d}}{\mathrm{d}t}\begin{bmatrix} q_i \\ p_i \end{bmatrix} = \begin{bmatrix} 0 & 1 \\ -1 & 0 \end{bmatrix} \begin{bmatrix} \partial_{q_i} \\ \partial_{p_i} \end{bmatrix} H. \tag{4.35b}$$

If the Hamiltonian can be expressed as

$$H(p, q) = T(p) + U(q) \tag{4.36}$$

where $T(p)$ is the kinetic energy of the system and $U(q)$ is the potential energy, then the equations of motion can be written as

$$\frac{\mathrm{d}p_i}{\mathrm{d}t} = -\frac{\partial U(q)}{\partial q_i} = F_i(q) \tag{4.37a}$$

$$\frac{\mathrm{d}q_i}{\mathrm{d}t} = \frac{\partial T(p)}{\partial p_i} = \frac{p_i}{m}, \tag{4.37b}$$

where $F_i(q)$ is the force along axis i resulting from the potential and $\frac{p_i}{m}$ corresponds to the velocity along the same axis.

4.4.1 General Forms

Unlike Runge-Kutta methods, symplectic integration methods do not update all elements of the solution simultaneously. Instead, these methods alternate between updating the position and the momentum/velocity of the system. This leads to two possible forms of the integration method, depending on which quantity is updated first. Hereafter, methods which update the momentum first will be referred to as *momentum-position* or *PQ* methods, while methods that first update the position will be referred to as *position-momentum* or *QP* methods. Specific examples of these methods can be found in Appendix B.1.1.

4.4.1.1 Momentum-Position Methods

The form for momentum-position methods can be expressed as

$$\vec{p}_n = \vec{p}_{n-1} + P_n F(\vec{q}_{n-1})\mathrm{d}t \tag{4.38a}$$

$$\vec{q}_n = \vec{q}_{n-1} + Q_n \frac{\vec{p}_n}{m}\mathrm{d}t \tag{4.38b}$$

with $\vec{p}_0 = \vec{p}(t)$ and $\vec{q}_0 = \vec{q}(t)$. Quantities P_n and Q_n are the integration coefficients. The updated quantities are $\vec{p}(t+\mathrm{d}t) = \vec{p}_N$ and $\vec{q}(t+\mathrm{d}t) = \vec{q}_N$ where N is the number of intermediate steps.

4.4.1.2 Position-Momentum Methods

The position-momentum form of symplectic integration can be expressed as

$$\vec{q}_n = \vec{q}_{n-1} + Q_n \frac{\vec{p}_{n-1}}{m}\mathrm{d}t \tag{4.39a}$$

$$\vec{p}_n = \vec{p}_{n-1} + P_n F(\vec{q}_n)\mathrm{d}t, \tag{4.39b}$$

with integration coefficients Q_n and P_n.

4.4.2 Energy Conservation

4.4.2.1 Simple Harmonic Oscillator

As shown in B.1.4, the energy drift in symplectic methods for the SHO is dominated by a phase dependent fluctuation, with a constant energy drift only appearing at higher orders. Furthermore, both components of the energy drift decrease as the method order increases. For example, the fourth order methods considered both have a fifth order phase dependent energy fluctuation and a tenth order constant energy drift. This can be compared to the fourth order Runge-Kutta methods which had a constant sixth order energy drift.

4.4.2.2 Particle in a Magnetic Field

While symplectic methods have a smaller constant energy drift for the SHO compared to Runge-Kutta methods, they are worse for a particle in a magnetic field. As shown in B.1.5, specifically Table B.21, the symplectic methods have a constant second order energy gain regardless of method order and which formulation of the equations of motion is used. Figure 4.2 demonstrates the violation of energy conservation. The physical scenario used here is defined in Chapter 4.5.5.1.

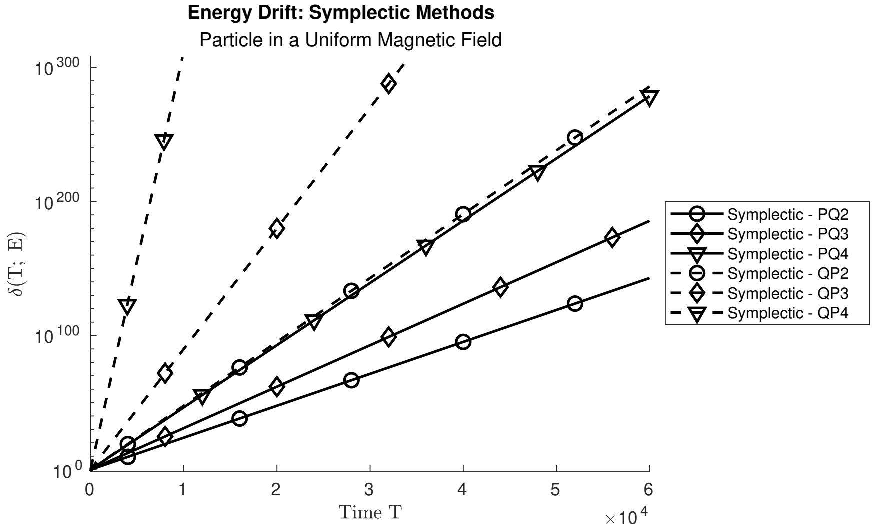

Figure 4.2: Energy drift in Symplectic methods for a particle in a uniform magnetic field. Method coefficient sets are defined in Appendix B.1.3.

4.5 Instantaneous Rotation Matrix Method

4.5.1 Basics

With the failure of both explicit Runge-Kutta methods and standard symplectic methods to conserve the kinetic energy of a particle in a magnetic field, it is clear that additional numerical methods need to be developed for this type of system. As previously stated, the approach used here is to develop a set of methods that take into account the physics of the system. The starting point for developing this new class of methods, hereafter called *Instantaneous Rotation Matrix Methods* (or *IRM Methods*), is to consider the instantaneous solution for a particle in a magnetic field. On a short enough time scale, the magnetic field can be approximated as a constant. Therefore, on this time scale, the solution is that the velocity vector will be rotated around the magnetic field vector by an angle equal to the product of the magnitude of the magnetic field and the step size. This rotation is done by decomposing the velocity into three orthogonal vectors using projection matrices derived from the orientation of the magnetic field.

To begin constructing the projection matrices, define orthogonal vectors $\vec{r}_1$, $\vec{r}_2$, and $\vec{r}_3$ as either

$$\vec{r}_1 = (-\omega_x, -\omega_y, -\omega_z), \tag{4.40a}$$

$$\vec{r}_2 = (\omega_x\omega_z, \omega_y\omega_z, -\omega_x^2 - \omega_y^2), \tag{4.40b}$$

$$\vec{r}_3 = (\omega_y, -\omega_x, 0) \tag{4.40c}$$

or, if $\omega_x^2 + \omega_y^2 = 0$, as

$$\vec{r}_1 = (0, 0, -1), \tag{4.41a}$$

$$\vec{r}_2 = (1, 0, 0), \tag{4.41b}$$

$$\vec{r}_3 = (0, -1, 0). \tag{4.41c}$$

These vectors have the following dot and cross product identities:

$$\vec{r}_i \cdot \vec{r}_j = 0 \text{ if } i \neq j, \tag{4.42a}$$

$$\vec{r}_1 \times \vec{r}_2 = |\vec{r}_1|^2 \vec{r}_3, \tag{4.42b}$$

$$\vec{r}_2 \times \vec{r}_3 = |\vec{r}_3|^2 \vec{r}_1, \tag{4.42c}$$

$$\vec{r}_3 \times \vec{r}_1 = \vec{r}_2, \tag{4.42d}$$

which will be used later. Next, define the series of matrices

$$\bar{\bar{R}}_{ij} = \frac{\vec{r}_i \otimes \vec{r}_j}{|\vec{r}_i||\vec{r}_j|} \tag{4.43}$$

where $\vec{r}_i \otimes \vec{r}_j$ is the outer product between the two vectors. In the case where $i = j$, the resulting matrix is a projection, and, by definition, the sum of all the projection matrices is equal to the identity matrix. Having defined $\vec{r}_1 = -\vec{\omega}$, the change in velocity can be written as

$$\frac{\mathrm{d}\vec{v}}{\mathrm{d}t} = \vec{r}_1 \times \vec{v}. \tag{4.44}$$

Since the magnetic field is assumed to be constant over the interval, the matrices $\bar{\bar{R}}_{ij}$ are also constant, and therefore the relation

$$\frac{\mathrm{d}}{\mathrm{d}t}\left[\sum_{i=1}^{3} \bar{\bar{R}}_{ii}\vec{v}\right] = \sum_{i=1}^{3} \bar{\bar{R}}_{ii}\frac{\mathrm{d}\vec{v}}{\mathrm{d}t} \tag{4.45}$$

can be used to split the force equation into three components.[3] This decomposition of the force yields

$$\bar{\bar{R}}_{11}\frac{\mathrm{d}\vec{v}}{\mathrm{d}t} = \frac{\mathrm{d}\vec{v}_1}{\mathrm{d}t} = \bar{\bar{R}}_{11}\left(\vec{r}_1 \times \vec{v}\right) = 0, \tag{4.46a}$$

---

[3] The requirement for this is that the total time derivative of the matrices is negligible. Additionally, since the result is still in the initial basis, it can be shown that sum of the derivatives must cancel as the derivative of the identity matrix is zero.

$$\bar{\bar{R}}_{22}\frac{\mathrm{d}\vec{v}}{\mathrm{d}t} = \frac{\mathrm{d}\vec{v}_2}{\mathrm{d}t} = \bar{\bar{R}}_{22}\left(\vec{r}_1 \times \vec{v}\right) = -\omega\bar{\bar{R}}_{23}\vec{v}, \tag{4.46b}$$

$$\bar{\bar{R}}_{33}\frac{\mathrm{d}\vec{v}}{\mathrm{d}t} = \frac{\mathrm{d}\vec{v}_3}{\mathrm{d}t} = \bar{\bar{R}}_{33}\left(\vec{r}_1 \times \vec{v}\right) = \omega\bar{\bar{R}}_{32}\vec{v}, \tag{4.46c}$$

where the triple scalar product has been used to remove the cross product. The solution to first order for each velocity component is therefore given by

$$\vec{v}_1(t+\mathrm{d}t) = \bar{\bar{R}}_{11}\vec{v}(t), \tag{4.47a}$$

$$\vec{v}_2(t+\mathrm{d}t) = \bar{\bar{R}}_{22}\vec{v}(t) - \omega\mathrm{d}t\bar{\bar{R}}_{23}\vec{v}(t), \tag{4.47b}$$

$$\vec{v}_3(t+\mathrm{d}t) = \bar{\bar{R}}_{33}\vec{v}(t) + \omega\mathrm{d}t\bar{\bar{R}}_{32}\vec{v}(t). \tag{4.47c}$$

As the known solution for charged particle moving in a static, uniform magnetic field is helical motion, the solution can be re-written as

$$\vec{v}_1(t+\mathrm{d}t) = \bar{\bar{R}}_{11}\vec{v}(t), \tag{4.48a}$$

$$\vec{v}_2(t+\mathrm{d}t) = \left[\cos(\omega\mathrm{d}t)\bar{\bar{R}}_{22} - \sin(\omega\mathrm{d}t)\bar{\bar{R}}_{23}\right]\vec{v}(t), \tag{4.48b}$$

$$\vec{v}_3(t+\mathrm{d}t) = \left[\cos(\omega\mathrm{d}t)\bar{\bar{R}}_{33} + \sin(\omega\mathrm{d}t)\bar{\bar{R}}_{32}\right]\vec{v}(t), \tag{4.48c}$$

such that the full equation for the velocity after a time interval with duration dt is

$$\vec{v}(t+\mathrm{d}t) = \left[\bar{\bar{R}}_{11} + \cos(\omega\mathrm{d}t)\left[\bar{\bar{R}}_{22} + \bar{\bar{R}}_{33}\right] + \sin(\omega\mathrm{d}t)\left[\bar{\bar{R}}_{32} - \bar{\bar{R}}_{23}\right]\right]\vec{v}(t). \tag{4.49a}$$

By integrating the velocity, the change in position is found to be

$$\begin{aligned}\vec{x}(t+\mathrm{d}t) = &\Big[\omega\mathrm{d}t\bar{\bar{R}}_{11} + \sin(\omega\mathrm{d}t)\left[\bar{\bar{R}}_{22} + \bar{\bar{R}}_{33}\right] \\ &\quad + \left[1 - \cos(\omega\mathrm{d}t)\right]\left[\bar{\bar{R}}_{32} - \bar{\bar{R}}_{23}\right]\Big]\frac{\vec{v}(t)}{\omega} + \vec{x}(t).\end{aligned} \tag{4.49b}$$

Using the relation between the projection matrices and the identity matrix, and the fact that $\bar{\bar{R}}_{32} - \bar{\bar{R}}_{23}$ can be reduced to $\bar{\bar{\omega}}/\omega$, the velocity and position equations can be rearranged to read

$$\vec{v}(t+\mathrm{d}t) = \left[\left[1 - \cos(\omega\mathrm{d}t)\right]\bar{\bar{R}}_{11} + \cos(\omega\mathrm{d}t)\bar{\bar{I}} + \frac{\sin(\omega\mathrm{d}t)}{\omega}\bar{\bar{\omega}}\right]\vec{v}(t) \tag{4.50a}$$

and

$$\vec{x}(t+\mathrm{d}t) = \left[\left[\omega\mathrm{d}t - \sin(\omega\mathrm{d}t)\right]\bar{\bar{R}}_{11} + \sin(\omega\mathrm{d}t)\bar{\bar{I}} + \frac{1 - \cos(\omega\mathrm{d}t)}{\omega}\bar{\bar{\omega}}\right]\frac{\vec{v}(t)}{\omega} + \vec{x}(t), \tag{4.50b}$$

respectively. For convenience in the following sections, the matrices $\bar{\bar{M}}$ and $\bar{\bar{M}}'$ can be respectively defined as

$$\bar{\bar{M}}(\vec{\omega}, \mathrm{d}t) = \big[1 - \cos(\omega \mathrm{d}t)\big]\bar{\bar{R}}_{11} + \cos(\omega \mathrm{d}t)\bar{\bar{I}} + \frac{\sin(\omega \mathrm{d}t)}{\omega}\bar{\bar{\omega}}, \tag{4.51a}$$

$$\bar{\bar{M}}'(\vec{\omega}, \mathrm{d}t) = \big[\omega \mathrm{d}t - \sin(\omega \mathrm{d}t)\big]\bar{\bar{R}}_{11} + \sin(\omega \mathrm{d}t)\bar{\bar{I}} + \frac{1 - \cos(\omega \mathrm{d}t)}{\omega}\bar{\bar{\omega}}. \tag{4.51b}$$

4.5.2 Method Construction

Having derived a general solution for an arbitrarily orientated magnetic field that is both uniform and static, methods to solve the equations of motion for a varying field can be derived, keeping in mind that the step size must be small enough so that the field can be approximated as constant over the interval (Section 4.5.3.3).

4.5.2.1 Euler Step Implementations

The simplest implementation of this method is an Euler step type method. In this method there are no intermediate steps, making it relatively fast for a single step. As an added benefit, the position and momentum can be updated simultaneously using (4.50). The disadvantage of this method is that the step size $\mathrm{d}t$ must be set quite small for spatially or temporally varying fields in order to maintain the required approximation.

4.5.2.2 Higher Order Implementations

Higher order methods can be derived with an implementation scheme similar to that used by symplectic methods. The reasoning behind this is that to perform consecutive rotations, the matrices must be multiplied rather than added. This is readily accomplished in the uneven consecutive intermediate points of symplectic methods compared to the averaging of Runge-Kutta methods. However, while the way that the intermediate steps are calculated in symplectic methods is ideal for using rotation matrices, the rotation methods requires using the particle velocity or momentum rather than the canonical momentum.

As with regular symplectic methods, there are two forms that can be used for implementing higher order rotational methods: either the momentum-position form or the position-momentum form. The equations for the intermediate steps in the momentum-position form are

$$\vec{v}_n = \bar{\bar{M}}(\vec{\omega}(\vec{x}_{n-1}, t), P_n \mathrm{d}t)\vec{v}_{n-1} \tag{4.52a}$$

$$\vec{x}_n = \vec{x}_{n-1} + Q_n \vec{v}_n \mathrm{d}t, \tag{4.52b}$$

or

$$\vec{x}_n = \vec{x}_{n-1} + Q_n \vec{v}_{n-1} \mathrm{d}t \tag{4.52c}$$

$$\vec{v}_n = \bar{\bar{M}}(\vec{\omega}(\vec{x}_n, t), P_n \mathrm{d}t) \vec{v}_n \tag{4.52d}$$

for the position-momentum form, where P_n and Q_n are the integration coefficients. The updated velocity will always have the same form:

$$\vec{v}(t + \mathrm{d}t) = \prod_{n=1}^{N} \bar{\bar{M}}_n \vec{v}(t), \tag{4.53}$$

where $\bar{\bar{M}}_n$ is the rotation matrix from the n^{th} step. From an analytical perspective, this will perfectly conserve the energy of the system, however, due to the way that floating point numbers are represented computationally, there can be a small error introduced into the system via truncation of the floating point values. This will be further addressed in 4.5.3 and then shown in 4.5.5.3.

On the other hand, the equation for the updated position depends on the form used, with the momentum-position form yielding

$$\vec{x}(t + \mathrm{d}t) = \vec{x}(t) + \sum_{n}^{N} Q_n \prod_{m=1}^{n} \bar{\bar{M}}_m \vec{v}(t) \mathrm{d}t \tag{4.54a}$$

and the position-momentum form yielding

$$\vec{x}(t + \mathrm{d}t) = \vec{x}(t) + \sum_{n}^{N} Q_n \prod_{m=0}^{n-1} \bar{\bar{M}}_m \vec{v}(t) \mathrm{d}t \tag{4.54b}$$

where $\bar{\bar{M}}_0 = \bar{\bar{I}}$. The advantage of using higher order methods is that the step size can be increased, equivalent to allowing the magnetic field a larger degree of change in the same interval. The disadvantage is that the updated position is no longer given by an exact equation. Before giving examples for this method, error analysis needs to be performed.

4.5.3 Error Analysis and Coefficient Derivation

There are three primary sources of error in the results of this type method: errors from the step size not being small enough (ϵ_I), errors from the truncation of floating point numbers (ϵ_F), and truncation errors from the method order (ϵ_O). While these sources of error are common to all numerical methods and can never be truly eliminated, what needs to be examined is where these errors are occurring and what quantities are effected by them. This will be done here by looking at the velocity and position solutions.

4.5.3.1 Velocity Solution

As mentioned earlier, the solution for the velocity perfectly conserves energy from an analytical perspective. This means that for the motion of a particle in a uniform, static field the velocity solution is also the exact solution. In this case, the only source of error comes from the floating point calculations, in contrast to Runge-Kutta and normal symplectic methods where the energy change is coming from the truncation due to method order. For a floating point value of type *double* (C++) or equivalent, this error should be on the order of $\epsilon_F \approx 2^{-52}$. For systems with spatially or temporally varying fields, the energy is still conserved, but there is now an error in the velocity related to how much the field changes over the interval. Furthermore, there is the question of how time is updated at the intermediate steps: in the methods described by (4.52), time is held constant over the interval. This goes back to the approximation that the magnetic field is constant over the interval and the way that the position and velocity are updated. As such, this type of method should not be blindly applied to systems where there are abrupt, large changes to the field. Instead, such systems could potentially deal with this by adjusting the interval length so that the constant field approximation is still valid over said interval.

4.5.3.2 Position Solution

While the error on the velocity is due entirely to floating point truncation and interval size, the error on the position comes from a combination of these and the truncation error resulting from the method order. The error associated with this last term can be calculated for a uniform, static magnetic field by Taylor expanding the rotation matrices. For a uniform, static magnetic field the product of rotation matrices can be written as

$$\prod_{m=0}^{n} \bar{\bar{M}}\left(\vec{\omega}, P_n \mathrm{d}t\right) = \bar{\bar{M}}\left(\vec{\omega}, \sum_{m=0}^{n} P_m \mathrm{d}t\right), \tag{4.55}$$

where $P_0 = 0$. In order to simplify the analysis, define

$$\mathrm{d}\phi = \omega \mathrm{d}t \tag{4.56a}$$

and

$$\xi_n = \sum_{m=0}^{n} P_m. \tag{4.56b}$$

In momentum-position methods the index of ξ runs from 1 to N, while for position-momentum methods it runs from 0 to $N-1$. The numerical solution for the position in momentum-position methods is therefore

$$\vec{x}(t + \mathrm{d}t) = \vec{x}(t) + \left[\sum_{n=0}^{N} Q_n \bar{\bar{M}}\left(\vec{\omega}, \xi_n \mathrm{d}t\right) \mathrm{d}\phi\right] \frac{\vec{v}(t)}{\omega}. \tag{4.57}$$

Comparing (4.50b) with (4.57) combined with (4.51a) and (4.55) with (4.50a), the following conditions for the coefficients in momentum-position methods are found:[4]

$$\sum_{n=1}^{N} Q_n = 1, \tag{4.58a}$$

$$\sum_{n=1}^{N} P_n = 1, \tag{4.58b}$$

$$\sum_{n=1}^{N} Q_n \cos(\xi_n \mathrm{d}\phi) \mathrm{d}\phi \approx \sin(\mathrm{d}\phi), \tag{4.58c}$$

$$\sum_{n=1}^{N} Q_n \sin(\xi_n \mathrm{d}\phi) \mathrm{d}\phi \approx 1 - \cos(\mathrm{d}\phi). \tag{4.58d}$$

The reason for conditions (4.58c) and (4.58d) being approximations is that the sine and cosine functions can be expanded into an infinite sum, leading to more equations than there are terms. As such, the chosen coefficients should satisfy

$$(2m-1) \sum_{n=1}^{N} Q_n \xi_n^{2m-2} = 1 \tag{4.59a}$$

$$(2m) \sum_{n=1}^{N} Q_n \xi_n^{2m-1} = 1 \tag{4.59b}$$

for as many values of $m > 1$ as possible. After a brief examination of the equations, it can be seen that they can be combined to read

$$m' \sum_{n=1}^{N} Q_n \xi_n^{m'-1} = 1 \tag{4.60}$$

---

[4] The conditions for the position-momentum methods can be found by replacing ξ_n with ξ_{n-1}.

where m' is the order of the term.[5] The lowest value of m' for which the chosen coefficients do not satisfy (4.60) is the order of the error in the position.

4.5.3.3 Temporal Updates

The last item of method construction to be addressed is the size of the time step used in this method. Due to the nature of the position solution in (4.57), the change in phase must be less than one. Furthermore, the ideal step size would be such that all terms in the Taylor expansion of sin and cos after the N^{th} term are effectively zero. This condition on the step size can be expressed as

$$\omega \mathrm{d}t \ll 1. \tag{4.61}$$

A separate condition on the time step comes from (4.45), which requires that the total time derivative of the projection matrices $\bar{\bar{R}}_{ii}$ be negligible:

$$\frac{\mathrm{d}}{\mathrm{d}t}\bar{\bar{R}}_{ii} \approx 0. \tag{4.62}$$

This is equivalent to requiring that the direction of the magnetic field varies over timescales greater than the size of the time step.

4.5.4 IRM Method Coefficients

Next, consider two different types of coefficients: the coefficients from the symplectic momentum-position methods and coefficients derived from (4.60) for the momentum-position form. The advantage of using the symplectic coefficients is that for the second and third order methods the coefficients are rational, thereby reducing the number of floating point errors that enter into the final result. The coefficients derived from (4.60), on the other hand, allow for better accuracy in the position calculations.

4.5.4.1 IRM Methods with Coefficients from Symplectic Methods

The coefficients taken from the symplectic methods are found in Tables B.2a (second order), B.3a (third order), and B.4a (fourth order). These are still referred to as second, third, or fourth order coefficients, as they satisfy (4.60) to that order, as shown in Table 4.2.

4.5.4.2 Derived IRM Method Coefficients

Using (4.60) to derive the coefficients for a two step method results yields a single set of real coefficients, while the three step method has two possible solutions. These

---

[5] The error will never be less than second order, since for $m' = 1$ (4.59) is equal to (4.58a).

(a) Second order		(b) Third order		(c) Fourth order	
m'	$m' \sum_{n=1}^{N} Q_n \xi_n^{m'-1}$	m'	$m' \sum_{n=1}^{N} Q_n \xi_n^{m'-1}$	m'	$m' \sum_{n=1}^{N} Q_n \xi_n^{m'-1}$
1	1	1	1	1	1
2	1	2	1	2	1
3	$\frac{3}{4}$	3	1	3	1
4	$\frac{1}{2}$	4	$\frac{101}{96}$	4	1
5	$\frac{5}{16}$	5	$\frac{475}{432}$	5	$\frac{280-5\cdot 2^{1/3}}{288}$

Table 4.2: Results of (4.60) to fifth order for the coefficients from symplectic methods.

n	Q_n	P_n	ξ_n
1	$\frac{3}{4}$	$\frac{1}{3}$	$\frac{1}{3}$
2	$\frac{1}{4}$	$\frac{2}{3}$	1

Table 4.3: Coefficients for the two step IRM method (IRM2).

are summarized in Tables 4.3 for the two step method and 4.4 for the three step method.

(a) First coefficient solution for the three step method (IRM3a)				(b) Second coefficient solution for the three step method (IRM3b)			
n	Q_n	P_n	ξ_n	n	Q_n	P_n	ξ_n
1	$\frac{16+\sqrt{6}}{36}$	$\frac{4+\sqrt{6}}{10}$	$\frac{4+\sqrt{6}}{10}$	1	$\frac{16-\sqrt{6}}{36}$	$\frac{4-\sqrt{6}}{10}$	$\frac{4-\sqrt{6}}{10}$
2	$\frac{16-\sqrt{6}}{36}$	$-\frac{2\cdot\sqrt{6}}{10}$	$\frac{4-\sqrt{6}}{10}$	2	$\frac{16+\sqrt{6}}{36}$	$\frac{2\cdot\sqrt{6}}{10}$	$\frac{4+\sqrt{6}}{10}$
3	$\frac{4}{36}$	$\frac{6+\sqrt{6}}{10}$	1	3	$\frac{4}{36}$	$\frac{6-\sqrt{6}}{10}$	1

Table 4.4: Coefficients for the three step IRM method.

4.5.5 Test Particle Results

To demonstrate the effectiveness and accuracy of the IRM method, a simple physical scenario will be presented (Section 4.5.5.1), to which the IRM method will be applied with the coefficients detailed in Section 4.5.4. Analysis will look at the resulting numerical energy conservation (Section 4.5.5.3), the difference in phase between the analytical and numerical solution (Section 4.5.5.4), and the displacement between the numerical and analytical solutions (Section 4.5.5.5).

4.5.5.1 Physical Scenario

With the accuracy of an individual step considered, the next step is to look how the total error behaves over time. To do this, the following scenario will be considered: a particle moves through a static, uniform magnetic field, where $\vec{\omega} = \pi/3\ \hat{z}$, with initial (unit-less) momentum $\gamma\vec{v}/c = \sqrt{3}\hat{x}$ and initial (unit-less) position $\gamma\vec{x} = 3 \cdot 3^{1/2}/\pi\ \hat{y}$. In this scenario, the orbital (Larmor) radius, R, of the particle is $R = 3 \cdot 3^{1/2}/\pi$, the orbital period is $T_0 = 6$, and the system is simulated out to $T = 6 \cdot 10^4$. Finally, the time step size used in this example is $\mathrm{d}T = 0.01$, and therefore a single orbit takes 600 steps. The type of floating point variable used is a 64-bit precision floating point variable, equivalent to the *double* variable type in standard *C* and *C++*.

4.5.5.2 Analysis: Theory

In the following subsections, the results of applying the IRM method to the scenario just described will be analyzed. To perform the analysis, first define the general function

$$\delta(T; f) = \frac{f_N(T) - f_A(T)}{f_0} \tag{4.63a}$$

for scalar quantities and

$$\delta(T; \vec{f}) = \frac{\left|\vec{f}_N(T) - \vec{f}_A(T)\right|}{f_0} \tag{4.63b}$$

for vector quantities, where f is the quantity being analyzed as a function of time T. Here, the quantity as calculated by the numerical method $f_N(T)$ is compared to what it should be as per the analytical solution $f_A(T)$. This result is then normalized to some value f_0 intrinsic to the quantity. An example of the use of the scalar function is calculating the energy drift, which is the first quantity that will be examined. In some cases, due to fluctuations in $\delta(T, f)$, the result is averaged over the last period worth of time T_0:

$$\left\langle \delta(T; f) \right\rangle = \frac{1}{T_0} \int\limits_{T-T_0}^{T} \mathrm{d}T\ \delta(T; f). \tag{4.64}$$

This is used in the analysis of the phase drift and solution displacements.

4.5.5.3 Analysis: Energy Conservation and Drift

When considering the energy error (energy drift), the function $\delta(T; E(T))$ can be written as

$$\delta(T; E) = \frac{E(T)}{E_0} - 1, \tag{4.65}$$

where we have used $f_0 = E(T = 0) = E_0$. Alternatively, the function can be expressed as

$$\delta(T; E) = \frac{p^2(T)}{p_0^2} - 1 \tag{4.66}$$

with $p(T)$ being the magnitude of the momentum. While the IRM method conserves energy from an analytical standpoint, numerically there will always be error due to the truncation of floating point values, as can be seen in Figure 4.3.

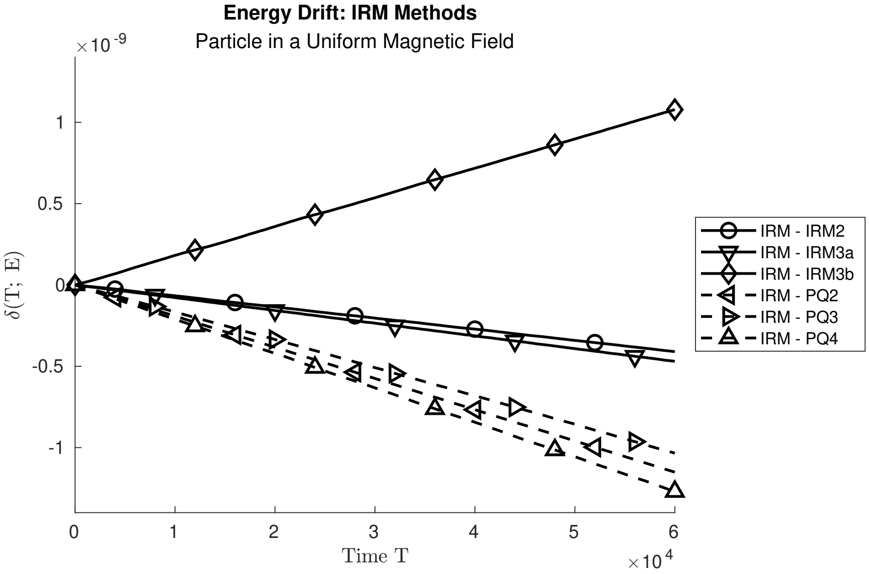

Figure 4.3: Energy drift in the IRM method due to floating point truncation.

4.5.5.4 Analysis: Phase Drift

When considering error in the phase of the solution (phase drift), the position phase needs to be considered separately from the momentum/velocity phase due to how the updates are calculated for each. In general, the change in the momentum phase ϕ_p is a weighted average as per (4.53) and (4.55), while the change in position phase ϕ_x is a result of (4.54). The general error function here is

$$\delta(T;\phi) = \frac{\phi_N(T) - \phi_A(T)}{2\pi} \tag{4.67}$$

where we have chosen to use $f_0 = 2\pi$. This results in (4.67) giving the total number of cycles that the numerical solution is out of phase by.

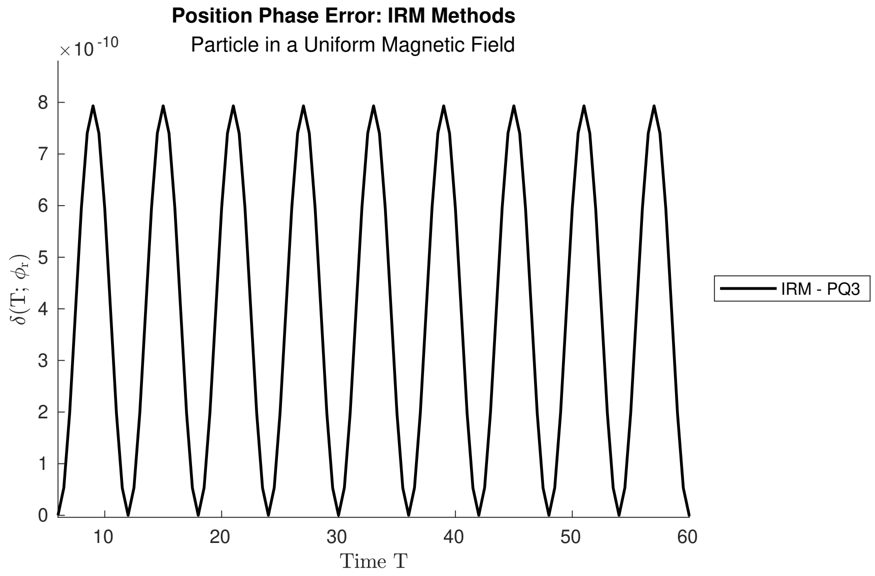

Figure 4.4: Position phase error for coefficients from the third order symplectic method. The phase error continues the oscillations shown here for the entire solution with a constant magnitude.

Figures 4.4 and 4.5 show the position phase error for the three step IRM method with the PQ3 (see Appendix B.1.3.2) and IRM3a (Table 4.4a) coefficient sets, respectively. Figures 4.6 and 4.7 show the period averaged position and momentum phase errors for the coefficient sets listed in Section 4.5.4.2.

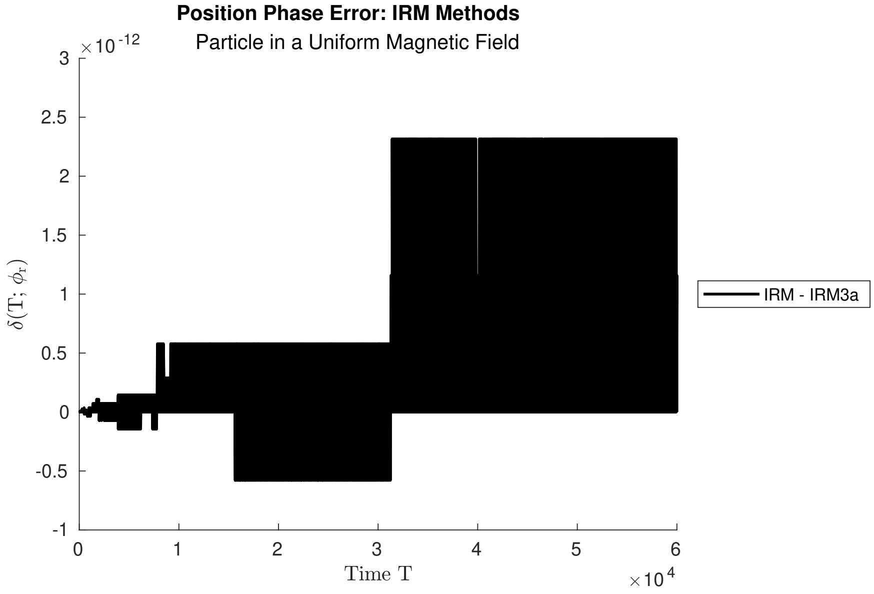

Figure 4.5: Position phase error for IRM3a coefficients.

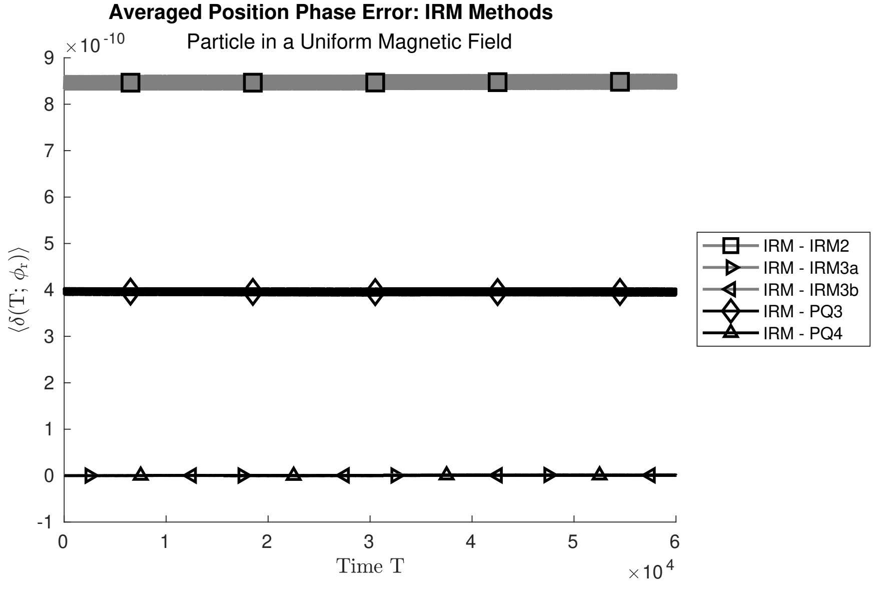

Figure 4.6: Period averaged position phase error for coefficients from Section 4.5.4.2. Not shown is the period averaged position error for the PQ2 coefficient set, which oscillates between $\pm 10^{-8}$. Coefficient sets IRM3a, IRM3b, and PQ4 all have period averaged position phase errors on the order of 10^{-12}.

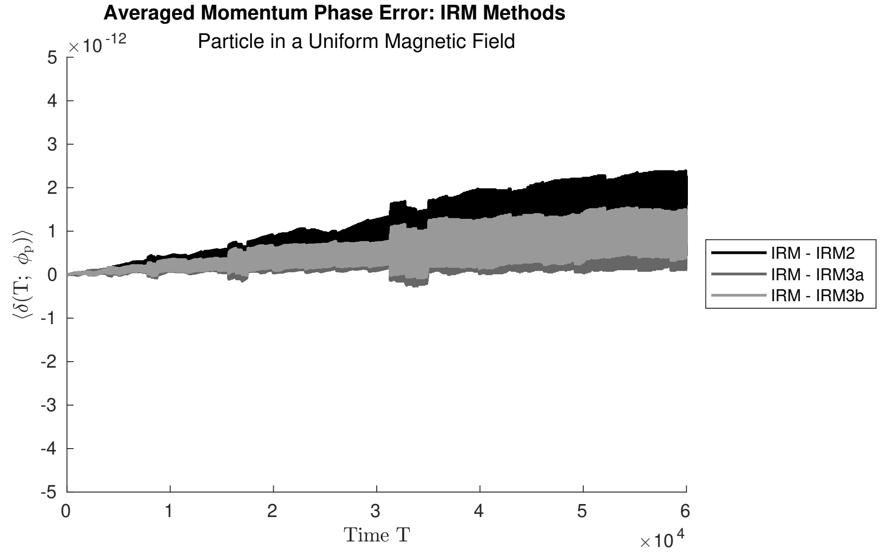

Figure 4.7: Period averaged momentum phase error for coefficients from Section 4.5.4.2. The coefficient sets from the symplectic methods have an average momentum phase error of the same magnitude as the ones in the figure.

4.5.5.5 Analysis: Solution Displacement

The last quantities to be analyzed are the solution displacements: the magnitude of the difference between the numerical solution and correct analytical solution. When analyzing the solution displacements, first consider the form of the position and momentum solutions:

$$\vec{x} = r(T) \begin{bmatrix} \sin\phi(T) \\ \cos\phi(T) \\ 0 \end{bmatrix} \tag{4.68a}$$

and

$$\vec{p} = p(T) \begin{bmatrix} \cos\phi(T) \\ \sin\phi(T) \\ 0 \end{bmatrix}, \tag{4.68b}$$

where $\phi(0) = 0$, $r(T)$ is the Larmor radius, and $p(T)$ is the magnitude of the particle momentum. In the analytical solution $r(T)$ and $p(T)$ are constant, while in the numerical solution they are not necessarily constant, which constitutes an error in the solution. From (4.67), the phase of the numerical solution can be written as

$$\phi_N(T) = \phi_A(T) + 2\pi\delta(T;\phi). \tag{4.69}$$

This allows the error function (4.63b) to be written as

$$\delta(T;\vec{x}) = \sqrt{1 + \frac{r^2(T)}{r_0^2} - 2\frac{r(T)}{r_0}\cos(2\pi\delta(T;\phi_x))} \tag{4.70a}$$

for the position and

$$\delta(T;\vec{p}) = \sqrt{1 + \frac{p^2(T)}{p_0^2} - 2\frac{p(T)}{p_0}\cos(2\pi\delta(T;\phi_p))} \tag{4.70b}$$

for the momentum.

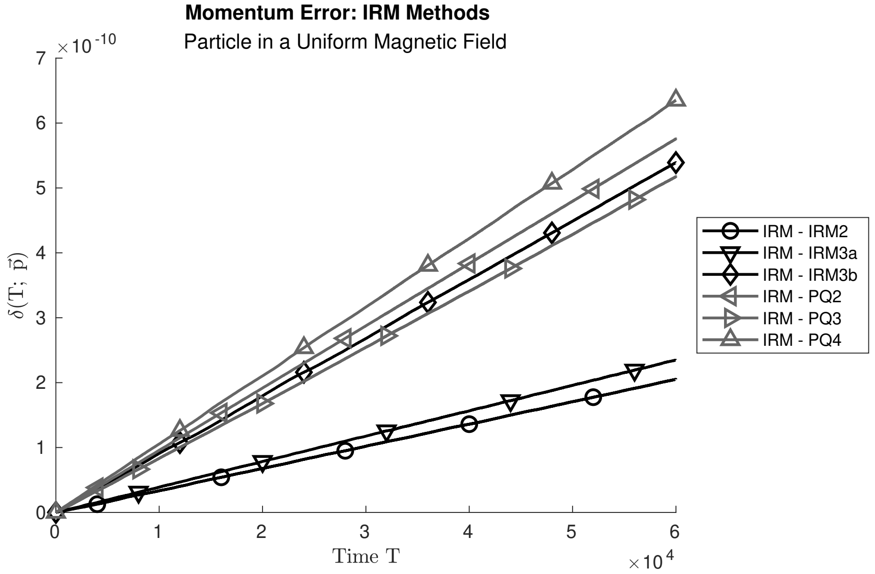

Figure 4.8: Momentum error for all considered coefficient sets.

Given the size of the phase errors shown in the previous section $\cos(2\pi\delta(T;\phi)) \approx 1$, which means (4.70) can be written as

$$\delta(T;\vec{x}) = \left|\frac{r(T)}{r_0} - 1\right| = |\delta(T;r)| \tag{4.71a}$$

and

$$\delta(T;\vec{p}) = \left|\frac{p(T)}{p_0} - 1\right| = |\delta(T;p)| \tag{4.71b}$$

respectively, where $\delta(T;r)$ is the error function for the gyro-radius and $\delta(T;p)$ is the error function for the magnitude of the momentum. Furthermore, the momentum error function can be related to the energy drift function by

$$\delta(T;\vec{p}) = \left|\sqrt{1+\delta(T;E)} - 1\right|. \tag{4.72}$$

Since magnitude of the energy drift is much less than one (Figure 4.3), (4.72) can be Taylor expanded to

$$\delta(T;\vec{p}) = \left|\frac{1}{2}\delta(T;E)\right|. \tag{4.73}$$

Figure 4.8 shows the momentum error for all considered coefficient sets, from which it can be seen that the momentum displacement is roughly half the absolute value of the energy drift, in line with (4.73).

The position error at early times for coefficient set PQ3 in Figure 4.9, while the period averaged position displacement for all considered coefficient sets is shown in Figure 4.10. The oscillatory pattern in Figure 4.9 suggests that the orbital radius oscillates around the correct orbit at half the frequency of the orbital motion for set of physical parameters used.

Figure 4.9: Position error for coefficient set PQ3. The pattern seen here repeats for the entire particle trajectory.

4.6 Comparison to Implicit Methods

Over the years, implicit methods have been developed specifically for particles in electromagnetic fields that analytically conserve energy. A recent review (Ripperda

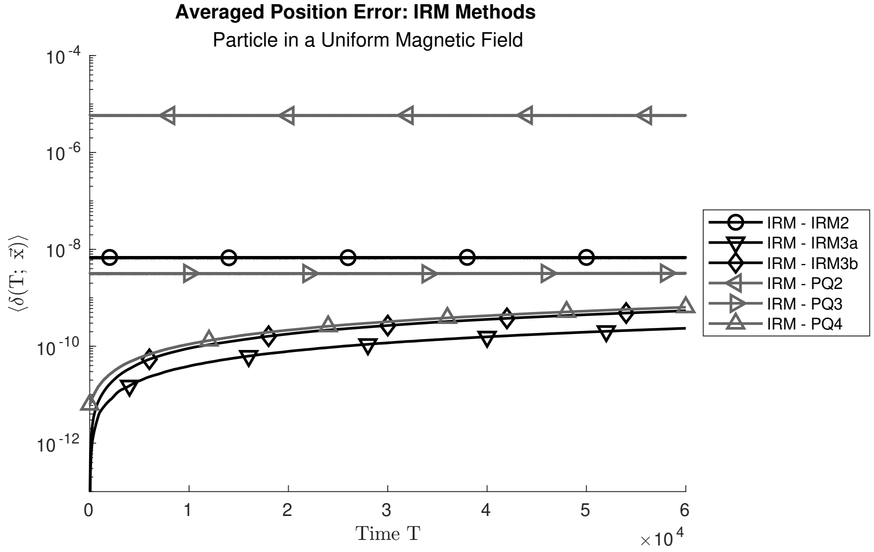

Figure 4.10: Period averaged position error for all considered coefficient sets.

et al., 2018) of these methods considered the resulting trajectories from several implicit methods compared to the results from fourth order RK methods for systems that included both electric and magnetic fields. Here, the second order methods of Boris (1970), Vay (2008), and Higuera and Cary (2017) will be considered in the forms given in Ripperda et al. (2018), although in cgs units instead of SI units.[6]

4.6.1 Analytical Equations for Implicit Methods

As discussed in Ripperda et al. (2018), the form that the considered implicit methods take is as follows:

$$\vec{x}_{n+1/2} = \vec{x}_n + \frac{1}{2}\frac{\vec{u}_n}{\gamma_n}\mathrm{d}t \tag{4.74a}$$

$$\frac{\vec{u}_{n+1} - \vec{u}_n}{\mathrm{d}t} = \frac{q}{m}\left[\vec{E}(\vec{x}_{n+1/2}) + \frac{1}{c}\left\langle\vec{v}\right\rangle \times \vec{B}(\vec{x}_{n+1/2})\right] \tag{4.74b}$$

$$\vec{x}_{n+1} = \vec{x}_{n+1/2} + \frac{1}{2}\frac{\vec{u}_{n+1}}{\gamma_{n+1}}\mathrm{d}t \tag{4.74c}$$

where $\vec{u}$ is the momentum per unit rest mass, given by

$$\vec{u} = \frac{\vec{p}}{m} = \gamma\vec{v}; \tag{4.75}$$

---

[6] The other two implicit methods considered by Ripperda et al. (2018) do not have analytical forms for the change in velocity/momentum.

γ is the Lorentz factor, given by

$$\gamma = \sqrt{1 + \frac{u^2}{c^2}}; \tag{4.76}$$

and $\langle \vec{v} \rangle$ is an average velocity whose form is method dependent. The momentum update is performed by inverting (4.74b), which requires that the average velocity be specified. Since the implicit methods considered here evaluate the fields at $\vec{x}_{n+1/2}$, define

$$\vec{E}_{n+1/2} = \vec{E}(\vec{x}_{n+1/2}) \tag{4.77a}$$

and

$$\vec{B}_{n+1/2} = \vec{B}(\vec{x}_{n+1/2}) \tag{4.77b}$$

to simplify the analysis of the methods.

4.6.1.1 Method of Boris

In the method of Boris (1970), the average velocity formula is

$$\langle \vec{v} \rangle_{Boris} = \frac{\vec{u}_{n+1} + \vec{u}_n}{2\gamma_{n+1/2}}. \tag{4.78}$$

This leads to the following inversion:

$$\vec{u}' = \vec{u}_n + \frac{1}{2}\frac{q\vec{E}_{n+1/2}}{m}\mathrm{d}t \tag{4.79a}$$

$$\vec{u}'' = \vec{u}' + \frac{2}{1 + |\vec{b}|^2}\left[\vec{u}' + (\vec{u}' \times \vec{b})\right] \times \vec{b} \tag{4.79b}$$

$$\vec{u}_n = \vec{u}'' + \frac{1}{2}\frac{q\vec{E}_{n+1/2}}{m}\mathrm{d}t. \tag{4.79c}$$

Here $\vec{b}$ is given by

$$\vec{b} = \frac{1}{2}\frac{q\vec{B}_{n+1/2}}{\gamma' mc}\mathrm{d}t = \frac{1}{2}\frac{\gamma_0}{\gamma'}\vec{\omega}\mathrm{d}t \tag{4.80}$$

where γ_0 is the Lorentz factor evaluated at the initial time, γ' is the Lorentz factor evaluated at $\vec{u}'$, and $\vec{\omega}$ is defined as per (4.7).

In the absence of any electric field, the momentum update for this method can be reduced to

$$\vec{u}_{n+1} = \left[\left[\frac{\frac{1}{2}\omega^2\mathrm{d}t^2}{1 + \frac{1}{4}\omega^2\mathrm{d}t^2}\right]\bar{\bar{R}}_{11} + \left[\frac{1 - \frac{1}{4}\omega^2\mathrm{d}t^2}{1 + \frac{1}{4}\omega^2\mathrm{d}t^2}\right]\bar{\bar{I}} + \left[\frac{\omega\mathrm{d}t}{1 + \frac{1}{4}\omega^2\mathrm{d}t^2}\right]\frac{\bar{\bar{\omega}}}{\omega}\right]\vec{u}_n, \tag{4.81}$$

where ω is defined per (4.7) and evaluated at $\vec{x}_{n+1/2}$. As the energy is conserved by (4.81), γ can be removed from the equations by absorbing it into $\vec{\omega}$ and $\vec{x}$. This is the form that will be used in comparisons to the IRM method.

4.6.1.2 Method of Vay

The average velocity formula for the method of Vay (2008) is

$$\langle\vec{v}\rangle = \frac{1}{2}\left[\frac{\vec{u}_n}{\gamma_n} + \frac{\vec{u}_{n+1}}{\gamma_{n+1}}\right], \tag{4.82}$$

for which the inversion of (4.74b) is

$$\vec{u}' = \vec{u}_n + \frac{q\vec{E}_{n+1/2}}{m}\mathrm{d}t + \vec{u}_n \times \frac{q\vec{B}_{n+1/2}}{\gamma_n mc}\frac{\mathrm{d}t}{2} \tag{4.83a}$$

$$\vec{u}_{n+1} = \frac{1}{1+|\vec{b}|^2}\left[\vec{u}' + (\vec{u}'\cdot\vec{b})\vec{b} + \vec{u}' \times \vec{b}\right]. \tag{4.83b}$$

The additional quantities required in these equations are

$$\vec{a} = \frac{1}{2}\frac{q\vec{B}_{n+1/2}}{mc}\mathrm{d}t = \frac{1}{2}\gamma_0\vec{\omega}\mathrm{d}t; \tag{4.84a}$$

$$\gamma' = \sqrt{1 + \left[\frac{\vec{u}'}{c}\right]^2}; \tag{4.84b}$$

$$\sigma = (\gamma')^2 - |\vec{a}|^2; \tag{4.84c}$$

$$\gamma_{n+1} = \sqrt{\frac{\sigma}{2} + \sqrt{\frac{\sigma^2}{4} + \left[|\vec{a}|^2 + \left[\frac{\vec{u}'\cdot\vec{a}}{c}\right]^2\right]}}; \tag{4.84d}$$

$$\vec{b} = \frac{1}{\gamma_{n+1}}\vec{a} = \frac{1}{2}\frac{\gamma_0}{\gamma''}\vec{\omega}\mathrm{d}t. \tag{4.84e}$$

For pure magnetic systems, γ_{n+1} reduces to γ_n, and the equations for $\vec{u}_{n+1}$ can be reduced to

$$\vec{u}_{n+1} = \left[\left[\frac{\frac{1}{2}\omega^2\mathrm{d}t^2}{1+\frac{1}{4}\omega^2\mathrm{d}t^2}\right]\bar{\bar{R}}_{11} + \left[\frac{1-\frac{1}{4}\omega^2\mathrm{d}t^2}{1+\frac{1}{4}\omega^2\mathrm{d}t^2}\right]\bar{\bar{I}} + \left[\frac{\omega\mathrm{d}t}{1+\frac{1}{4}\omega^2\mathrm{d}t^2}\right]\frac{\bar{\bar{\omega}}}{\omega}\right]\vec{u}_n, \tag{4.85}$$

which is exactly the same as the method of Boris. The difference therefore between the method of Boris and the method of Vay is in how they are implemented and how they handle the electric field.

4.6.1.3 Method of Higuera-Cary

In the method of Higuera and Cary (2017), the average velocity is

$$\langle \vec{v} \rangle = \frac{\vec{u}_n + \vec{u}_{n+1}}{2\sqrt{1 + \left|\frac{\vec{u}_n + \vec{u}_{n+1}}{2c}\right|^2}} \tag{4.86}$$

and the resulting inversion is[7]

$$\vec{u}' = \vec{u}_n + \frac{1}{2}\frac{q\vec{E}_{n+1/2}}{m}\mathrm{d}t \tag{4.87a}$$

$$\vec{u}'' = \frac{1}{1 + |\vec{b}|^2}\left[\vec{u}' + (\vec{u}' \cdot \vec{b})\vec{b} + \vec{u}' \times \vec{b}\right] \tag{4.87b}$$

$$\vec{u}_{n+1} = \vec{u}'' + \frac{1}{2}\frac{q\vec{E}_{n+1/2}}{m}\mathrm{d}t + \vec{u}'' \times \vec{b}. \tag{4.87c}$$

The additional quantities required in this method are

$$\vec{a} = \frac{1}{2}\frac{q\vec{B}_{n+1/2}}{mc}\mathrm{d}t = \frac{1}{2}\gamma_0\vec{\omega}\mathrm{d}t; \tag{4.88a}$$

$$\gamma' = \sqrt{1 + \left[\frac{\vec{u}'}{c}\right]^2}; \tag{4.88b}$$

$$\sigma = (\gamma')^2 - |\vec{a}|^2; \tag{4.88c}$$

$$\gamma'' = \sqrt{\frac{\sigma}{2} + \sqrt{\frac{\sigma^2}{4} + \left[|\vec{a}|^2 + \left[\frac{\vec{u}' \cdot \vec{a}}{c}\right]^2\right]}}; \tag{4.88d}$$

$$\vec{b} = \frac{1}{\gamma''}\vec{a} = \frac{1}{2}\frac{\gamma_0}{\gamma''}\vec{\omega}\mathrm{d}t. \tag{4.88e}$$

In pure magnetic systems, the equations for $\vec{u}_{n+1}$ reduce to

$$\vec{u}_{n+1} = \left[\left[\frac{\frac{1}{2}\alpha^2\omega^2\mathrm{d}t^2}{1 + \frac{1}{4}\alpha^2\omega^2\mathrm{d}t^2}\right]\bar{\bar{R}}_{11} + \left[\frac{1 - \frac{1}{4}\alpha^2\omega^2\mathrm{d}t^2}{1 + \frac{1}{4}\alpha^2\omega^2\mathrm{d}t^2}\right]\bar{\bar{I}} + \left[\frac{\alpha\omega\mathrm{d}t}{1 + \frac{1}{4}\alpha^2\omega^2\mathrm{d}t^2}\right]\frac{\bar{\bar{\omega}}}{\omega}\right]\vec{u}_n, \tag{4.89}$$

---

[7] The author suspects that there is a typo in Ripperda et al. (2018) in the equation for $\vec{u}_{n+1}$ (equation 21 in Ripperda et al. (2018)), as energy is not conserved for pure magnetic systems for the equations in Ripperda et al. (2018). The equations as listed here do conserve energy in pure magnetic systems.

where α is given by

$$\alpha = \frac{\gamma}{\gamma''} = \left[\frac{\left[1 - \frac{1}{4}\omega^2 \mathrm{d}t^2\right] + \sqrt{\left[1 + \frac{1}{4}\omega^2 \mathrm{d}t^2\right]^2 - \left[\frac{\vec{u}_n \times \vec{\omega}}{\gamma c}\mathrm{d}t\right]^2}}{2} \right]^{-1/2} \tag{4.90}$$

and $\gamma = \gamma_n = \gamma_{n+1}$. The form of the solution is similar to that of Boris and Vay, however the effective rotation angle is altered, which changes the period of rotation, although the energy of the particle is still conserved. If γ'' is externally set to one, the result is identical to that of Boris and Vay, meaning that any differences in results come from the implementation of the method.

4.6.2 Analysis of Implicit Method Results

4.6.2.1 Implicit Method Energy Conservation

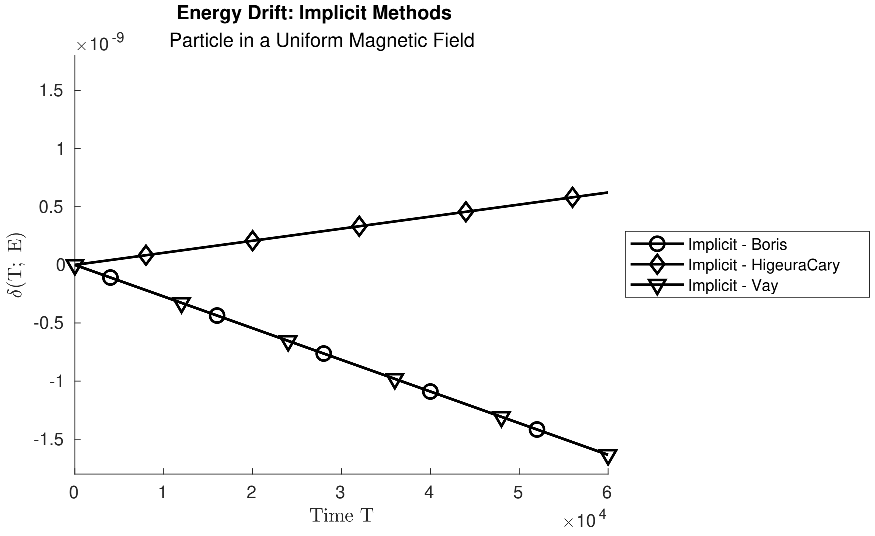

Figure 4.11: Energy drift in Implicit methods for a particle in a uniform magnetic field.

While the considered implicit methods conserve energy analytically, when actually running the calculations numerically there will always be errors due to floating point truncation, as shown in Figure 4.11. Differences between the results here and those in Ripperda et al. (2018) are due to how the method was implemented: the results here are from using (4.81) and (4.89). The energy drift is calculated as per (4.65).

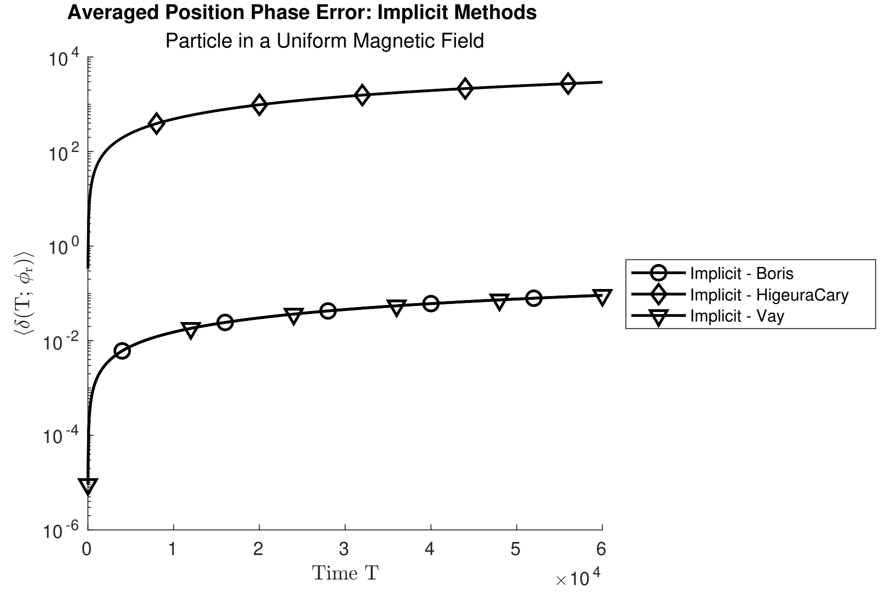

Figure 4.12: Position phase lag in Implicit methods for a particle in a uniform magnetic field.

4.6.2.2 Implicit Method Phase Error

As the equations for the momentum updates in the implicit methods are not true rotation matrices but rather approximations of them, the phase is not expected to be completely accurate. Figures 4.12 and 4.13 show the resulting error in ϕ for both the position and the momentum.

The Boris and Vay methods have a relatively small phase drift, being less than one rotation out of phase after 10^4 cycles for the given input parameters. The Higuera-Cary method, on the other hand, is drastically out of phase with the analytical solution, due to the modified rotation angle. It is important to note that for the given parameters, the particle rotates counter-clockwise, and therefore ϕ is a decreasing function. This means that a positive phase error corresponds to the numerical solution lagging behind the analytical solution.

4.7 Conclusions

Having shown that neither Runge-Kutta nor basic symplectic integration schemes can conserve the kinetic energy of a charged particle in a magnetic field, the *Instantaneous Rotation Matrix Method* (*IRM Method*) is introduced and described. Analysis of the new method using a uniform, static magnetic field reveals that, for a

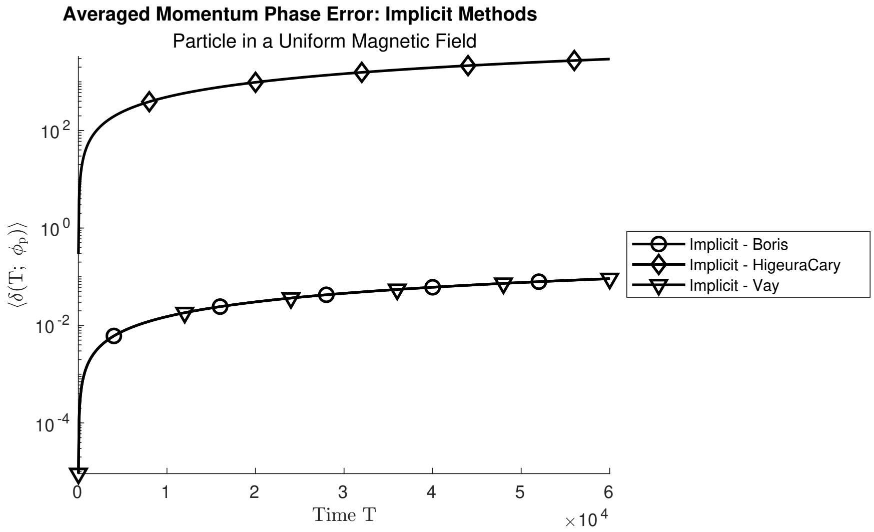

Figure 4.13: Momentum phase lag in Implicit methods for a particle in a uniform magnetic field.

given step size, the IRM method conserves energy (Figure 4.3) better than common Runge-Kutta fourth order methods (Figure 4.1). Furthermore, compared to common adaptive fourth order Runge-Kutta methods (see Appendix A), the three step *IRM* method still performs better with a constant step size as the adaptive method require six or more intermediate steps to calculate the updated trajectory points compared to the three steps required by the *IRM* method. To match the total number of field evaluations required, adaptive methods would have to on average use double the step size, which would have the effect of increasing the energy drift by a factor of at least 32 based on the equations in Appendix A.[8] Conversely, to obtain a similar error adaptive Runge-Kutta methods would need to settle on a time step that is smaller than that used in the *IRM* method, which would mean that the total number of field evalulations for the Runge-Kutta method would be more than double that of *IRM* method.

Also considered were several implicit methods, which conserve the kinetic energy. For pure magnetic systems, these methods are similar to the IRM method in that the momentum update has a similar form and the particle energy is analytically conserved. Figure 4.14 shows the energy drift of the IRM method as compared to the implicit methods and Runge-Kutta methods of Dormand and Prince (1980) and

---

[8] Based on the assumption of a uniform distribution of step sizes around the average. In this case the energy drift could increase by as much as a factor of 585.

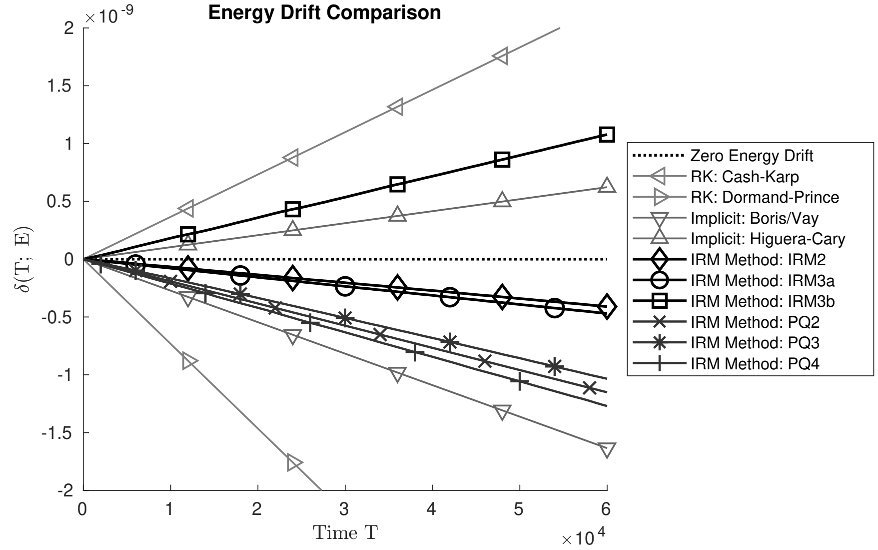

Figure 4.14: Comparison of the energy drift between the Runge-Kutta, Implicit, and IRM methods using a constant step size.

Cash and Karp (1990). Implicit methods, however, use an approximation of an actual rotation matrix, meaning that the phase of the numerical solution drifts away from the analytical solution phase (see Figures 4.12 and 4.13). In constrast, the IRM method conserves the phase to a much higher accuracy, with the phase drift primarily occurring in the position (Figure 4.6), not the momentum (Figure 4.7). Therefore it can be concluded that the IRM method is superior to both Runge-Kutta methods and implicit methods for a particle in a magnetic field.

Acknowledgements

Support by the Natural Sciences and Engineering Research Council (NSERC) of Canada is acknowledged. I would also like to thank Dr. Andreas Shalchi and Lawrence Arendt, P. Eng., for their feedback on the written content of this article, and Dr. Jason Fiege for discussions regarding the method concepts.

List of Corrections

The following is a list of corrections made when reproducing Arendt (2023):

- Fixed caption for Table 4.4b: designation of coefficient set is IRM3b, not IRM3a.
- Fixed **Implicit Method Phase Error** (4.6.2.2) so that it is a sub-sub-section.

- Fixed the caption on Figure 4.3: it is floating point *truncation* not floating point *trunction*.
- Fixed a typo in Section 4.5.5.2 where the word “method” was missing in “numerical method”.
- Removed the final sentence from Appendix B.1.2.2 as it was redundant.

Chapter 5

ACEPTS

In order to perform the particle trajectory simulations discussed in Chapter 6, a *C++* program was developed to generate magnetic turbulence based on parameters contained in an input file and then propagate particles through this turbulence. Named the *Astrophysical Charged Energetic Particle Transport Simulator* or *ACEPTS*, the program takes advantage of several aspects of object orientated programming to allow the equations used in the program to appear almost exactly as they would if written normally. Combined with object inheritance, this allows for easier modification of the code should changes need to be made, such as adding in additional turbulence models.[1]

A single ACEPTS simulation consists of a group of particles moving through a turbulent magnetic field. As particle–particle interactions are ignored, particles are simulated sequentially. A *data set* is a collection of simulations run in parallel, each with the same inputs but different realizations of the magnetic field. A *parameter set* is a collection of data sets with the same physical parameters such as the turbulence energy density or particle rigidity, but different internal parameters such as the number and range of wave modes or the maximum simulation time. Described in this chapter are the methods used to numerically represent the magnetic field, calculate the particle trajectories, and analyze the results.

---

[1] Simulation source code available by contacting the author at arendtv.physics@gmail.com

5.1 Numerical Representation of Turbulence

As already discussed in Chapter 2.1, the models of turbulence considered in this work are defined in Fourier space via a spectral tensor and spectral function. Analytically, the magnetic field is defined by (2.4), which can also be expressed as

$$\vec{B}(\vec{x},t) = B_0\hat{z} + \int \mathrm{d}^3k\, \tilde{A}(\vec{k},t)\hat{\delta B}(\vec{k},t)e^{i\vec{k}\vec{x}} \tag{5.1}$$

where $\tilde{A}(\vec{k},t)$ is the complex amplitude associated with wave vector $\vec{k}$ and $\hat{\delta B}(\vec{k})$ is the orientation vector of the wave field. Given that the magnetic field needs to be real at all points in physical space and that the turbulence is axi–symmetric in Fourier space, the complex amplitude and orientation vector must satisfy the following relations:

$$\tilde{A}(\vec{k},t) = \tilde{A}(k_z,k_r,t) \qquad \text{axi–symmetry,} \tag{5.2a}$$

$$\tilde{A}(-\vec{k},t)\hat{\delta B}(-\vec{k},t) = \pm\tilde{A}^{\dagger}(\vec{k},t)\hat{\delta B}(\vec{k},t) \qquad \text{real valued.} \tag{5.2b}$$

With these relations, the integral defining the turbulence can be expressed as

$$\begin{aligned}&\int \mathrm{d}^3k\, \tilde{A}(\vec{k},t)\hat{\delta B}(\vec{k},t)e^{i\vec{k}\vec{x}}\\ &\quad= \frac{1}{2}\int \mathrm{d}^3k\, \left[\tilde{A}(\vec{k},t)\hat{\delta B}(\vec{k},t)e^{i\vec{k}\vec{x}} \pm \tilde{A}^{\dagger}(\vec{k},t)\hat{\delta B}(\vec{k},t)e^{-i\vec{k}\vec{x}}\right].\end{aligned} \tag{5.3}$$

As a complex scalar, $\tilde{A}(\vec{k},t)$ can be expressed as

$$\tilde{A}(\vec{k},t) = A(\vec{k},t)e^{i\phi(\vec{k})} \tag{5.4}$$

where $\phi(\vec{k})$ is the angle between the real and imaginary components and $A(\vec{k},t)$ is the absolute value of the amplitude. The turbulence can therefore be expressed either

$$\vec{\delta B}(x,t) = \int \mathrm{d}^3k\, A(\vec{k},t)\hat{\delta B}(\vec{k},t)\cos(\vec{k}\vec{x}+\phi(\vec{k})) \tag{5.5a}$$

or

$$\vec{\delta B}(x,t) = \int \mathrm{d}^3k\, A(\vec{k},t)\hat{\delta B}(\vec{k},t)\sin(\vec{k}\vec{x}+\phi(\vec{k})). \tag{5.5b}$$

It should be noted that the only requirement on the angle $\phi(\vec{k})$ is that $\phi(\vec{k}) = \phi(-\vec{k})$ in order to satisfy (5.2b). Once the field is written using either (5.5a) or (5.5b), $\phi(\vec{k})$

can be given by a random value, such that $\phi(\vec{k}_1)$ and $\phi(\vec{k}_2)$ are completely unrelated.

5.1.1 Numerical Fourier Transforms

When using a superposition of waves to create synthetic turbulence numerically, there are two general approaches, each with its own advantages and disadvantages. The approach that most people would be familiar with is to use a *Fast Fourier Transform* (*FFT*), which uses (5.1) as its starting point. In this approach, the wave modes in each direction are evenly spaced with

$$\Delta k_i = \frac{2k_{i,max}}{N_i - 1} \tag{5.6a}$$

for waves modes running from $-k_{i,max}$ to $k_{i,max}$ or

$$\Delta k_i = \frac{k_{i,max}}{N_i - 1} \tag{5.6b}$$

for wave modes running from 0 to $k_{i,max}$, where N_i is the number of wave modes along axis i. Once both the grid of wave numbers and wave amplitudes have been created, the FFT algorithm is used to switch from Fourier space to physical space, and the field is then found by interpolating between points. The advantage of this method is clear: the transformation from Fourier space to physical space needs to only be performed once and calculation of the field at a given location can occur quickly by interpolation. On the other hand, the disadvantage comes from the number of wave modes needed to properly represent the turbulence.

Consider the maximum wave number required: large wave numbers represent small physical scales, and therefore any interaction with the particles moving through the turbulence will be noticeable sooner and have a greater overall effect. Ergo, the question that needs be asked is: “How large a wave number is needed?”, and the answer can be found by considering the wave spectrum (see Chapter 2.1, Figure 2.2). Figure 5.1 shows the integral of the spectrum from 0 to k, from which it is easy to see that the majority of the turbulence energy is in waves with wave numbers between 10^{-3} and 10^4. When using a FFT this presents a problem: the smallest wave number is equal to both the wave spacing and the inverse of the length of the ‘box’ the particles are contained in. Using a maximum wave number of 10^4 and a wave spacing of 10^{-3} would require 10^7 waves along one axis and the ‘box’ length would be 10^3 length units. Increasing the ‘box’ length to 10^5 ($\Delta k = 10^{-5}$) would require 10^9

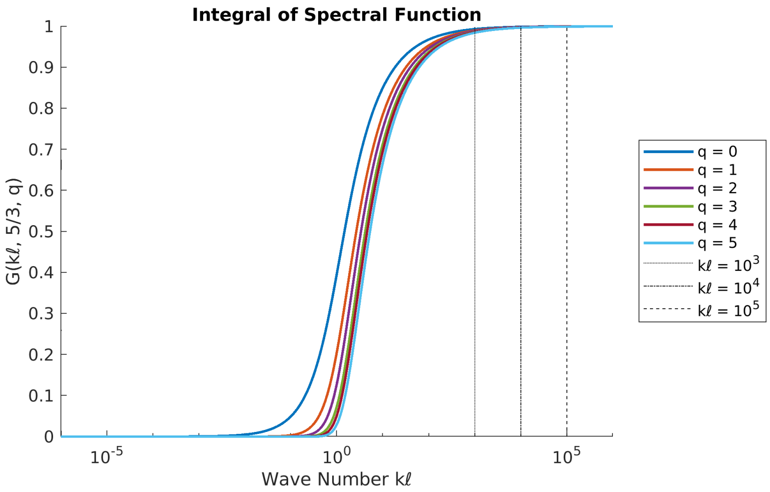

Figure 5.1: Integral of the power law spectrum from 0 to k, using $s = 5/3$ and integer values of q. For odd values of q, the integral was calculated using (2.20); for even values of q, the method described in Section 5.1.4.1 was used.

wave modes per axis (10^{27} wave modes for the full 3D model).[2] If the wave modes are stored as standard 8 byte floating point types (*C, C++ double*), using the slab model with 10^9 wave modes requires approximately 22.4 gigabytes of memory for the array of wave modes and associated amplitudes.[3] While this may not seem like much for modern HPC facilities, the memory listed is per instance of the simulation; if multiple instances of the the simulation are run at once with each simulation having a unique field configuration, multiple allocations of memory will be required.

The second approach, initially formulated by Giacalone and Jokipii (1999), is to represent the field using logarithmically spaced wave modes, calculating the field at the particle position exactly rather than via interpolation. The advantages and disadvantages of this method are opposite that of the FFT and interpolation method: the memory requirements are drastically lower but the computation time is increased. The turbulence field in this method is calculated using the discrete version of (5.5a) or (5.5b). While both forms are equivalent, the discrete version of (5.5a) is the form

---

[2] Reduced dimensional or noisy full dimensional models (ie: the noisy slab model) can ignore wave modes for which the spectrum is zero, thereby reducing the required number of wave modes.

[3] The slab model has the minimum memory requirements. Since the wave modes are only along the z axis and the field is confined to the xy-plane; all three quantities (k, δB_x, δB_y) can be represented as one dimensional arrays.

that is used in this work. The turbulence is therefore calculated using

$$\delta\vec{B}(\vec{x}) = \sum_{n=0}^{N-1} A_n \delta\hat{B}_n \cos(\vec{k}_n \vec{x} + \phi_n) \tag{5.7a}$$

for reduced dimensional models and

$$\delta\vec{B}(\vec{x}) = \sum_{n=0}^{N-1} \sum_{m=0}^{M-1} A_{nm} \delta\hat{B}_{nm} \cos(\vec{k}_{nm} \vec{x} + \phi_{nm}) \tag{5.7b}$$

for full dimensional models.[4]

5.1.2 Wave Number Range

There are two mathematically equivalent ways to calculate logarithmically spaced waves numbers. The first method (see Hussein et al. (2015) for example) is

$$k_n = k_{min}\, e^{\frac{n}{N-1} \log\left(\frac{k_{max}}{k_{min}}\right)} \tag{5.8}$$

where N is the total number of waves being used and n is the wave index running from 0 to $N-1$. The spacing between the wave numbers is

$$\Delta k_n = \begin{cases} \mathrm{d}k_n^+ = k_{n+1} - k_n = k_n\,(c-1) & \text{(forward spacing)} \\ \mathrm{d}k_n^- = k_n - k_{n-1} = k_n\left(1 - c^{-1}\right) & \text{(reverse spacing)} \end{cases} \tag{5.9}$$

where

$$c = e^{\frac{1}{N-1} \log\left(\frac{k_{max}}{k_{min}}\right)}. \tag{5.10}$$

The alternative method is to rearrange c so that

$$c = \left[\frac{k_{max}}{k_{min}}\right]^{\frac{1}{N-1}} \tag{5.11}$$

and

$$k_n = k_{min} \left[\frac{k_{max}}{k_{min}}\right]^{\frac{n}{N-1}}. \tag{5.12}$$

A variation of (5.12), given by

$$k_n = k_{min} 10^{\frac{n}{N-1}}, \tag{5.13}$$

---

[4] Since the models described in Chapter 2.2 are all static, the time component has been left out of the equation here.

is useful when the range of wave numbers needs to be extended while holding constant the number of waves per order of magnitude. In this case N is the number of waves per decade (order of magnitude), and $k_{n+N-1} = 10k_n$. If the minimum and maximum wave numbers are held constant, (5.13) will result in only one additional wave mode compared to (5.12).

5.1.2.1 Minimum Wave Number: Box Size

As mentioned in the introduction to this section, the size of the box the particles are in is proportional to the inverse of the smallest wave number when using a FFT. This is because all wave numbers are integer multiples of this value. When using logarithmically spaced wave numbers, however, any two consecutive wave numbers will in general not be integer multiples of each other. Consider (5.9): if $k_n \Delta x = 2\pi m$, where m is some integer then $k_{n+1}\Delta x = 2\pi mc$. Unless c is a rational number, there is no distance Δx at which all waves will be in the same phase at points x and $x \pm \Delta x$. Therefore, there is no true boundary to the box. In the simulation results presented in this work the minimum wave number was set to $k_0 = 10^{-5}$ in order to provide large scale structure to the turbulence and be consistent with earlier works such as Hussein et al. (2015).

5.1.2.2 Maximum Wave Number

While increasing the maximum wave number does not cause the same drastic increase in array size and associated memory usage in a logarithmic spacing scheme as it would in a linear one, there is still the question of how large does the maximum wave number need to be. To begin with, consider the particle rigidity $\vec{R}$: to first order, the change in position is given by

$$\Delta\vec{X} = \vec{R}\mathrm{d}T, \tag{5.14}$$

meaning that the change in the phase of any given wave in the field is

$$\frac{\mathrm{d}\phi}{\mathrm{d}T} = \vec{k}\vec{R}. \tag{5.15}$$

As such, the waves that meaningfully contribute to any change in the magnetic field are those that have a component parallel to the direction of motion and for which $\vec{k}\vec{R}$ is not negligible. This means that, at minimum, the magnitude of the maximum wave vector should be

$$k_{max} \geq 1/R. \tag{5.16}$$

At the same time, there is also the resonance condition from (3.64) to take into consideration. With this condition, the maximum parallel wave number needs to follow

$$k_{\|,max} \geq \frac{1}{R|\mu|}. \tag{5.17}$$

Unfortunately, μ is a continuous variable; however, it needs to be kept in mind that the resonance condition was derived using QLT, which does not accurately calculate the parallel and perpendicular diffusion coefficients. There is also the spectrum of the turbulence to consider: for wave numbers with $k_p \ell_p \gg 1$, where k_p is the primary wave component for the model and ℓ_p the associated length scale (see 5.1.4 for a definition), the spectrum follows (2.18) which goes to zero as the wave number goes to infinity. Therefore, it should be expected that at some value there isn't enough energy in the waves the particle is resonating with to have a discernible effect on the particle orbit. That said, the key words here are 'discernible effect': just because there is no *immediately* discernible effect doesn't mean that there isn't a *cumulative* effect resulting from multiple interactions. As such, while it is much easier to use a common minimum wave number, the maximum wave number required needs to be verified as other parameters are changed.

5.1.3 Calculating Wave and Field Unit Vectors

In Tautz and Dosch (2013), a method for generating isotropically distributed wave vectors was described. In this method the orientation is a function of two quantities: η, the cosine of the angle between the wave vector and the z axis; and ϕ, the angle from the x axis. The wave vector is then constructed by the equation

$$\vec{k}_n = k_n \begin{bmatrix} \sqrt{1-\eta_n^2}\cos k_{\phi n} \\ \sqrt{1-\eta_n^2}\sin k_{\phi n} \\ \eta_n \end{bmatrix} \tag{5.18}$$

where k_n is the magnitude of the wave vector. To achieve an isotropic distribution, the values of η and ϕ are each taken from a uniform random distribution given by

$$-1 \leq \eta_n \leq 1 \tag{5.19a}$$

and

$$0 \leq k_{\phi n} < 2\pi. \tag{5.19b}$$

The equation for the field unit vector $\hat{\delta B}$ associated with the wave vector $\vec{k}$ is

$$\hat{\delta B}_n = \begin{bmatrix} -\sin k_{\phi n} \\ \cos k_{\phi n} \\ 0 \end{bmatrix} \cos \alpha_n + \begin{bmatrix} \eta_n \cos k_{\phi n} \\ \eta_n \sin k_{\phi n} \\ -\sqrt{1-\eta_n^2} \end{bmatrix} \sin \alpha_n \tag{5.20}$$

where α_n is a model dependent angle. Non-isotropic distributions can be obtained by changing either the distribution range or the distribution shape, or a combination of the two. Comparing this to the turbulence wave vectors in Chapter 2, it can be seen that

$$k_{\parallel n} = k_n \eta_n \tag{5.21a}$$

and

$$k_{\perp n} = k_n \sqrt{1-\eta_n^2}. \tag{5.21b}$$

The method used in ACEPTS to generate the field unit vectors is similar to that just described, except rather than a general set of equations used by all models, the generation mechanism has been tailored for each model. This is done by taking advantage of various aspects of object orientated programming, specifically the use of object inheritance and function overloading.

As the field is confined to the xy plane in incompressible turbulence, $\alpha = 0$ and therefore $\hat{\delta B}_n$ can be written as

$$\hat{\delta B}(\vec{k}) = \frac{\vec{k} \times \hat{z}}{k_\perp} = \hat{k}_\perp \times \hat{z}, \tag{5.22}$$

which is how the field unit vector is calculated in ACEPTS. The exception to this is the slab model as the wave modes are parallel to the mean field. In this case either (5.20) or

$$\hat{\delta B}_n = \begin{bmatrix} \cos k_{\phi n} \\ \sin k_{\phi n} \\ 0 \end{bmatrix} \tag{5.23}$$

can be used, with the angle in the later being equal to the former plus a shift of $-\pi/2$.

5.1.4 Turbulence Amplitude Calculations

The final component in the creation of turbulence is the calculation of the field amplitude. To derive an equation for the amplitude, first consider the magnetic correlation tensor (2.2) for both the analytical (2.4) and numerical (5.7) forms of the turbulence:[5]

$$R^A_{ml}(\vec{x},\vec{x}_0) = \Big\langle \int \mathrm{d}^3k \int \mathrm{d}^3k' \, \delta\tilde{\vec{B}}_m(\vec{k})\delta\tilde{\vec{B}}^\dagger_l(\vec{k}')e^{i\left[\vec{k}\vec{x}-\vec{k}'\vec{x}_0\right]}\Big\rangle, \tag{5.24a}$$

$$R^N_{ml}(\vec{x},\vec{x}_0) = \Big\langle \sum_n \sum_{n'} A_n A_{n'} \delta\vec{B}_{m,n}\delta\vec{B}_{l,n'} \cos(\vec{k}_n\vec{x}+\phi_n)\cos(\vec{k}_{n'}\vec{x}_0+\phi_{n'})\Big\rangle. \tag{5.24b}$$

Next, set $\vec{x} = \vec{x}_0$ and average over all space to find

$$\frac{1}{\mathbb{V}}\int \mathrm{d}\mathbb{V}\, R^A_{ml}(\vec{x}) = \Big\langle \int \mathrm{d}^3k \int \mathrm{d}^3k' \, \delta\tilde{\vec{B}}_m(\vec{k})\delta\tilde{\vec{B}}^\dagger_l(\vec{k}')\delta^3(\vec{k}-\vec{k}')\Big\rangle, \tag{5.25a}$$

and

$$\frac{1}{\mathbb{V}}\int \mathrm{d}\mathbb{V}\, R^N_{ml}(\vec{x}) = \frac{1}{2}\Big\langle \sum_n \sum_{n'} A_n A_{n'} \delta\vec{B}_{m,n}\delta\vec{B}_{l,n'}\delta_{nn'}\Big\rangle. \tag{5.25b}$$

respectively, where $\frac{1}{\mathbb{V}}\int \mathrm{d}\mathbb{V}$ is the volume averaging integral. Here the relations

$$\frac{1}{\mathbb{V}}\int \mathrm{d}\mathbb{V}\, e^{i(\vec{k}-\vec{k}')\vec{x}} = \delta^3(\vec{k}-\vec{k}'), \tag{5.26a}$$

and

$$\frac{1}{\mathbb{V}}\int \mathrm{d}\mathbb{V}\, \cos(\vec{k}_n\vec{x}+\phi_n)\cos(\vec{k}_{n'}\vec{x}_0+\phi_{n'}) = \frac{1}{2}\delta_{nn'} \tag{5.26b}$$

were used to calculate the integrals. This allows the results to simplified to

$$\frac{1}{\mathbb{V}}\int \mathrm{d}\mathbb{V}\, R^A_{ml}(\vec{x}) = \int \mathrm{d}^3k \, \Big\langle \delta\tilde{\vec{B}}_m(\vec{k})\delta\tilde{\vec{B}}^\dagger_l(\vec{k})\Big\rangle, \tag{5.27a}$$

and

$$\frac{1}{\mathbb{V}}\int \mathrm{d}\mathbb{V}\, R^N_{ml}(\vec{x}) = \frac{1}{2}\sum_n \Big\langle A_n^2 \delta\vec{B}_{m,n}\delta\vec{B}_{l,n}\Big\rangle. \tag{5.27b}$$

respectively.

---

[5] Here it has been assumed that the turbulence wave modes are written with a single index n.

Given that (5.27a) and (5.27b) both represent the same field, they should be equal to each other:

$$\frac{1}{2}\sum_n \left\langle A_n^2 \delta\vec{B}_{m,n}\delta\vec{B}_{l,n}\right\rangle = \int \mathrm{d}^3k \left\langle \delta\tilde{\vec{B}}_m(\vec{k})\delta\tilde{\vec{B}}_l^\dagger(\vec{k})\right\rangle. \tag{5.28}$$

The right hand side of the equation can be recognized as the spectral tensor (2.7) for a static field and decomposed into the spectral function and orientation tensor via (2.11) so that

$$\frac{1}{2}\sum_n \left\langle A_n^2 \delta\vec{B}_{m,n}\delta\vec{B}_{l,n}\right\rangle = \int \mathrm{d}^3k\, g(\vec{k})\sigma_{ml}(\vec{k}). \tag{5.29}$$

Since the turbulence being considered is axi-symmetric and incompressible, the orientation of the field must be independent of k_z and k_r while the spectrum needs to be independent of k_ϕ. This allows the right hand side to be written as

$$\int \mathrm{d}^3k\, g(\vec{k})\sigma_{ml}(\vec{k}) = \int_{-\infty}^{\infty} \mathrm{d}k_\parallel \int_0^\infty \mathrm{d}k_\perp\, k_\perp g(k_\parallel, k_\perp) \int_0^{2\pi} \mathrm{d}k_\phi\, \sigma_{ml}(k_\phi) \tag{5.30}$$

and the left hand side as

$$\frac{1}{2}\sum_n \left\langle A_n^2 \delta\vec{B}_{m,n}\delta\vec{B}_{l,n}\right\rangle = \frac{1}{2}\sum_n A_n^2 \left\langle \delta\vec{B}_{m,n}\delta\vec{B}_{l,n}\right\rangle. \tag{5.31}$$

In these forms, it can be seen that

$$\left\langle \delta\vec{B}_{m,n}\delta\vec{B}_{l,n}\right\rangle = \int_0^{2\pi} \mathrm{d}k_\phi\, \sigma_{ml}(k_\phi) \tag{5.32a}$$

and

$$\frac{1}{2}\sum_n A_n^2 = \int_{-\infty}^{\infty} \mathrm{d}k_\parallel \int_0^\infty \mathrm{d}k_\perp\, k_\perp g(k_\parallel, k_\perp). \tag{5.32b}$$

By using (2.39) to write the spectral tensor, it can be seen that

$$\sigma_{xx}(k_\phi) = g_\phi(k_\phi) \tag{5.33a}$$

and

$$g(k_\parallel, k_\perp) = \ell_\parallel \ell_\perp^2 g_\parallel(k_\parallel) g_\perp(k_\perp). \tag{5.33b}$$

Models	k_p	$G'_p(k_p)$	k_s	$G'_s(k_s)$
Slab	$k_\parallel \ell_\parallel$	$\left[1+k_p^2\right]^{-\frac{s}{2}}$	$k_\perp \ell_\perp$	$\delta(k_s)$
2D	$k_\perp \ell_\perp$	$\dfrac{k_p^q}{\left[1+k_p^2\right]^{\frac{s+q}{2}}}$	$k_\parallel \ell_\parallel$	$\delta(k_s)$
NRMHD	$k_\perp \ell_\perp$	$\dfrac{k_p^q}{\left[1+k_p^2\right]^{\frac{s+q}{2}}}$	$k_\parallel \ell_\parallel$	$\Theta(1-k_s)$
Standard Noisy Slab	$k_\parallel \ell_\parallel$	$\left[1+k_p^2\right]^{-\frac{s}{2}}$	$k_\perp \ell_\perp$	$\Theta(1-k_s)$
Modified Noisy Slab	$k_\parallel \ell_\parallel$	$\left[1+k_p^2\right]^{-\frac{s}{2}}$	$k_\perp \ell_\perp$	$k_s^p \Theta(1-k_s)$
Gaussian Noisy Slab	$k_\parallel \ell_\parallel$	$\left[1+k_p^2\right]^{-\frac{s}{2}}$	$k_\perp \ell_\perp$	$\dfrac{1}{2} k_s^3 e^{-\frac{1}{2}k_s^2}$
Full 3D	$k_\parallel \ell_\parallel$	$\left[1+k_p^2\right]^{-\frac{s}{2}}$	$k_\perp \ell_\perp$	$\dfrac{k_s^q}{\left[1+k_s^2\right]^{\frac{s+q}{2}}}$

Table 5.1: Primary and secondary wave modes and spectral functions for the models discussed in Chapter 2.

Before proceeding further, define

$$k_\perp g(k_\parallel, k_\perp) = N(s,q)\delta b^2 G'_p(k_p, s, q) G'_s(k_s) \tag{5.34}$$

where $N(s,q)$ is the spectrum normalization as determined by the model, δb^2 is the turbulence energy density relative to the mean field, $G'_p(k_p, s, q)$ is given by

$$G'_p(k_p, s, q) = \frac{k_p^q}{\left[1+k_p^2\right]^{\frac{s+q}{2}}}, \tag{5.35}$$

and $G'_s(k_s)$ is model dependent. The quantities k_p and k_s are respectively the primary and secondary wave numbers multiplied by their corresponding length scales. The primary wave number is the component of the wave vector on which the turbulence is primarily dependent, while the secondary wave number is the component of the wave vector which is either absent from the model ($k_s = 0$) or provides the noise component of the turbulence. For example, in the slab and noisy slab model, the parallel wave number is the primary, while the perpendicular wave number is the secondary, whereas in the 2D and NRMHD models the wave number roles are reversed. For the full 3D model we use the same definitions for primary and secondary wave modes as the noisy slab model. Table 5.1 summarizes the functions $G'_p(k_p)$ and $G'_s(k_s)$ for each of the models listed in Chapter 2.

Next, consider the combination of (5.32b) and (5.34):[6]

$$\frac{1}{2}\sum_{n,m} A_{nm}^2 = N'(s,q)\delta b^2 \int_0^\infty \mathrm{d}k_p\, G'_p(k_p,s,q) \int_0^\infty \mathrm{d}k_s\, G'_s(k_s), \tag{5.36}$$

where $N'(s,q)$ is the normalization factor $N(s,q)$ multiplied by the results of integration over k_ϕ. At this point, the integral on the right hand side is broken up into a sum of integrals by

$$\int_0^\infty \mathrm{d}k_p\, G'_p(k_p,s,q) = \sum_n \int_{k_n-\mathrm{d}k_n^-}^{k_n+\mathrm{d}k_n^+} \mathrm{d}k_p\, G'_p(k_p,s,q) \tag{5.37a}$$

and

$$\int_0^\infty \mathrm{d}k_s\, G'_s(k_s) = \sum_m \int_{k_m-\mathrm{d}k_m^-}^{k_m+\mathrm{d}k_m^+} \mathrm{d}k_s\, G'_s(k_s,s,q) \tag{5.37b}$$

such that

$$\frac{1}{2}\sum_{n,m} A_{nm}^2 = N'(s,q)\delta b^2 \sum_{nm} \begin{bmatrix} \left[G_p(k_n+\mathrm{d}k_n^+,s,q) - G_p(k_n-\mathrm{d}k_n^-,s,q)\right] \\ \times \left[G_s(k_m+\mathrm{d}k_m^+) - G_s(k_m-\mathrm{d}k_m^-)\right] \end{bmatrix} \tag{5.38}$$

where $G_p(x,s,q)$ is defined as per (2.19) and $G_s(x)$ is the integral of $G'_s(x)$. From this it can be clearly seen that the amplitude A_{nm} is calculated by

$$A_{nm} = \sqrt{2N'(s,q)\delta b^2 \begin{bmatrix} \left[G_p(k_n+\mathrm{d}k_n^+,s,q) - G_p(k_n-\mathrm{d}k_n^-,s,q)\right] \\ \times \left[G_s(k_m+\mathrm{d}k_m^+) - G_s(k_m-\mathrm{d}k_m^-)\right] \end{bmatrix}}. \tag{5.39}$$

Therefore, the analytical quantities $G_p^A(k_n,s,q)$ and $G_s^A(k_m)$ can be defined as

$$G_p^A(k_n,s,q) = G_p(k_n+\mathrm{d}k_n^+,s,q) - G_p(k_n-\mathrm{d}k_n^-,s,q) \tag{5.40a}$$

and

$$G_s^A(k_m) = G_s(k_m+\mathrm{d}k_m^+) - G_s(k_m-\mathrm{d}k_m^-) \tag{5.40b}$$

---

[6] Here we assume that the amplitude has two indices, n and m, with n being for the primary wave modes and m being for the secondary wave modes. For slab and 2D the index m can be dropped.

respectively. Note that at this point $\mathrm{d}k_n^{\pm}$ and $\mathrm{d}k_m^{\pm}$ have not been specified, and therefore (5.40) is a general definition.

While (5.39) can be considered the ideal calculation of the wave amplitude, there are several problems when it comes to implementing it: the first of which is that $G(x, s, q)$ does not have general analytical form. The second problem is that the range of wave numbers used does not extend to infinity.

5.1.4.1 Numerical Implementation of the Integral

As noted in 2.1.2, outside of odd values of q, the power law spectrum $G'_p(x, s, q)$ does not have an analytical form. As such, the integral needs to be calculated numerically, for which there are multiple methods. A common approach (for example, see Giacalone and Jokipii (1999), Tautz and Dosch (2013), Hussein et al. (2015)) is to calculate the integral using a basic Euler step method:

$$G_p^N(k_n, s, q) = G'_p(k_n, s, q)\mathrm{d}k_n^{\pm}, \tag{5.41}$$

where $G_p^N(k, s, q)$ is the numerical approximation of the integral and $\mathrm{d}k_n^{\pm}$ is defined by (5.9). Unfortunately, this method is extremely inaccurate, even after normalizing the result. Forward Euler integration ends up with a reduced amount of energy at small wave numbers and excess energy at large wave numbers, while backwards Euler integration reverses this effect.

In this work, the integral is calculated using a split trapezoid method, which is done by first writing the integral as

$$\int\limits_{k_n-\frac{1}{2}\mathrm{d}k_n^-}^{k_n+\frac{1}{2}\mathrm{d}k_n^+} \mathrm{d}k_p\, G'_p(k_p, s, q) = \int\limits_{k_n-\frac{1}{2}\mathrm{d}k_n^-}^{k_n} \mathrm{d}k_p\, G'_p(k_p, s, q) + \int\limits_{k_n}^{k_n+\frac{1}{2}\mathrm{d}k_n^+} \mathrm{d}k_p\, G'_p(k_p, s, q). \tag{5.42}$$

Next, the integrals on the right hand side are calculated using a standard trapezoid method and the results combined so that the integral is approximated as

$$G_p^N(k_n, s, q) = \frac{1}{4}\begin{bmatrix} G'_p\Big(k_n - \frac{1}{2}\mathrm{d}k_n^-, s, q\Big)\mathrm{d}k_n^- \\ +G'_p\Big(k_n, s, q\Big)\Big[\mathrm{d}k_n^- + \mathrm{d}k_n^+\Big] \\ +G'_p\Big(k_n + \frac{1}{2}\mathrm{d}k_n^+, s, q\Big)\mathrm{d}k_n^+ \end{bmatrix}. \tag{5.43}$$

The final point to consider when calculating the wave amplitudes is that the wave numbers used in the numerical simulation are not between 0 and infinity, but rather between k_{min} and k_{max}, which are non-zero and finite. As a result, the total energy contained in the turbulence will not be equal to δb^2 if the normalization factor $N(s,q)$ is used. To rectify this, the amplitude is calculated as

$$A_{nm} = \sqrt{2\delta b^2 \frac{G_p^N(k_n,s,q)G_s^N(k_m)}{\sum\limits_{n,m} G_p^N(k_n,s,q)G_s^N(k_m)}}. \tag{5.44}$$

This has the effect of slightly increasing the energy of all wave modes, regardless of the integration method used.

Figure 5.2 shows the relative error on the amplitude for the Euler and split trapezoid integration methods. By using $q = 1$ and $q = 3$ for the comparison, (2.19) can be used to calculate the exact value of the integral. The 128 wave modes used were generated according to (5.12).

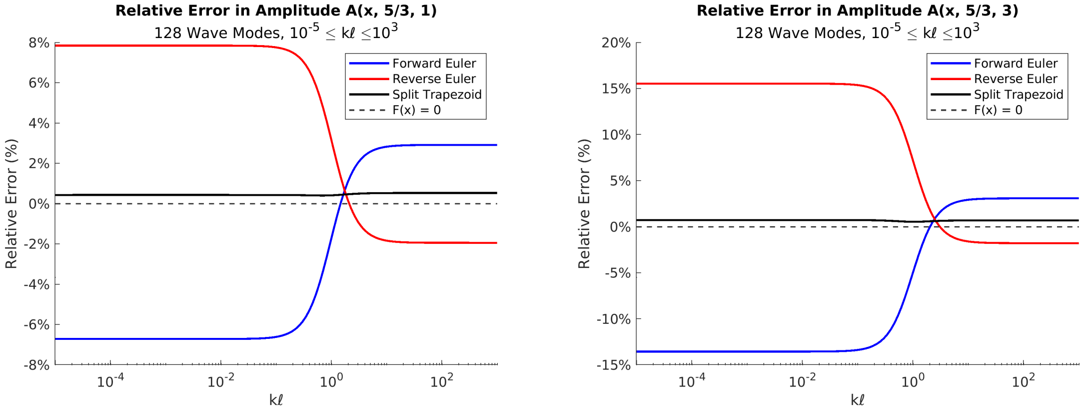

(a) $q = 1$ (b) $q = 3$

Figure 5.2: Comparison of amplitude calculated via Euler and split trapezoid integration methods with energy spectral indices $q = 1$ (left) and $q = 3$ (right).

5.2 Trajectory Calculation and Basic Analysis

5.2.1 Trajectory Calculation

Once the magnetic field has been generated, the next step is to compute the particle trajectories. Each particle in the simulation is placed at a random position $\vec{X}_p$ within a sphere of radius r centered on the origin and with a randomly orientated rigidity (velocity) $\vec{R}_p$ of constant magnitude. An isotropic distribution is used for both the position vector and the rigidity unit vector, using (5.18) as the base for the unit vector orientation of both. The use of an isotropic rigidity distribution ensures that the assumptions on the initial velocity distribution made in Chapter 3.3 are correct. The random initial position means that the particles don't necessarily all start at the same point, and therefore the starting magnetic field is different for each particle. The simulations discussed in this work all used a unit-less distribution radius of $r = 10$.

Once a particle has been initialized, its trajectory is then calculated using the IRM method described in the previous chapter using the third order symplectic coefficients. The coefficients can be found in Table B.3a while Table 4.2b shows the accuracy calculations. The reason for using these coefficients instead of those specific to the IRM method is the method was originally developed by modifying the symplectic integration method. As the third order coefficients from the symplectic method are both rational and result in third order accuracy in the modified method, they were kept and used in the author's previously published work. It was only during the generalization of the method to any order that the IRM specific coefficients were derived.

In particle transport theory, the diffusion coefficient κ_{ii} is the value of running diffusion coefficient in the limit of infinite time, as discussed in Chapter 1. That said, particle trajectories cannot be simulated for an infinite amount of time, since the simulation would never finish. Instead, the particles are simulated for a duration of time, T_{max}, typically in thousands or tens of thousands units of time, with the units given by (1.13). The physical argument for this is that in space, particles don't have an infinite amount of time either, and therefore the mathematical limit of $t \to \infty$ can be viewed as being in the regime of very long periods of time.

The maximum value of T_{max} is limited by several constraints, the first of which is that the calculation of an individual particle trajectory must finish within the time allocated for the simulation by whatever server it is running on. For this work, all simulations were run on servers provided by Compute Canada (now the Digital Research Alliance of Canada). As these servers are used by researchers across the country, a maximum run time of 7 days (168 hours) is imposed on all submitted tasks. For its part, ACEPTS is designed such that it writes data to file only at specific points in the simulation, one of which is whenever a trajectory has been fully calculated. It can therefore be restarted from the last finished trajectory calculation, but not from in the middle of a calculation. As a result, the trajectory calculation must finish within the allocated time, or no results will be kept.

The second constraint relates T_{max} to the number of particles per simulation and the desired accuracy of the results. From statistics, it is expected that noise on the final calculated quantities (ie: the diffusion coefficients) will decrease as the total number of particle trajectories used in the calculation increases. However, increasing the number of particles per simulation will increase the required run time. Therefore, in order for a simulation to finish in a reasonable amount of time, both the number of particles and T_{max} must be considered.

As an example of these constraints, the noisy slab simulations for parameter sets with $R = 0.01$ and $T_{max} = 10^6$ required around six days per particle. With six particles per simulation, the total time for each simulation in each parameter set was a minimum of six weeks. Given that normal diffusion was never observed in the perpendicular direction and the first constraint had been reached, it made no sense to further increase the maximum time, as the simulations would not finish within the physical time constraint.

5.2.2 Basic Analysis

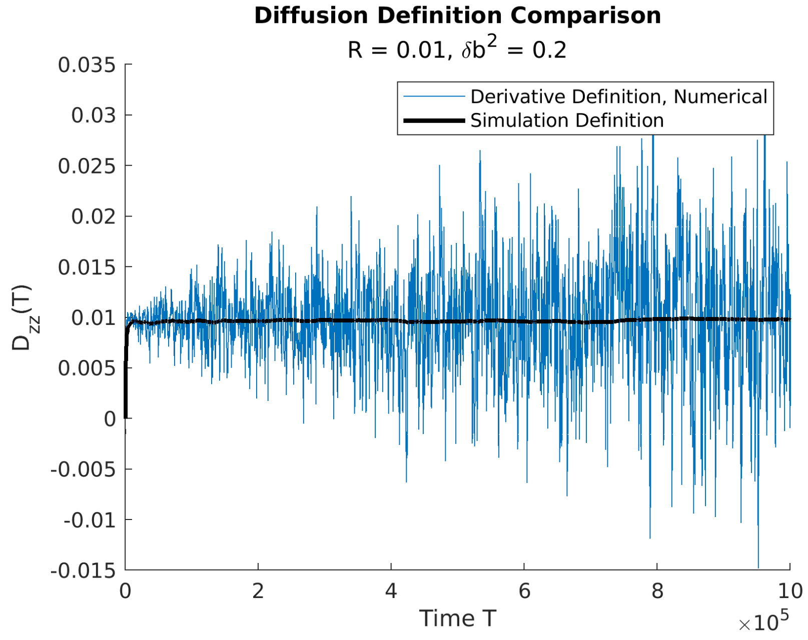

Figure 5.3: Comparison of the running parallel diffusion coefficient calculated using (1.28) (black) and a numerical derivative (blue).

After all simulations in a parameter set have been completed, the results are analyzed and the running diffusion coefficients computed. As was noted at the end of Chapter 1.2.2.1, taking the time derivative of the mean square displacement analytically or numerically amplifies any noise in the signal. Therefore, (1.28) is used to calculate the running diffusion coefficients. Figure 5.3 shows the results of the two different definitions, demonstrating the need for using (1.28).

5.3 Scaling of Quantities in Simulation

Before discussing the methods used to solve the equations for various transport theories, the scaling of all quantities used in simulation and theory needs to be discussed. As already discussed in Chapter 1.2.1.1, basic scaling can be derived from the equations of motion, the results of which are summarized in the first four lines of Table 5.2. From this starting point, it follows that the wave vector in simulations must be scaled as

$$\vec{k}^S = \vec{k}\ell_0 \tag{5.45}$$

so that the wave phase

$$\phi = \vec{k} \cdot \vec{x} + \phi_0 = \vec{k}\ell_0 \cdot \vec{x}/\ell_0 + \phi_0 = \vec{k}^S \cdot \vec{X} + \phi_0 \tag{5.46}$$

remains unchanged. As a direct result of this, the parallel and perpendicular wave modes have the same scale.

When it comes to calculating the amplitude of the waves, the use of a single length scale presents a minor problem in that the turbulence has its own set of length scales. For turbulence in which there is only one relevant length scale, such as the slab model (parallel wave number) or the 2D model (perpendicular wave number), this can easily be overcome by setting ℓ_0 equal to the characteristic length scale of the model. On the other hand, for turbulence which has multiple length scales the question becomes "Which length scale should be used?". From the original way ℓ_0 was defined in Chapter 1.2.1.1, ℓ_0 should be equal to the primary length scale of the turbulence, which was defined in Section 5.1.4 as the length scale corresponding to the wave number on which the turbulence is primarily dependent. As also stated in Section 5.1.4, this corresponds to the parallel length scale in slab, noisy slab (including variants), and full 3D turbulence, and the perpendicular length scale in 2D and NRMHD turbulence.

Quantity	Unscaled	Scaled	Scale Factor	Scale Name
Time	t	$T = \Omega t$	$\Omega = \frac{qB_0}{\gamma mc}$	Synchrotron Frequency
Position	$\vec{x}$	$\vec{X} = \vec{x}/\ell_p$	ℓ_p	Primary Characteristic Length
Velocity	$\vec{v}$	$\vec{R} = \vec{v}/\Omega\ell_p$	$\Omega\ell_p = \frac{qB_0\ell_p}{\gamma mc}$	
Magnetic Field	$\vec{B}$	$\vec{b} = \vec{B}/B_0$	B_0	Mean Field
Turbulence Energy Density	δB^2	$\delta b^2 = \delta B^2/B_0^2$	B_0^2	Mean Field Energy Density
Wave Vector	$\vec{k}$	$\vec{k}^S = \vec{k}\ell_p$	ℓ_p	
Parallel Wave Vector	$k_\parallel$	$k_\parallel^S = k_\parallel \ell_p$	ℓ_p	
Perpendicular Wave Vector	$k_\perp$	$k_\perp^S = k_\perp \ell_p$	ℓ_p	
Running Diffusion Coefficient	$d_{ii}(t) = \frac{\left\langle (\Delta x(t))^2 \right\rangle}{2t}$	$d_{ii}^S(T) = \frac{d_{ii}(t)}{\Omega\ell_p^2}$	$\Omega\ell_p^2 = \frac{qB_0\ell_p^2}{\gamma mc}$	

Table 5.2: Summary of quantity scaling used in simulations. For the slab and noisy slab models $\ell_p = \ell_\parallel$.

From this, it therefore follows that the running diffusion coefficient calculated by the simulation using (1.28) has the form

$$d_{ii}^S(T) = \frac{\left\langle (\Delta X_i(T))^2 \right\rangle}{2T} \tag{5.47}$$

and is related to the physical running diffusion coefficient by

$$d_{ii}^S(T) = \frac{d_{ii}(t)}{\Omega\ell_p^2}. \tag{5.48}$$

Table 5.2 summarizes the scaling of quantities used by the simulation. Since this work focuses on the noisy slab and full 3D models, the primary length scale in the result is the parallel length scale.

5.4 Solving Equations From Theory

In this section the unit–less versions of the equations for describing field line diffusion and particle transport (see Chapter 3) will be discussed. Additionally, alternate parameterizations for several of the equations will be introduced. In the analysis of simulation results the equations discussed here were solved using MATLAB, so that the results could be compared visually.

5.4.1 Parallel Transport Equations

As was discussed in Chapter 3.3.2, the equations for the parallel mean square displacement $\left\langle (\Delta z(t))^2 \right\rangle$ are given by (3.85):

$$\left\langle (\Delta z(t))^2 \right\rangle = \begin{cases} \frac{2}{3} v \lambda_\parallel t - \frac{2}{3} \lambda_\parallel^2 \left[1 - \exp\left(-\frac{v}{\lambda_\parallel} t \right) \right] & \text{Mean Free Path} \\ 2\kappa_\parallel t - \frac{6\kappa_\parallel^2}{v^2} \left[1 - \exp\left(-\frac{v^2}{3\kappa_\parallel} t \right) \right] & \text{Diffusion Coefficient} \end{cases}$$

where v is the particle velocity, $\lambda_\parallel$ is the parallel mean free path, and $\kappa_\parallel$ is the parallel diffusion coefficient, with $\lambda_\parallel$ and $\kappa_\parallel$ being related to each other by (3.81). In Arendt and Shalchi (2018), a unit–less version of the running parallel diffusion equation was derived by defining

$$T = \Omega t \qquad R = \frac{v}{\Omega \ell_\parallel} \qquad K_\parallel = \frac{\kappa_\parallel}{\Omega \ell_\parallel^2} \qquad D_\parallel(T) = \frac{d_\parallel(t)}{\Omega \ell_\parallel^2} \tag{5.49}$$

and combining the parallel mean square displacement equation with the numerical definition of $d_\parallel$ to find

$$D_\parallel(T) = K_\parallel - \frac{3K_\parallel^2}{R^2 T} \left[1 - \exp\left(-\frac{R^2}{3K_\parallel} T \right) \right]. \tag{5.50}$$

In order to find a unit–less version of the equation using the mean free path, define

$$\Lambda_\parallel = \frac{\lambda_\parallel}{\ell_\parallel} \tag{5.51}$$

so that the unit–less equation is

$$D_\parallel(T) = \frac{R\Lambda_\parallel}{3} - \frac{\Lambda_\parallel^2}{3T} \left[1 - \exp\left(-\frac{R}{\Lambda_\parallel} T \right) \right]. \tag{5.52}$$

In addition to the two forms of the parallel mean square displacement described in (3.85), there is a third form of the equation. To derive this form, first define the *parallel scattering time*, $\tau_\parallel$, as

$$\tau_\parallel = \frac{\lambda_\parallel}{v} = \frac{3\kappa_\parallel}{v^2}. \tag{5.53}$$

Writing the mean square displacement in terms of τ results in

$$\left\langle (\Delta z(t))^2 \right\rangle = \frac{2}{3} v^2 \left[\tau_\parallel t - \tau_\parallel^2 \left[1 - \exp\left(-\frac{t}{\tau_\parallel} \right) \right] \right]. \tag{5.54}$$

To make this equation unit–less, define

$$\sigma_z^2 = \frac{\left\langle (\Delta z(t))^2 \right\rangle}{\ell_\parallel^2} \tag{5.55a}$$

and

$$\tau'_\parallel = \Omega \tau_\parallel = \frac{\Lambda_\parallel}{R}, \tag{5.55b}$$

such that the equation becomes

$$\sigma_z^2 = \frac{2}{3} R^2 \left[\tau'_\parallel T - {\tau'_\parallel}^2 \left[1 - \exp\left(-\frac{T}{\tau'_\parallel} \right) \right] \right]. \tag{5.56}$$

With this form of the mean square displacement, the running diffusion coefficient is

$$D_\parallel(T) = \frac{R^2}{3} \left[\tau'_\parallel - \frac{{\tau'_\parallel}^2}{T} \left[1 - \exp\left(-\frac{T}{\tau'_\parallel} \right) \right] \right]. \tag{5.57}$$

5.4.1.1 Summary and Numerical Implementation of Parallel Transport Equations

In the analysis and results presented in Chapter 6, (5.56) is used to determine the scattering time, while (5.57) is used to plot the diffusion coefficient. The parallel scattering time is determined by using MATLAB to fit (5.56) to the numerical data. Table 5.3 lists all the quantities discussed and the scaling used for each, while Table 5.4 shows the conversion between simulation and theory scaling. Conversions for the parallel diffusion coefficient, mean free path, and scattering time are not listed as these quantities are not computed directly in the simulation. Furthermore, the results presented in Chapter 6 are plotted using the theory scaling, not the simulation scaling.[7]

---

[7] Technically, the theory and simulation scales are identical for the noisy slab and full 3D models.

Quantity	Unscaled	Scaled	Scale Factor	Defined in
Time	t	$T = \Omega t$	$\Omega = \frac{qB_0}{\gamma mc}$	(1.13)
Particle Velocity	v	$R = \frac{v}{\Omega \ell_\parallel}$	$\frac{1}{\Omega \ell_\parallel} = \frac{\gamma mc}{qB_0 \ell_\parallel}$	(5.49)
Parallel Mean Square Displacement	$\left\langle (\Delta z)^2 \right\rangle$	$\sigma_z^2 = \frac{\left\langle (\Delta z)^2 \right\rangle}{\ell_\parallel^2}$	$\frac{1}{\ell_\parallel^2}$	(5.55a)
Parallel Running Diffusion Coefficient	$d_\parallel(t)$	$D_\parallel(T) = \frac{d_\parallel(t)}{\Omega \ell_\parallel^2}$	$\frac{1}{\Omega \ell_\parallel^2} = \frac{\gamma mc}{qB_0 \ell_\parallel^2}$	(5.49)
Parallel Diffusion Coefficient	$\kappa_\parallel$	$K_\parallel = \frac{\kappa_\parallel}{\Omega \ell_\parallel^2}$	$\frac{1}{\Omega \ell_\parallel^2} = \frac{\gamma mc}{qB_0 \ell_\parallel^2}$	(5.49)
Parallel Mean Free Path	$\lambda_\parallel$	$\Lambda_\parallel = \frac{\lambda_\parallel}{\ell_\parallel}$	$\frac{1}{\ell_\parallel}$	(5.51)
Parallel Scattering Time	$\tau_\parallel$	$\tau'_\parallel = \Omega \tau_\parallel$	$\Omega = \frac{qB_0}{\gamma mc}$	(5.53), (5.55b)

Table 5.3: Summary of scaled quantities used in parallel transport equations.

5.4.2 Perpendicular Transport Equations

Before deriving the scaled versions of the various theoretical equations for calculating the perpendicular diffusion coefficient, first consider the common functions and quantities. For analysis purposes, the xx component of the spectral tensor is written in the form given by (2.39). The functions and quantities that need to be considered are therefore the wave numbers $k_\parallel$ and $k_\perp$, the spectral functions $g_\parallel(k_\parallel)$ and $g_\perp(k_\perp)$, and the perpendicular diffusion coefficient $\kappa_\perp$ itself. The perpendicular diffusion coefficient can be scaled similarly to (5.49) by

$$K_\perp = \frac{\kappa_\perp}{\Omega \ell_\perp^2}. \tag{5.58a}$$

Alternatively, the unit–less diffusion coefficient can be defined as

$$K'_\perp = \frac{\tau_\parallel}{\ell_\perp^2} \kappa_\perp = \frac{\tau'_\parallel}{\Omega \ell_\perp^2} \kappa_\perp \tag{5.58b}$$

such that

$$K_\perp = \frac{K'_\perp}{\tau'_\parallel}, \tag{5.58c}$$

Quantity	Simulation	Theory	Conversion
Time	$T^S = \Omega t$	$T^T = \Omega t$	$T^T = T^S$
Particle Velocity	$R^S = v/\Omega\ell_p$	$R^T = v/\Omega\ell_\parallel$	$R^T = \frac{\ell_p}{\ell_\parallel} R^S$
Parallel Mean Square Displacement	$[\sigma_z^2]^S = \frac{\langle(\Delta z)^2\rangle}{\ell_p^2}$	$[\sigma_z^2]^T = \frac{\langle(\Delta z)^2\rangle}{\ell_\parallel^2}$	$[\sigma_z^2]^T = \frac{\ell_p^2}{\ell_\parallel^2}[\sigma_z^2]^S$
Parallel Running Diffusion Coefficient	$D_\parallel^S(T) = \frac{d_\parallel(t)}{\Omega\ell_p^2}$	$D_\parallel^T(T) = \frac{d_\parallel(t)}{\Omega\ell_\parallel^2}$	$D_\parallel^T(T) = \frac{\ell_p^2}{\ell_\parallel^2} D_\parallel^S(T)$

Table 5.4: Conversion between simulation and theory scales for parallel transport.

where $\tau_\parallel$ is the parallel scattering time defined in (5.53).[8]

Given (5.58) and the form of the parallel and perpendicular spectral functions in Table 2.1, the natural scaling for these functions is

$$g_z(k_z) = g_\parallel(k_z/\ell_\parallel) \tag{5.59a}$$

and

$$g_r(k_r) = g_\perp(k_r/\ell_\perp), \tag{5.59b}$$

respectively, where (3.46) has been used to scale $k_\parallel$ and $k_\perp$. This scaling is used when solving the equations for all analytical theories used in the analysis of simulations in Chapter 6.

5.4.2.1 Time–Dependent UNLT Theory

In the time–dependent UNLT theory, the equation for perpendicular transport is (3.134):

$$\frac{\mathrm{d}^2}{\mathrm{d}t^2}\left\langle(\Delta x)^2\right\rangle = 2a^2\frac{\delta B_x^2}{B_0^2}\int\limits_{-\infty}^{\infty}\mathrm{d}k_\parallel\,\ell_\parallel\,g_\parallel(k_\parallel)\xi(k_\parallel,t)\int\limits_{0}^{\infty}\mathrm{d}k_\perp\,k_\perp\ell_\perp^2\,g_\perp(k_\perp)e^{-\frac{1}{2}\left\langle(\Delta x)^2\right\rangle k_\perp^2},$$

a non–linear, second–order differential equation, with

$$\xi(k_\parallel,t) = \frac{v^2}{3}\frac{\omega_+e^{\omega_+t} - \omega_-e^{\omega_-t}}{\omega_+ - \omega_-},$$

---

[8] The reason for using this definition of the unit–less diffusion coefficient is so that the scaling is consistent with that used for the time–dependent UNLT equations.

$$\omega_\pm = -\frac{v}{2\lambda_\parallel} \pm \sqrt{\left[\frac{v}{2\lambda_\parallel}\right]^2 - \frac{1}{3}\left[vk_\parallel\right]^2}$$

as per (3.131) and (3.132), respectively. As with the parallel diffusion coefficient, there is more than one way to scale the equation. To derive the parameterization used in this work, first consider the equation for $\omega_\pm$. The common component in each term is the velocity, and one possible way to parameterize the equations is to use $t' = vt$, which removes any direct reference to the particle energy. In the method used in this work, both the particle velocity and the parallel mean free path are factored out of $\omega_\pm$, so that

$$\omega_\pm = -\frac{v}{2\lambda_\parallel} \pm \sqrt{\left[\frac{v}{2\lambda_\parallel}\right]^2 - \frac{1}{3}\left[vk_\parallel\right]^2} = -\frac{v}{2\lambda_\parallel}\left[1 \mp \sqrt{1 - \frac{4}{3}\lambda_\parallel^2 k_\parallel^2}\right] = -\frac{1}{2\tau_\parallel}\omega'_\mp, \quad (5.60)$$

where $\omega'_\pm$ is defined as

$$\omega'_\pm = \begin{cases} 1 \pm \sqrt{1 - \frac{4}{3}\lambda_\parallel^2 k_\parallel^2} & \text{Unscaled} \\ 1 \pm \sqrt{1 - \frac{4}{3}\Lambda_\parallel^2 k_z^2} & \text{Scaled.} \end{cases} \quad (5.61)$$

Additionally, for reasons which will be made clear shortly, define

$$\omega_0 = \frac{1}{2}\left[\omega'_+ - \omega'_-\right] = \begin{cases} \sqrt{1 - \frac{4}{3}\lambda_\parallel^2 k_\parallel^2} & \text{Unscaled} \\ \sqrt{1 - \frac{4}{3}\Lambda_\parallel^2 k_z^2} & \text{Scaled.} \end{cases} \quad (5.62)$$

With this parameterization, the equation for $\xi(k_\parallel, t)$ can be expressed as

$$\xi(k_\parallel, t) = \frac{1}{3}\frac{\lambda_\parallel^2}{\tau^2}\frac{\omega'_+ e^{-\frac{\omega'_+ t}{2\tau}} - \omega'_- e^{-\frac{\omega'_- t}{2\tau}}}{2\omega_0} \quad (5.63)$$

with (5.53) being used to replace v. As a result, the differential equation becomes

$$\frac{\mathrm{d}^2}{\mathrm{d}t^2}\left\langle(\Delta x)^2\right\rangle = \frac{2}{3}a^2\frac{\lambda_\parallel^2}{\tau^2}\frac{\delta B_x^2}{B_0^2}\int\limits_{-\infty}^{\infty}\mathrm{d}k_\parallel\,\ell_\parallel\,g_\parallel(k_\parallel)\frac{\omega'_+ e^{-\frac{\omega'_+ t}{2\tau}} - \omega'_- e^{-\frac{\omega'_- t}{2\tau}}}{2\omega_0}$$
$$\times\int\limits_0^{\infty}\mathrm{d}k_\perp\,k_\perp\ell_\perp^2\,g_\perp(k_\perp)e^{-\frac{1}{2}\left\langle(\Delta x)^2\right\rangle k_\perp^2}. \quad (5.64)$$

While it is possible to apply the same scaling used for in parallel transport and diffusive UNLT at this point, there is one additional step used in this work: define t' as

$$t' = \frac{t}{\tau_\parallel} = \frac{T}{\tau_\parallel'}, \tag{5.65}$$

such that $\xi(k_\parallel, t)$ becomes

$$\xi(k_\parallel, t) = \frac{1}{3}\frac{\lambda_\parallel^2}{\tau_\parallel^2}\epsilon(k_\parallel \ell_\parallel, t/\tau_\parallel) \tag{5.66}$$

where

$$\epsilon(k_z, t') = \frac{\omega_+' e^{-\frac{\omega_+' t'}{2}} - \omega_-' e^{-\frac{\omega_-' t'}{2}}}{2\omega_0}. \tag{5.67}$$

As a result, the differential equation can be written as

$$\begin{aligned} \frac{\mathrm{d}^2}{\mathrm{d}t'^2}\left\langle (\Delta x)^2 \right\rangle = \frac{2}{3}a^2\lambda_\parallel^2 \frac{\delta B_x^2}{B_0^2} \int\limits_{-\infty}^{\infty} \mathrm{d}k_\parallel \, \ell_\parallel \, g_\parallel(k_\parallel)\, \epsilon(k_\parallel \ell_\parallel, t') \\ \times \int\limits_{0}^{\infty} \mathrm{d}k_\perp \, k_\perp \ell_\perp^2 \, g_\perp(k_\perp) e^{-\frac{1}{2}\left\langle (\Delta x)^2 \right\rangle k_\perp^2}, \end{aligned} \tag{5.68}$$

and the fully unit–less form is therefore

$$\frac{\mathrm{d}^2 \sigma_x^2}{\mathrm{d}t'^2} = \frac{2}{3}a^2 \Lambda_\parallel^2 K^2 \int\limits_{-\infty}^{\infty} \mathrm{d}k_z \, g_z(k_z) \epsilon(k_z, t') \int\limits_{0}^{\infty} \mathrm{d}k_r \, k_r g_r(k_r) e^{-\frac{1}{2}\sigma_x^2 k_r^2}. \tag{5.69}$$

where σ_x^2 is defined using (3.46).[9]

There are two points to be aware of when evaluating the parallel integral in (5.69), both related to (5.67). The first point is that ω_0 is equal to zero at $k_z = \sqrt{3}/2\Lambda_\parallel$, meaning that there is a potential singularity at this value. The second is that ω_0 becomes complex for values of k_z greater than $\sqrt{3}/2\Lambda_\parallel$. The latter issue can be solved by writing the function in terms of sine and cosine functions for $k_z > \sqrt{3}/2\Lambda_\parallel$; while the former can be solved by taking the limit $k_z \to \sqrt{3}/2\Lambda_\parallel$. The equation is

---

[9] In this case the mean square displacement is that of the particles.

therefore numerically evaluated as

$$\epsilon(k_z,t') = \begin{cases} \dfrac{\omega'_+ e^{-\frac{\omega'_+ t'}{2}} - \omega'_- e^{-\frac{\omega'_- t'}{2}}}{2\omega_0} & k_z < \sqrt{3}/2\Lambda_\parallel \\ e^{-\frac{t'}{2}}\left[1-\dfrac{t'}{2}\right] & k_z = \sqrt{3}/2\Lambda_\parallel \\ e^{-\frac{t'}{2}}\left[\cos\left(\dfrac{\omega_0 t'}{2}\right) - \dfrac{1}{\omega_0}\sin\left(\dfrac{\omega_0 t'}{2}\right)\right] & k_z > \sqrt{3}/2\Lambda_\parallel \end{cases} . \tag{5.70}$$

Writing $\epsilon(k_z,t')$ in terms of hyperbolic trigonometric functions for $k_z < \sqrt{3}/2\Lambda_\parallel$ is problematic as it results in a $0\cdot\infty$ for $t' \gg 1$, which is numerically undefined.

When using the noisy slab model, the integrals can be partially solved as per (3.142), for which the unit-less version is

$$\frac{\mathrm{d}^2\sigma_x^2}{\mathrm{d}t'^2} = \frac{2}{3}\Lambda_\parallel^2 K^2 \sqrt{\frac{\pi}{2\sigma_x^2}}\,\mathrm{erf}\left(\sqrt{\frac{\sigma_x^2}{2}}\right)\int\limits_{-\infty}^{\infty}\mathrm{d}k_z\,\epsilon(k_z,t')\frac{2C(s)}{[1+k_z^2]^{\frac{s}{2}}} \tag{5.71}$$

where $\mathrm{erf}(x)$ is the error function. On the other hand, the UNLT equation for the full 3D model,

$$\frac{\mathrm{d}^2\sigma_x^2}{\mathrm{d}t'^2} = \frac{2}{3}\Lambda_\parallel^2 K^2 \int\limits_{-\infty}^{\infty}\mathrm{d}k_z\,\epsilon(k_z,t')\frac{2C(s)}{[1+k_z^2]^{\frac{s}{2}}}\int\limits_{0}^{\infty}\mathrm{d}k_r\,4D(s,q)\frac{k_r^q}{[1+k_r^2]^{\frac{s+q}{2}}}e^{-\frac{1}{2}\sigma_x^2 k_r^2}, \tag{5.72}$$

can not be simplified at all. The method used to solve these equations is discussed in Section 5.4.2.4.

5.4.2.2 FLPD Equations

For FLPD theory, both (3.163)

$$\frac{\mathrm{d}^2}{\mathrm{d}t^2}\left\langle(\Delta x(t))^2\right\rangle = 2\frac{\delta B_x^2}{B_0^2}\int\limits_{-\infty}^{\infty}\mathrm{d}k'_\parallel\,\xi(k'_\parallel,t)\int\limits_{0}^{\infty}\mathrm{d}k_\perp\,k_\perp\ell_\perp^2\,g_\perp(k_\perp)e^{-\frac{1}{2}\left\langle(\Delta x)^2\right\rangle k_\perp^2}$$
$$\times\int\limits_{-\infty}^{\infty}\mathrm{d}k_\parallel\,\ell_\parallel\,g_\parallel(k_\parallel)\,R(k_\parallel,k_\perp,k'_\parallel)$$

and (3.57)

$$\kappa_{FL} = \frac{\delta B_x^2}{B_0^2}\int\limits_{-\infty}^{\infty}\mathrm{d}k_\parallel\,\ell_\parallel\,g_\parallel(k_\parallel)\int\limits_{0}^{\infty}\mathrm{d}k_\perp\,k_\perp\ell_\perp^2\,g_\perp(k_\perp)\frac{\kappa_{FL}k_\perp^2}{k_\parallel^2+\kappa_{FL}^2k_\perp^4}$$

need to be made unit–less. To start, consider the field line diffusion coefficient equation: by using (5.58), the equation can be written as

$$\kappa_{FL} = K^2 \int\limits_{-\infty}^{\infty} \mathrm{d}k_z\, g_z(k_z) \int\limits_{0}^{\infty} \mathrm{d}k_r\, k_r\, g_r(k_r) \frac{\kappa_{FL} k_r^2}{k_z^2 + \frac{\ell_\parallel^2}{\ell_\perp^4} \kappa_{FL}^2 k_r^4} \tag{5.73}$$

To determine the ideal scaling for the field line diffusion coefficient, next consider the resonance function (3.156a),

$$R_\pm(\vec{k}, k'_\parallel) = \frac{1}{2\pi} \frac{\kappa_{FL} k_\perp^2}{(k_\parallel \pm k'_\parallel)^2 + \kappa_{FL}^2 k_\perp^4}.$$

By working through the units of each quantity in the resonance function, it can be seen that $R_\pm$ has units of length. As there is also an additional integral involving $k'_\parallel$, the ideal length scale for $R_\pm$ is $\ell_\parallel$, so that the integral can be transformed from $k'_\parallel$ to $k'_z = k'_\parallel \ell_\parallel$. By combining this with (5.58), the resonance functions become

$$R_\pm(\vec{k}, k'_\parallel) = \frac{\ell_\parallel}{2\pi} \frac{K_{FL} k_r^2}{\left[k_z \pm k'_z\right]^2 + K_{FL}^2 k_r^4} = \ell_\parallel R'_\pm(k_z, k_r, k'_z) \tag{5.74}$$

were the field line diffusion coefficient has been scaled as

$$K_{FL} = \frac{\ell_\parallel \kappa_{FL}}{\ell_\perp^2}. \tag{5.75}$$

Alternatively, the same scaling can be derived by considering the original definition of the field line diffusion coefficient:

$$\kappa_{FL} = \lim_{z\to\infty} \frac{1}{2} \frac{\mathrm{d}}{\mathrm{d}z} \left\langle (\Delta x)^2 \right\rangle. \tag{5.76}$$

Using (3.46), the equation becomes

$$\kappa_{FL} = \frac{\ell_\perp^2}{\ell_\parallel} \lim_{Z\to\infty} \frac{1}{2} \frac{\mathrm{d}\sigma_x^2}{\mathrm{d}Z} \tag{5.77}$$

which can be rearranged to find

$$\frac{\ell_\parallel \kappa_{FL}}{\ell_\perp^2} = \lim_{Z\to\infty} \frac{1}{2} \frac{\mathrm{d}\sigma_x^2}{\mathrm{d}Z} = K_{FL}, \tag{5.78}$$

yielding the same scaling as in (5.75).

Using (5.58) and (5.75), the scaled resonance functions can be written as

$$R'_\pm(k_z, k_r, k'_z) = \frac{1}{2\pi} \frac{K_{FL} k_r^2}{\left[k_z \pm k'_z\right]^2 + K_{FL}^2 k_r^4} \tag{5.79a}$$

and

$$R'(k_z, k_r, k_z') = R'_+(k_z, k_r, k_z') + R'_-(k_z, k_r, k_z'). \tag{5.79b}$$

Therefore, the scaled field line diffusion coefficient equation is

$$K_{FL} = K^2 \int\limits_{-\infty}^{\infty} \mathrm{d}k_z \, g_z(k_z) \int\limits_{0}^{\infty} \mathrm{d}k_r \, k_r \, g_r(k_r) \, \frac{K_{FL} k_r^2}{k_z^2 + K_{FL}^2 k_r^4}, \tag{5.80}$$

while the scaled FLPD equation is

$$\frac{\mathrm{d}^2 \sigma_x^2}{\mathrm{d}t'^2} = \frac{2}{3} \Lambda_\parallel^2 K^2 \int\limits_{-\infty}^{\infty} \mathrm{d}k_z' \int\limits_{0}^{\infty} \mathrm{d}k_r \int\limits_{-\infty}^{\infty} \mathrm{d}k_z \, \epsilon(k_z', t') g_z(k_z) R'(k_z, k_r, k_z') k_r \, g_r(k_r) e^{-\frac{1}{2}\sigma_x^2 k_r^2}. \tag{5.81}$$

Applying the field line equations to the noisy slab and full 3D models results in

$$K_{FL} = 2K^2 \int\limits_{0}^{\infty} \mathrm{d}k_z \int\limits_{0}^{1} \mathrm{d}k_r \left[\frac{K_{FL} k_r^2}{k_z^2 + K_{FL}^2 k_r^4} \right] \left[\frac{2C(s)}{[1 + k_z^2]^{\frac{s}{2}}} \right] \tag{5.82}$$

and

$$K_{FL} = 2K^2 \int\limits_{0}^{\infty} \mathrm{d}k_z \int\limits_{0}^{\infty} \mathrm{d}k_r \left[\frac{K_{FL} k_r^2}{k_z^2 + K_{FL}^2 k_r^4} \right] \left[\frac{2C(s)}{[1 + k_z^2]^{\frac{s}{2}}} \right] \left[4D(s,q) \frac{k_r^q}{[1 + k_r^2]^{\frac{s+q}{2}}} \right] \tag{5.83}$$

respectively.

Given that the integral over k_z in the FLPD equation does not depend on any quantities related to the particles, such as the particle velocity or mean free path, it can be performed independently of any simulation by defining

$$f(k_r, k_z') = \int\limits_{-\infty}^{\infty} \mathrm{d}k_z \, g_z(k_z) R'(k_z, k_r, k_z') \, k_r \, g_r(k_r). \tag{5.84}$$

With this, the scaled FLPD equation can be written as

$$\frac{\mathrm{d}^2 \sigma_x^2}{\mathrm{d}t'^2} = \frac{2}{3} \Lambda_\parallel^2 K^2 \int\limits_{-\infty}^{\infty} \mathrm{d}k_z' \int\limits_{0}^{\infty} \mathrm{d}k_r \, \epsilon(k_z', t') f(k_r, k_z') e^{-\frac{1}{2}\sigma_x^2 k_r^2}, \tag{5.85}$$

where all information on the spectrum is contained in $f(k_r, k_z')$. For the noisy slab model, (5.84) becomes

$$f_{SNS}(k_r, k_z') = \int\limits_{-\infty}^{\infty} \mathrm{d}k_z \, R'(k_z, k_r, k_z') \left[\frac{2C(s)}{[1 + k_z^2]^{\frac{s}{2}}} \right] \Theta(1 - k_r), \tag{5.86}$$

whereas for the full 3D model it becomes

$$f_{F3D}(k_r, k_z') = \int\limits_{-\infty}^{\infty} \mathrm{d}k_z \, R'(k_z, k_r, k_z') \left[\frac{2C(s)}{[1+k_z^2]^{\frac{s}{2}}} \right] \left[4D(s,q) \frac{k_r^q}{[1+k_r^2]^{\frac{s+q}{2}}} \right]. \tag{5.87}$$

It should be noted that $f(k_r, k_z')$ is related to the field line diffusion coefficient by

$$K_{FL} = 2\pi K^2 \int\limits_0^{\infty} \mathrm{d}k_r \, f(k_r, 0). \tag{5.88}$$

5.4.2.3 Compound Sub–Diffusion Equations

The last set of equations for perpendicular transport that need scaling are those for compound sub–diffusion (3.103):

$$\left\langle (\Delta x)^2 \right\rangle = 4\kappa_{FL} \sqrt{\frac{\kappa_\parallel t}{\pi}}$$

and (3.105)

$$d_\perp(t) = 2\kappa_{FL} \sqrt{\frac{\kappa_\parallel}{\pi t}}.$$

Since these equations do not need to be solved, as they have no unknowns and are just overlaid on the simulation data, the scaling that is applied to the UNLT and FLPD equations for time is not used here. Instead, the equations are scaled using (5.49) for the parallel diffusion coefficient and (5.75) for the field line diffusion coefficient to find

$$\sigma_x^2 = 4K_{FL} \sqrt{\frac{K_\parallel T}{\pi}} \tag{5.89a}$$

and

$$\frac{d_\perp(t)}{\Omega \ell_\perp^2} = 2K_{FL} \sqrt{\frac{K_\parallel}{\pi T}} \tag{5.89b}$$

for the mean square displacement and running diffusion coefficient, respectively.

5.4.2.4 Summary and Numerical Implementation of Perpendicular Transport Equations

Having scaled all the equations used in the analysis of the results presented in Chapter 6, a brief summary is discussed here. The time–dependent UNLT theory equation for noisy slab turbulence (5.71) is

$$\frac{\mathrm{d}^2\sigma_x^2}{\mathrm{d}t'^2} = \frac{2}{3}\Lambda_\parallel^2 K^2 \sqrt{\frac{\pi}{2\sigma_x^2}}\,\mathrm{erf}\left(\sqrt{\frac{\sigma_x^2}{2}}\right)\int\limits_{-\infty}^{\infty}\mathrm{d}k_z\,\epsilon(k_z,t')\frac{2C(s)}{[1+k_z^2]^{\frac{s}{2}}},$$

while the equation for full 3D turbulence (5.72) is

$$\frac{\mathrm{d}^2\sigma_x^2}{\mathrm{d}t'^2} = \frac{2}{3}\Lambda_\parallel^2 K^2 \int\limits_{-\infty}^{\infty}\mathrm{d}k_z\,\epsilon(k_z,t')\frac{2C(s)}{[1+k_z^2]^{\frac{s}{2}}}\int\limits_{0}^{\infty}\mathrm{d}k_r\,4D(s,q)\frac{k_r^q}{[1+k_r^2]^{\frac{s+q}{2}}}e^{-\frac{1}{2}\sigma_x^2k_r^2}.$$

Here $\epsilon(k_z,t')$ is given by (5.70):

$$\epsilon(k_z,t') = \begin{cases} \dfrac{\omega'_+e^{-\omega'_+t'/2}-\omega'_-e^{-\omega'_+t'/2}}{2\omega_0} & k_z < \sqrt{3}/2\Lambda_\parallel \\ e^{-t'/2}\left[1-\dfrac{t'}{2}\right] & k_z = \sqrt{3}/2\Lambda_\parallel \\ e^{-t'/2}\left[\cos\left(\dfrac{\omega_0 t'}{2}\right)-\dfrac{1}{\omega_0}\sin\left(\dfrac{\omega_0 t'}{2}\right)\right] & k_z > \sqrt{3}/2\Lambda_\parallel \end{cases}.$$

The scaled quantities $\omega'_\pm$ and ω_0 are respectively given by (5.61) and (5.62):

$$\omega'_\pm = 1 \pm \sqrt{1-\frac{4}{3}\Lambda_\parallel^2k_z^2},$$
$$\omega_0 = \sqrt{1-\frac{4}{3}\Lambda_\parallel^2k_z^2}.$$

The noisy slab and full 3D field line diffusion coefficient equations, required for FLPD theory, are respectively given by (5.82) and (5.83)

$$K_{FL} = 2K^2\int\limits_0^{\infty}\mathrm{d}k_z\int\limits_0^{1}\mathrm{d}k_r\begin{cases}\left[\dfrac{2C(s)}{[1+k_z^2]^{\frac{s}{2}}}\right]\left[\dfrac{K_{FL}k_r^2}{k_z^2+K_{FL}^2k_r^4}\right] & \text{Noisy Slab}\\ \left[\dfrac{2C(s)}{[1+k_z^2]^{\frac{s}{2}}}\right]\left[\dfrac{K_{FL}k_r^2}{k_z^2+K_{FL}^2k_r^4}\right]\left[4D(s,q)\dfrac{k_r^q}{[1+k_r^2]^{\frac{s+q}{2}}}\right] & \text{Full 3D}\end{cases}$$

while the FLPD theory equations are (5.85)

$$\frac{\mathrm{d}^2\sigma_x^2}{\mathrm{d}t'^2} = \frac{2}{3}\Lambda_\parallel^2K^2\int\limits_{-\infty}^{\infty}\mathrm{d}k'_z\int\limits_0^{\infty}\mathrm{d}k_r\,\epsilon(k'_z,t')f(k_r,k'_z)e^{-\frac{1}{2}\sigma_x^2k_r^2}.$$

The function $f(k_r, k_z')$, given by (5.84), is

$$f(k_r, k_z') = \int\limits_{-\infty}^{\infty} \mathrm{d}k_z\, R'(k_z, k_r, k_z') \begin{cases} \left[\dfrac{2C(s)}{[1+k_z^2]^{\frac{s}{2}}}\right] \Theta(1-k_r) & \text{Noisy Slab} \\ \left[\dfrac{2C(s)}{[1+k_z^2]^{\frac{s}{2}}}\right] \left[4D(s,q)\dfrac{k_r^q}{[1+k_r^2]^{\frac{s+q}{2}}}\right] & \text{Full 3D.} \end{cases}$$

as per equations (5.86) and (5.87).

A summary of the quantities appearing in these equations is found in Table 5.6, while the conversion between simulation and theory scaling can be found in Table 5.5. Note that the parameters derived from the parallel transport ($\tau_\parallel'$, $\Lambda_\parallel$) don't need to be re-scaled for use in the perpendicular transport equations.

Quantity	Simulation	Theory	Conversion
Time	$T^S = \Omega t$	$T^T = t/\tau_\parallel$	$T^T = \frac{1}{\tau_\parallel'} T^S$
Perpendicular Mean Square Displacement	$\sigma_x^S = \frac{\left\langle (\Delta x)^2 \right\rangle}{\ell_p^2}$	$\sigma_x^T = \frac{\left\langle (\Delta x)^2 \right\rangle}{\ell_\perp^2}$	$\sigma_x^T = \frac{\ell_p^2}{\ell_\perp^2} \sigma_x^S$
Perpendicular Running Diffusion Coefficient	$D_\perp^S(T) = \frac{d_\perp(t)}{\Omega \ell_p^2}$	$D_\perp^T(T) = \frac{\tau_\parallel' d_\perp(t)}{\Omega \ell_\perp^2}$	$D_\perp^T(T) = \tau_\parallel' \frac{\ell_p^2}{\ell_\perp^2} D_\perp^S(T)$

Table 5.5: Conversion between simulation and theory scales for perpendicular transport.

When it comes to solving the equations describing perpendicular transport, there are two solution methods needed. First, the equations for field line diffusion coefficient and diffusive UNLT theory need to be solved using either an iterative method or with a root finder. The iterative method has the potential to be faster than the root finder, provided it converges. The root finder, on the other hand, should be more robust than the iterative method. Unfortunately for both methods, the equations have at least two positive roots, one of which is zero. That said, it was found that so long as the initial guess isn't zero, the iterative method will converge to the non–trivial value.

The second solution method needed is an ODE solver for the time–dependent UNLT and FLPD equations. In this work MATLAB's *ode45* solver, the fourth order Runge–Kutta method of Dormand and Prince (1980), is used to solve the equations.

Quantity	Unscaled	Scaled	Scale Factor	Defined in
Time	t	$t' = t/\tau_\parallel$	$\frac{1}{\tau_\parallel} = \frac{v}{\lambda_\parallel}$	(5.65)
Particle Velocity	v	$R = \frac{v}{\Omega \ell_\parallel}$	$\frac{1}{\Omega \ell_\parallel} = \frac{\gamma mc}{qB_0 \ell_\parallel}$	(1.5)
Parallel Mean Free Path	$\lambda_\parallel$	$\Lambda_\parallel = \frac{\lambda_\parallel}{\ell_\parallel}$	$\frac{1}{\ell_\parallel}$	(5.51)
Parallel Scattering Time	$\tau_\parallel$	$\tau'_\parallel = \Omega \tau_\parallel$	$\Omega = \frac{qB_0}{\gamma mc}$	(5.53), (5.55b)
Turbulence Energy Density	δB^2	$K^2 = \frac{\ell_\parallel^2}{\ell_\perp^2} \frac{\delta B^2}{B_0^2}$	$\frac{\ell_\parallel^2}{\ell_\perp^2} \frac{1}{B_0^2}$	(3.52)
Spectral Normalization Factor	$C(s),\ D(s,q)$	$C(s),\ D(s,q)$		(2.25)
Parallel Wave Number	$k_\parallel$	$k_z = k_\parallel \ell_\parallel$	$\ell_\parallel$	(5.58)
Perpendicular Wave Number	$k_\perp$	$k_r = k_\perp \ell_\perp$	$\ell_\perp$	(5.58)
Field Line Diffusion Coefficient	κ_{FL}	$K_{FL} = \frac{\ell_\parallel \kappa_{FL}}{\ell_\perp^2}$	$\frac{\ell_\parallel}{\ell_\perp^2}$	(5.75)
Perpendicular Mean Square Displacement	$\left\langle (\Delta x)^2 \right\rangle$	$\sigma_x^2 = \frac{\left\langle (\Delta x)^2 \right\rangle}{\ell_\perp^2}$	$\frac{1}{\ell_\perp^2}$	(3.46)
Perpendicular Running Diffusion Coefficient	$d_\perp(t)$	$D_\perp(t') = \frac{\tau'_\parallel d_\perp}{\Omega \ell_\perp^2}$	$\frac{\tau'_\parallel}{\Omega \ell_\perp^2} = \frac{\lambda_\parallel}{v \ell_\perp^2}$	(5.58)
Perpendicular Diffusion Coefficient	$\kappa_\perp$	$K_\perp = \frac{\tau'_\parallel \kappa_\perp}{\Omega \ell_\perp^2}$	$\frac{\tau'_\parallel}{\Omega \ell_\perp^2} = \frac{\lambda_\parallel}{v \ell_\perp^2}$	(5.58)

Table 5.6: Summary of scaled quantities used in perpendicular transport equations.

Chapter 6

Results

Statement of Originality

This chapter contains both figures (6.1a and 6.4) and variations of figures (6.1b and 6.3a) for particle transport in noisy slab turbulence that were originally published in Shalchi and Arendt (2024b), Brazilian Journal of Physics, Volume 54, p. 126, 2024 by Springer Nature. They have been reproduced under the publishing agreement with Springer Nature. Figure titles and axis labels have been modified to be consistent with the rest of this work.

The analysis figures for parallel and perpendicular transport in full 3D turbulence are a variation of figures set to appear in an upcoming article (Arendt and Shalchi, 2025), which has been submitted to Advances in Space Research. Figure titles and axis labels have been modified to be consistent with the rest of this work.

As the name of the chapter implies, the results of the noisy slab and full 3D model simulations performed for this work are presented here, along with the corresponding analysis. The parameter sets (see the beginning of Chapter 5 for a definition) used in this work are summarized in Table 6.1. In order to limit the number of internal parameters that need to be determined, a set of guidelines were used. These guidelines are:

- Each simulation consists of the trajectories of at least six particles. A data set is, at minimum, one thousand simulations (each with a unique field) for a total of 6000 particles per data set.

- The initial sphere that all particles are created within is set to a radius of $r = 10$. This allows for variation in the field due to both parallel and perpendicular Fourier mode components.

- The integration time step size is set based on the particle rigidity.

  $$\mathrm{d}T = \begin{cases} 0.01 & R \leq 1 \\ 0.001 & R > 1 \end{cases}$$

- The data is output at an interval given by

  $$\Delta T = \max\left(5, \frac{T_{max}}{2000}\right).$$

  This reduces the number of points that need to be stored and later analyzed to a manageable amount.

- As stated in Chapter 5, the minimum Fourier wave number is set to 10^{-5}. More specifically, the minimum Fourier wave number is set to $10^{-5}\ell_p/\ell_i$, where ℓ_p is the primary length scale and ℓ_i is the length scale for the direction in question. This means that the minimum perpendicular Fourier wave number is $5 \cdot 10^{-6}$ for $\ell_\perp = 2\ell_\parallel$.

- The maximum Fourier wave number, which needs to be determined, is set to $k_{i,max} = 10^n$, where n is an integer greater than or equal to 3 and i is the Fourier wave mode axis.
  - For the noisy slab model, the maximum perpendicular Fourier wave number is $k_{\perp,max}\ell_\parallel = \ell_\parallel/\ell_\perp$.

- The number of parallel (N) and perpendicular (M) modes used is given by either a power of two or a sum of two powers of two. Equation 5.12 is used to generate the Fourier modes both when determining how many modes are needed and for the final simulations. Equation 5.13 is used when varying the maximum mode.
  - To simplify the analysis and reduce the number of data sets needed, it is assumed that the required values of N and M are independent of one another.

Parameter Name	Parameter Symbol	Parameter Value(s)
Particle Rigidity	R	0.01, 0.1, 1.0, 10.0
Field Energy Density	δb^2	0.2, 0.5, 1.0, 2.0
Primary Length Scale	ℓ_p	$\ell_p = \ell_\parallel$
Secondary Length Scale	ℓ_s	$\ell_s = \ell_\perp = 2\ell_\parallel$
Kubo Number	K	$\frac{1}{2\sqrt{10}}, \frac{1}{4}, \frac{1}{2\sqrt{2}}, \frac{1}{2}$

Table 6.1: List of physical parameters used in this work. Altogether there are 16 parameter sets examined per field model, one for each combination of the field energy density and particle rigidity. The Kubo number is calculated as per (3.52).

With the goal of studying the predictions of analytical theory in the limit of small Kubo numbers, Hussein et al. (2015) was chosen as a baseline when selecting model parameters, as it contained data regarding the diffusion coefficients for various particle energies for a single Kubo number for noisy slab turbulence. For this work, the range of Kubo numbers was expanded from a single value to four different values, with four particle rigidities per Kubo number (see Table 6.1). Using Hussein et al. (2015) as a starting point meant that the number of parallel and perpendicular modes used in the noisy slab simulations should be $N = 32$ and $M = 256$, respectively, and a maximum time of $t_{max} = 10^5$. The influence of the number of parallel and perpendicular modes, as well as the maximum parallel mode, were investigated using field energy density ratios of $\delta b^2 = 0.2$ and $\delta b^2 = 2.0$. What was found was that the number of parallel modes needed to be increased to 256, while at low particle rigidities ($R < 1$) the number of perpendicular modes could be reduced to 16. At higher particle rigidities ($R \geq 1$), the number of perpendicular modes needed to be increased to at least 64. The maximum parallel mode had negligible effect at low turbulence energy densities, whereas at higher energy densities it needed to be increased by at least an order of magnitude. Details on the calibration of the turbulence parameters, using $R = 0.01$ as an example, can be found in Appendix C.

One of the difficulties encountered with low rigidity particles was that, compared to theoretical predictions and simulations with $R = 1$, the system took much longer to transition from a state of compound sub–diffusion to a state of normal diffusion in the perpendicular direction. Specifically, the simulations with $R = 0.01$ and $R = 0.10$ were still in a compound sub–diffusive state at a maximum times of $T = 10^6$ for the former and $T = 10^5$ for the latter. Compounding this was the fact that the simulations were reaching the maximum run time allowed on the computational servers being used. In order to be able to perform the simulations with an increased maximum time, several changes to the simulation parameters were made. First, the integration method was changed from the three–step, third–order IRM to the single–step exact method (see Chapter 4). Secondly, the number of parallel modes was decreased from 256 to 128. Finally, the step size used in the integration method was increased from $\mathrm{d}T = 0.01$ to $\mathrm{d}T = 0.02$.[1] The combination of these changes allowed for the maximum time to be increased to $T_{max} = 10^7$, where normal perpendicular diffusion was found using particles with rigidity $R = 0.10$ in noisy slab turbulence with $\delta b^2 = 1.0$. The reason for this delay in the transition from compound sub–diffusion to normal diffusion is discussed in Shalchi and Arendt (2024b), where it is shown that the long–range correlations in the magnetic field are the cause of the delay. As a result of this, the majority of the low rigidity noisy slab simulations are not used in this work outside of Appendix C, where the $R = 0.01$ simulations are used as an example for the field calibration. Only the noisy slab simulation used in Shalchi and Arendt (2024b) is shown in this chapter, as it shows that the system does reach a state of normal diffusion in the perpendicular direction.

With this in mind, the simulations were repeated with the same physical parameters (see Table 6.1) using the full 3D turbulence model, as it does not have the long–range correlations that the noisy slab model does. Unlike the noisy slab model, the full 3D model did not go through the same calibration process for N, M, and k_{max}. Instead, these values were determined in simulations of the field line random walk performed by A. Shalchi, and as a result this data is not presented in this work. The simulation results for the full 3D model can be found in Section 6.2, while the noisy slab results are discussed next.

---

[1] The number of particles used in the simulation was also decreased to 2000. Since particles are simulated and written to file sequentially, this didn't affect the run time per particle. Rather, it decreased the number of times the simulation needed to be repeated.

6.1 Noisy Slab Model Results

Rigidity	Field Energies	N	M	K_{max}	Source
0.10	1.0	128	16	10^3	Shalchi and Arendt (2024b)
1.00	0.2, 0.5	128	64	10^3	This Work
1.00	1.0, 2.0	288	64	10^4	This Work
1.00	0.2, 0.5	256	64	10^3	This Work
1.00	1.0, 2.0	320	128	10^5	This Work

Table 6.2: Noisy slab model parameters per rigidity and field energy.

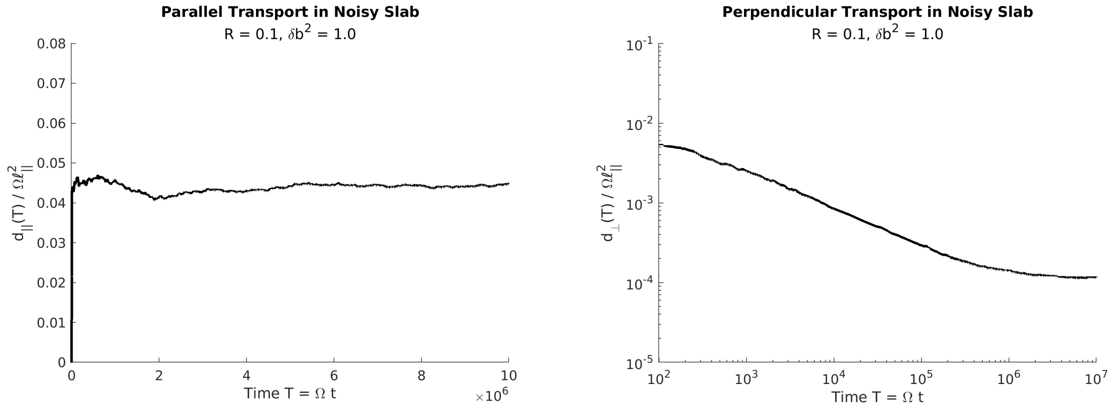

(a) Parallel transport (b) Perpendicular transport

Figure 6.1: Running diffusion coefficients in the noisy slab model with $R = 0.10$ and $\delta b^2 = 1$. Shown is the data from Shalchi and Arendt (2024b). As can be seen, the system does transition to normal diffusion in the perpendicular direction. *Reproduced with permission from Springer Nature.*

The field parameters used in the simulations presented here are listed in Table 6.2. Figure 6.1 shows the results published in Shalchi and Arendt (2024b) without the accompanying analysis, from which it can be seen that although the system is sub–diffusive for a large period of time initially, it does in fact transition to normal diffusion in the perpendicular plane. Figure 6.2 shows the results of simulations without any accompanying analysis, such as parallel curve fitting or theoretical predictions for perpendicular transport.

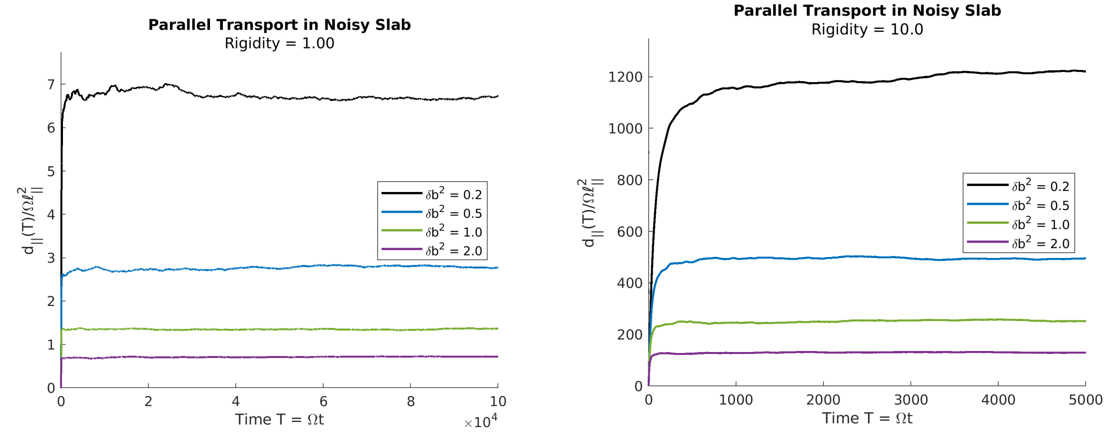

(a) Rigidity = 1.00, Parallel Transport (b) Rigidity = 10.0, Parallel Transport

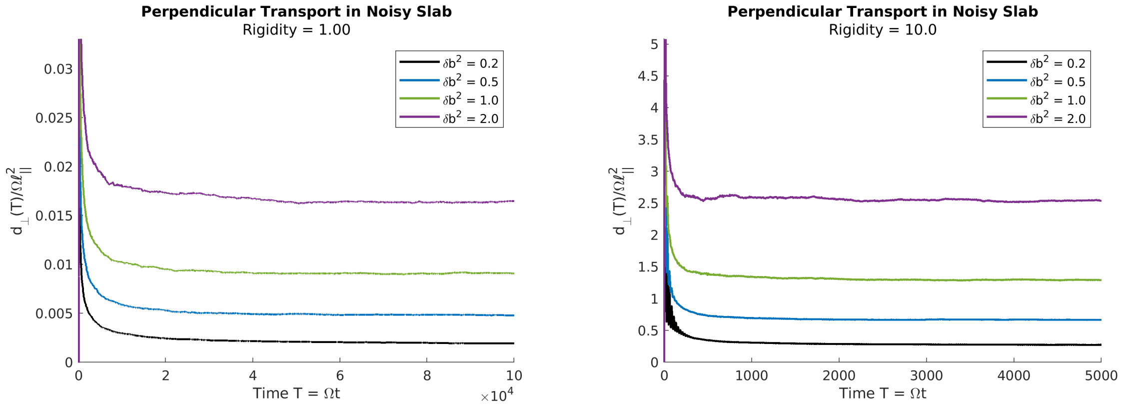

(c) Rigidity = 1.00, Perpendicular Transport (d) Rigidity = 10.0, Perpendicular Transport

Figure 6.2: Parallel and perpendicular running diffusion in noisy slab turbulence. Colour coding by turbulence energy: $\delta b^2 = 0.2$, $\delta b^2 = 0.5$, $\delta b^2 = 1.0$, $\delta b^2 = 2.0$.

6.1.1 Parallel Transport Analysis

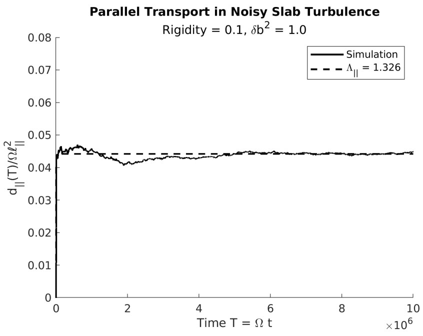

(a) Rigidity $= 0.10$

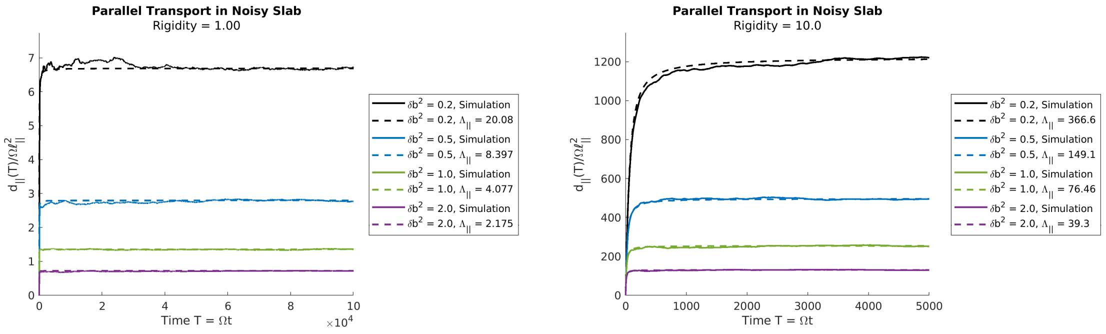

(b) Rigidity $= 1.00$

(c) Rigidity $= 10.0$

Figure 6.3: Parallel running diffusion in noisy slab turbulence. Shown is the simulation data (solid lines) and fit of the theoretical equation (dashed lines). Colour coding by turbulence energy in sub–figures (b) and (c): $\delta b^2 = 0.2$, $\delta b^2 = 0.5$, $\delta b^2 = 1.0$, $\delta b^2 = 2.0$.

$\Lambda_\parallel = \lambda_\parallel/\ell_\parallel$		Field Energy Density			
		0.2	0.5	1.0	2.0
Rigidity	1.00	20.08	8.397	4.077	2.175
	10.0	366.6	149.1	76.46	39.30

Table 6.3: Parallel mean free path in noisy slab turbulence.

As discussed in Section 5.4.1, (5.55a) is fitted to the simulation data to determine the parallel scattering time $\tau'_\parallel$, which is combined with (5.55b) to get the parallel mean free path. Figure 6.3 shows the resulting theoretical functions overlaid on the simulation results, while the computed parallel mean free paths are listed in Table

6.3. Parallel transport is seen to be well described by the theoretical equations in Chapter 3.3.2.

6.1.2 Perpendicular Transport Analysis

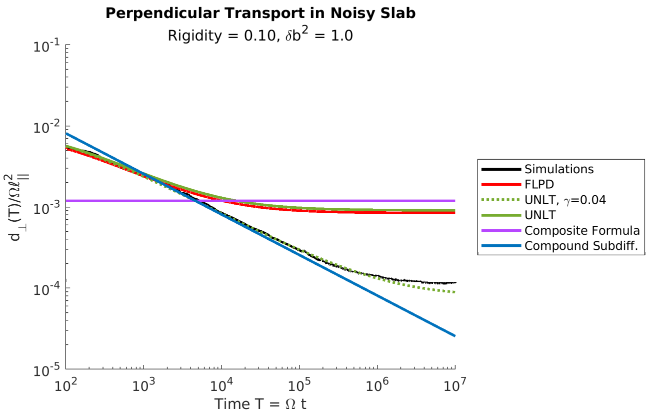

Figure 6.4: Comparison of simulation results and analytical theory in noisy slab turbulence for $R = 0.10$. *Originally published in Shalchi and Arendt (2024b).*

Figure 6.4 (originally published in Shalchi and Arendt (2024b)) contains the results for perpendicular transport in noisy slab turbulence with $B_0^2 = B_0$ and $R = 0.10$. In addition to compound sub–diffusion, UNLT theory, and FLPD theory, Shalchi and Arendt (2024b) also considered several other methods of calculating the perpendicular diffusion coefficient. The composite formula referenced in the figure is an equation derived from heuristic arguments in Shalchi (2019b):

$$\kappa_\perp = \frac{\ell_\perp^2 v^2}{16\kappa_\parallel}\left[\sqrt{1+8\frac{\kappa_{FL}\kappa_\parallel}{\ell_\perp^2 v}}-1\right]^2. \tag{6.1}$$

Also considered was a modification of UNLT theory, where "delay" factor γ is introduced into the equation via

$$\left\langle e^{i\vec{k}_\perp \vec{x}}\right\rangle = e^{-\frac{1}{2}\gamma\left\langle(\Delta x)^2\right\rangle k_\perp^2}. \tag{6.2}$$

The standard UNLT equation can be recovered by setting $\gamma = 1$. Shalchi and Arendt (2024b) found that a delay factor of $\gamma = 0.04$ could reproduce the results for the noisy slab model and its variants better than standard UNLT or FLPD theory. This was not found for the full 3D model however. In the figure it can be seen that the system is in a compound sub–diffusive state till between $T = 10^4$ and $T = 10^5$. The noticeable divergence from compound sub–diffusion and transition to normal diffusion occurs for

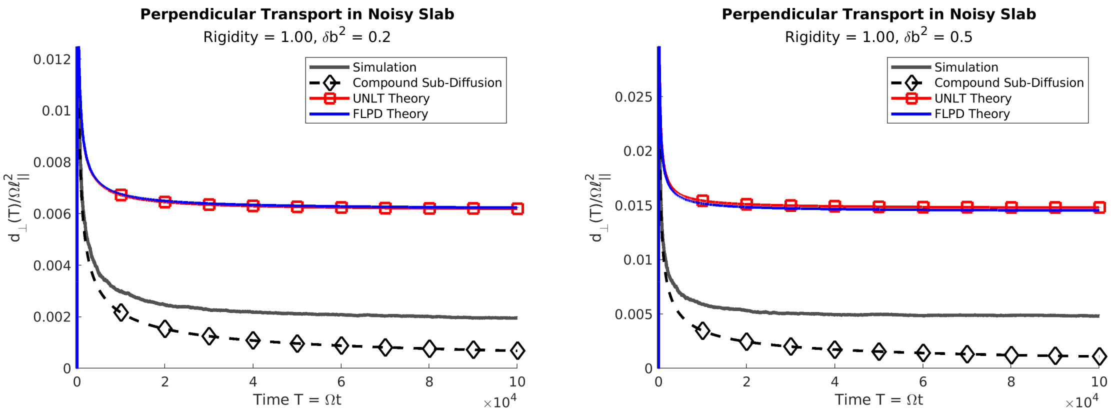

(a) $\delta B^2 = 0.2 B_0^2$ (b) $\delta B^2 = 0.5 B_0^2$

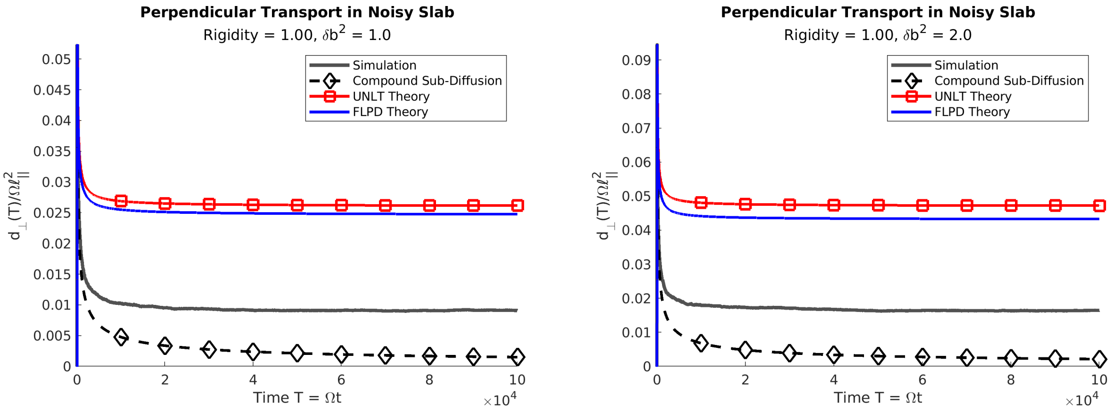

(c) $\delta B^2 = 1.0 B_0^2$ (d) $\delta B^2 = 2.0 B_0^2$

Figure 6.5: Comparison of simulation results and time–dependent analytical theory in noisy slab turbulence for $R = 1.00$. Colour coding: simulation, compound sub–diffusion (dashed, diamond markers), UNLT (square markers), FLPD.

$T > 10^5$. This can be contrasted with the results for $R = 1$ (see Figure 6.5), where the system is in normal diffusive state by $T = 10^5$, and with the results for the full 3D model with $R = 0.10$ (see Figure 6.13), where the system is in a normal diffusive state by $T = 5 \cdot 10^4$.

Figures 6.5, and 6.6 show the time–dependent UNLT and FLPD theoretical predictions for particles with $R = 1.00$ and $R = 10.0$, respectively. In both figures it can be seen that FLPD theory results become equal to UNLT theory results in the limit of small Kubo numbers for the noisy slab model. Comparing the ratio of the FLPD theory prediction to the simulation results shows that the theoretical predictions are with an order magnitude of the simulation results (see Table 6.4). The simulation

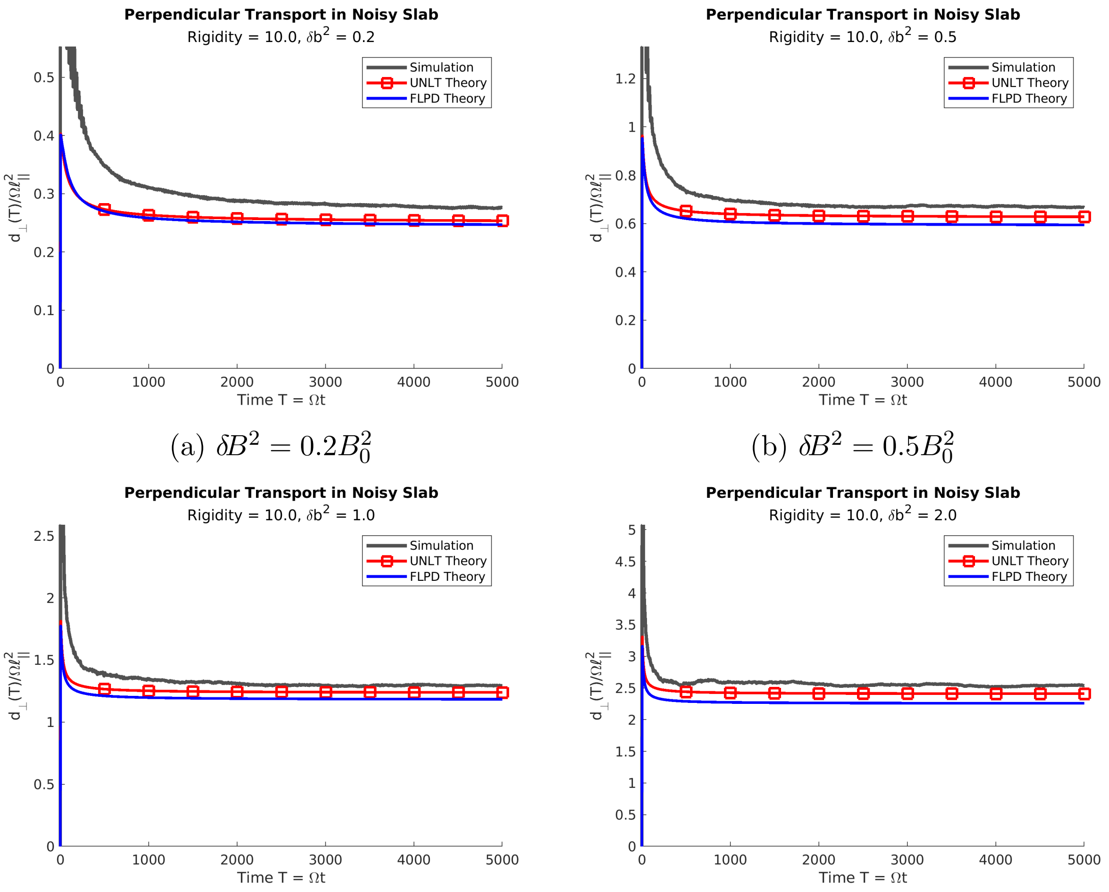

(a) $\delta B^2 = 0.2 B_0^2$ (b) $\delta B^2 = 0.5 B_0^2$

(c) $\delta B^2 = 1.0 B_0^2$ (d) $\delta B^2 = 2.0 B_0^2$

Figure 6.6: Comparison of simulation results and analytical theory in noisy slab turbulence for $R = 10.0$. Colour coding: simulation, UNLT (square markers), FLPD.

results are calculated by averaging the last 50 data points, whereas the FLPD result is the value obtained from theory at T_{max}.

$\lambda_\perp^{FLPD}/\lambda_\perp^{Sim}$		Field Energy Density			
		0.2	0.5	1.0	2.0
Rigidity	1.00	3.192	3.016	2.716	2.630
	10.0	0.896	0.891	0.914	0.888

Table 6.4: Ratio of the predictions of FLPD theory and simulation results for noisy slab turbulence.

6.2 Full 3D Model Results

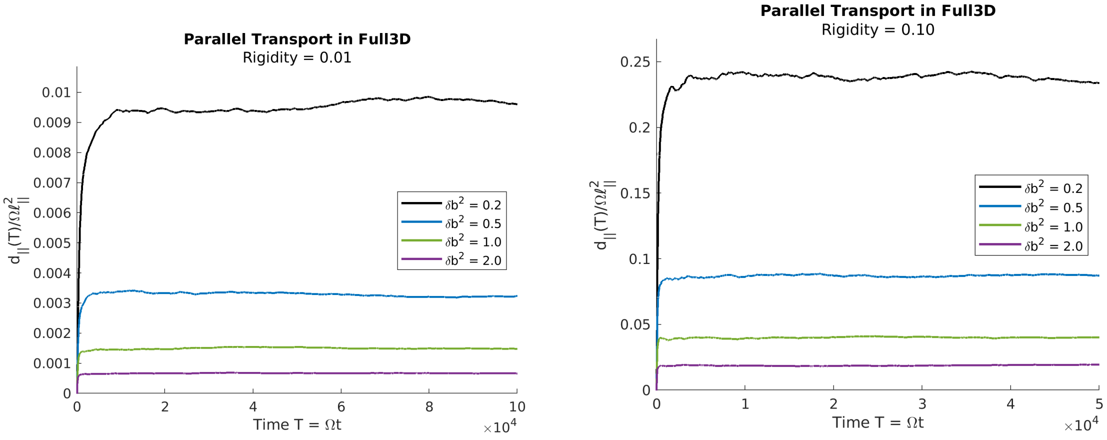

(a) Rigidity = 0.01 (b) Rigidity = 0.10

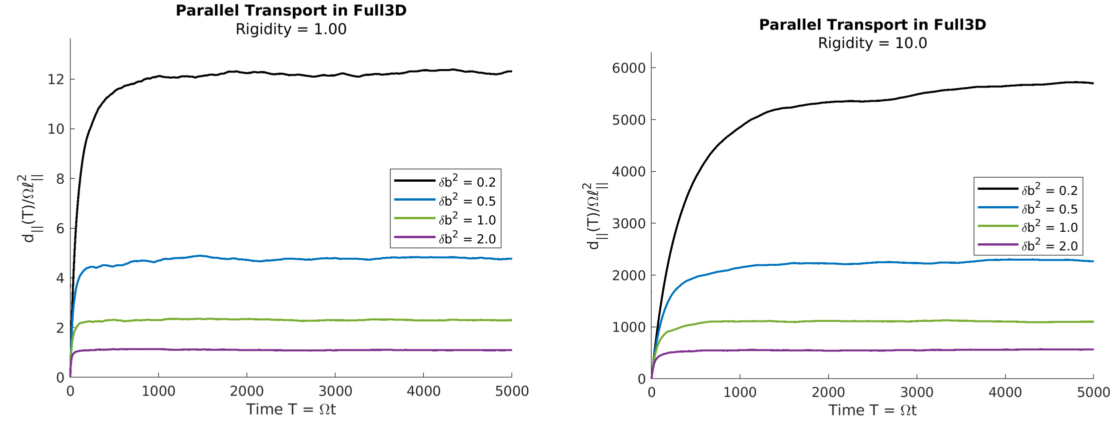

(c) Rigidity = 1.00 (d) Rigidity = 10.0

Figure 6.7: Parallel running diffusion in full 3D turbulence. Data is colour coded based on the magnetic field energy density $\delta b^2 = 0.2$, $\delta b^2 = 0.5$, $\delta b^2 = 1.0$, $\delta b^2 = 2.0$.

As was mentioned at the start of this chapter, the internal field parameters (N, M, k_{max}) were determined in simulations of the field line random walk performed by A. Shalchi. These parameters were set to $N = M = 128$ and $k_{max} = 10^3$, with each simulation using the same parameters. The results of the simulations are shown in Figures 6.7 (parallel transport) and 6.8 (perpendicular transport). In Figure 6.8 it can be seen that system does not fully reach a normal diffusive state within the time frame considered for $R = 0.01$; however, it will be shown in Section 6.2.2 that the system is not in a compound sub–diffusive state either. Due to the fact that the

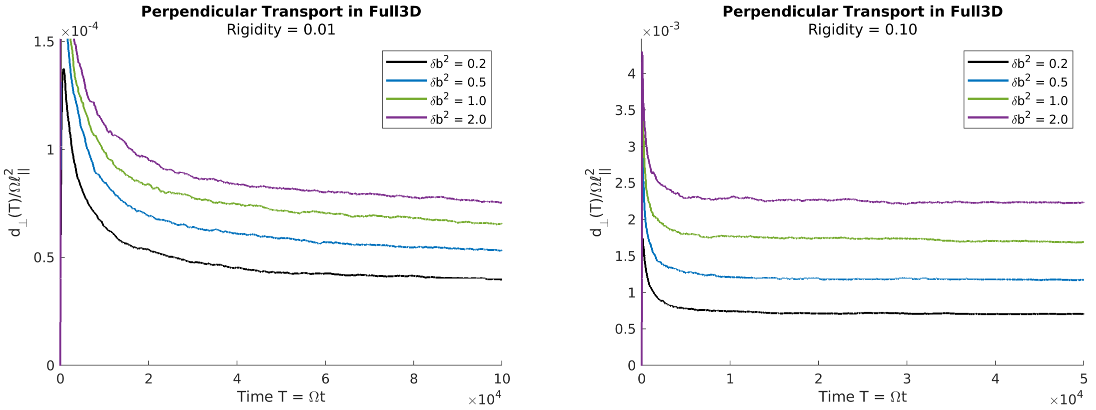

(a) Rigidity = 0.01

(b) Rigidity = 0.10

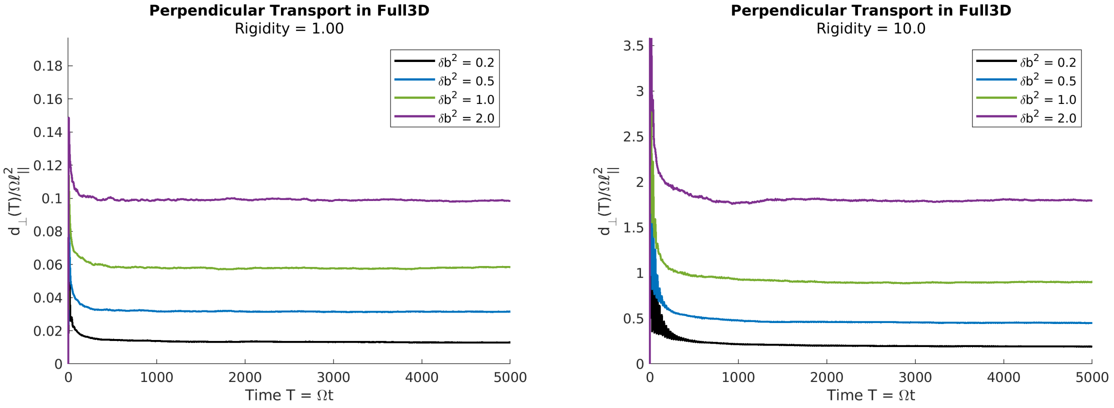

(c) Rigidity = 1.00

(d) Rigidity = 10.0

Figure 6.8: Perpendicular running diffusion in full 3D turbulence. Data is colour coded based on the magnetic field energy density $\delta b^2 = 0.2$, $\delta b^2 = 0.5$, $\delta b^2 = 1.0$, $\delta b^2 = 2.0$.

total number of wave modes used for the full 3D model is four times greater than that used in the noisy slab model, extending the maximum time was not much of an option. Therefore, the diffusion coefficient for these data sets can be viewed as an upper limit.[2] It is also possible that normal diffusion has already been reached and is just obscured due the definition of the diffusion coefficient being used (see Chapter 1.2.2.1).

---

[2] Longer times could be simulated by switching the integration method to use fewer intermediate steps, such as the single step version of the IRM method, as was used for Shalchi and Arendt (2024b). However, in order to be consistent, this was not done.

6.2.1 Parallel Transport Analysis

$\Lambda_\parallel = \frac{\lambda_\parallel}{\ell_\parallel}$		Field Energy Density			
		0.2	0.5	1.0	2.0
Rigidity	0.01	2.918	0.977	0.452	0.204
	0.10	7.156	2.629	1.209	0.575
	1.00	37.17	14.45	6.950	3.307
	10.0	1769	695.3	335.7	169.5

Table 6.5: Parallel mean free paths in full 3D turbulence.

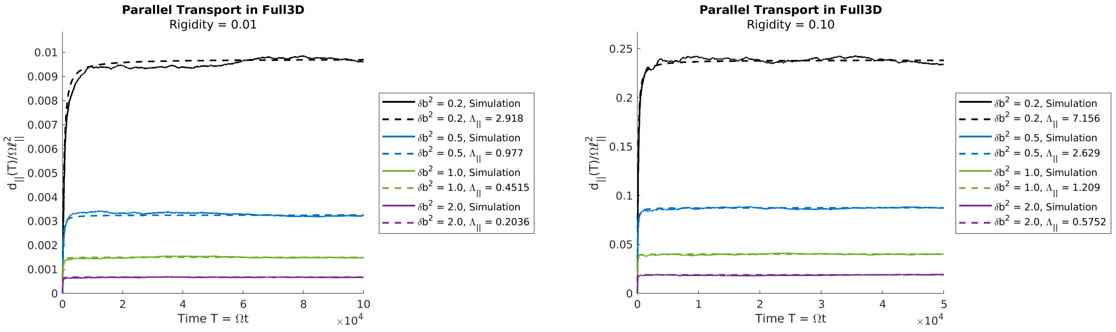

(a) Rigidity = 0.01 (b) Rigidity = 0.10

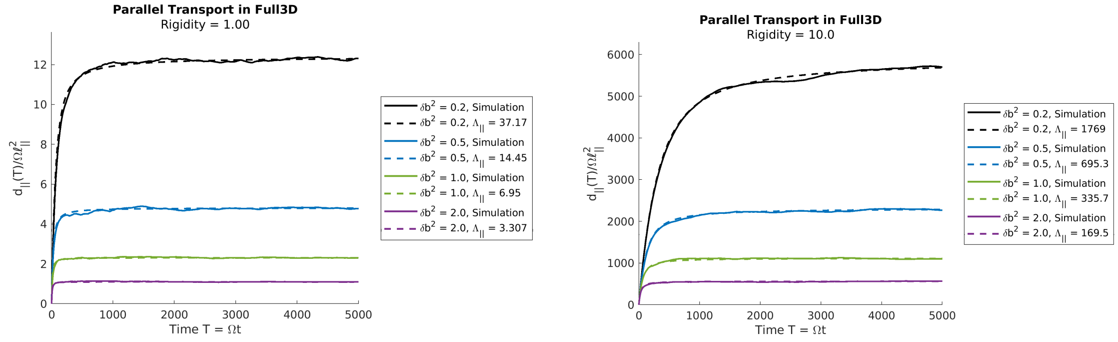

(c) Rigidity = 1.00 (d) Rigidity = 10.0

Figure 6.9: Parallel running diffusion in full 3D turbulence. Data is colour coded based on the magnetic field energy density $\delta B^2/B_0^2$: $\delta b^2 = 0.2$, $\delta b^2 = 0.5$, $\delta b^2 = 1.0$, $\delta b^2 = 2.0$. Solid lines are the simulation data, the dashed lines are the result of fitting the theoretical equation.

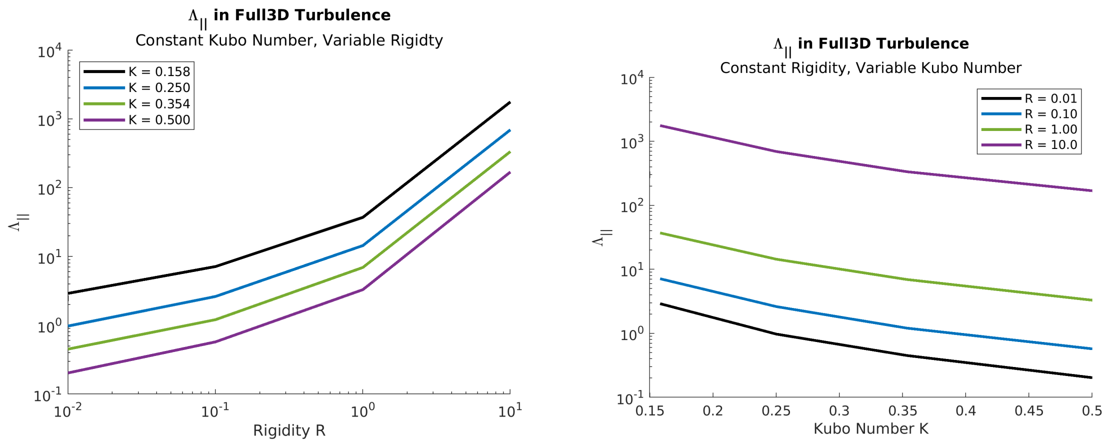

(a) Parallel mean free path as a function of rigidity for constant Kubo number.

(b) Parallel mean free path as a function of Kubo number for constant rigidity.

Figure 6.10: Parallel mean free path in full 3D turbulence as a function of rigidity (left) and Kubo number (right). Results are colour coded by the variable that is held constant in each figure.

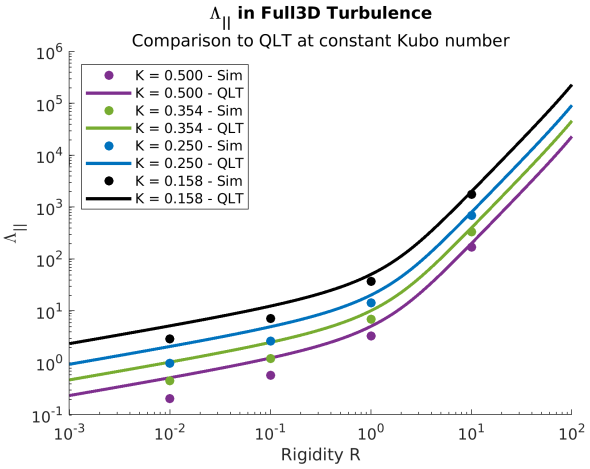

Figure 6.11: Parallel mean free path comparison between simulation results (solid circles) and QLT predictions (lines). Data is colour coded based on the magnetic field energy density $\delta B^2/B_0^2$: $\delta b^2 = 0.2$, $\delta b^2 = 0.5$, $\delta b^2 = 1.0$, $\delta b^2 = 2.0$.

As with the noisy slab model, (5.55a) is fitted to simulation data to determine the parallel scattering time, from which the parallel mean free path and diffusion coefficient can be calculated. The computed parallel mean free paths for particles in full 3D turbulence are summarized in Table 6.5, while the theoretical parallel running diffusion coefficients are compared to simulation data in Figure 6.9. As was found for the noisy slab model, the theoretical equation for the running parallel diffusion coefficient readily describes the simulation behaviour. Figure 6.10 shows the parallel mean free path as a function of particle rigidity (left) and Kubo number (right). Figure 6.11 shows the comparison between simulation results and QLT predictions. The ratio of the QLT predictions and simulation results are given in Table 6.6. The QLT calculations were performed by A. Shalchi for Arendt and Shalchi (2025), and take into consideration finite gyro–radius effects. From the figure and table it can be seen that as the rigidity increases the agreement between simulation and theory increases.

$\lambda_{\parallel}^{QLT}/\lambda_{\parallel}^{Sim}$		Field Energy Density			
		0.2	0.5	1.0	2.0
Rigidity	0.01	1.774	2.120	2.294	2.543
	0.10	1.736	1.890	2.055	2.160
	1.00	1.362	1.401	1.457	1.531
	10.0	1.131	1.150	1.191	1.180

Table 6.6: Ratio of QLT predictions and Full 3D simulation results.

6.2.2 Perpendicular Transport Analysis

In the introduction to this section, it was mentioned that the perpendicular transport for a rigidity of $R = 0.01$ does not reach a normal diffusive state within the time frame simulated. What can be seen in Figure 6.12 is that while the system is not in a normal diffusive state,[3] neither is it in a state of compound sub–diffusion, and therefore the perpendicular diffusion coefficient for $R = 0.01$ can be taken as upper limits. For rigidities of $R = 0.1$ (Figure 6.13) and $R = 1$ (Figure 6.14) we find that the system is diffusive within the time frame considered, with almost perfect agreement between FLPD theory and simulation results for $R = 1$ and $\delta B^2 = B_0^2$. At a rigidity of $R = 10$ (Figure 6.15), analytical theory predicts that the system becomes diffusive much faster than it actually does. However, at this particle energy *finite gyroradius effects* are present, especially at lower turbulence energy densities (sub–figures (a) and (b)). Finite gyroradius effects are due to the fact the magnetic field at the particle location is not the same the magnetic field at the particle's guiding center. For low energy particles, the difference is negligible, but as the energy of the

---

[3] It is easier to see that the system is not diffusive in Figure 6.8(a) due to the range on the y–axis.

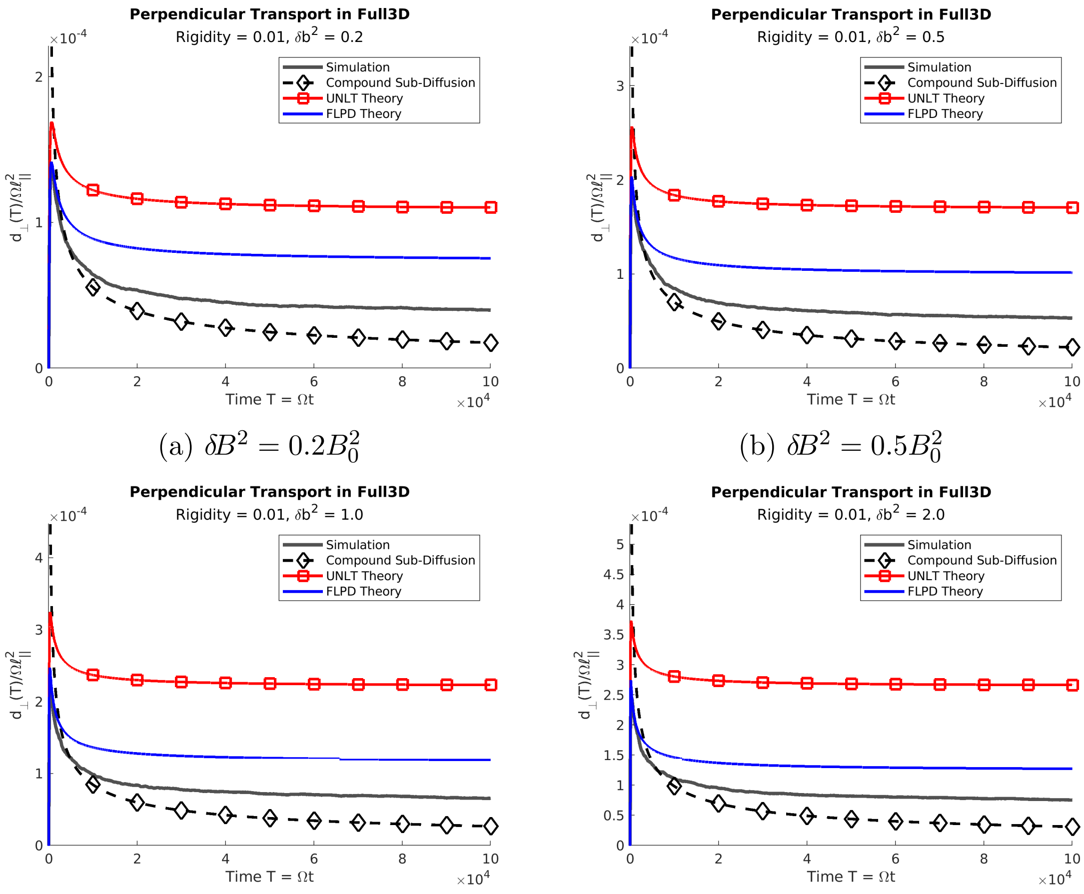

(a) $\delta B^2 = 0.2B_0^2$

(b) $\delta B^2 = 0.5B_0^2$

(c) $\delta B^2 = 1.0B_0^2$

(d) $\delta B^2 = 2.0B_0^2$

Figure 6.12: Comparison of simulation results and analytical theory in full 3D turbulence for $R = 0.01$. Colour coding: simulation, compound sub–diffusion (dashed, diamond markers), UNLT (square markers), FLPD.

particle increases, these effects become important (see Neuer and Spatschek (2006), Shalchi (2015, 2016) and Qin and Shalchi (2016)). Figure 6.16 shows the signature oscillations in the running diffusion coefficient of finite gyroradius effects for $R = 10$ at early times. It can be seen in this figure that these oscillations are present for all turbulence energy densities considered, with the effect being stronger for weaker turbulence.

Figure 6.17 shows the perpendicular mean free paths (see Table 6.7) as a function of rigidity (left) and Kubo number (left). The value of the perpendicular mean free path from simulation data is computed by averaging the last 50 data points and using (3.81) to relate the diffusion coefficient to the mean free path. Figure 6.18 plots the

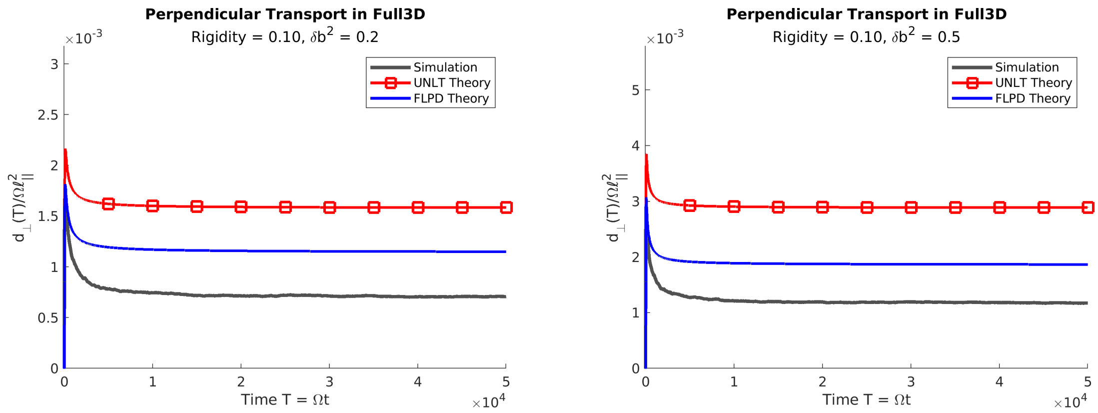

(a) $\delta B^2 = 0.2B_0^2$ (b) $\delta B^2 = 0.5B_0^2$

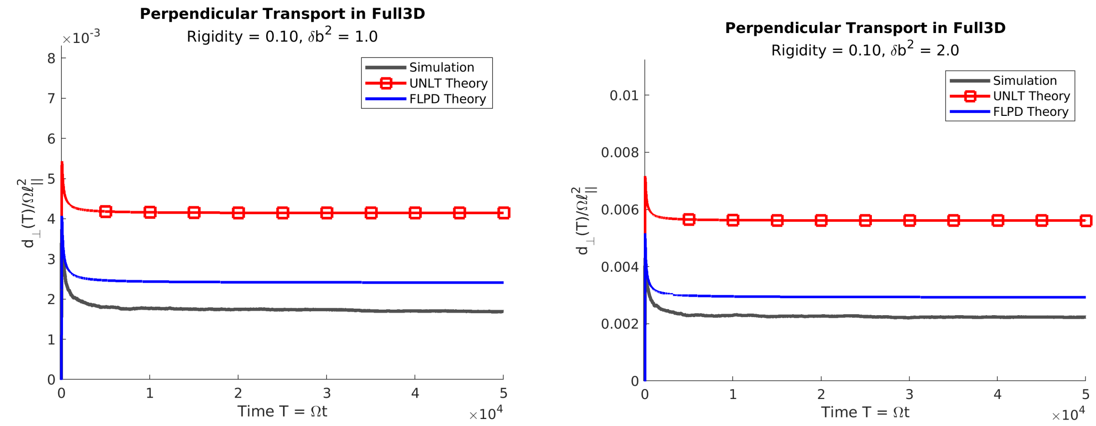

(c) $\delta B^2 = 1.0B_0^2$ (d) $\delta B^2 = 2.0B_0^2$

Figure 6.13: Comparison of simulation results and analytical theory in full 3D turbulence for $R = 0.10$. Colour coding: simulation, UNLT (square markers), FLPD.

ratio of the perpendicular and parallel mean free paths as a function of rigidity (right) and Kubo number (left). In addition to the simulation results, the figures also show the FLPD and UNLT theory predictions. In Figure 6.18a it can be seen that the agreement in the mean free path ratio between simulation and theory increases with increasing rigidity for constant Kubo number, with the agreement between UNLT theory and FLPD theory also increasing. This can also be seen in Figure 6.17a, as well as Table 6.8, where the ratio of the FLPD theory predictions to simulation results is listed. Figure 6.18 shows that the mean free path ratio (simulation data) converges with increasing Kubo number for low rigidity particles.

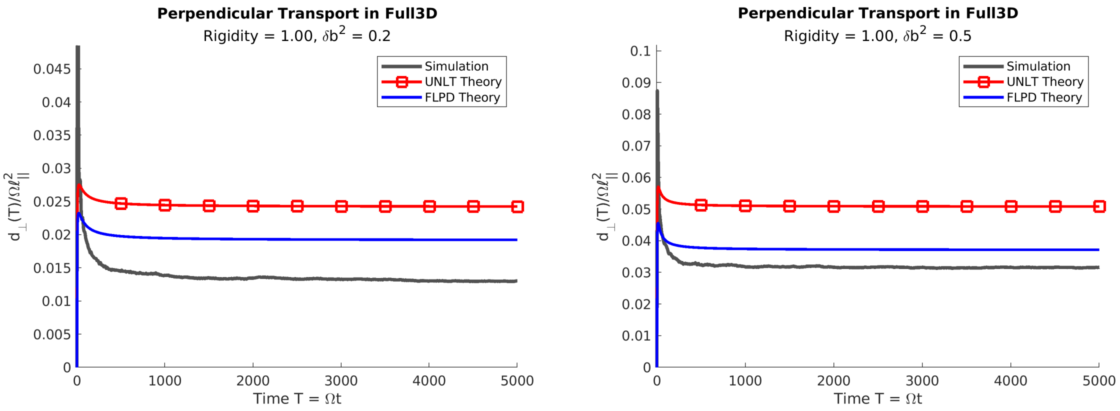

(a) $\delta B^2 = 0.2B_0^2$ (b) $\delta B^2 = 0.5B_0^2$

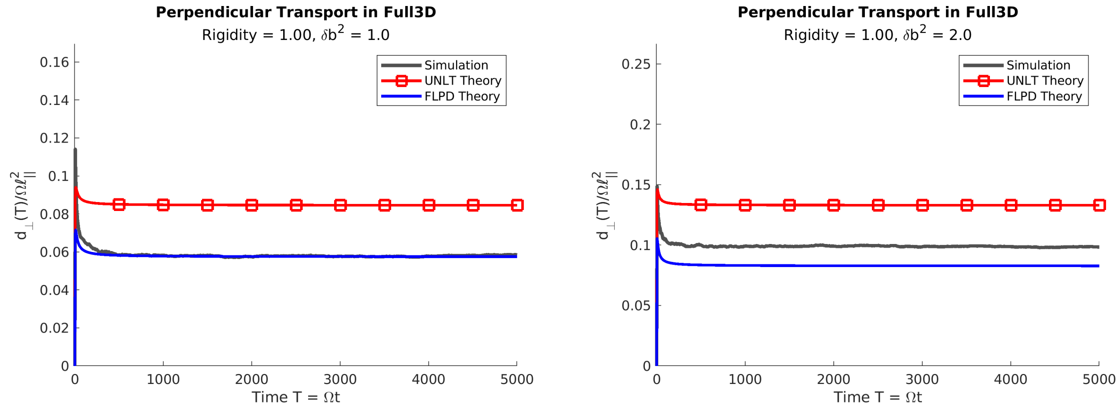

(c) $\delta B^2 = 1.0B_0^2$ (d) $\delta B^2 = 2.0B_0^2$

Figure 6.14: Comparison of simulation results and analytical theory in full 3D turbulence for $R = 1.00$. Colour coding: simulation, UNLT (square markers), FLPD.

$\Lambda_\perp = \frac{\lambda_\perp}{\ell_\parallel}$		Field Energy Density			
		0.2	0.5	1.0	2.0
Rigidity	0.01	0.0120	0.0160	0.0197	0.0227
	0.10	0.0213	0.0352	0.0507	0.0670
	1.00	0.0390	0.0948	0.1757	0.2961
	10.0	0.0576	0.1351	0.2705	0.5393

Table 6.7: Perpendicular mean free paths in full 3D turbulence. The value of $\Lambda_\perp$ for the $R = 0.01$ are upper values.

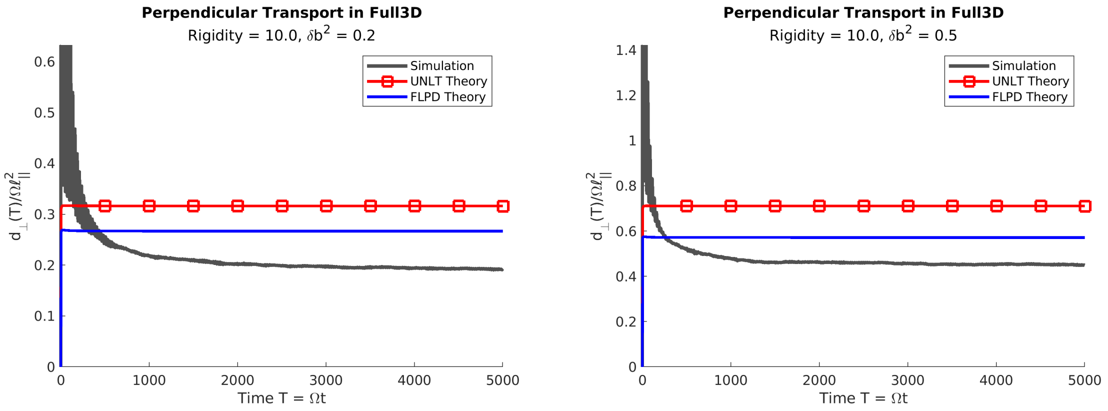

(a) $\delta B^2 = 0.2B_0^2$ (b) $\delta B^2 = 0.5B_0^2$

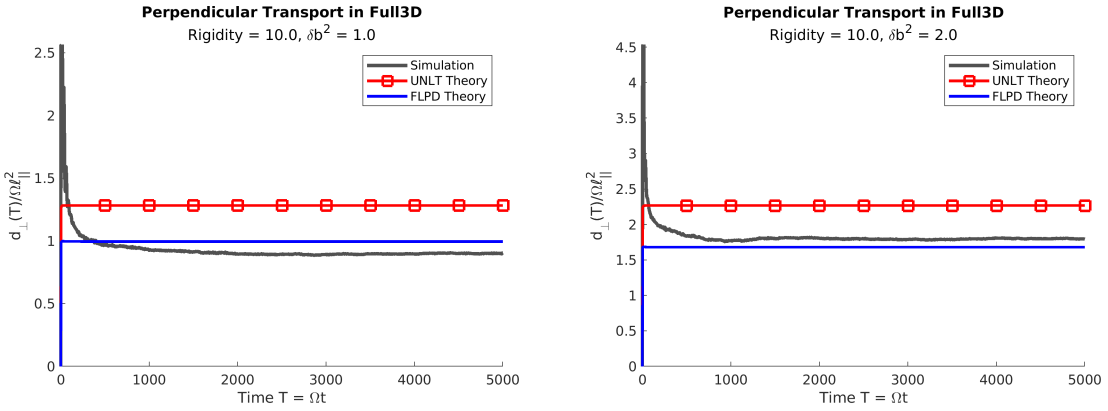

(c) $\delta B^2 = 1.0B_0^2$ (d) $\delta B^2 = 2.0B_0^2$

Figure 6.15: Comparison of simulation results and analytical theory in full 3D turbulence for $R = 10.0$. Colour coding: simulation, UNLT (square markers), FLPD.

$\lambda_\perp^{FLPD}/\lambda_\perp^{Sim}$		Field Energy Density			
		0.2	0.5	1.0	2.0
Rigidity	0.01	1.890	1.904	1.818	1.686
	0.10	1.625	1.594	1.432	1.317
	1.00	1.481	1.177	0.983	0.840
	10.0	1.390	1.270	1.105	0.935

Table 6.8: Ratio of QLT predictions and Full 3D simulation results.

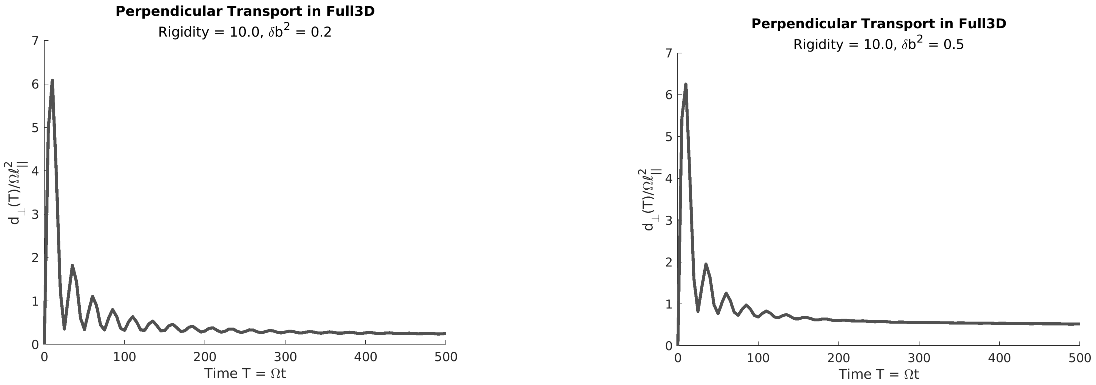

(a) $\delta B^2 = 0.2B_0^2$ (b) $\delta B^2 = 0.5B_0^2$

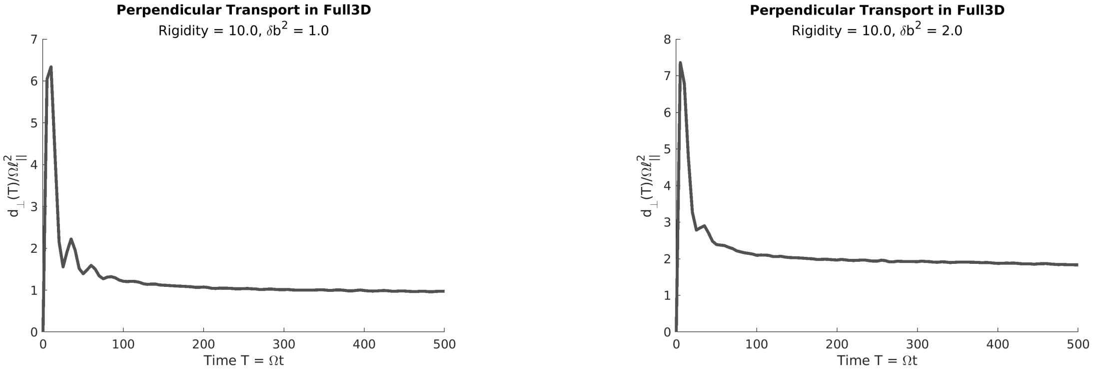

(c) $\delta B^2 = 1.0B_0^2$ (d) $\delta B^2 = 2.0B_0^2$

Figure 6.16: Close up of the finite gyroradius effect for $R = 10.0$ in full 3D turbulence. The oscillations in the running perpendicular diffusion coefficient at early times for high rigidity particles is the signature of the effect.

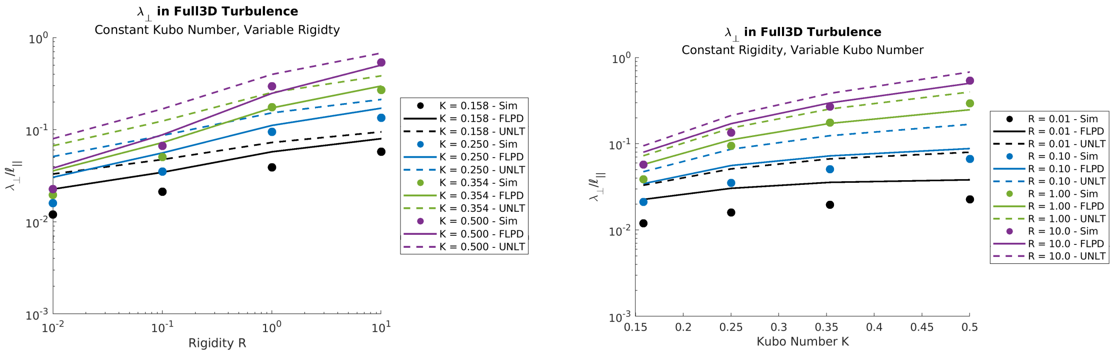

(a) $\lambda_\perp$ as a function of rigidity for constant Kubo number.

(b) $\lambda_\perp$ as a function of Kubo number for constant rigidity.

Figure 6.17: Perpendicular mean free path in full 3D turbulence as a function of rigidity (left) and Kubo number (right). Simulation results (solid circles) are plotted along with FLPD (solid line) and UNLT (dashed line) predictions. Results are colour coded by the variable that is held constant in each figure.

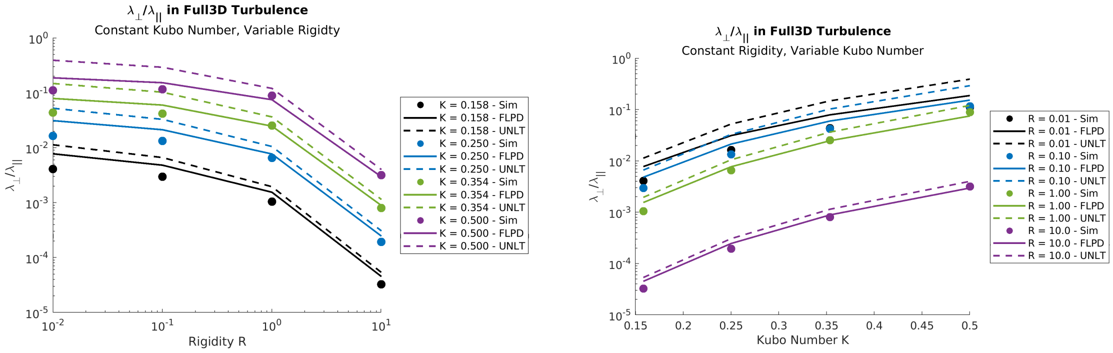

(a) $\lambda_\parallel/\lambda_\perp$ as a function of rigidity for constant Kubo number.

(b) $\lambda_\parallel/\lambda_\perp$ as a function of Kubo number for constant rigidity.

Figure 6.18: Ratio of $\lambda_\perp$ to $\lambda_\parallel$ full 3D turbulence as a function of rigidity (left) and Kubo number (right). Simulation results (solid circles) are plotted along with FLPD (solid line) and UNLT (dashed line) predictions. Results are colour coded by the variable that is held constant in each figure.

Chapter 7

Conclusions

7.1 Numerical Method and Simulation Summary

Presented in Chapter 4 was a new method for calculating the motion of a particle in a magnetic field. Named the *Instantaneous Rotation Matrix Method*, the method was based on the idea of using an exact infinitesimal rotation rather than an approximation. As shown in Chapter 4 it produces results with increased accuracy in both the position and velocity phase compared to not only Runge–Kutta method but also single step implicit methods such as those of Boris (1970), Vay (2008), and Higuera and Cary (2017). Expanding the method to include electric fields for both relativistic and non–relativistic particles would allow the IRM method to be used as a replacement for other implicit methods in various applications, such as in particle–mesh particle-in-cell simulations.

7.1.1 ACEPTS Summary

Chapter 5 introduces the *Astrophysical Charged Energetic Particle Transport Simulator* code, abbreviated as *ACEPTS*. A copy of the source code for *ACEPTS* can be obtained from the author at *arendtv.physics@gmail.com*. This simulation code was designed to compute the trajectories of energetic and electrically charged particles in magnetic turbulence, with the aim of minimizing numerical errors in the calculations whenever possible. To that end, the particle trajectory is calculated using the numerical method presented in Chapter 4, which has the advantages outlined above. The same philosophy of numerical error mitigation applies to the calculation of the amplitudes of the magnetic field Fourier modes. Rather than following the common approach of using an Euler integration method for the field amplitudes (see Giacalone and Jokipii (1999) or Hussein et al. (2015) for examples), *ACEPTS* calculates the amplitude using what is referred to as a split trapezoid method. While this method does not remove the numerical error completely, it does greatly minimize it as seen in Figure 5.2. The dominant error in this calculation is now due to the fact that the spectrum is re-normalized for the range of wave numbers used. Furthermore, by determining the magnetic field model to use at run time, the simulation code does not need to be recompiled whenever the model or model parameters are changed.

The greatest weakness of the *ACEPTS* program comes from flip side of one of its strengths. The goal of minimizing numerical error was extended to the calculation of the mean square displacement and the related diffusion coefficients. Since one of the greatest sources of fluctuations in statistical calculations comes from the number of sample points, *ACEPTS* was designed such that additional particle trajectories could be added to the simulation in order to increase the number of sample points. As part of the implementation of this, the simulation is incapable of extending the maximum time of previously computed trajectories. The result of this is that the trajectory calculation for a single particle must finish within the allotted time when running on high performance computing facilities. This was a major constraint for the simulations of low rigidity particles in noisy slab turbulence, and is the reason why particles with a rigidity of $R = 0.01$ were not done for a maximum time of $T > 10^6$.

7.1.1.1 ACEPTS Future Research

There are several improvements that can be made to *ACEPTS* as part of future research, either professional or personal. The first of these is the modification of how particle trajectories are written to file so that the maximum time the trajectory is calculated for can be extended. This would allow for *ACEPTS* to be used to study particle transport in magnetic fields that require long time frames for the ensemble of particles to reach a state of normal diffusion, such as that seen in the simulations of low rigidity particles in noisy slab turbulence. Another important upgrade is improving the procedure for adding new magnetic field models. The current procedure requires directly modifying the source code; ideal improvements would allow for custom field models to be compiled as a separate library that is then imported into the simulation at run time. This type of improvement would simplify the work needed to be done to add new models, and also reduce the amount of source code the researcher would need to be familiar with. A third upgrade to *ACEPTS* would be to update the numerical method to be able to handle electric fields. This would allow $ACEPTS$ to be used in the study of momentum diffusion, rather than only spatial diffusion.

7.2 Conclusions Concerning Particle Transport

In Chapter 6, the results of particle transport simulations in noisy slab and full 3D turbulence were presented. These simulations were performed using the three–step, third–order IRM method presented in Chapter 4. The noisy slab simulations for $R < 1$ demonstrated that it takes a long time for the particles to transition from a state of compound sub–diffusion to a normal diffusive state in the perpendicular direction, but that this transition does occur (Figure 6.4). For particles with $R \geq 1$ normal diffusion in noisy slab turbulence was reached within the simulated time frame. Comparison of these results to FLPD theory shows that the theoretical predictions are within an order of magnitude, with the predictions for $R = 1$ being roughly three times larger than simulation and the predictions for $R = 10$ being roughly 10% smaller than simulation.

For particle motion in full 3D turbulence, it was found that systems with $R \geq 0.1$ are diffusive in the perpendicular direction within the time frame considered in simulations. Systems with $R = 0.01$ were not found to be diffusive within the considered time frame, but at the same time are not in a compound sub-diffusive state. As a result, the listed perpendicular diffusion coefficients for the full 3D model with $R = 0.01$ can be taken as upper limits. For parallel transport in the full 3D model, QLT predictions are shown to give more accurate results as the particle rigidity increases. For perpendicular transport, the Field Line – Particle Decorrelation theory predictions were closer to the simulation results than those from the Unified Non-Linear Transport theory. Furthermore, the FLPD result for full 3D turbulence with $\delta B^2 = B_0^2$ and a particle rigidity of one is a near perfect match with the simulation results. At a rigidity of $R = 10$ the system experiences finite gyro–radius effects which are not accounted for in the theoretical equations being used. Despite this, FLPD theory results are still closer to the simulation data than UNLT theory. This reinforces FLPD as a superior theory to UNLT, although there is still room for improvement.

7.2.1 Considerations for Future Research

Based on the results of this research, there are multiple considerations for future research with the models used here. For the noisy slab model, two options that need to be considered for future research come from Shalchi and Arendt (2024b), either "*Our existing theories for perpendicular transport are incomplete since they work only for a certain family of turbulence models, namely models for which the magnetic correlations decay exponentially. Therefore, such theories need to be improved so that they can be applied for any possible turbulence model*," or "*One is only interested in turbulence models for which the correlation function is exponential or something very similar. This is, for instance, the case for commonly used models such as the slab/2D model with dominant two-dimensional modes. The latter model is often used to approximate solar wind turbulence. An improvement of existing theories for perpendicular diffusion is not required because such theories only fail for academic cases which have not much to do with real turbulence. However, any model which is used in particle transport theory needs to get tested to explore whether the correlation function decays exponentially or not.*" If the second option is true, then the noisy slab results can effectively be ignored in future research. On the other hand, if the first option is true, then based on the results presented here more work is required to explore the parameter dependence of the observed effects.

As noted in Arendt and Shalchi (2025), the full 3D model can be considered to be "*a three-dimensional version of the slab/2D model often used to approximate solar wind turbulence.*"[1] In theory, therefore, the full 3D model has the potential to be used as an alternative to the slab/2D model in solar wind studies. In order to do this, however, future research would need to compare simulation results using the full 3D model to data from the solar wind to determine the validity of this replacement. Furthermore, for large studies, it would need to be determined if this improvement in replicating solar wind data is worth the increased computational cost of the full 3D model, since it requires many more wave modes than the two–component model. If the improvement is large enough to warrant the increase in computation costs, then the full 3D model could be used instead of the two–component model in both simulations and analytical theory calculations for the solar wind.

---

[1] The two–component model (see Chapter 2.2.3) is also referred to as the slab/2D model.

Appendix A

Analysis of Runge-Kutta Methods

Statement of Originality

The contents of this appendix were originally published as Appendix A in **Numerical Methods, Energy Conservation, And A New Method For Particle Motion in Magnetic Fields** in the journal *Mathematics and Computers in Simulation* (Arendt, 2023). The journal publishing agreement allows the author to reuse the contents of the article in this thesis. As the sole author of the article, no other permissions are required. The first appendix has therefore been reproduced here, while the body of the article has been reproduced in Chapter 4 and the second appendix in Appendix B. Due to differences in page formatting, figures and tables may not appear in the same locations in the text or be formatted the same compared to the original article. Cross–referencing between figures, tables, chapters, sections, and appendices was also updated to be consistent with the rest of this thesis.

On Mathematical Notation and Scaling

As in Chapter 4, the mathematical notation and scaling of quantities used in this appendix are the same as used in Arendt (2023), which is not the same as that used in the rest of this work. Conversions between the quantities found in Arendt (2023) and the rest of this work are shown in Table 4.1.

A.1 Analysis of Runge-Kutta Methods

Here we consider the application of explicit Runge–Kutta methods as described by (4.27) to the test cases outlined in Chapter 4.2 and the resulting energy drifts. First though, we consider the general application to particle motion.

A.1.1 Particle Motion

If the differential equations being solved are equations of motion then y is a $2DM$ element vector, where D is the number of dimensions per particle and M is the number of particles in the system. In these situations the independent variable is time t, y can be expressed as $y = (\vec{x}, \vec{v})$, and the function $f(y,t) = (\vec{v}, \vec{F}(\vec{x}, \vec{v}, t))$ where $\vec{F}$ is the force per unit mass (acceleration)[1]. The intermediate times t_n and points y_n can be calculated via

$$t_n = t_0 + c_n h, \tag{A.1a}$$

$$y_n = y_0 + h \sum_{i=0}^{n-1} a_{ni} k_i. \tag{A.1b}$$

The intermediate position and velocity of individual particles can be expressed as

$$\begin{aligned} \vec{x}_n &= \vec{x}_0 + h \sum_{i=0}^{n-1} a_{ni} \vec{v}_i \\ &= \vec{x}_0 + \vec{v}_0 h \sum_{i=0}^{n-1} a_{ni} + h^2 \sum_{i=0}^{n-1} \sum_{j=0}^{i-1} a_{ni} a_{ij} \vec{F}(\vec{x}_j, \vec{v}_j, t_j), \end{aligned} \tag{A.2a}$$

$$\vec{v}_n = \vec{v}_0 + h \sum_{i=0}^{n-1} a_{ni} \vec{F}(\vec{x}_i, \vec{v}_i, t_i), \tag{A.2b}$$

and the final position and velocity is then

$$\vec{x}(t_0 + h) = \vec{x}_0 + \vec{v}_0 h \sum_{n=0}^{N} b_n + h^2 \sum_{n=0}^{N} \sum_{i=0}^{n-1} b_n a_{ni} \vec{F}(\vec{x}_i, \vec{v}_i, t_i), \tag{A.3a}$$

$$\vec{v}(t_0 + h) = \vec{v}_0 + h \sum_{n=0}^{N} b_n \vec{F}(\vec{x}_n, \vec{v}_n, t_n). \tag{A.3b}$$

---

[1] This notation is used to prevent confusion with the integration coefficients a_{ij}

A.1.1.1 Taylor Expanding the Solution

If $\vec{x}$, $\vec{v}$, and $\vec{F}(\vec{x}, \vec{v}, t)$ vary slowly enough, the force can be Taylor expanded to first order such that

$$\begin{aligned}\vec{F}(\vec{x} + \delta\vec{x}, \vec{v} + \delta\vec{v}, t + \delta t) \approx\ & \vec{F}(\vec{x}, \vec{v}, t) + \partial_t \vec{F}(\vec{x}, \vec{v}, t)\ \delta t \\ & + \left[\delta\vec{x} \cdot \vec{\nabla}_x\right] \vec{F}(\vec{x}, \vec{v}, t) + \left[\delta\vec{v} \cdot \vec{\nabla}_v\right] \vec{F}(\vec{x}, \vec{v}, t).\end{aligned} \tag{A.4}$$

From (A.1a), the first order change in time is $\delta t_n = c_n h$, while the intermediate position and velocity are respectively

$$\delta\vec{x}_n = \vec{v}h \sum_{i=0}^{n-1} a_{ni} \tag{A.5a}$$

and

$$\delta\vec{v}_n = \vec{F}(\vec{x}_0, \vec{v}_0, t_0) h \sum_{i=0}^{n-1} a_{ni}. \tag{A.5b}$$

as found from (A.2). The assumption used here is that the force at intermediate points is approximately equal to the force at the initial point. In practice, this can be used either for systems in which the force varies slowly or by setting the step size such that the force changes little. If the Runge–Kutta method being used has coefficients that satisfy the property

$$c_n = \sum_{i=0}^{n-1} a_{ni}, \tag{A.6}$$

then the force per unit mass can be approximated as

$$\begin{aligned}\vec{F}(\vec{x}_n, \vec{v}_n, t_n) &\approx \vec{F}(\vec{x}_0, \vec{v}_0, t_0) + c_n h \Big[\partial_t \vec{F}(\vec{x}_0, \vec{v}_0, t_0) \\ &\quad + (\vec{v}_0 \cdot \vec{\nabla}_x)\vec{F}(\vec{x}_0, \vec{v}_0, t_0) + \left[\vec{F}(\vec{x}_0, \vec{v}_0, t_0) \cdot \vec{\nabla}_v\right] \vec{F}(\vec{x}_0, \vec{v}_0, t_0)\Big] \\ &\approx \vec{F}(\vec{x}_0, \vec{v}_0, t_0) \\ &\quad + c_n h \left[\left[\vec{v}_0 \cdot \vec{\nabla}_x\right] + \left[\vec{F}(\vec{x}_0, \vec{v}_0, t_0) \cdot \vec{\nabla}_v\right] + \partial_t\right] \vec{F}(\vec{x}_0, \vec{v}_0, t_0) \\ &\approx \vec{F}(\vec{x}_0, \vec{v}_0, t_0) + c_n h\ \mathrm{d}_t \vec{F}(\vec{x}_0, \vec{v}_0, t_0).\end{aligned} \tag{A.7}$$

With this, the final results of a single step can be approximated as

$$\begin{aligned}\vec{x}(t_0 + h) \approx \vec{x}_0 + \vec{v}_0 h \sum_{n=0}^{N} b_n + \vec{F}(\vec{x}_0, \vec{v}_0, t_0) h^2 \sum_{n=0}^{N} b_n c_n \\ + \mathrm{d}_t \vec{F}(\vec{x}_0, \vec{v}_0, t_0) h^3 \sum_{n=0}^{N} \sum_{i=0}^{n-1} b_n a_{ni} c_i,\end{aligned} \tag{A.8a}$$

$$\vec{v}(t_0 + h) \approx \vec{v}_0 + \vec{F}(\vec{x}_0, \vec{v}_0, t_0) h \sum_{n=0}^{N} b_n + \mathrm{d}_t \vec{F}(\vec{x}_0, \vec{v}_0, t_0) h^2 \sum_{n=0}^{N} b_n c_n. \tag{A.8b}$$

While this is only an approximation, it can be used in some situations to provide a simple analysis as to whether or not a specific method is suitable for the problem at hand. Furthermore, the expansion will be used later when considering particles in a magnetic field.

A.1.2 Test Case: Simple Harmonic Oscillator

When numerically solving the equations for a simple harmonic oscillator using explicit Runge–Kutta methods, both the intermediate steps and the final updated point can be recursively expanded to find the exact numerical result. The expansion of the intermediate steps yields

$$\begin{aligned} q_n &= q_0 + p_0 c_n h - h^2 \sum_{i=0}^{n-1} \sum_{j=0}^{i-1} a_{ni} a_{ij} q_i \\ &= q_0 + p_0 c_n h - q_0 h^2 \sum_{i=0}^{n-1} a_{ni} c_i - p_0 h^3 \sum_{i=0}^{n-1} \sum_{j=0}^{i-1} a_{ni} a_{ij} c_j \\ &\quad + h^4 \sum_{i=0}^{n-1} \sum_{j=0}^{i-1} \sum_{k=0}^{j-1} \sum_{l=0}^{k-1} a_{ni} a_{ij} a_{jk} a_{kl} q_l \\ &= \cdots \end{aligned} \tag{A.9a}$$

$$\begin{aligned} p_n &= p_0 - h \sum_{i=0}^{n-1} a_{ni} q_i \\ &= p_0 - q_0 c_n h - p_0 h^2 \sum_{i=0}^{n-1} a_{ni} c_i + h^3 \sum_{i=0}^{n-1} \sum_{j=0}^{i-1} \sum_{k=0}^{j-1} a_{ni} a_{ij} a_{jk} q_k \\ &= \cdots \end{aligned} \tag{A.9b}$$

while the updated step becomes

$$\begin{aligned} q(t+h) &= q_0 + p_0 h \sum_{n=0}^{N} b_n - h^2 \sum_{n=0}^{N} \sum_{i=0}^{n-1} b_n a_{ni} q_i \\ &= q_0 + p_0 h \sum_{n=0}^{N} b_n - q_0 h^2 \sum_{n=0}^{N} b_n c_n - p_0 h^3 \sum_{n=0}^{N} \sum_{i=0}^{n-1} b_n a_{ni} c_i \\ &\quad + q_0 h^4 \sum_{n=0}^{N} \sum_{i=0}^{n-1} \sum_{j=0}^{i} b_n a_{ni} a_{ij} c_j + \cdots \end{aligned} \tag{A.10a}$$

$$\begin{aligned} p(t+h) &= p_0 - h \sum_{n=0}^{N} b_n q_n \\ &= p_0 - q_0 h \sum_{n=0}^{N} b_n - p_0 h^2 \sum_{n=0}^{N} b_n c_n + q_0 h^3 \sum_{n=0}^{N} \sum_{i=0}^{n-1} b_n a_{ni} c_i \\ &\quad + p_0 h^4 \sum_{n=0}^{N} \sum_{i=0}^{n-1} \sum_{j=0}^{i-1} b_n a_{ni} a_{ij} c_j + \cdots \end{aligned} \tag{A.10b}$$

The results can be simplified by defining the following quantities:

$$\beta_1 = \sum_{n=0}^{N} b_n \tag{A.11a}$$

$$\beta_2 = \bar{\bar{b}}\bar{\bar{c}} \tag{A.11b}$$

$$\beta_m = \bar{\bar{b}}\bar{\bar{a}}^{m-2}\bar{\bar{c}} \quad m \geq 3 \tag{A.11c}$$

where $\bar{\bar{b}}$, $\bar{\bar{a}}$, and $\bar{\bar{c}}$ are the matrix representation of the integration coefficients as per the method's Butcher-Tableau. With this, the results of a single step can be written as

$$\begin{aligned} q(t+h) &= q(t) \left[1 - \beta_2 h^2 + \beta_4 h^4 - \beta_6 h^6 + \cdots\right] \\ &\quad + p(t) \left[\beta_1 h - \beta_3 h^3 + \beta_5 h^5 - \beta_7 h^7 + \cdots\right], \end{aligned} \tag{A.12a}$$

$$\begin{aligned} p(t+h) &= p(t) \left[1 - \beta_2 h^2 + \beta_4 h^4 - \beta_6 h^6 + \cdots\right] \\ &\quad - q(t) \left[\beta_1 h - \beta_3 h^3 + \beta_5 h^5 - \beta_7 h^7 + \cdots\right], \end{aligned} \tag{A.12b}$$

where q_0 and p_0 have been replaced with $q(t)$ and $p(t)$, respectively.

Having derived an exact equation for the updated position and momentum in terms of the state at the start of the step, the step size, and the integration coefficients, it is now possible to calculate what the energy of the system will be after a single step. The result is

$$E(t+h) = E(t)\begin{bmatrix} \left[1-\beta_2 h^2+\beta_4 h^4-\beta_6 h^6+\cdots\right]^2 \\ +\left[\beta_1 h-\beta_3 h^3+\beta_5 h^5-\beta_7 h^7+\cdots\right]^2 \end{bmatrix}. \tag{A.13}$$

Given the nature of the result, all terms will be of even order in respect to the step size. As such, the energy at the end of each step can be written as

$$E(t+h) = E(t)\left[1+\sum_{m=1}^{M}\alpha_{2m}h^{2m}\right], \tag{A.14}$$

where M is the total number of terms, given by $M = N + 1$. From this it can be seen that, regardless of the step size or step direction, there will be a unidirectional change in energy as all terms are of even power with respect to h. The direction of this change is determined by the sign of the first non–zero α term, with a negative value leading to a exponential decrease in energy and a positive value leading to an exponential increase in energy. In adaptive methods, the goal of taking as large a step as possible will only amplify the violation of energy conservation.

A.1.3 Test Case: Particle in a Magnetic Field

A.1.3.1 Newtonian Formulation

The expansion of the solution given by explicit Runge–Kutta methods for the Newtonian formulation of a particle in a magnetic field is rather straight forward. To begin, define

$$\bar{\bar{\omega}}_n = \bar{\bar{\omega}}(\vec{x}_n, t_n) \tag{A.15a}$$

$$\approx \bar{\bar{\omega}}(\vec{x}_0, t_0) + c_n h\left[\frac{\partial}{\partial t}+\vec{v}_0\vec{\nabla}\right]\bar{\bar{\omega}}(\vec{x},t)|_{\vec{x}_0,t_0}$$

$$\approx \bar{\bar{\omega}}_0 + c_n h\bar{\bar{\omega}}_0', \tag{A.15b}$$

so that the intermediate velocities can be written as

$$\vec{v}_n = \vec{v}_0 + h\sum_{i=0}^{n-1}a_{ni}\bar{\bar{\omega}}_i\vec{v}_0 + h^2\sum_{i=0}^{n-1}a_{ni}\bar{\bar{\omega}}_i\sum_{j=0}^{i-1}a_{ij}\bar{\bar{\omega}}_j\vec{v}_0+\cdots \tag{A.16}$$

and the updated velocity as

$$\vec{v}(t+h) = \vec{v}(t) + h\sum_{n=0}^{N}b_n\bar{\bar{\omega}}_n\vec{v}(t) + h^2\sum_{n=0}^{N}\sum_{i=0}^{n-1}b_n a_{ni}\bar{\bar{\omega}}_n\bar{\bar{\omega}}_i\vec{v}(t)+\cdots. \tag{A.17}$$

Uniform Static Field For a uniform, static field $\bar{\bar{\omega}}_n = \bar{\bar{\omega}}$ and the solution becomes

$$\begin{aligned}\vec{v}(t+h) &= \vec{v}(t) + \bar{\bar{\omega}}\vec{v}(t)h\sum_{n=0}^{N} b_n + \bar{\bar{\omega}}^2\vec{v}(t)h^2\sum_{n=0}^{N} b_n c_n + \cdots \\ &= \left[\bar{\bar{I}} + \bar{\bar{\omega}}h\sum_{n=0}^{N} b_n + \bar{\bar{\omega}}^2 h^2 \sum_{n=0}^{N} b_n c_n + \cdots\right]\vec{v}(t)\end{aligned} \tag{A.18}$$

where $\bar{\bar{I}}$ is the identity matrix. The coefficient on each term can be identified as β_n from the result of the simple harmonic oscillator, and the entire solution can therefore be written as

$$\vec{v}(t+h) = \left[\bar{\bar{I}} + \sum_n \beta_n \bar{\bar{\omega}}^n h^n\right]\vec{v}(t), \tag{A.19}$$

with energy

$$E(t+h) = \vec{v}^{\intercal}(t)\left[\bar{\bar{I}} + \sum_m (-1)^m \alpha_{2m}\bar{\bar{\omega}}^{2m}h^{2m}\right]\vec{v}(t). \tag{A.20}$$

As with the SHO, the system energy is not conserved, although in this situation it is the kinetic energy of the particle coming from motion perpendicular to the magnetic field that is affected. The velocity of the particle parallel to the field will not be affected and therefore the energy change can be expressed as

$$E(t+h) = E_{\|}(t) + E_{\perp}(t)\left[1 + \sum_{m=1}^{N} \alpha_{2m}|\vec{\omega}h|^{2m}\right], \tag{A.21}$$

taking into account the fact that $\vec{v}^{\intercal}(t)\bar{\bar{\omega}}^{2m}\vec{v}(t) = (-1)^m|\vec{\omega}|^{2m}E_{\perp}(t)$ where $|\vec{\omega}|$ is the magnitude of the field.

Non-Uniform Non-Static Field If the field varies with either space or time (or both), the field can be expanded using the same technique from (A.7) so that the result can be written as

$$\begin{aligned}\vec{v}(t+h) &= \vec{v}(t) + h\sum_{n=0}^{N} b_n\left[\bar{\bar{\omega}}_0 + c_n h\bar{\bar{\omega}}_0'\right]\vec{v}(t) \\ &\quad + h^2\sum_{n=0}^{N}\sum_{i=0}^{n-1} b_n a_{ni}\left[\bar{\bar{\omega}}_0 + c_n h\bar{\bar{\omega}}_0'\right]\left[\bar{\bar{\omega}}_0 + c_i h\bar{\bar{\omega}}_0'\right]\vec{v}(t) + \cdots .\end{aligned} \tag{A.22}$$

Expanding each term leads to

$$\begin{aligned}\vec{v}(t+h) = \left[\bar{\bar{I}} + \sum_{n} \beta_n \bar{\bar{\omega}}_0^n h^n\right] \vec{v}(t) + \bar{\bar{\omega}}_0' \vec{v}(t) h^2 \sum_{n=0}^{N} b_n c_n \\ + h^3 \sum_{n=0}^{N} \sum_{i=0}^{n-1} b_n a_{ni} \left[c_n \bar{\bar{\omega}}_0' \bar{\bar{\omega}}_0 + c_i \bar{\bar{\omega}}_0 \bar{\bar{\omega}}_0' + c_n c_i h {\bar{\bar{\omega}}_0'}^2\right] \vec{v}(t) + \cdots\end{aligned} \tag{A.23}$$

It can already be seen that the energy will, at minimum, follow the same trend as if the field was constant.

A.1.3.2 Hamiltonian Formulation

For the Hamiltonian formulation of a charged particle in a magnetic field, consider the case of a uniform field as per (4.19) and (4.26). Expanding the intermediate evaluations (k_n) of $f(y)$ leads to

$$\dot{\vec{p}}_n = \frac{1}{2}\left[\bar{\bar{\omega}} + \bar{\bar{\omega}}^2 h \sum_{i=0}^{n-1} a_{ni} + \bar{\bar{\omega}}^3 h^2 \sum_{i=0}^{n-1} \sum_{j=0}^{i-1} a_{ni} a_{ij} + \cdots\right] \dot{\vec{r}}_0 \tag{A.24a}$$

and

$$\dot{\vec{r}}_n = \left[\bar{\bar{I}} + \bar{\bar{\omega}} h \sum_{i=0}^{n-1} a_{ni} + \bar{\bar{\omega}}^2 h^2 \sum_{i=0}^{n-1} \sum_{j=0}^{i-1} a_{ni} a_{ij} + \cdots\right] \dot{\vec{r}}_0, \tag{A.24b}$$

where $\dot{\vec{r}}_0 = \left(\vec{p}_0 + \frac{1}{2}\bar{\bar{\omega}}\vec{r}_0\right)$. Since the Hamiltonian is independent of time, it must be conserved by the solution. Furthermore, it can be seen from (4.14) and (4.20a) that the Hamiltonian is equal to the kinetic energy of the particle, and that $\dot{\vec{r}}$ is the particle velocity. Therefore, after calculating the updated position and canonical momentum, the updated particle velocity is

$$\vec{v}(t+h) = \left[\bar{\bar{\omega}} + \beta_1 h \bar{\bar{\omega}} + \beta_2 h^2 \bar{\bar{\omega}}^2 + \cdots\right] \vec{v}(t), \tag{A.25}$$

which is the same result as for the Newtonian formulation, and therefore the energy drift is given by (A.21).

A.1.4 Analysis of Select Fourth Order Runge–Kutta Methods

Next, several Runge–Kutta methods will be examined for energy conservation in the context of the presented test cases. The methods considered are: the "standard" non–adaptive fourth order method, the fourth order adaptive method of Fehlberg

(1969), the adaptive method of Dormand and Prince (1980), and the adaptive method of Cash and Karp (1990).

A.1.4.1 “Standard” Non–Adaptive Method

The Butcher Tableau for the “standard” RK4 method and the resulting SHO coefficients are shown respectively in Tables A.1a and A.1b.

$$\begin{array}{c|cccc} 0 & & & & \\ \frac{1}{2} & \frac{1}{2} & & & \\ \frac{1}{2} & & \frac{1}{2} & & \\ 1 & & & 1 & \\ \hline & \frac{1}{6} & \frac{1}{3} & \frac{1}{3} & \frac{1}{6} \end{array}$$

(a) Butcher Tableau for the “standard” non-adaptive 4^{th} order Runge-Kutta method.

m	β_m
1	1
2	$\frac{1}{2}$
3	$\frac{1}{6}$
4	$\frac{1}{24}$

(b) Resulting SHO coefficients β_m.

Table A.1: Butcher Tableau and the resulting SHO coefficients for the RK4 method.

The energy change with this method for the SHO and a particle in a magnetic field are respectively

$$E(t+h) = E(t)\left[1 - \frac{1}{72}h^6 + \frac{1}{576}h^8\right] \tag{A.26a}$$

and

$$E(t+h) = E_{\|}(t) + E_{\perp}(t)\left[1 - \frac{1}{72}|\vec{\omega}h|^6 + \frac{1}{576}|\vec{\omega}h|^8\right]. \tag{A.26b}$$

This means that energy is continuously bled from the system for both the SHO and a particle in a magnetic, regardless of the step size or sign.

A.1.4.2 Fehlberg Method

The Butcher Tableau for the 4^{th} order Runge–Kutta–Fehlberg method and the resulting SHO coefficients are shown respectively in Tables A.2a and A.2b.

The energy change with the Fehlberg method for the SHO and a particle in a magnetic field are respectively

$$E(t+h) = E(t)\left[1 + \frac{17}{9360}h^6 - \frac{7}{12480}h^8 + \frac{11}{374400}h^{10} + \frac{1}{4326400}h^{12}\right] \tag{A.27a}$$

0						
$\frac{1}{4}$	$\frac{1}{4}$					
$\frac{3}{8}$	$\frac{3}{32}$	$\frac{9}{32}$				
$\frac{12}{13}$	$\frac{1932}{2197}$	$-\frac{7200}{2197}$	$\frac{7296}{2197}$			
1	$\frac{439}{216}$	-8	$\frac{3680}{513}$	$-\frac{845}{4104}$		
$\frac{1}{2}$	$-\frac{8}{27}$	2	$-\frac{3544}{2565}$	$\frac{1859}{4104}$	$-\frac{11}{40}$	
	$\frac{16}{135}$	0	$\frac{6656}{12825}$	$\frac{28561}{56430}$	$-\frac{9}{50}$	$\frac{2}{55}$
	$\frac{25}{216}$	0	$\frac{1408}{2565}$	$\frac{2197}{4104}$	$-\frac{1}{5}$	0

(a) Butcher Tableau for the adaptive 4^{th} order Runge-Kutta-Fehlberg method.

m	β_m	β^*_m	d_m
1	1	1	0
2	$\frac{1}{2}$	$\frac{1}{2}$	0
3	$\frac{1}{6}$	$\frac{1}{6}$	0
4	$\frac{1}{24}$	$\frac{1}{24}$	0
5	$\frac{1}{120}$	$\frac{1}{104}$	$-\frac{1}{780}$
6	$\frac{1}{2080}$	0	$\frac{1}{2080}$

(b) Resulting SHO coefficients β_m, secondary solution (y^*) coefficients β^*_m, and error estimate ($y - y^*$) coefficients d_m.

Table A.2: Butcher Tableau and the resulting SHO coefficients for the 4^{th} order Runge-Kutta-Fehlberg method.

and

$$E(t+h) = E_{\parallel}(t) + E_{\perp}(t)\left[\begin{aligned} &1 + \frac{17}{9360}|\vec{\omega}h|^6 - \frac{7}{12480}|\vec{\omega}h|^8 \\ &+ \frac{11}{374400}|\vec{\omega}h|^{10} + \frac{1}{4326400}|\vec{\omega}h|^{12} \end{aligned}\right]. \tag{A.27b}$$

The energy change for this method is opposite that of the "standard" method, although the direction of the change is also independent of step size and sign. However, this energy change is amplified when using an adaptive step size, as the method tries to take as large a step as possible.

A.1.4.3 Dormand-Prince Method

The Butcher Tableau for the 4^{th} order Dormand–Prince method and the resulting SHO coefficients are shown respectively in Tables A.3 and A.4.

The energy change with the Dormand–Prince method for the SHO and a particle in a magnetic field are respectively

$$E(t+h) = E(t)\left[1 - \frac{1}{1800}h^6 + \frac{1}{1600}h^8 - \frac{1}{14400}h^{10} + \frac{1}{360000}h^{12}\right] \tag{A.28a}$$

$$
\begin{array}{c|ccccccc}
0 & & & & & & & \\
\frac{1}{5} & \frac{1}{5} & & & & & & \\
\frac{3}{10} & \frac{3}{40} & \frac{9}{40} & & & & & \\
\frac{4}{5} & \frac{44}{45} & -\frac{56}{15} & \frac{32}{9} & & & & \\
\frac{8}{9} & \frac{19372}{6561} & -\frac{25360}{2187} & \frac{64448}{6561} & -\frac{212}{729} & & & \\
1 & \frac{9017}{3168} & -\frac{355}{33} & \frac{46732}{5247} & \frac{49}{176} & -\frac{5103}{18656} & & \\
1 & \frac{35}{384} & 0 & \frac{500}{1113} & \frac{125}{192} & -\frac{2187}{6784} & \frac{11}{84} & \\
\hline
 & \frac{35}{384} & 0 & \frac{500}{1113} & \frac{125}{192} & -\frac{2187}{6784} & \frac{11}{84} & 0 \\
 & \frac{5179}{57600} & 0 & \frac{7571}{16695} & \frac{393}{640} & -\frac{92097}{339200} & \frac{187}{2100} & \frac{1}{40}
\end{array}
$$

Table A.3: Butcher Tableau for the adaptive 4^{th} order method of Dormand and Prince.

m	β_m	β^*_m	d_m
1	1	1	0
2	$\frac{1}{2}$	$\frac{1}{2}$	0
3	$\frac{1}{6}$	$\frac{1}{6}$	0
4	$\frac{1}{24}$	$\frac{1}{24}$	0
5	$\frac{1}{120}$	$\frac{1097}{120000}$	$-\frac{97}{120000}$
6	$\frac{1}{600}$	$\frac{161}{120000}$	$\frac{13}{40000}$
7	0	$\frac{1}{24000}$	$-\frac{1}{24000}$

Table A.4: Resulting SHO coefficients β_m, secondary solution (y^*) coefficients β^*_m, and error estimate $(y - y^*)$ coefficients d_m for the Dormand–Prince method.

and

$$E(t+h) = E_{\|}(t) + E_{\perp}(t)\begin{bmatrix} 1 - \frac{1}{1800}|\vec{\omega}h|^6 + \frac{1}{1600}|\vec{\omega}h|^8 \\ - \frac{1}{14400}|\vec{\omega}h|^{10} + \frac{1}{360000}|\vec{\omega}h|^{12} \end{bmatrix}. \tag{A.28b}$$

The energy drift for this method is similar to that of the "standard" method, although at a slower rate. As with the Fehlberg method, using an adaptive step size has the potential to amplify the energy drift rate.

A.1.4.4 Cash-Karp Method

The Butcher Tableau for the 4^{th} order Cash–Karp method and the resulting SHO coefficients are shown respectively in Tables A.5 and A.6.

$$\begin{array}{c|cccccc}
0 & & & & & & \\
\frac{1}{5} & \frac{1}{5} & & & & & \\
\frac{3}{10} & \frac{3}{40} & \frac{9}{40} & & & & \\
\frac{3}{5} & \frac{3}{10} & -\frac{9}{10} & \frac{6}{5} & & & \\
1 & -\frac{11}{54} & \frac{5}{2} & -\frac{70}{27} & \frac{35}{27} & & \\
\frac{7}{8} & \frac{1631}{55296} & \frac{175}{512} & \frac{575}{13824} & \frac{44275}{110592} & \frac{253}{4096} & \\
\hline
 & \frac{37}{378} & 0 & \frac{250}{621} & \frac{125}{594} & 0 & \frac{512}{1771} \\
 & \frac{2825}{27648} & 0 & \frac{18575}{48384} & \frac{13525}{55296} & \frac{277}{14336} & \frac{1}{4}
\end{array}$$

Table A.5: Butcher Tableau for the adaptive 4^{th} order Cash-Karp method.

m	β_m	β^*_m	d_m
1	1	1	0
2	$\frac{1}{2}$	$\frac{1}{2}$	0
3	$\frac{1}{6}$	$\frac{1}{6}$	0
4	$\frac{1}{24}$	$\frac{1}{24}$	0
5	$\frac{1}{120}$	$\frac{10517}{1228800}$	$-\frac{277}{1228800}$
6	$\frac{1}{800}$	$\frac{1771}{1638400}$	$\frac{277}{1638400}$

Table A.6: Resulting SHO coefficients β_m, secondary solution (y^*) coefficients β^*_m, and error estimate ($y - y^*$) coefficients d_m.

The energy drift with the Cash–Karp method for the SHO and a particle in a magnetic field are respectively

$$E(t+h) = E(t)\left[1 + \frac{1}{3600}h^6 + \frac{1}{4800}h^8 - \frac{1}{28800}h^{10} + \frac{1}{640000}h^{12}\right] \tag{A.29a}$$

and

$$E(t+h) = E_{\|}(t) + E_{\perp}(t)\begin{bmatrix} 1 + \frac{1}{3600}|\vec{\omega}h|^6 + \frac{1}{4800}|\vec{\omega}h|^8 \\ - \frac{1}{28800}|\vec{\omega}h|^{10} + \frac{1}{640000}|\vec{\omega}h|^{12} \end{bmatrix}. \tag{A.29b}$$

The energy drift for this method is similar to that of the Fehlberg method, although at a slower rate. As with the Fehlberg and Dormand-Prince methods, using an adaptive step size has the potential to amplify the energy drift rate.

A.1.4.5 Summary of Fourth Order Methods

In each of the methods analyzed, the energy drift is sixth order for the SHO and a particle in a magnetic field. For these methods, the energy conservation to the first non–zero term can be written as

$$E(t+h) = E(t)\left(1 + \alpha_6 h^6\right) \tag{A.30a}$$

for the SHO and

$$E(t+h) = E_{\|}(t) + E_{\perp}(t)\left(1 + \alpha_6|\vec{\omega}h|^6\right) \tag{A.30b}$$

for a particle in a magnetic field.

Method	α_6	Energy Drift Trend
“Standard”	$-\frac{1}{72}$	Energy loss
Fehlberg	$+\frac{17}{9360}$	Energy gain
Dormand–Prince	$-\frac{1}{1800}$	Energy loss
Cash–Karp	$+\frac{1}{3600}$	Energy gain

Table A.7: Summary of the analysis of various fourth order Runge–Kutta methods to first non-zero term.

The values of α_6 for the methods considered are summarized in Table A.7, along with the direction of the energy drift. From the table it can be seen that for a given step size, the Cash-Karp method has the lowest energy drift rate. This is offset, however, by the fact that Cash-Karp method is adaptive and will therefore attempt to use as large a step as possible (or allowed if there is an upper limit).

Appendix B

Analysis of Select Symplectic Methods of Various Orders

Statement of Originality

The contents of this appendix were originally published as Appendix B in **Numerical Methods, Energy Conservation, And A New Method For Particle Motion in Magnetic Fields** in the journal *Mathematics and Computers in Simulation* (Arendt, 2023). The journal publishing agreement allows the author to reuse the contents of the article in this thesis. As the sole author of the article, no other permissions are required. The second appendix has therefore been reproduced here, while the body of the article has been reproduced in Chapter 4 and the first appendix in Appendix A. Due to differences in page formatting, figures and tables may not appear in the same locations in the text or be formatted the same compared to the original article. Cross–referencing between figures, tables, chapters, sections, and appendices was also updated to be consistent with the rest of this thesis.

On Mathematical Notation and Scaling

As in Chapter 4, the mathematical notation and scaling of quantities used in this appendix are the same as used in Arendt (2023), which is not the same as that used in the rest of this work. Conversions between the quantities found in Arendt (2023) and the rest of this work are shown in Table 4.1.

B.1 Analysis of Select Symplectic Methods of Various Orders

Here we consider the application of explicit symplectic methods to the test cases outlined in Chapter 4.2 and the resulting energy fluctations and drifts. First, the test case solutions will be examined fo both the momentum–position form (4.38) and position–momentum form (4.39) using generic coefficients.

B.1.1 Test Case: Simple Harmonic Oscillator

The equations for an intermediate step in a symplectic integration method for the simple harmonic oscillator, as defined in (4.1) and (4.2), are either

$$p_n = p_{n-1} - P_n q_{n-1} \mathrm{d}t \tag{B.1a}$$

$$q_n = q_{n-1} + Q_n p_n \mathrm{d}t \tag{B.1b}$$

for momentum–position methods or

$$q_n = q_{n-1} + Q_n p_{n-1} \mathrm{d}t \tag{B.2a}$$

$$p_n = p_{n-1} - P_n q_n \mathrm{d}t \tag{B.2b}$$

for position–momentum methods.

One of the simplest ways to analyze the energy conservation of symplectic methods for this system is via recursion relations. The first step in this analysis is to assume that the solution after a pair of intermediate steps can be written as

$$q_n = q_0 \left[1 + \sum_{m=1}^{n} (-1)^m A_{nm} \mathrm{d}t^{2m}\right] + p_0 \left[\sum_{m=1}^{n} (-1)^{m-1} B_{nm} \mathrm{d}t^{2m-1}\right] \tag{B.3a}$$

$$p_n = p_0 \left[1 + \sum_{m=1}^{n} (-1)^m C_{nm} \mathrm{d}t^{2m}\right] - q_0 \left[\sum_{m=1}^{n} (-1)^{m-1} D_{nm} \mathrm{d}t^{2m-1}\right]; \tag{B.3b}$$

where A_{nm}, B_{nm}, C_{nm}, and D_{nm} are the coefficients that need to be found. The resulting recursion relations are shown in Table B.1.

	Momentum–position methods		Position–momentum methods	
$A_{n,m}$	1	$m = 0$	1	$m = 0$
	$A_{n-1,m} + Q_n D_{n,m}$	$m \leq n$	$A_{n-1,m} + Q_n D_{n-1,m}$	$m < n$
$B_{n,m}$	$B_{n-1,m} + Q_n C_{n,m-1}$	$m \leq n$	$B_{n-1,m} + Q_n C_{n-1,m-1}$	$m \leq n$
$C_{n,m}$	1	$m = 0$	1	$m = 0$
	$C_{n-1,m} + P_n B_{n-1,m}$	$m < n$	$C_{n-1,m} + P_n B_{n,m}$	$m \leq n$
$D_{n,m}$	$D_{n-1,m} + P_n A_{n-1,m-1}$	$m \leq n$	$D_{n-1,m} + P_n A_{n,m-1}$	$m \leq n$

Table B.1: Recursion relations for coefficients in the solution the SHO via symplectic methods.

The resulting energy after a single step is

$$
\begin{aligned}
E(t + \mathrm{d}t) = E(t) &+ \sum_{n=1}^{N} (-1)^n \big[D_{N,n} - B_{N,n} \big] q_0 p_0 \ \mathrm{d}t^{2n-1} \\
&+ \sum_{n=1}^{N} (-1)^n \big[A_{N,n} q_0^2 + C_{N,n} p_0^2 \big] \mathrm{d}t^{2n} \\
&+ \sum_{\substack{n=1 \\ m=1}}^{N} (-1)^{n+m} \big[C_{N,n} D_{N,m} - A_{N,n} B_{N,m} \big] q_0 p_0 \ \mathrm{d}t^{2(n+m)-1} \\
&+ \sum_{\substack{n=1 \\ m=1}}^{N} (-1)^{n+m} \left[\frac{A_{N,n} A_{N,m}}{2} q_0^2 + \frac{C_{N,n} C_{N,m}}{2} p_0^2 \right] \mathrm{d}t^{2(n+m)} \\
&+ \sum_{\substack{n=1 \\ m=1}}^{N} (-1)^{n+m} \left[\frac{D_{N,n} D_{N,m}}{2} q_0^2 + \frac{B_{N,n} B_{N,m}}{2} p_0^2 \right] \mathrm{d}t^{2(n+m-1)}.
\end{aligned}
\tag{B.4}
$$

Alternatively, the change in energy can be expressed as

$$
\begin{aligned}
\Delta E(t + \mathrm{d}t) &= E(t + \mathrm{d}t) - E(t) \\
&= \sum_{n=1}^{2N} \Big[\lambda_n q^2(t) + \gamma_n p^2(t) \Big] \mathrm{d}t^{2n} + q(t) p(t) \sum_{n=1}^{2N} \sigma_n \mathrm{d}t^{2n-1},
\end{aligned}
\tag{B.5}
$$

where λ_n, γ_n, and σ_n are the coefficients resulting from (B.4). Without specifying the terms Q_n and P_n, it is not possible to fully examine all terms; however general outcomes can be considered.

For terms of odd order, there are two possible cases: either σ_n is zero or it isn't, with a non-zero value meaning that there is a phase dependent change in energy. For terms of even order, there are multiple cases to consider:

- If $\lambda_n = \gamma_n = 0$, then there is no change in energy
- If $\lambda_n = \gamma_n \neq 0$, then the change in energy is constant.
- If $\lambda_n = -\gamma_n$, then the change in energy is phase dependent.
- In all other cases, there will be a combination of a constant change and a phase dependent change.

If the numerical solution is a close enough approximation to the analytical solution, then the frequency of the phase dependent energy changes will be double the frequency of the oscillator and will average to zero over the cycle. As such, the average change in energy per step occurs at the order for which $\lambda_n + \gamma_n \neq 0$. For the sets of coefficients analyzed in B, the energy fluctuations are dominated by phase dependent fluctuations, with the steady energy drift only occurring at higher orders and therefore with smaller amplitude.

B.1.2 Test Case: Particle in a Magnetic Field

Technically, the symplectic methods described previously are designed to handle separable Hamiltonians (Yoshida, 1992), and the Hamiltonian for a charged particle in a magnetic field is nonseparable. Although there are methods for splitting nonseparable Hamiltonians (Tao, 2016b), and other methods have been specifically developed for this type of system (Qin et al., 2016, Xiao et al., 2015, Tao, 2016a), the analysis of this system will be done with method forms described in (4.38) and (4.39).

B.1.2.1 Hamiltonian Formulation

One of the simplest adaptions of integration equations is

$$\vec{p}_n = \vec{p}_{n-1} - P_n \vec{\nabla}_q H(\vec{r}_{n-1}, \vec{p}_{n-1}) \mathrm{d}t \tag{B.6a}$$

$$\vec{r}_n = \vec{r}_{n-1} + Q_n \vec{\nabla}_p H(\vec{r}_{n-1}, \vec{p}_n) \mathrm{d}t \tag{B.6b}$$

for momentum–position methods and

$$\vec{r}_n = \vec{r}_{n-1} + Q_n \vec{\nabla}_p H(\vec{r}_{n-1}, \vec{p}_{n-1}) \mathrm{d}t \tag{B.7a}$$

$$\vec{p}_n = \vec{p}_{n-1} - P_n \vec{\nabla}_q H(\vec{r}_n, \vec{p}_{n-1}) \mathrm{d}t \tag{B.7b}$$

for position–momentum methods. Using the form of the Hamiltonian from (4.19), the intermediate points can be expanded to

$$\vec{p}_n = \left[\bar{\bar{I}} + \frac{1}{2}P_n\mathrm{d}t\bar{\bar{\omega}}\right]\vec{p}_{n-1} + \left[\frac{1}{4}P_n\mathrm{d}t\bar{\bar{\omega}}^2\right]\vec{r}_{n-1} \tag{B.8a}$$

$$\vec{r}_n = \left[\bar{\bar{I}} + \frac{1}{2}Q_n\mathrm{d}t\bar{\bar{\omega}} + \frac{1}{4}Q_nP_n\mathrm{d}t^2\bar{\bar{\omega}}^2\right]\vec{r}_{n-1} + \left[Q_n\mathrm{d}t\bar{\bar{I}} + \frac{1}{2}Q_nP_n\mathrm{d}t^2\bar{\bar{\omega}}\right]\vec{p}_{n-1} \tag{B.8b}$$

or

$$\vec{r}_n = \left[\bar{\bar{I}} + \frac{1}{2}Q_n\mathrm{d}t\bar{\bar{\omega}}\right]\vec{r}_{n-1} + \left[Q_n\mathrm{d}t\bar{\bar{I}}\right]\vec{p}_{n-1} \tag{B.9a}$$

$$\vec{p}_n = \left[\bar{\bar{I}} + \frac{1}{2}P_n\mathrm{d}t\bar{\bar{\omega}} + \frac{1}{4}Q_nP_n\mathrm{d}t^2\bar{\bar{\omega}}^2\right]\vec{p}_{n-1} + \left[\frac{1}{4}P_n\mathrm{d}t\bar{\bar{\omega}}^2 + \frac{1}{8}Q_nP_n\mathrm{d}t^2\bar{\bar{\omega}}^2\right]\vec{r}_{n-1} \tag{B.9b}$$

depending on the method used.

An interesting aspect of this problem appears if the particle velocity is considered after a pair of steps have occurred, calculated by

$$\vec{v}_n = \vec{p}_n + \frac{1}{2}\bar{\bar{\omega}}\vec{r}_n. \tag{B.10}$$

The velocity is found to be given by

$$\vec{v}_n = \left[\bar{\bar{I}} + \frac{1}{2}(Q_n + P_n)\mathrm{d}t\bar{\bar{\omega}} + \frac{1}{4}Q_nP_n\mathrm{d}t^2\bar{\bar{\omega}}^2\right]\vec{v}_{n-1} \tag{B.11}$$

regardless of which method is used. This means that the velocity at $t + \mathrm{d}t$ is given by

$$\vec{v}(t + \mathrm{d}t) = \left[\bar{\bar{I}} + \sum_{n}^{2N} \beta_n\mathrm{d}t^n\bar{\bar{\omega}}^n\right]\vec{v}(t) \tag{B.12}$$

where β_n is the set of coefficients calculated from the product of (B.11) over all values of the index n. The energy will therefore change in a similar fashion to that described in equation (A.21).

B.1.2.2 Newtonian Formulation

While symplectic integration methods are designed to solve Hamilton's equations of motion, the Newtonian formulation of a particle in a magnetic field will be considered for the purpose of of comparing with the Hamiltonian formulation and with Runge-Kutta methods. However, only the case of a time independent field will be considered.

First, define the matrix $\bar{\bar{\omega}}_n$ as per (A.15a), so that the numerical integration equations are either[1]

$$\vec{p}_n = \vec{p}_{n-1} + P_n \; \bar{\bar{\omega}}_{n-1}\vec{p}_{n-1} \; \mathrm{d}t, \tag{B.13a}$$

$$\vec{r}_n = \vec{r}_{n-1} + Q_n \; \vec{p}_n \; \mathrm{d}t; \tag{B.13b}$$

or

$$\vec{r}_n = \vec{r}_{n-1} + Q_n \; \vec{p}_{n-1} \; \mathrm{d}t, \tag{B.14a}$$

$$\vec{p}_n = \vec{p}_{n-1} + P_n \; \bar{\bar{\omega}}_n\vec{p}_{n-1} \; \mathrm{d}t. \tag{B.14b}$$

The final, updated momentum/velocity of the particle is

$$\vec{p}(t+\mathrm{d}t) = \prod_{n=1}^{N} \left[\bar{\bar{I}} + P_n\mathrm{d}t \; \bar{\bar{\omega}}_{n-1}\right] \vec{p}(t) \tag{B.15a}$$

for momentum–position methods and

$$\vec{p}(t+\mathrm{d}t) = \prod_{n=1}^{N} \left[\bar{\bar{I}} + P_n\mathrm{d}t \; \bar{\bar{\omega}}_{n}\right] \vec{p}(t) \tag{B.15b}$$

for position–momentum methods. The solution is of the same form as that of the Hamiltonian formulation although here the magnetic field is no longer constant.

In the case of spatially varying field, the intermediate position $\vec{r}_n$ to first order is

$$\vec{r}_n \approx \vec{r}_0 + \sum_{m=1}^{n} Q_n\mathrm{d}t \; \vec{p}_0, \tag{B.16}$$

regardless of the method used. If the magnetic field varies slowly enough, it can be approximated as

$$\bar{\bar{\omega}}_n \approx \bar{\bar{\omega}}_0 + \sum_{m=1}^{n} Q_n\mathrm{d}t \; \bar{\bar{\omega}}_0', \tag{B.17}$$

similar to (A.15). This means that the change in momentum can be approximated as either

$$\vec{p}(t+\mathrm{d}t) = \prod_{n=1}^{N} \left[\bar{\bar{I}} + P_n\mathrm{d}t \; \bar{\bar{\omega}}_0 + P_n \sum_{m=1}^{n-1} Q_n\mathrm{d}t^2 \; \bar{\bar{\omega}}_0'\right] \vec{p}(t) \tag{B.18a}$$

---

[1] As noted earlier, for a system in which there are no electric fields, particle momentum and particle velocity are interchangeable.

or

$$\vec{p}(t + \mathrm{d}t) = \prod_{n=1}^{N} \left[\bar{\bar{I}} + P_n \mathrm{d}t \; \bar{\bar{\omega}}_0 + P_n \sum_{m=1}^{n} Q_n \mathrm{d}t^2 \; \bar{\bar{\omega}}_0' \right] \vec{p}(t), \tag{B.18b}$$

depending on the method used. If the field is also uniform, then the change in momentum can be calculated by setting $\bar{\bar{\omega}}_0' = 0$. In this case, the momentum can be written in the same form as (B.12), with the coefficients calculated similarily.

B.1.3 Symplectic Methods of Various Orders

Given that the energy fluctuations and violations cannot be as neatly summerized for symplectic methods as they can for Runge-Kutta methods, the listing of the methods and their analysis are split. Listed here are symplectic methods of second, third, and fourth order. Analysis of these methods can be found in B.1.4 for the SHO and B.1.5 for a particle in a magnetic field.

B.1.3.1 Second Order

The second order method Ruth (1983), also referred to a leapfrog method, is setup such that the one of the quantities (momentum or position) is only updated once, while the other is updated using the average of its derivative evaluated at the initial and final points of the first quantity. This can be seen from the coefficients in Table B.2.

(a) Coefficients for the second order momentum-position method (PQ2)			(b) Coefficients for the second order position-momentum method (QP2)		
n	Q_n	P_n	n	Q_n	P_n
1	1	$\frac{1}{2}$	1	$\frac{1}{2}$	1
2	0	$\frac{1}{2}$	2	$\frac{1}{2}$	0

Table B.2: Second order symplectic integration method coefficients.

B.1.3.2 Third Order

The third order method analyzed here, first discovered by Ruth (1983), involves both forward and reverse intermediate steps (see Table B.3). Ruth (1983) specifically formulated the coefficients for the momentum–position form; others, such as Yoshida (1992), use them for the position–momentum form.

(a) Coefficients for the third order momentum-position method (PQ3)

n	Q_n	P_n
1	$\frac{2}{3}$	$\frac{7}{24}$
2	$-\frac{2}{3}$	$\frac{18}{24}$
3	1	$-\frac{1}{24}$

(b) Coefficients for the third order position-momentum method (QP3)

n	Q_n	P_n
1	$\frac{7}{24}$	$\frac{2}{3}$
2	$\frac{18}{24}$	$-\frac{2}{3}$
3	$-\frac{1}{24}$	1

Table B.3: Third order symplectic integration method coefficients.

B.1.3.3 Fourth Order

Coefficients for a fourth order symplectic integrator were discovered by Forest and Ruth (1990), while Yoshida (1990) showed that higher order methods can be constructed via compositions of lower order methods, provided the method order is even. The fourth order coefficients are shown in Table B.4.

(a) Coefficients for the fourth order momentum-position method (PQ4)

n	Q_n	P_n
1	$\frac{2\cdot 2^{1/3}+2^{2/3}+4}{6}$	$\frac{2\cdot 2^{1/3}+2^{2/3}+4}{12}$
2	$-\frac{2\cdot 2^{1/3}+2^{2/3}+1}{3}$	$\frac{2-2^{2/3}-2\cdot 2^{1/3}}{12}$
3	$\frac{2\cdot 2^{1/3}+2^{2/3}+4}{6}$	$\frac{2-2^{2/3}-2\cdot 2^{1/3}}{12}$
4	0	$\frac{2\cdot 2^{1/3}+2^{2/3}+4}{12}$

(b) Coefficients for the fourth order position-momentum method (QP4)

n	Q_n	P_n
1	$\frac{2\cdot 2^{1/3}+2^{2/3}+4}{12}$	$\frac{2\cdot 2^{1/3}+2^{2/3}+4}{6}$
2	$\frac{2-2^{2/3}-2\cdot 2^{1/3}}{12}$	$-\frac{2\cdot 2^{1/3}+2^{2/3}+1}{3}$
3	$\frac{2-2^{2/3}-2\cdot 2^{1/3}}{12}$	$\frac{2\cdot 2^{1/3}+2^{2/3}+4}{6}$
4	$\frac{2\cdot 2^{1/3}+2^{2/3}+4}{12}$	0

Table B.4: Fourth order symplectic integration method coefficients.

B.1.4 Analysis of Symplectic Methods for the SHO

Here, we present the results of the analysis of the considered symplectic methods for the simple harmonic oscillator. Results are grouped by order method with a summary included after (Section B.1.4.4).

B.1.4.1 Second Order Methods

Table B.5 shows the resulting coefficients for the solution to the SHO, while Table B.6 shows the coefficients for the energy. The resulting equation for the energy after

(a) SHO solution coefficients as per the second order momentum–position method.

n	$A_{2,n}$	$B_{2,n}$	$C_{2,n}$	$D_{2,n}$
1	$\frac{1}{2}$	1	$\frac{1}{2}$	1
2	0	0	0	$\frac{1}{4}$

(b) SHO solution coefficients as per the second order position–momentum method.

n	$A_{2,n}$	$B_{2,n}$	$C_{2,n}$	$D_{2,n}$
1	$\frac{1}{2}$	1	$\frac{1}{2}$	1
2	0	$\frac{1}{4}$	0	0

Table B.5: Solution coefficients for the simple harmonic oscillator using the second order methods.

(a) SHO energy coefficients as per the second order momentum–position method.

n	λ_n	γ_n	σ_n
1	0	0	0
2	$-\frac{1}{8}$	$\frac{1}{8}$	$\frac{1}{4}$
3	$\frac{1}{32}$	0	$-\frac{1}{8}$

(b) SHO energy coefficients as per the second order position–momentum method.

n	λ_n	γ_n	σ_n
1	0	0	0
2	$\frac{1}{8}$	$-\frac{1}{8}$	$-\frac{1}{4}$
3	0	$\frac{1}{32}$	$\frac{1}{8}$

Table B.6: Energy coefficients for the simple harmonic oscillator using the second order methods.

a step has been completed is

$$\begin{aligned} E_{pq}(t+\mathrm{d}t) = E(t) + q(t)^2 \frac{1}{32}\mathrm{d}t^6 \\ + q(t)p(t)\left[\frac{1}{4}\mathrm{d}t^3 - \frac{1}{8}\mathrm{d}t^5\right] - \left[q^2(t) - p^2(t)\right]\frac{1}{8}\mathrm{d}t^4 \end{aligned} \tag{B.19a}$$

for the momentum–position method, or

$$\begin{aligned} E_{qp}(t+\mathrm{d}t) = E(t) + p(t)^2 \frac{1}{32}\mathrm{d}t^6 \\ - q(t)p(t)\left[\frac{1}{4}\mathrm{d}t^3 - \frac{1}{8}\mathrm{d}t^5\right] + \left[q^2(t) - p^2(t)\right]\frac{1}{8}\mathrm{d}t^4 \end{aligned} \tag{B.19b}$$

for the position–momentum method. By assuming that $q(t)$ and $p(t)$ are accurate representations of 4.4 and any affect of the energy drift on the phase of the oscillator is negligible over a single oscillation period, the energy drift can be written as

$$\begin{aligned}\frac{E_{pq}(t+\mathrm{d}t)}{E(t)} &= 1+\frac{1}{32}\mathrm{d}t^6\\ &\quad+\sin(2\phi(t))\left[\frac{1}{4}\mathrm{d}t^3\right]\left[1-\frac{1}{2}\mathrm{d}t^2\right]\\ &\quad-\cos(2\phi(t))\left[\frac{1}{4}\mathrm{d}t^4\right]\left[1-\frac{1}{8}\mathrm{d}t^2\right]\end{aligned} \tag{B.20a}$$

and

$$\begin{aligned}\frac{E_{qp}(t+\mathrm{d}t)}{E(t)} &= 1+\frac{1}{32}\mathrm{d}t^6\\ &\quad-\sin(2\phi(t))\left[\frac{1}{4}\mathrm{d}t^3\right]\left[1-\frac{1}{2}\mathrm{d}t^2\right]\\ &\quad+\cos(2\phi(t))\left[\frac{1}{4}\mathrm{d}t^4\right]\left[1-\frac{1}{8}\mathrm{d}t^2\right]\end{aligned} \tag{B.20b}$$

where $\phi(t)$ is the phase of the oscillator at time t. From (B.20), it can be seen that the constant component of the energy drift is the same for both forms of the second order method, and is given by and is given by

$$\frac{E(t+\mathrm{d}t)}{E(t)} = 1+\frac{1}{32}\mathrm{d}t^6. \tag{B.21}$$

Comparing this result to the various fourth order Runge-Kutta methods, it can be seen that the second order symplectic methods have the same order for the average fractional change in energy per step. What is not taken into account with this comparison is effect of the lower order terms on the energy as a function of time. These terms result in a fluctuation in the energy, where the frequency of the fluctuations is double that of the oscillator. Furthermore, the lower order terms will dominate the change in energy with a relative amplitude of $1/4\mathrm{d}t^3$ compared to the relative magnitude of the constant increase at $1/32\mathrm{d}t^6$, assuming a step size that is less than one.

B.1.4.2 Third Order Methods

(a) SHO solution coefficients as per the third order momentum–position method.

n	$A_{2,n}$	$B_{2,n}$	$C_{2,n}$	$D_{2,n}$
1	$\frac{1}{2}$	1	$\frac{1}{2}$	1
2	$\frac{5}{72}$	$\frac{1}{6}$	$\frac{1}{72}$	$\frac{1}{6}$
3	$\frac{7}{1728}$	$\frac{1}{72}$	0	$\frac{7}{1728}$

(b) SHO solution coefficients as per the third order position–momentum method.

n	$A_{2,n}$	$B_{2,n}$	$C_{2,n}$	$D_{2,n}$
1	$\frac{1}{2}$	1	$\frac{1}{2}$	1
2	$\frac{1}{72}$	$\frac{1}{6}$	$\frac{5}{72}$	$\frac{1}{6}$
3	0	$\frac{7}{1728}$	$\frac{7}{1728}$	$\frac{1}{72}$

Table B.7: Solution coefficients for the simple harmonic oscillator using the third order methods.

(a) SHO energy coefficients as per the third order momentum–position method.

n	λ_n	γ_n	σ_n
2	$\frac{1}{36}$	$-\frac{1}{36}$	0
3	$-\frac{1}{48}$	$\frac{1}{48}$	$\frac{113}{1728}$
4	$\frac{13}{3456}$	$-\frac{23}{10368}$	$-\frac{7}{384}$
5	$-\frac{1631}{5971968}$	$\frac{1}{10368}$	$\frac{197}{124416}$
6	$\frac{49}{5971968}$	0	$-\frac{7}{124416}$

(b) SHO energy coefficients as per the third order position–momentum method.

n	λ_n	γ_n	σ_n
2	$-\frac{1}{36}$	$\frac{1}{36}$	0
4	$-\frac{23}{10368}$	$\frac{13}{3456}$	$\frac{7}{384}$
4	$-\frac{23}{10368}$	$\frac{13}{3456}$	$\frac{7}{384}$
5	$\frac{1}{10368}$	$-\frac{1631}{5971968}$	$-\frac{197}{124416}$
6	0	$\frac{49}{5971968}$	$\frac{7}{124416}$

Table B.8: Energy coefficients for the simple harmonic oscillator using the third order methods.

Table B.7 shows the resulting coefficients for the solution to the SHO, while Table B.8 shows the coefficients for the energy. The resulting equation for the energy after a step has been completed is

$$\begin{aligned} E_{pq}(t+\mathrm{d}t) = E(t) &+ q^2(t)\left[\frac{1}{648}\mathrm{d}t^8 - \frac{1055}{5971968}\mathrm{d}t^{10} + \frac{49}{5971968}\mathrm{d}t^{12}\right] \\ &+ q(t)p(t)\left[\frac{113}{1728}\mathrm{d}t^5 - \frac{7}{384}\mathrm{d}t^7 + \frac{197}{124416}\mathrm{d}t^9 - \frac{7}{124416}\mathrm{d}t^{11}\right] \\ &+ \left[q^2(t) - p^2(t)\right]\left[\frac{1}{36}\mathrm{d}t^4 - \frac{1}{48}\mathrm{d}t^6 + \frac{23}{10368}\mathrm{d}t^8 - \frac{1}{10368}\mathrm{d}t^{10}\right] \end{aligned} \tag{B.22a}$$

for the momentum–position method, or

$$\begin{aligned}E_{qp}(t+\mathrm{d}t) = E(t) + p^2(t)&\left[\frac{1}{648}\mathrm{d}t^8 - \frac{1055}{5971968}\mathrm{d}t^{10} + \frac{49}{5971968}\mathrm{d}t^{12}\right] \\ - q(t)p(t)&\left[\frac{113}{1728}\mathrm{d}t^5 - \frac{7}{384}\mathrm{d}t^7 + \frac{197}{124416}\mathrm{d}t^9 - \frac{7}{124416}\mathrm{d}t^{11}\right] \\ - \left[q^2(t) - p^2(t)\right]&\left[\frac{1}{36}\mathrm{d}t^4 - \frac{1}{48}\mathrm{d}t^6 + \frac{23}{10368}\mathrm{d}t^8 - \frac{1}{10368}\mathrm{d}t^{10}\right]\end{aligned} \tag{B.22b}$$

for the position–momentum method. As with the second order method, (4.4) is used for $q(t)$ and $p(t)$ to find

$$\begin{aligned}\frac{E_{pq}(t+\mathrm{d}t)}{E(t)} &= 1 + \frac{1}{648}\mathrm{d}t^8 - \frac{1055}{5971968}\mathrm{d}t^{10} + \frac{49}{5971968}\mathrm{d}t^{12} \\ &+ \sin(2\phi(t))\left[\frac{113}{1728}\mathrm{d}t^5\right]\left[1 - \frac{63}{226}\mathrm{d}t^2 + \frac{197}{8136}\mathrm{d}t^4 - \frac{7}{8136}\mathrm{d}t^6\right] \\ &+ \cos(2\phi(t))\left[\frac{1}{18}\mathrm{d}t^4\right]\begin{bmatrix}1 - \frac{3}{4}\mathrm{d}t^6 + \frac{31}{288}\mathrm{d}t^8 \\ - \frac{2207}{331776}\mathrm{d}t^{10} + \frac{49}{331776}\mathrm{d}t^{12}\end{bmatrix}\end{aligned} \tag{B.23a}$$

and

$$\begin{aligned}\frac{E_{pq}(t+\mathrm{d}t)}{E(t)} &= 1 + \frac{1}{648}\mathrm{d}t^8 - \frac{1055}{5971968}\mathrm{d}t^{10} + \frac{49}{5971968}\mathrm{d}t^{12} \\ &- \sin(2\phi(t))\left[\frac{113}{1728}\mathrm{d}t^5\right]\left[1 - \frac{63}{226}\mathrm{d}t^2 + \frac{197}{8136}\mathrm{d}t^4 - \frac{7}{8136}\mathrm{d}t^6\right] \\ &- \cos(2\phi(t))\left[\frac{1}{18}\mathrm{d}t^4\right]\begin{bmatrix}1 - \frac{3}{4}\mathrm{d}t^6 + \frac{31}{288}\mathrm{d}t^8 \\ - \frac{2207}{331776}\mathrm{d}t^{10} + \frac{49}{331776}\mathrm{d}t^{12}\end{bmatrix}\end{aligned} \tag{B.23b}$$

As with the second order method, the constant energy drift component is the same for both methods:

$$\frac{E(t+\mathrm{d}t)}{E(t)} = 1 + \frac{1}{648}\mathrm{d}t^8 - \frac{1055}{5971968}\mathrm{d}t^{10} + \frac{49}{5971968}\mathrm{d}t^{12}. \tag{B.24}$$

Comparing this result to the various fourth order Runge-Kutta methods, it can be seen that the constant energy drift component for the third order symplectic methods is smaller than the Runge-Kutta methods, provided the step size is less than one. That said, the phase dependent fluctuations dominate the change in energy compared to the constant component.

B.1.4.3 Fourth Order Methods

Tables B.9 and B.10 shows the SHO solution coefficients, while Tables B.11 and B.12 show the coefficients for the energy when using either the momentum–position method or the position–momentum method, respectively. For these coefficients, the lowest order change in energy is fifth order, and the average change per cycle is tenth order.

n	1	2	3	4
$A_{4,n}$	$\frac{1}{2}$	$\frac{1}{24}$	$-\frac{5\cdot 2^{1/3}+4\cdot 2^{2/3}+6}{288}$	0
$B_{4,n}$	1	$\frac{1}{6}$	$-\frac{4\cdot 2^{1/3}+3\cdot 2^{2/3}+4}{144}$	0
$C_{4,n}$	$\frac{1}{2}$	$\frac{1}{24}$	$-\frac{5\cdot 2^{1/3}+4\cdot 2^{2/3}+6}{288}$	0
$D_{4,n}$	1	$\frac{1}{6}$	$-\frac{2^{1/3}+2^{2/3}}{144}$	$-\frac{20\cdot 2^{1/3}+16\cdot 2^{2/3}+25}{1728}$

Table B.9: SHO solution coefficients as per the fourth order momentum–position method.

n	1	2	3	4
$A_{4,n}$	$\frac{1}{2}$	$\frac{1}{24}$	$-\frac{5\cdot 2^{1/3}+4\cdot 2^{2/3}+6}{288}$	0
$B_{4,n}$	1	$\frac{1}{6}$	$-\frac{2^{1/3}+2^{2/3}}{144}$	$-\frac{20\cdot 2^{1/3}+16\cdot 2^{2/3}+25}{1728}$
$C_{4,n}$	$\frac{1}{2}$	$\frac{1}{24}$	$-\frac{5\cdot 2^{1/3}+4\cdot 2^{2/3}+6}{288}$	0
$D_{4,n}$	1	$\frac{1}{6}$	$-\frac{4\cdot 2^{1/3}+3\cdot 2^{2/3}+4}{144}$	0

Table B.10: SHO solution coefficients as per the fourth order position–momentum method.

B.1.4.4 Symplectic SHO Analysis Summary

In each of the symplectic methods analyzed, the energy drift is dominated by phase dependent fluctuations while the constant component of the energy drift is several orders higher. Table B.13 shows the results to lowest order for each component.

n	λ_n	γ_n	σ_n
3	$\frac{3\cdot 2^{1/3}+2\cdot 2^{2/3}+4}{288}$	$-\frac{3\cdot 2^{1/3}+2\cdot 2^{2/3}+4}{288}$	$-\frac{3\cdot 2^{1/3}+2\cdot 2^{2/3}+4}{144}$
4	$\frac{14\cdot 2^{1/3}+12\cdot 2^{2/3}+17}{3456}$	$-\frac{14\cdot 2^{1/3}+12\cdot 2^{2/3}+17}{3456}$	$-\frac{2\cdot 2^{1/3}+4\cdot 2^{2/3}+1}{1728}$
5	$-\frac{16\cdot 2^{1/3}+13\cdot 2^{2/3}+20}{13824}$	$\frac{20\cdot 2^{1/3}+16\cdot 2^{2/3}+25}{10368}$	$\frac{17\cdot 2^{1/3}+14\cdot 2^{2/3}+21}{3456}$
6	$\frac{54\cdot 2^{1/3}+43\cdot 2^{2/3}+68}{165888}$	$\frac{92\cdot 2^{1/3}+73\cdot 2^{2/3}+116}{165888}$	$-\frac{74\cdot 2^{1/3}+59\cdot 2^{2/3}+93}{41472}$
7	$\frac{504\cdot 2^{1/3}+400\cdot 2^{2/3}+635}{1990656}$	0	$-\frac{373\cdot 2^{1/3}+296\cdot 2^{2/3}+470}{497664}$

Table B.11: SHO energy coefficients as per the fourth order momentum–position method.

n	λ_n	γ_n	σ_n
3	$-\frac{3\cdot 2^{1/3}+2\cdot 2^{2/3}+4}{288}$	$\frac{3\cdot 2^{1/3}+2\cdot 2^{2/3}+4}{288}$	$\frac{3\cdot 2^{1/3}+2\cdot 2^{2/3}+4}{144}$
4	$-\frac{14\cdot 2^{1/3}+12\cdot 2^{2/3}+17}{3456}$	$\frac{14\cdot 2^{1/3}+12\cdot 2^{2/3}+17}{3456}$	$\frac{2\cdot 2^{1/3}+4\cdot 2^{2/3}+1}{1728}$
5	$\frac{20\cdot 2^{1/3}+16\cdot 2^{2/3}+25}{10368}$	$-\frac{16\cdot 2^{1/3}+13\cdot 2^{2/3}+20}{13824}$	$-\frac{17\cdot 2^{1/3}+14\cdot 2^{2/3}+21}{3456}$
6	$\frac{92\cdot 2^{1/3}+73\cdot 2^{2/3}+116}{165888}$	$\frac{54\cdot 2^{1/3}+43\cdot 2^{2/3}+68}{165888}$	$\frac{74\cdot 2^{1/3}+59\cdot 2^{2/3}+93}{41472}$
7	0	$\frac{504\cdot 2^{1/3}+400\cdot 2^{2/3}+635}{1990656}$	$\frac{373\cdot 2^{1/3}+296\cdot 2^{2/3}+470}{497664}$

Table B.12: SHO energy coefficients as per the fourth order position–momentum method.

Form	Order	Phase dependent drift	Constant drift
PQ	2	$+\frac{1}{4}\mathrm{d}t^3\sin(2\phi(t))$	$\frac{1}{32}\mathrm{d}t^6$
QP	2	$-\frac{1}{4}\mathrm{d}t^3\sin(2\phi(t))$	$\frac{1}{32}\mathrm{d}t^6$
PQ	3	$+\frac{1}{18}dt^4\cos(2\phi(t))$	$\frac{1}{648}\mathrm{d}t^8$
QP	3	$-\frac{1}{18}dt^4\cos(2\phi(t))$	$\frac{1}{648}\mathrm{d}t^8$
PQ	4	$-\frac{3\cdot 2^{1/3}+2\cdot 2^{2/3}+4}{144}\mathrm{d}t^5\sin(2\phi(t))$	$\frac{32\cdot 2^{1/3}+25\cdot 2^{2/3}+40}{41472}\mathrm{d}t^{10}$
QP	4	$+\frac{3\cdot 2^{1/3}+2\cdot 2^{2/3}+4}{144}\mathrm{d}t^5\sin(2\phi(t))$	$\frac{32\cdot 2^{1/3}+25\cdot 2^{2/3}+40}{41472}\mathrm{d}t^{10}$

Table B.13: Lowest order terms for the energy drift in Symplectic integration methods for the SHO.

B.1.5 Analysis of Symplectic Methods for a Particle in a Magnetic Field

Next, we present the results of the analysis of the considered symplectic methods for a particle in a magnetic field. As with the SHO analysis, results are grouped by order method with a summary included after (Section B.1.4.4).

B.1.5.1 Second Order Methods

The velocity and energy coefficients for the Hamiltonian formulation of a particle in a magnetic field are shown in Table B.14. The coefficients are same for both forms of the method, as per (B.11), since the coefficients are swapped between forms. The results for the Newtonian formulation are shown in Table B.15.

n	β_n	α_{2n}
1	1	$\frac{3}{8}$
2	$\frac{5}{16}$	$\frac{9}{256}$
3	$\frac{1}{32}$	$\frac{1}{1024}$
4	0	0

Table B.14: Solution (β) and energy (α) coefficients for the particle in a uniform, static magnetic field using the second order methods and the Hamiltonian formulation. Since the method forms swap coefficients, the results are same for both forms.

(a) Particle in a magnetic field solution and energy coefficients as per the second order momentum–position method.

n	β_n	α_{2n}
1	1	$\frac{1}{2}$
2	$\frac{1}{4}$	$\frac{1}{16}$

(b) Particle in a magnetic field solution and energy coefficients as per the second order position–momentum method.

n	β_n	α_{2n}
1	1	1
2	0	0

Table B.15: Solution (β) and energy (α) coefficients for the particle in a uniform, static magnetic field using the second order methods and the Newtonian formulation. Note that unlike with the Hamiltonian formulation, the coefficients are not the same.

The energy drift, to lowest order, of the Hamiltonian formulation for this these methods is therefore

$$E(t + \mathrm{d}t) = E_{\|}(t) + E_{\perp}(t)\left[1 + \frac{3}{8}|\vec{\omega}\mathrm{d}t|^2\right], \tag{B.25}$$

while the Newtonian formulation has an energy drift of

$$E(t + \mathrm{d}t) = E_{\|}(t) + E_{\perp}(t)\left[1 + \frac{1}{2}|\vec{\omega}\mathrm{d}t|^2\right] \tag{B.26a}$$

for the momentum–position method and

$$E(t + \mathrm{d}t) = E_{\|}(t) + E_{\perp}(t)\left[1 + |\vec{\omega}\mathrm{d}t|^2\right] \tag{B.26b}$$

for the position–momentum method. Note that the energy drift is second order for both methods regardless of the formulation used.

B.1.5.2 Third Order Methods

As expected, the third order methods fail for a particle in a magnetic field regardless of whether the Hamiltonian or Newtonian formulation is used. As with the second order methods examined, the energy drift is of second order and positive, as per Tables B.16 and B.17 leading to an exponential increase. To lowest order, the energy drift is

$$E(t + \mathrm{d}t) = E_{\|}(t) + E_{\perp}(t)\left[1 + \frac{731}{1152}|\vec{\omega}\mathrm{d}t|^2\right] \tag{B.27}$$

for the Hamiltonian formulation, while the Newtonian formulation has an energy drift of

$$E(t + \mathrm{d}t) = E_{\|}(t) + E_{\perp}(t)\left[1 + \frac{187}{288}|\vec{\omega}\mathrm{d}t|^2\right] \tag{B.28a}$$

for the momentum–position form and

$$E(t + \mathrm{d}t) = E_{\|}(t) + E_{\perp}(t)\left[1 + \frac{17}{9}|\vec{\omega}\mathrm{d}t|^2\right] \tag{B.28b}$$

for the position–momentum form.

B.1.5.3 Fourth Order Methods

Table B.18 show the solution and energy coefficients for the particle in a uniform, static magnetic field using the fourth order methods and the Hamiltonian formulation. Note that since the methods swap coefficients, the results are identical. To lowest

n	β_n	α_{2n}
1	1	$\frac{731}{1152}$
2	$\frac{421}{2304}$	$\frac{261203}{1769472}$
3	$-\frac{185}{2048}$	$\frac{47562769}{3057647616}$
4	$-\frac{11021}{331776}$	$\frac{78094609}{110075314176}$
5	$-\frac{383}{165888}$	$\frac{524819}{55037657088}$
6	$\frac{7}{110592}$	$\frac{49}{12230590464}$

Table B.16: Solution (β) and energy (α) coefficients for the particle in a uniform, static magnetic field using the third order methods and the Hamiltonian formulation. Since the method forms swap coefficients, the results are same for both forms.

(a) Particle in a magnetic field solution and energy coefficients as per the third order momentum–position method.

n	β_n	α_{2n}
1	1	$\frac{187}{288}$
2	$\frac{101}{576}$	$\frac{16249}{331776}$
3	$-\frac{7}{768}$	$\frac{49}{589824}$

(b) Particle in a magnetic field solution and energy coefficients as per the third order position–momentum method.

n	β_n	α_{2n}
1	1	$\frac{17}{9}$
2	$-\frac{4}{9}$	$\frac{88}{81}$
3	$-\frac{4}{9}$	$\frac{16}{81}$

Table B.17: Solution and energy coefficients for the particle in a uniform, static magnetic field using the second order methods and the Newtonian formulation. Note that unlike with the Hamiltonian formulation, the coefficients are not the same.

order, the energy drift for the fourth order methods and Hamiltonian formulation is

$$E(t + \mathrm{d}t) = E_{\parallel}(t) + E_{\perp}(t)\left[1 + \frac{17 + 11 \cdot 2^{1/3} + 9 \cdot 2^{2/3}}{24}|\vec{\omega}\mathrm{d}t|^2\right]. \tag{B.29}$$

Tables B.19 and B.20 show the solution and energy coefficients for the particle in a uniform, static magnetic field using the fourth order methods and the Newtonian formulation. Note that unlike with the Hamiltonian formulation, the coefficients are not the same. The energy drift with the Newtonian formulation is given by

$$E(t + \mathrm{d}t) = E_{\parallel}(t) + E_{\perp}(t)\left[1 + \frac{3 + 2^{1/3} + 2^{2/3}}{6}|\vec{\omega}\mathrm{d}t|^2\right] \tag{B.30a}$$

n	β_n	α_{2n}
1	1	$\frac{17+11\cdot 2^{1/3}+9\cdot 2^{2/3}}{24}$
2	$\frac{7-11\cdot 2^{1/3}-9\cdot 2^{2/3}}{48}$	$\frac{666+518\cdot 2^{1/3}+413\cdot 2^{2/3}}{1536}$
3	$-\frac{34+43\cdot 2^{1/3}+35\cdot 2^{2/3}}{192}$	$\frac{9606+7604\cdot 2^{1/3}+6039\cdot 2^{2/3}}{73728}$
4	$-\frac{524+526\cdot 2^{1/3}+431\cdot 2^{2/3}}{9216}$	$\frac{243396+193091\cdot 2^{1/3}+153266\cdot 2^{2/3}}{14155776}$
5	$\frac{76+42\cdot 2^{1/3}+29\cdot 2^{2/3}}{18432}$	$\frac{50840+40347\cdot 2^{1/3}+32023\cdot 2^{2/3}}{56623104}$
6	$\frac{65+50\cdot 2^{1/3}+39\cdot 2^{2/3}}{36864}$	$\frac{14961+11874\cdot 2^{1/3}+9424\cdot 2^{2/3}}{1358954496}$
7	$-\frac{25+20\cdot 2^{1/3}+16\cdot 2^{2/3}}{221184}$	$\frac{635+504\cdot 2^{1/3}+400\cdot 2^{2/3}}{16307453952}$
8	0	0

Table B.18: Solution (β) and energy (α) coefficients for the particle in a uniform, static magnetic field using the fourth order methods and the Hamiltonian formulation. Since the method forms swap coefficients, the results are same for both forms.

n	β_n	α_{2n}
1	1	$\frac{3+2^{1/3}+2^{2/3}}{6}$
2	$\frac{3-2^{2/3}-2^{1/3}}{12}$	$\frac{10+6\cdot 2^{1/3}+5\cdot 2^{2/3}}{96}$
3	$-\frac{2^{1/3}+2^{2/3}}{24}$	$\frac{6+4\cdot 2^{1/3}+3\cdot 2^{2/3}}{1152}$
4	$\frac{2\cdot 2^{1/3}+2^{2/3}+4}{576}$	$\frac{4+3\cdot 2^{1/3}+2\cdot 2^{2/3}}{55296}$

Table B.19: Particle in a magnetic field solution (β) and energy (α) coefficients as per the fourth order momentum–position method with the Newtonian formulation.

for the momentum–position form and

$$E(t+\mathrm{d}t) = E_{\parallel}(t) + E_{\perp}(t)\left[1 + \frac{7 + 5\cdot 2^{1/3} + 4\cdot 2^{2/3}}{3}|\vec{\omega}\mathrm{d}t|^2\right] \tag{B.30b}$$

for the position–momentum form. As with the second and third order methods, the fourth order method does not conserve the kinetic energy of a particle moving through a magnetic field.

B.1.5.4 Symplectic SHO Analysis Summary

As has been demonstrated here, none of the symplectic methods considered conserve the kinetic energy of a particle in a magnetic field, with the energy drift being

n	β_n	α_{2n}
1	1	$\frac{7+5\cdot 2^{1/3}+4\cdot 2^{2/3}}{3}$
2	$-\frac{4+5\cdot 2^{1/3}+4\cdot 2^{2/3}}{6}$	$\frac{56+44\cdot 2^{1/3}+35\cdot 2^{2/3}}{12}$
3	$-\frac{6+5\cdot 2^{1/3}+4\cdot 2^{2/3}}{6}$	$\frac{116+92\cdot 2^{1/3}+73\cdot 2^{2/3}}{36}$
4	0	0

Table B.20: Particle in a magnetic field solution (β) and energy (α) coefficients as per the fourth order position–momentum method with the Newtonian formulation.

Form	Method Order	Hamiltonian α_2	Newtonian α_2
PQ	2	$\frac{3}{8}$	$\frac{1}{2}$
QP	2	$\frac{3}{8}$	1
PQ	3	$\frac{731}{1152}$	$\frac{187}{288}$
QP	3	$\frac{731}{1152}$	$\frac{17}{9}$
PQ	4	$\frac{17+11\cdot 2^{1/3}+9\cdot 2^{2/3}}{24}$	$\frac{3+2^{1/3}+2^{2/3}}{6}$
QP	4	$\frac{17+11\cdot 2^{1/3}+9\cdot 2^{2/3}}{24}$	$\frac{7+5\cdot 2^{1/3}+4\cdot 2^{2/3}}{3}$

Table B.21: Lowest order terms for the energy drift in Symplectic integration methods for a particle in a magnetic field.

second order regardless of the method order. Moreover, the energy drift rate increase with method order, as can be seen from the increase in the value of α_n as the method order increases. Results are summarized, to lowest order, in Table B.21.

Appendix C

Noisy Slab Field Calibration

As discussed in Chapter 5, the determination of the number of waves modes and range of wave modes required for a given parameter set needs to take into account the particle energy due to the parallel resonance prediction of QLT. Furthermore, it is reasonable to assume that the strength of any resonance is a function of the energy contained in the wave with which the resonance is occurring. As a result, stronger turbulence should have stronger parallel scattering, leading to a lower parallel diffusion coefficient. This is readily demonstrated with the results presented here and in Chapter 6.

Two basic questions that arise from this are “How many Fourier modes are needed?” and “How large should the maximum mode number be?”. The first question is related to the distribution of energy among the wave modes. Since the total energy in the turbulence is fixed, the total energy between wave modes k_1 and k_2 is also fixed; increasing the number of modes between k_1 and k_2 means that the energy in each mode will decrease. This decrease in energy will reduce the strength of the resulting scattering when a particle interacts with a particular mode. Opposing this reduced scattering is the increase in the number of potential scattering interactions resulting from the increase in the number of modes. Therefore, what the first question is fundamentally asking is this: “How many modes are required such that the combination of decreased scattering per mode balances out the increase in potential scattering interactions, resulting in a stable diffusion coefficient?”. Given the QLT parallel resonance, it can be expected that for a given model the number of waves required is primarily dependent on the particle energy.

The second question is related to the amount of energy contained in wave modes with large wave numbers. Using the general spectrum given by (2.15), the energy per mode goes to zero as the wave number k goes to infinity. While the implications of this were discussed in Chapter 5, it was left open as to how large a maximum wave number is needed for a given parameter set. To address this, consider the following: as the turbulence energy density (δb^2) increases, the amplitude of all the waves used increases. As it is expected that the scattering is a function of the energy (amplitude) of the mode the particle is interacting with, this increase in amplitude should increase the strength of the resulting scattering. Conversely, decreasing the turbulence energy density decreases the wave amplitude, lowering the scattering strength. Based on this reasoning, it should be expected that if there is a difference in the required maximum wave number for the parameters considered, it will be most obvious when comparing $\delta b^2 = 0.2$ and $\delta b^2 = 2.0$.

C.1 Rigidity: $R = 0.01$

The running diffusion coefficients for $R = 0.01$ and turbulence energy density ratios of $\delta b^2 = 0.2$ and $\delta b^2 = 2.0$ are shown in Figures C.1 and C.2, respectively, for various values of N and M. It can clearly be seen that the results for the lower turbulence energy density are more dependent on the number of parallel waves than the higher turbulence energy density.

Averaging over the different values of M (sub–figures (c) and (d) C.1 and C.2) used indicates that for the low turbulence energy a minimum of $N = 256$ parallel modes are needed. For the higher turbulence energy density, the parallel results are not as clear due to the fluctuations in the $N = 128$ results. In the perpendicular data however, values of $N > 128$ produce nearly identical results. As a result, it was determined that the minimum value of $N = 256$ would be used in further simulations.

Having established the number of parallel waves needed, the next step was to determine the required number of perpendicular waves. From sub–figures (e) and (f) in C.1 and C.2, it can be seen that the value of M has very little effect on the results. The apparent difference in effect on the perpendicular transport can be attributed to noise in the results, due to the fact that the effect reverses itself between the high and low energy fields.[1] Based on this, the number of perpendicular waves to be used

---

[1] The effect could also be real, although it is quite small compared the effect of the number of parallel modes.

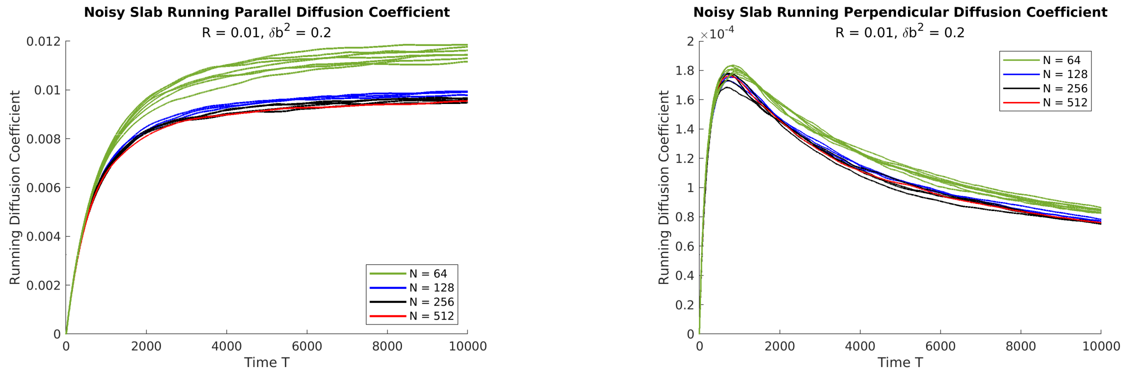

(a) Parallel transport: raw data

(b) Perpendicular transport: raw data

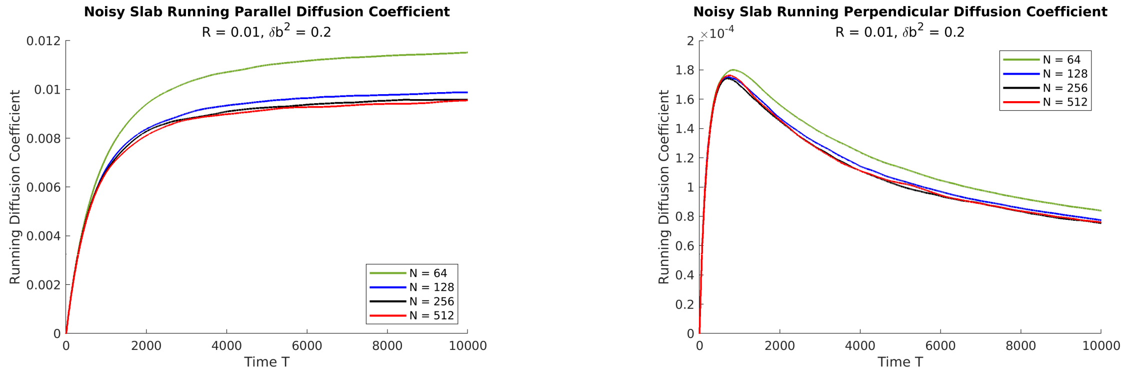

(c) Parallel transport: averaged data, parallel wave mode density

(d) Perpendicular transport: averaged data, parallel wave mode density

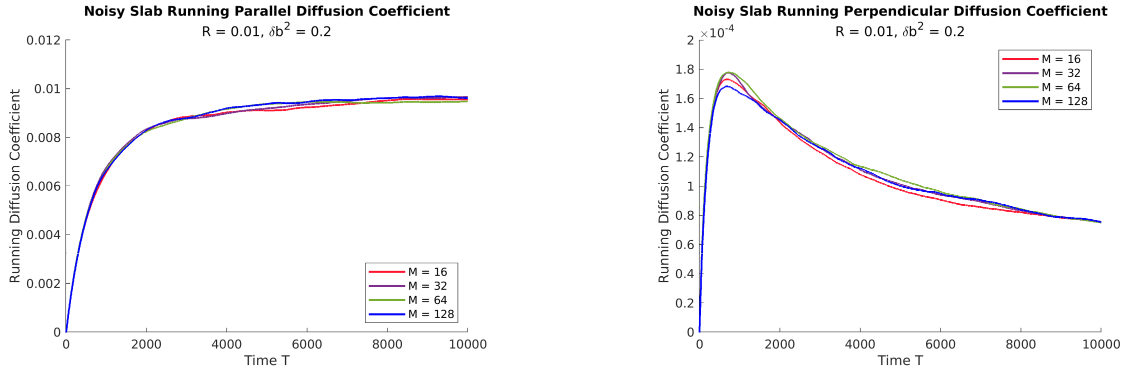

(e) Parallel transport: averaged data, perpendicular wave mode density, $N = 256$

(f) Perpendicular transport: averaged data, perpendicular wave mode density, $N = 256$

Figure C.1: The effect of wave number density on the running diffusion coefficients for particles with $R = 0.1$ and $\delta b^2 = 0.2$. Colour coding: sub–figures (a)–(d), number of parallel wave modes; sub–figures (e)–(f), number of perpendicular wave modes.

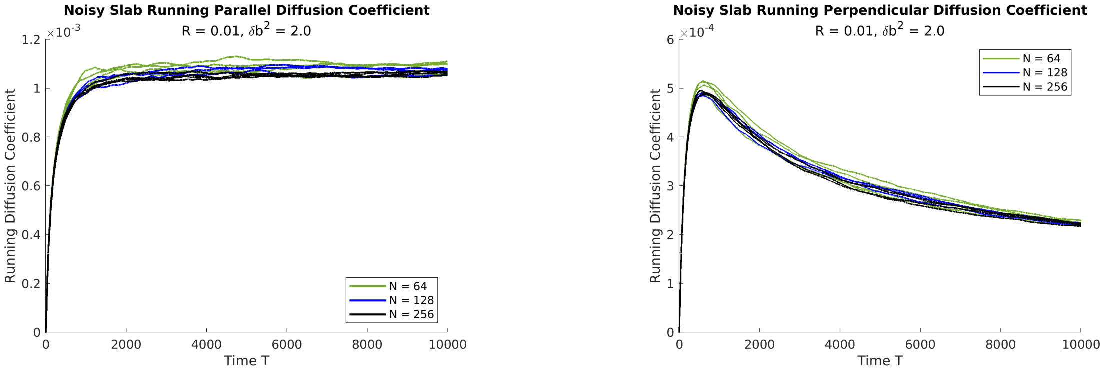

(a) Parallel transport: raw data

(b) Perpendicular transport: raw data

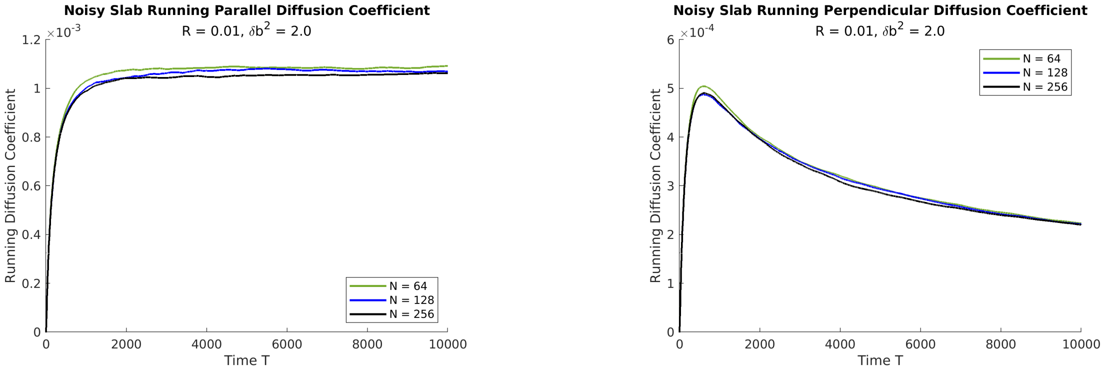

(c) Parallel transport: averaged data, parallel wave mode density

(d) Perpendicular transport: averaged data, parallel wave mode density

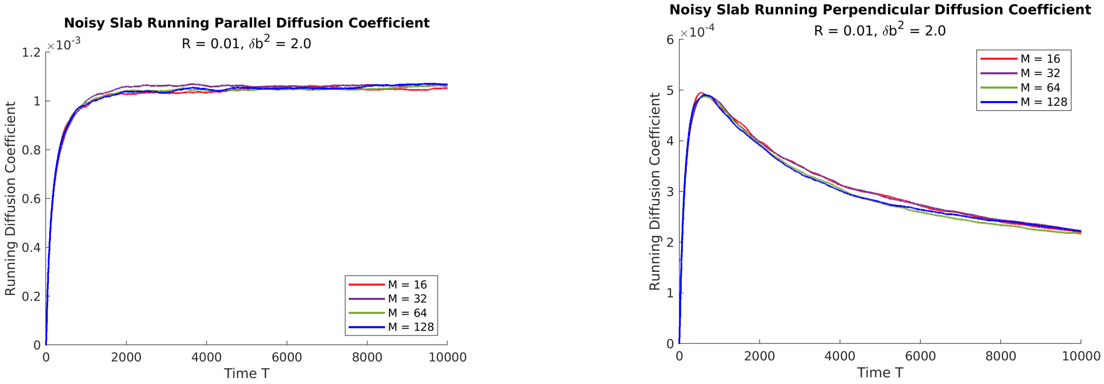

(e) Parallel transport: averaged data, perpendicular wave mode density, $N = 256$

(f) Perpendicular transport: averaged data, perpendicular wave mode density, $N = 256$

Figure C.2: The effect of wave number density on the running diffusion coefficients for particles with $R = 0.1$ and $\delta B^2 = 2.0$. Colour coding: sub–figures (a)–(d), number of parallel wave modes; sub–figures (e)–(f), number of perpendicular wave modes.

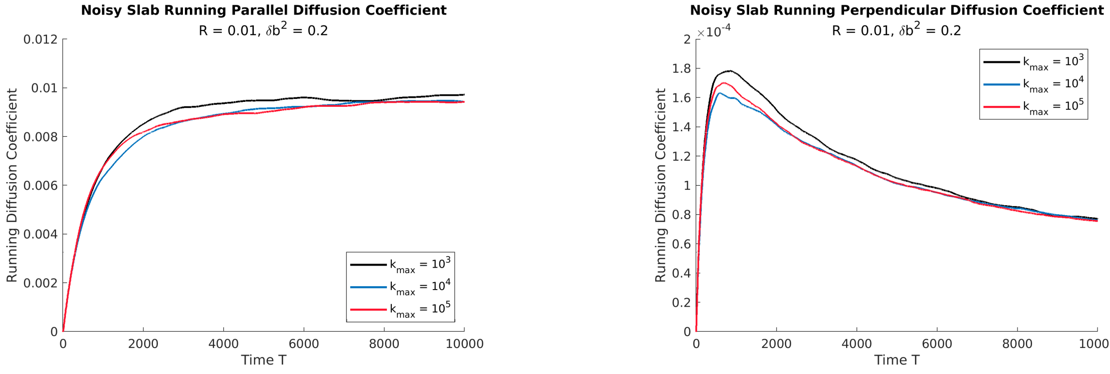

(a) Parallel transport (b) Perpendicular transport

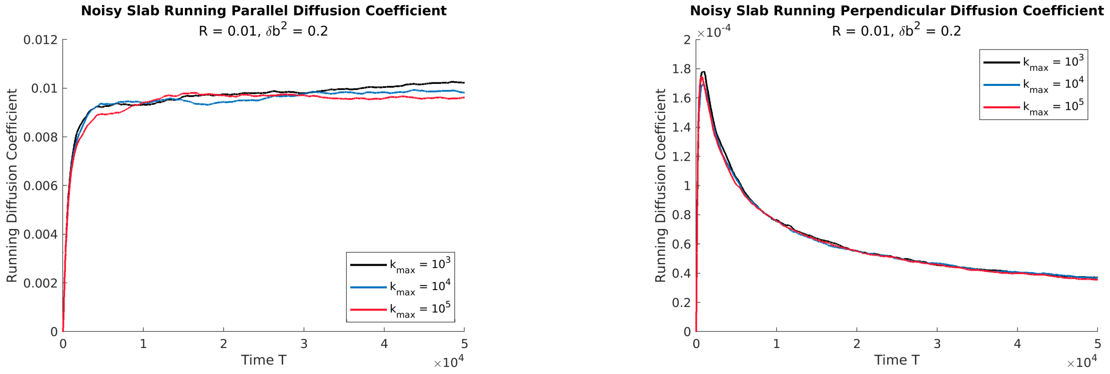

(c) Parallel transport (d) Perpendicular transport

Figure C.3: The effect of the maximum wave number on the running diffusion coefficients for particles with $R = 0.01$ and $\delta b^2 = 0.2$. Results are colour coded based on the maximum wave number. Top: $T_{max} = 10^4$. Bottom: $T_{max} = 5 \cdot 10^4$.

at this rigidity was set to 16.

The final quantity that was determined is the maximum parallel mode required. While the number of parallel and perpendicular waves needed are assumed to be independent, the same assumption cannot be applied to the the relation between the number of parallel waves and the maximum parallel mode. For simplicity, in this work the assumption that is made in this work is that the required number of waves per order magnitude is constant, such that

$$N_d = \frac{N-1}{\log_{10}\left(\frac{k_{max}}{10^{-5}}\right)}, \tag{C.1}$$

which allows for N and k_{max} to be determined independently. From the initial value of $k_{max} = 10^3$ and 256 parallel modes, the minimum mode density is 31.875 waves

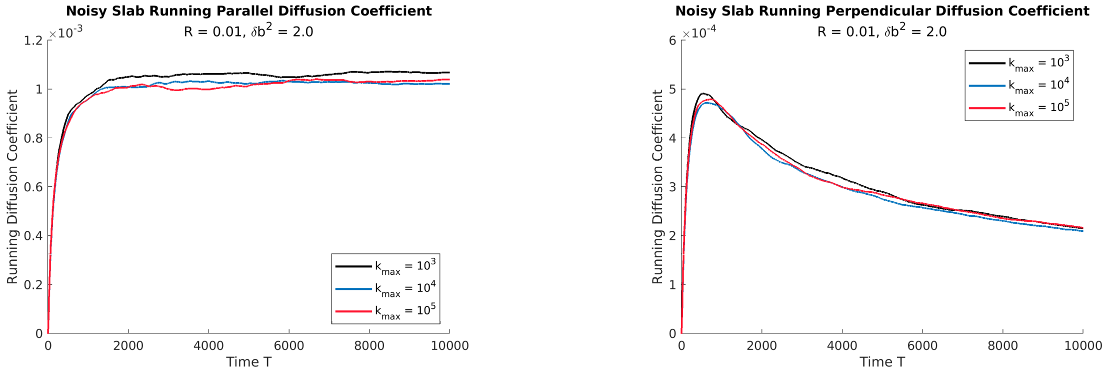

(a) Parallel transport (b) Perpendicular transport

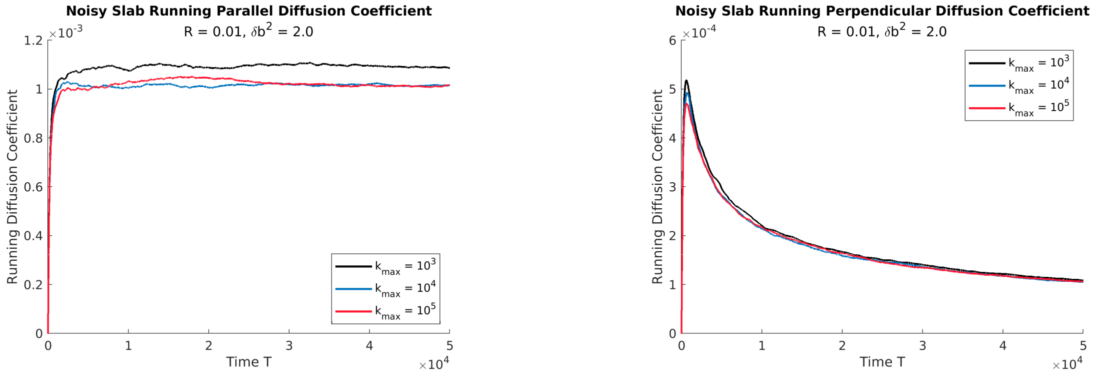

(c) Parallel transport (d) Perpendicular transport

Figure C.4: The effect of the maximum wave number on the running diffusion coefficients for particles with $R = 0.01$ and $\delta b^2 = 2.0$. Results are colour coded based on the maximum wave number. Top: $T_{max} = 10^4$. Bottom: $T_{max} = 5 \cdot 10^4$.

per order magnitude. Using the previously listed guidelines, the number of waves per order magnitude used is $N_{d,used} = 2^{\text{ceil}(\log_2(N_d))} + 1 = 33$. Figures C.3 and C.4 shows the effect of increasing the number of modes. Unfortunately, due to a calculation error at the time, the Fourier mode density for the lower energy turbulence (Figure C.3) was set to $N_d = 17$, not $N_d = 33$. Since there is clear separation between the parallel transport results for $k_{max} = 10^3$ and $k_{max} = 10^4$ for the higher energy turbulence (Figure C.4), the maximum Fourier mode at low particle energies ($R = 0.01, 0.1$) was set to $k_{max} = 10^4$ with $N = 288$ parallel modes for higher energy turbulence ($\delta b^2 = 1, 2$).

Once the initial calibration of the field has been completed, it does not need to be redone in its entirety when changing the particle energy. Rather, it simply needs to be verified for each new rigidity, which can be done using fewer data sets. Table C.1 shows the calibration results for the noisy slab turbulence model, and is an extension of Table 6.2.

Rigidity	Field Energies	N	M	K_{max}	Source
0.01	0.2, 0.5	256	16	10^3	This work
0.01	1.0, 2.0	288	16	10^4	This work
0.10	0.2, 0.5	256	16	10^3	This Work
0.10	1.0, 2.0	288	16	10^4	This Work
0.10	1.0	128	16	10^3	Shalchi and Arendt (2024b)
1.00	0.2, 0.5	128	64	10^3	This Work
1.00	1.0, 2.0	288	64	10^4	This Work
1.00	0.2, 0.5	256	64	10^3	This Work
1.00	1.0, 2.0	320	128	10^5	This Work

Table C.1: Noisy slab model parameters per rigidity and field energy, determined by calibration.

A critical point to consider is that the maximum time used for the low energy particles ($R < 1$) is smaller than the time required for the system to reach a diffusive state in the perpendicular direction. This is, of course, due to the fact that normal diffusion is not restored until a much later time (see Figure 6.1). As such, the apparent lack of effect from the number of perpendicular modes on the diffusion coefficients is due to the simulation time. It is entirely possible that the number of perpendicular modes needs to be higher than 16 for $R < 1$ for accurate calculations, but time required to do so makes such a determination unfeasible.

As discussed in Chapter 6, several modifications to the parameters used in Shalchi and Arendt (2024b) needed to be made in order to make the simulations feasible. Beyond increasing the time step and reducing the number of particles, the values of N and K_{max} were modified, as can be seen in Table C.1. This was done to keep the maximum run time per particle to under seven days, as was required by the computational servers used to perform the simulations for this work.

C.2 Numerical Method and Statistics Testing

In addition to calibrating the magnetic turbulence parameters, both the numerical method and the statistical fluctuation in the diffusion coefficients were tested. To

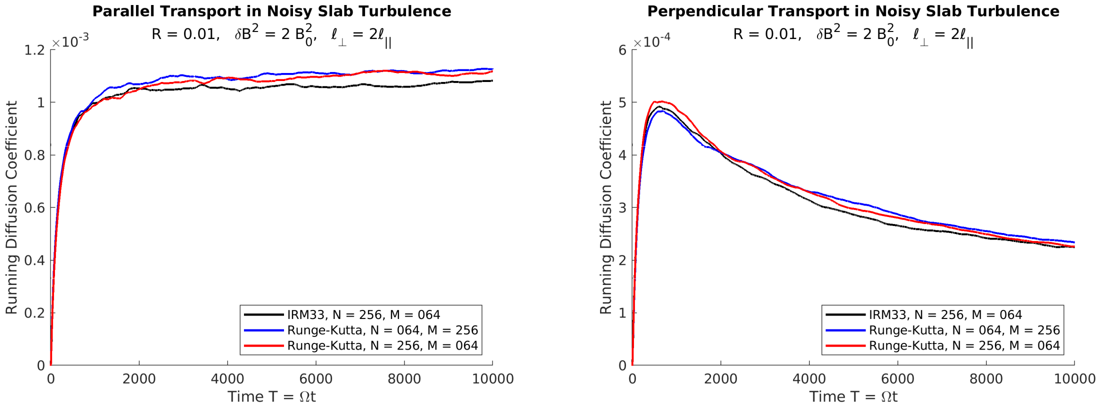

(a) Parallel diffusion coefficient.

(b) Perpendicular diffusion coefficient.

Figure C.5: Comparison of the running diffusion coefficients from simulations using the IRM33 and RK4 methods. As the non–adaptive RK4 method requires an additional evaluation of the magnetic field per time step (see Appendix A), it could not be run out to as large a maximum time.

test the numerical method, the non–adaptive 4^{th} order Runge–Kutta method was employed using $N = 64$ and $M = 256$ as listed in Hussein et al. (2015), as well as with $N = 256$ and $M = 64$, since it was found that the number of parallel modes had an effect on the diffusion coefficients. Since the Runge–Kutta method requires an additional field evaluation per time step and the simulations were done for comparison purposes rather than to reach normal diffusion, these were only run out to $T = 10^4$. The innate perpendicular energy loss from the Runge–Kutta method, described in Appendix A.1.4.1, is estimated to be on the order of 10^{-5} or smaller, and therefore not important in this example.[2] Figure C.5 shows the results of this, where it can be seen that there is little to no difference between the two Runge–Kutta simulations. While the Runge–Kutta simulations have running diffusion coefficients that are slightly larger than those computed from the IRM method simulations, this difference needs to be viewed in the context of the statistical fluctuations on the results.

In order to test the level of statistical fluctuations in the diffusion coefficients, simulations with the basic slab model were performed. These simulations used 3600 particles with $R = 1$, moving in slab turbulence comprised of 256 modes and a

---

[2] Using $\mathrm{d}T = 0.02$ and $T_{max} = 10^7$, as was required to find diffusion for low rigidity particles in noisy slab turbulence, has the potential for a much higher energy loss.

field energy density of $\delta b^2 = 1$. This was repeated 90 times in order to measure the statistical fluctuations, illustrated in Figure C.6. The black lines are the resulting running diffusion coefficients, while the grey lines are the running diffusion coefficients for the 90 individual data sets. Assuming a Gaussian distribution, the expected fluctuation level is calculated as the time averaged ratio of the standard deviation to the mean. This results in a fluctuation level of 2.4% for the parallel coefficient and 3.7% for the perpendicular coefficient. Due to these results, the number of particles per noisy slab and full 3D data set was set to a minimum of 6000 particles. The reason for using the basic slab model for the statistical fluctuation analysis is that the simulations do not require a significant amount of time to complete.

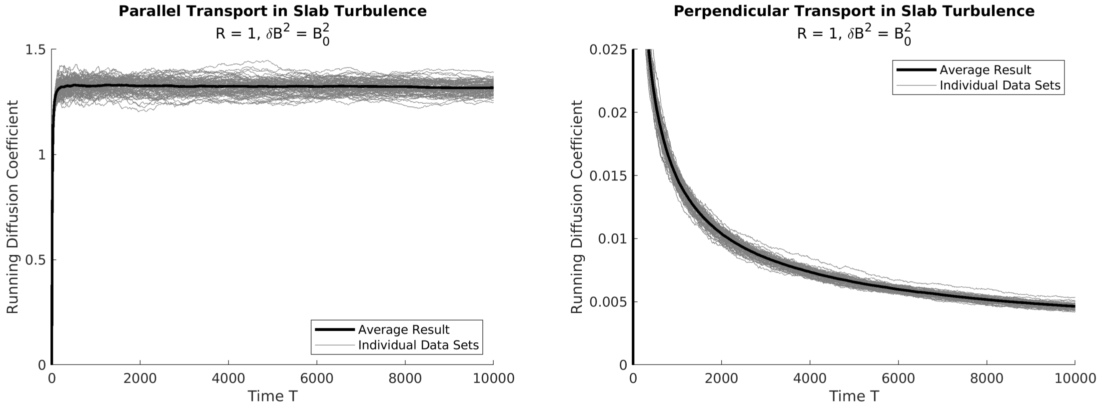

(a) Parallel diffusion coefficient.

(b) Perpendicular diffusion coefficient.

Figure C.6: Statistical fluctuations in running diffusion coefficients using slab turbulence. Black: average running diffusion coefficient. Grey: running diffusion coefficient of individual data sets.

Bibliography

M. Ackermann, M. Ajello, A. Allafort, L. Baldini, J. Ballet, G. Barbiellini, M. G. Baring, and et al. Detection of the Characteristic Pion-Decay Signature in Supernova Remnants. *Science*, 339(6121):807–811, February 2013. doi: 10.1126/science.1231160.

H. Alfvén. Existence of Electromagnetic-Hydrodynamic Waves. *Nature*, 150(3805): 405–406, Oct 1942. ISSN 1476-4687. doi: 10.1038/150405d0. URL `https://doi.org/10.1038/150405d0`.

V. Arendt. Numerical methods, energy conservation, and a new method for particle motion in magnetic fields. *Mathematics and Computers in Simulation*, 205:142–185, mar 2023. ISSN 0378-4754. doi: https://doi.org/10.1016/j.matcom.2022.09.015. URL `https://www.sciencedirect.com/science/article/pii/S0378475422003925`.

V. Arendt and A. Shalchi. Time-dependent transport of energetic particles in magnetic turbulence: computer simulations versus analytical theory. *Astrophysics and Space Science*, 363(6):116, Jun 2018. doi: 10.1007/s10509-018-3338-6.

V. Arendt and A. Shalchi. Detailed test-particle simulations of energetic particles interacting with magnetized plasmas I. Two-component turbulence. *Advances in Space Research*, 66(8):2001–2023, Oct 2020. doi: 10.1016/j.asr.2020.07.024.

V. Arendt and A. Shalchi. Detailed Test-Particle Simulations of Energetic Particles Interacting with Magnetized Plasmas II. Three-Dimensional Turbulence with Small Kubo Numbers. *Advances in Space Research*, 2025. ISSN 0273-1177. doi: https://doi.org/10.1016/j.asr.2025.01.041. URL `https://www.sciencedirect.com/science/article/pii/S0273117725000572`.

E. G. Berezhko and H. J. Völk. Spectrum of Cosmic Rays Produced in Supernova Remnants. *The Astrophysical Journal*, 661(2):L175–L178, June 2007. doi: 10.1086/518737.

E. G. Berezhko, L. T. Ksenofontov, and H. J. Völk. Emission of SN 1006 produced by accelerated cosmic rays. *Astronomy and Astrophysics*, 395:943–953, December 2002. doi: 10.1051/0004-6361:20021219.

J. W. Bieber and W. H. Matthaeus. Perpendicular Diffusion and Drift at Intermediate Cosmic-Ray Energies. ApJ, 485(2):655–659, Aug 1997. doi: 10.1086/304464.

J. W. Bieber, W. H. Matthaeus, C. W. Smith, W. Wanner, M.-B. Kallenrode, and G. Wibberenz. Proton and Electron Mean Free Paths: The Palmer Consensus Revisited. ApJ, 420:294, Jan 1994. doi: 10.1086/173559.

J. W. Bieber, W. Wanner, and W. H. Matthaeus. Dominant two-dimensional solar wind turbulence with implications for cosmic ray transport. J. Geophys. Res., 101 (A2):2511–2522, Feb 1996. doi: 10.1029/95JA02588.

L. Biermann. Kometenschweife und solare Korpuskularstrahlung. *Zeitschrift fur Astrophysik*, 29:274, January 1951.

L. Biermann. Über den Schweif des Kometen Halley im Jahre 1910. *Zeitschrift Naturforschung Teil A*, 7(1):127–136, January 1952. doi: 10.1515/zna-1952-0122.

L. Biermann. Solar corpuscular radiation and the interplanetary gas. *The Observatory*, 77:109–110, June 1957.

M. L. Boas. *Mathematical Methods in the Physical Sciences.* John Wiley & Sons, Inc, third edition, 2006.

J. P. Boris. Proceeding of the fourth conference on numerical simulations of plasmas. page 3. Naval Research Laboratory, Washington DC, 1970, 1970.

L. F. Burlaga, V. Florinski, and N. F. Ness. In Situ Observations of Magnetic Turbulence in the Local Interstellar Medium. *The Astrophysical Journal*, 804(2):L31, May 2015. doi: 10.1088/2041-8205/804/2/L31.

L. F. Burlaga, V. Florinski, and N. F. Ness. Turbulence in the Outer Heliosheath. *The Astrophysical Journal*, 854(1):20, February 2018. doi: 10.3847/1538-4357/aaa45a.

J. C. Butcher. On Runge-Kutta processes of high order. *Journal of the Australian Mathematical Society*, 4(2):179–194, 1964. doi: 10.1017/S1446788700023387.

J. R. Cash and A. H. Karp. A Variable Order Runge-Kutta Method for Initial Value Problems with Rapidly Varying Right-Hand Sides. *ACM Trans. Math. Softw.*, 16 (3):201–222, Sep 1990. ISSN 0098-3500. doi: 10.1145/79505.79507.

S. Corrsin. Progress Report on Some Turbulent Diffusion Research. *Advances in Geophysics*, 6:161, 1959. doi: 10.1016/S0065-2687(08)60102-8.

K. U. Denskat and F. M. Neubauer. Observations of hydromagnetic turbulence in the solar wind. In *NASA Conference Publication*, volume 228 of *NASA Conference Publication*, page 0..81, November 1983.

J. R. Dormand and P.J. Prince. A family of embedded Runge-Kutta formulae. *Journal of Computational and Applied Mathematics*, 6(1):19–26, 1980. ISSN 0377-0427. doi: https://doi.org/10.1016/0771-050X(80)90013-3.

N. Eugene Engelbrecht, F. Effenberger, V. Florinski, M. S. Potgieter, D. Ruffolo, R. Chhiber, A. V. Usmanov, J. S. Rankin, and P. L. Els. Theory of Cosmic Ray Transport in the Heliosphere. *Space Science Reviews*, 218(4):33, Jun 2022. doi: 10.1007/s11214-022-00896-1.

E. Fehlberg. Low-order classical Runge-Kutta formulas with stepsize control and their application to some heat transfer problems. Technical report, NASA, July 1969.

S. E. Forbush. Three Unusual Cosmic-Ray Increases Possibly Due to Charged Particles from the Sun. *Physical Review*, 70(9-10):771–772, November 1946. doi: 10.1103/PhysRev.70.771.

E. Forest and R. D. Ruth. Fourth-order symplectic integration. *Physica D Nonlinear Phenomena*, 43(1):105–117, May 1990. doi: 10.1016/0167-2789(90)90019-L.

C. W. Gardiner. *Handbook of Stochastic Methods for Physics, Chemistry and the Natural Sciences*. Springer, 2nd edition, 1985.

J. Giacalone. Cosmic-Ray Transport and Interaction with Shocks. Space Sci. Rev., 176(1-4):73–88, Jun 2013. doi: 10.1007/s11214-011-9763-2.

J. Giacalone and J. R. Jokipii. Charged-Particle Motion in Multidimensional Magnetic Field Turbulence. ApJ, 430:L137, Aug 1994. doi: 10.1086/187457.

J. Giacalone and J. R. Jokipii. The Transport of Cosmic Rays across a Turbulent Magnetic Field. ApJ, 520(1):204–214, Jul 1999. doi: 10.1086/307452.

I. S. Gradshteyn and I. M Ryzhik. *Table of integrals, series, and products*. Academic Press, 2000.

M. S. Green. Brownian Motion in a Gas of Noninteracting Molecules. J. Chem. Phys., 19(8):1036–1046, Aug 1951. doi: 10.1063/1.1748449.

D. A. Gurnett and W. S. Kurth. Plasma densities near and beyond the heliopause from the Voyager 1 and 2 plasma wave instruments. *Nature Astronomy*, 3:1024–1028, November 2019. doi: 10.1038/s41550-019-0918-5.

A. V. Higuera and J. R. Cary. Structure-preserving second-order integration of relativistic charged particle trajectories in electromagnetic fields. *Physics of Plasmas*, 24(5):052104, May 2017. doi: 10.1063/1.4979989.

M. Honda and Y. S. Honda. Filamentary Jets as a Cosmic-Ray “Zevatron”. *The Astrophysical Journal*, 617(1):L37–L40, December 2004. doi: 10.1086/427067.

M. Hussein, R. C. Tautz, and A. Shalchi. The influence of different turbulence models on the diffusion coefficients of energetic particles. *Journal of Geophysical Research (Space Physics)*, 120(6):4095–4111, Jun 2015. doi: 10.1002/2015JA021060.

J. R. Jokipii. Cosmic-Ray Propagation. I. Charged Particles in a Random Magnetic Field. ApJ, 146:480, Nov 1966. doi: 10.1086/148912.

J. R. Jokipii, J. Kota, and J. Giacalone. Perpendicular transport in 1- and 2-dimensional shock simulations. Geophys. Res. Lett., 20(17):1759–1761, Sep 1993. doi: 10.1029/93GL01973.

F. C. Jones, J. R. Jokipii, and M. G. Baring. Charged-Particle Motion in Electromagnetic Fields Having at Least One Ignorable Spatial Coordinate. ApJ, 509(1):238–243, Dec 1998. doi: 10.1086/306480.

B. B. Kadomtsev and O. P. Pogutse. Electron heat conductivity of the plasma across a 'braided' magnetic field. In *Plasma Physics and Controlled Nuclear Fusion Research 1978, Volume 1*, volume 1, pages 649–662, January 1979.

A. Kolmogorov. The Local Structure of Turbulence in Incompressible Viscous Fluid for Very Large Reynolds' Numbers. *Akademiia Nauk SSSR Doklady*, 30:301–305, Jan 1941.

P. P. Kronberg and R. V. E. Lovelace. Extragalactic circuits, transmission lines, and CR particle acceleration. In *European Physical Journal Web of Conferences*, volume 99 of *European Physical Journal Web of Conferences*, page 13005, Aug 2015. doi: 10.1051/epjconf/20159913005.

R. Kubo. Statistical-Mechanical Theory of Irreversible Processes. I. *Journal of the Physical Society of Japan*, 12(6):570–586, Jun 1957. doi: 10.1143/JPSJ.12.570.

R. Kubo. Stochastic Liouville Equations. *Journal of Mathematical Physics*, 4(2): 174–183, Feb 1963. doi: 10.1063/1.1703941.

J. Lasuik and A. Shalchi. Time-dependent Perpendicular Transport of Energetic Particles for Different Turbulence Configurations and Parallel Transport Models. ApJ, 847(1):9, Sep 2017. doi: 10.3847/1538-4357/aa8720.

J. Lasuik and A. Shalchi. The influence of non-Gaussian distribution functions on the time-dependent perpendicular transport of energetic particles. *Advances in Space Research*, 61(11):2827–2836, Jun 2018. doi: 10.1016/j.asr.2018.03.014.

J. Lasuik and A. Shalchi. Subspace approximations to the cosmic ray Fokker-Planck equation. MNRAS, 485(2):1635–1650, May 2019. doi: 10.1093/mnras/stz474.

M. A. Malkov and L. O'C. Drury. Nonlinear theory of diffusive acceleration of particles by shock waves. *Reports on Progress in Physics*, 64(4):429–481, Apr 2001. doi: 10.1088/0034-4885/64/4/201.

W. H. Matthaeus, M. L. Goldstein, and D. A. Roberts. Evidence for the presence of quasi-two-dimensional nearly incompressible fluctuations in the solar wind. J. Geophys. Res., 95:20673–20683, Dec 1990. doi: 10.1029/JA095iA12p20673.

W. H. Matthaeus, P. C. Gray, Jr. Pontius, D. H., and J. W. Bieber. Spatial Structure and Field-Line Diffusion in Transverse Magnetic Turbulence. Phys. Rev. Lett., 75 (11):2136–2139, Sep 1995. doi: 10.1103/PhysRevLett.75.2136.

W. H. Matthaeus, S. Ghosh, S. Oughton, and D. A. Roberts. Anisotropic three-dimensional MHD turbulence. J. Geophys. Res., 101(A4):7619–7630, Apr 1996. doi: 10.1029/95JA03830.

W. H. Matthaeus, G. Qin, J. W. Bieber, and G. P. Zank. Nonlinear Collisionless Perpendicular Diffusion of Charged Particles. ApJ, 590(1):L53–L56, Jun 2003. doi: 10.1086/376613.

W. H. Matthaeus, J. W. Bieber, D. Ruffolo, P. Chuychai, and J. Minnie. Spectral Properties and Length Scales of Two-dimensional Magnetic Field Models. ApJ, 667(2):956–962, Oct 2007. doi: 10.1086/520924.

D. J. McComas, H. A. Elliott, N. A. Schwadron, J. T. Gosling, R. M. Skoug, and B. E. Goldstein. The three-dimensional solar wind around solar maximum. *Geophysical Research Letters*, 30(10):1517, May 2003. doi: 10.1029/2003GL017136.

M. Neuer and K. H. Spatschek. Diffusion of test particles in stochastic magnetic fields for small Kubo numbers. Phys. Rev. E, 73(2):026404, Feb 2006. doi: 10.1103/PhysRevE.73.026404.

NOAA. Real Time Solar Wind, Jun 2024. URL `https://www.swpc.noaa.gov/products/real-time-solar-wind`. Accessed June 18, 2024.

Nobel Prize Outreach. Award ceremony speech. NobelPrize.org, 1936. URL `https://www.nobelprize.org/prizes/physics/1936/ceremony-speech/`. Accessed Wed. 26 Jun 2024.

S. Oughton, E. R. Priest, and W. H. Matthaeus. The influence of a mean magnetic field on three-dimensional magnetohydrodynamic turbulence. *Journal of Fluid Mechanics*, 280:95–117, Jan 1994. doi: 10.1017/S0022112094002867.

I. D. Palmer. Transport coefficients of low-energy cosmic rays in interplanetary space. *Reviews of Geophysics and Space Physics*, 20:335–351, May 1982. doi: 10.1029/RG020i002p00335.

E. N. Parker. Dynamics of the Interplanetary Gas and Magnetic Fields. *The Astrophysical Journal*, 128:664, November 1958. doi: 10.1086/146579.

E. N. Parker. The passage of energetic charged particles through interplanetary space. Planet. Space Sci., 13(1):9–49, Jan 1965. doi: 10.1016/0032-0633(65)90131-5.

Pierre Auger Collaboration, J. Abraham, P. Abreu, M. Aglietta, C. Aguirre, D. Allard, I. Allekotte, J. Allen, P. Allison, C. Alvarez, and et al. Correlation of the Highest-Energy Cosmic Rays with Nearby Extragalactic Objects. *Science*, 318: 938, Nov 2007. doi: 10.1126/science.1151124.

G. Qin and A. Shalchi. Numerical Test of Different Approximations Used in the Transport Theory of Energetic Particles. ApJ, 823(1):23, May 2016. doi: 10.3847/0004-637X/823/1/23.

G. Qin, W. H. Matthaeus, and J. W. Bieber. Subdiffusive transport of charged particles perpendicular to the large scale magnetic field. Geophys. Res. Lett., 29 (4):1048, Feb 2002. doi: 10.1029/2001GL014035.

H. Qin, J. Liu, J. Xiao, R. Zhang, Y. He, Y. Wang, Y. Sun, J. W. Burby, L. Ellison, and Y. Zhou. Canonical symplectic particle-in-cell method for long-term large-scale simulations of the Vlasov-Maxwell equations. *Nuclear Fusion*, 56(1):014001, Jan 2016. doi: 10.1088/0029-5515/56/1/014001.

B. Ripperda, F. Bacchini, J. Teunissen, C. Xia, O. Porth, L. Sironi, G. Lapenta, and R. Keppens. A Comprehensive Comparison of Relativistic Particle Integrators. *The Astrophysical Journal Supplement Series*, 235(1):21, Mar 2018. doi: 10.3847/1538-4365/aab114.

D. Ruffolo and W. H. Matthaeus. Theory of magnetic field line random walk in noisy reduced magnetohydrodynamic turbulence. *Physics of Plasmas*, 20(1):012308, Jan 2013. doi: 10.1063/1.4789606.

R. D. Ruth. A Canonical Integration Technique. *IEEE Transactions on Nuclear Science*, 30(4):2669, Aug 1983. doi: 10.1109/TNS.1983.4332919.

R. Schlickeiser. *Cosmic Ray Astrophysics*. Springer, 2002.

Y. Sekido, T. Masuda, S. Yoshida, and M. Wada. The Crab Nebula as an Observed Point Source of Cosmic Rays. *Physical Review*, 83(3):658–659, August 1951. doi: 10.1103/PhysRev.83.658.2.

A. Shalchi. Time-dependent transport and subdiffusion of cosmic rays. *Journal of Geophysical Research (Space Physics)*, 110(A9):A09103, Sep 2005a. doi: 10.1029/2005JA011214.

A. Shalchi. Second-order quasilinear theory of cosmic ray transport. *Physics of Plasmas*, 12(5):052905–052905, May 2005b. doi: 10.1063/1.1895805.

A. Shalchi. Analytical forms of correlation functions and length scales of astrophysical turbulence. Ap&SS, 315(1-4):31–43, Jun 2008. doi: 10.1007/s10509-008-9788-5.

A. Shalchi. *Nonlinear Cosmic Ray Diffusion Theories*, volume 362 of *Astrophysics and Space Science Library*. Springer, 2009. doi: 10.1007/978-3-642-00309-7.

A. Shalchi. A Unified Particle Diffusion Theory for Cross-field Scattering: Subdiffusion, Recovery of Diffusion, and Diffusion in Three-dimensional Turbulence. ApJ, 720(2):L127–L130, Sep 2010. doi: 10.1088/2041-8205/720/2/L127.

A. Shalchi. Magnetic Field Line Random Walk in Two-dimensional Turbulence: Markovian Diffusion versus Superdiffusion. *Contributions to Plasma Physics*, 51 (10):920–930, Dec 2011. doi: 10.1002/ctpp.201100106.

A. Shalchi. Perpendicular diffusion of energetic particles in collisionless plasmas. *Physics of Plasmas*, 22(1):010704, Jan 2015. doi: 10.1063/1.4906359.

A. Shalchi. Finite gyroradius corrections in the theory of perpendicular diffusion 2. Strong velocity diffusion. *Advances in Space Research*, 57(1):431–442, Jan 2016. doi: 10.1016/j.asr.2015.10.032.

A. Shalchi. Time-dependent perpendicular transport of energetic particles in magnetic turbulence with transverse complexity. *Physics of Plasmas*, 24(5):050702, May 2017. doi: 10.1063/1.4982805.

A. Shalchi. Field line random walk, field line separation, and particle transport in turbulence with weak transverse complexity. *Advances in Space Research*, 64(12): 2426–2438, Dec 2019a. doi: 10.1016/j.asr.2019.03.005.

A. Shalchi. Heuristic Description of Perpendicular Diffusion of Energetic Particles in Astrophysical Plasmas. *The Astrophysical Journal*, 881(2):L27, August 2019b. doi: 10.3847/2041-8213/ab379d.

A. Shalchi. Perpendicular Transport of Energetic Particles in Magnetic Turbulence. Space Sci. Rev., 216(2):23, Feb 2020. doi: 10.1007/s11214-020-0644-4.

A. Shalchi. Perpendicular Diffusion of Energetic Particles: A Complete Analytical Theory. ApJ, 923(2):209, Dec 2021. doi: 10.3847/1538-4357/ac2363.

A. Shalchi and V. Arendt. Distribution Functions of Energetic Particles Experiencing Compound Subdiffusion. *The Astrophysical Journal*, 890(2):147, Feb 2020. doi: 10.3847/1538-4357/ab6c69.

A. Shalchi and V. Arendt. Simulations of field line random walk in noisy slab turbulence. *Advances in Space Research*, 74(9):4238–4249, Nov 2024a. doi: 10.1016/j.asr.2023.12.017.

A. Shalchi and V. Arendt. On the Relevance of Magnetic Correlation Functions in Energetic Particle Transport Theory. *Brazilian Journal of Physics*, 54(4):126, Aug 2024b. doi: 10.1007/s13538-024-01508-9.

A. Shalchi and I. Kourakis. Analytical description of stochastic field-line wandering in magnetic turbulence. *Physics of Plasmas*, 14(9):092903–092903, Sep 2007. doi: 10.1063/1.2776905.

A. Shalchi and B. Weinhorst. Random walk of magnetic field lines: Subdiffusive, diffusive, and superdiffusive regimes. *Advances in Space Research*, 43(9):1429–1435, May 2009. doi: 10.1016/j.asr.2008.12.022.

A. Shalchi, J. W. Bieber, W. H. Matthaeus, and R. Schlickeiser. Parallel and Perpendicular Transport of Heliospheric Cosmic Rays in an Improved Dynamical Turbulence Model. ApJ, 642(1):230–243, May 2006. doi: 10.1086/500728.

A. Shalchi, T. Skoda, R. C. Tautz, and R. Schlickeiser. Analytical description of nonlinear cosmic ray scattering: isotropic and quasilinear regimes of pitch-angle diffusion. A&A, 507(2):589–597, Nov 2009. doi: 10.1051/0004-6361/200912755.

A. Shalchi, R. C. Tautz, and T. J. Rempel. Test-particle transport: higher-order correlations and time-dependent diffusion. *Plasma Physics and Controlled Fusion*, 53(10):105016, Oct 2011. doi: 10.1088/0741-3335/53/10/105016.

M. Tao. Explicit high-order symplectic integrators for charged particles in general electromagnetic fields. *Journal of Computational Physics*, 327:245–251, Dec 2016a. doi: 10.1016/j.jcp.2016.09.047.

M. Tao. Explicit symplectic approximation of nonseparable Hamiltonians: Algorithm and long time performance. *Physical Review E*, 94(4):043303, Oct 2016b. doi: 10.1103/PhysRevE.94.043303.

R. C. Tautz and A. Dosch. On numerical turbulence generation for test-particle simulations. *Physics of Plasmas*, 20(2):022302, Feb 2013. doi: 10.1063/1.4789861.

R. C. Tautz, A. Shalchi, and R. Schlickeiser. Solving the 90° Scattering Problem in Isotropic Turbulence. ApJ, 685(2):L165, Oct 2008. doi: 10.1086/592498.

G. I. Taylor. Diffusion by Continuous Movements. *Proceedings of the London Mathematical Society*, s2-20(1):196–212, 1922. doi: 10.1112/plms/s2-20.1.196.

A. Teufel and R. Schlickeiser. Analytic calculation of the parallel mean free path of heliospheric cosmic rays. I. Dynamical magnetic slab turbulence and random sweeping slab turbulence. *Astronomy and Astrophysics*, 393:703–715, Oct 2002. doi: 10.1051/0004-6361:20021046.

J.-L. Vay. Simulation of beams or plasmas crossing at relativistic velocity. *Physics of Plasmas*, 15(5):056701, May 2008. doi: 10.1063/1.2837054.

G. M. Webb, G. P. Zank, E. Kh. Kaghashvili, and J. A. le Roux. Compound and Perpendicular Diffusion of Cosmic Rays and Random Walk of the Field Lines. I. Parallel Particle Transport Models. ApJ, 651(1):211–236, Nov 2006. doi: 10.1086/507415.

R. T. Wicks, S. C. Chapman, and R. O. Dendy. Spatial Correlation of Solar Wind Fluctuations and Their Solar Cycle Dependence. *The Astrophysical Journal*, 690 (1):734–742, January 2009. doi: 10.1088/0004-637X/690/1/734.

R. T. Wicks, M. J. Owens, and T. S. Horbury. The Variation of Solar Wind Correlation Lengths Over Three Solar Cycles. *Solar Physics*, 262(1):191–198, March 2010. doi: 10.1007/s11207-010-9509-4.

J. Xiao, H. Qin, J. Liu, Y. He, R. Zhang, and Y. Sun. Explicit high-order non-canonical symplectic particle-in-cell algorithms for Vlasov-Maxwell systems. *Physics of Plasmas*, 22(11):112504, Nov 2015. doi: 10.1063/1.4935904.

H. Yoshida. Construction of higher order symplectic integrators. *Physics Letters A*, 150(5-7):262–268, Nov 1990. doi: 10.1016/0375-9601(90)90092-3.

H. Yoshida. Symplectic Integrators for Hamiltonian Systems: Basic Theory. In S. Ferraz-Mello, editor, *Chaos, Resonance, and Collective Dynamical Phenomena in the Solar System*, volume 152, page 407, Jan 1992.

G. P. Zank. Faltering Steps Into the Galaxy: The Boundary Regions of the Heliosphere. *Annual Review of Astronomy and Astrophysics*, 53:449–500, August 2015. doi: 10.1146/annurev-astro-082214-122254.

G. P. Zank and W. H. Matthaeus. Nearly incompressible fluids. II: Magnetohydrodynamics, turbulence, and waves. *Physics of Fluids A*, 5(1):257–273, Jan 1993. doi: 10.1063/1.858780.

G. P. Zank, Gang Li, V. Florinski, W. H. Matthaeus, G. M. Webb, and J. A. Le Roux. Perpendicular diffusion coefficient for charged particles of arbitrary energy. *Journal of Geophysical Research (Space Physics)*, 109(A4):A04107, Apr 2004. doi: 10.1029/2003JA010301.

G. P. Zank, L. Adhikari, P. Hunana, D. Shiota, R. Bruno, and D. Telloni. Theory and Transport of Nearly Incompressible Magnetohydrodynamic Turbulence. *The Astrophysical Journal*, 835(2):147, February 2017. doi: 10.3847/1538-4357/835/2/147.

G. P. Zank, M. Nakanotani, and G. M. Webb. Compressible and Incompressible Magnetic Turbulence Observed in the Very Local Interstellar Medium by Voyager 1. *The Astrophysical Journal*, 887(2):116, Dec 2019. doi: 10.3847/1538-4357/ab528c.

Y. Zhou and W. H. Matthaeus. Phenomenology treatment of magnetohydrodynamic turbulence with nonequipartition and anisotropya). *Physics of Plasmas*, 12(5): 056503, May 2005. doi: 10.1063/1.1887187.

D. Zwillinger. *Standard Mathematical Tables and Formulae*. CRC Press, 2012.